Universität Rostock Traditio et Innovatio

Optical Properties of yellow Excitons in Cuprous Oxide

Dissertation

zur

Erlangung des akademischen Grades

doctor rerum naturalium (Dr. rer. nat.)

der Mathematisch-Naturwissenschaftlichen Fakultät

der Universität Rostock

vorgelegt von

Dipl.-Phys. Florian Schöne, geboren am 06.03.1988 in Rostock

Rostock, den 06.11.2017

urn:nbn:de:gbv:28-diss2018-0080-1

Gutachter: Prof. Dr. Heinrich Stolz
(Universität Rostock, Institut für Physik)

Prof. Dr. Frank Jahnke
(Universität Bremen, Institut für Theoretische Physik)

Datum der Einreichung: 06.11.2017

Datum der Verteidigung: 13.04.2018

Abstract

Cuprous oxide (Cu_2O) has proven historically as well as contemporarily to be one of the most suitable materials for the research of excitons in bulk semiconductors. This thesis concerns itself with the theoretical description of some optical properties of the yellow exciton series in Cu_2O and is divided into two parts. The first part aims at the determination of the basic excitonic properties by considering central-cell corrections. For large principal quantum numbers n the nonparabolicity of the highest valence band is treated and the concept of quantum defects is introduced. For the analysis of the yellow 1S paraexciton the additional coupling to LO phonons is addressed. The second part examines the absorption edge of the Γ_3^- phonon-assisted transition into the 1S yellow orthoexciton and determines the corresponding deformation potential. The deformation potential is further utilised to calculate the Auger coefficient of the phonon-assisted decay mechanism.

Zusammenfassung

Kupferoxydul (Cu_2O) zeigte sowohl historisch als auch in der Neuzeit, dass es eines der am besten geeigneten Materialien für die Untersuchung von Exzitonen in Halbleitern ist. Die vorliegende Dissertation untersucht einige optische Eigenschaften der gelben Exzitonenserie in Cu_2O und lässt sich in zwei Teile unterteilen. Im ersten Teil werden grundlegende Exzitonenparameter unter Berücksichtigung von *central-cell* Korrekturen bestimmt. Für große Hauptquantenzahlen n wurde hierfür die Nichtparabolizität des höchsten Valenzbandes betrachtet und das Konzept des Quantendefekts eingeführt. Für die Analyse des gelben 1S Paraexzitons musste zusätzlich der Einfluss von LO Phononen berücksichtigt werden. Der zweite Teil befasst sich mit der Absorptionskante des Γ_3^- phononassistierten Übergangs in das gelbe 1S Orthoexziton und bestimmt das dazugehörige Deformationspotential. Mit dem Deformationspotential wurde der Augerkoeffizient für den phononassistierten Zerfall berechnet.

Contents

Chapter 1.

Introduction

Historically, cuprous oxide (Cu_2O) is one of the most significant materials when it comes to research of excitons in bulk semiconductors. While the concept of excitons was already developed theoretically in the 1930s, primarily by J. Frenkel, R. Peierls, and G. Wannier [1–4], they were observed for the first time in 1952 by E. Gross and N. Karryev [5–7], incidentally in Cu_2O. The same discovery was made independently by M. Hayashi and K. Katsuki [8] in the same year. Already back then, the formation of an excitonic series, similar to the excited states of the hydrogen atom, was seen up to a principal quantum number of $n = 8$. This was an impressive feat at the time, considering the spectra were captured on microphotograph back in the day. The exciton series of Cu_2O was always one of the most distinct in bulk semiconductors, for a long time ranging up to a principal quantum number $n = 12$ [9]. The reasoning for this generally refers to their long lifetime and relatively large binding energies [10]. In 2014, there occurred a major discovery as T. Kazimierczuk *et al.* were able to measure highly excited exciton states up to a principal quantum number $n = 25$ [11]. In this regime, it became custom to refer to these states as Rydberg excitons, following their highly excited counterparts known from atomic physics. With this, we just recently entered the realm of Rydberg physics of excitons, i.e. the research on effects that are already known from atomic physics. The great advantage of excitons over atomic systems is a generally easier experimental handling, e.g. similar effects can be observed at higher temperatures with standard laser settings in the visible range and without the need of external field traps.

One effect that was observed in [11] is the Rydberg blockade. The dipole moment of an excited state increases the linewidth of the respective resonance, as well as inducing an energetical shift upon the neighbouring states [12]. The average radius of an exciton of principal quantum number $n = 25$ already reaches a range of approximately $\langle r_{25} \rangle \simeq 1\,\mu\mathrm{m}$, effectively covering a considerable portion of typical samples used for experiments. Another example would be the appearance of quantum coherences between Rydberg excitons due to the spectral proximity of adjacent states [13]. The complex influence of external magnetic fields on the absorption spectrum was investigated theoretically, as well as experimentally [14–16]. This is the basis for the potential creation of giant-dipole states with excitons, as the properties of

the relative motion are easily tuned via external electromagnetic fields. However, the material parameters of the semiconductor need to fulfill certain conditions to enable the creation of a giant-dipole potential [17,18]. Here, the specific properties of Cu_2O excitons, apart from being a prime example for the general behaviour of semiconductor excitons, also recommend them in this novel field of research.
However, apart from phenomena already known, we need to be aware of potentially new characteristics that might emerge due to the unique setting within the crystal. More general issues are presented for example by the mixing of different excitonic series [19–25], the interaction with phonons [26–30], or the influence of defects in the crystal. As an example, an electron-hole plasma induced band-gap shift limits the upper boundary for possibly excitable n [31].
An earlier field of research that was assumed to be a promising application for semiconductor excitons was the creation of an excitonic Bose-Einstein condensate (BEC), due to their small masses compared to atoms. First propositions for a realisation were made already in the 1960s [32, 33], with first experimental attempts made in the 1970s [34, 35]. Again Cu_2O was deemed to be one of the most viable materials due to the long lifetime of its paraexciton state and the band gap being in an energy range that is easily accessible by laser excitation. Although distinct signatures have been seen [36], it was not yet managed to fulfill all criteria to confirm the detection [37]. Although excitons were supposedly thought to be better suited than atomic systems, it was noticed that additional effects inhibit the exciton gas to reach the necessary threshold densities for condensation. A few theoretical attempts were made to explain this phenomenon, e.g. by an excitonic Auger decay [38, 39] or biexciton formation with a subsequent recombination [40] which, however, did not show good alignment with experimental findings [41–43]. The excitonic BEC should not be confused with the condensation of exciton-polaritons which was already realised [44].
Besides its applications in fundamental research, Cu_2O does not gain too much recognition and technical applications were generally not of high priority in the last decades. In the early years of electrical engineering, it was commonly used for all kinds of components, primarily rectifiers; however, it was quickly dismissed for other materials, most prominently silicon. The main reasons are its fairly brittle texture, low durability and frankly the lack of efficiency as an electrical component compared to other semiconductors. The current industrial disinterest entails that the artificial production of crystals is of no high concern. This explains why, up to this point, naturally formed crystals are still preferred by reseachers due to their superior composition and purity. However, some new interest sparked for the application in solar cells quite recently, as it serves as a sustainable, cost-efficient and nontoxic alternative to, e.g. Cadmium solar-cells [45–48].

In this thesis, we will attempt to describe a potpourri of fundamental exciton properties in Cu_2O. Chapter 2 will be used to present the basic properties of our semiconductor of choice, as well as discussing fundamental processes whose existence and rudimentary understanding are mandatory for the forthcoming examinations. Three parts are of particular importance:

First and foremost the origin and properties of the band structure. It presents the origin of all optical properties in semiconductors and, therefore, plays a predominant role in most of this works investigations. For practical applications, we derive the Hamiltonian that will be used to describe the band dispersions around the band gap at zone centre. Second, the emerging exciton series are discussed, since they represent the major focus of this work. Third, we provide a rudimentary description of the occurring phonons as their interactions with the exciton states also tend to play an important role.

In chapter 3 we will solve an enhanced Wannier equation by utilising the approximative band Hamiltonian to include the nonparabolicity of the valence band dispersion. Unlike previous approaches for such a calculation, we solve the problem in momentum space. The deviation of the result from the solution of the ideal Wannier equation will be presented via the quantum defect, a concept taken from atomic physics.

We will notice that this approach is not well suited to describe low n states of the excitonic series due to a phonon-induced energy dependence of the material permittivity. For this, we introduce in chapter 4 a different approach by solving the general two-particle Hamiltonian via a variational method. This enables us to additionally compute the excitonic dispersion, as well as exciton Bohr radius and mass for arbitrary exciton momenta.

In chapter 5 we revise the textbook solution for the description of the phonon-assisted absorption in semiconductors. This is done via second-order perturbation theory and requires the virtual transition over an extra state. In the textbook solution the excitonic nature of those virtual intermediate states is neglected, which will be taken into account in this work. This generalisation reveals the need to treat the deformation potential, that models the phonon interaction, as a momentum dependent quantity.

With the knowledge gained in chapter 5, we will proceed to chapter 6 to revisit earlier calculations on the excitonic Auger recombination rate. This chapter is connected to the previous one as we will transfer over the concept of excitonic intermediate states and momentum dependent deformation potentials to improve upon existing theoretical work.

The final chapter will present a brief summary of all results, their achievements and their shortcomings, as well as an outlook on what might be the prospect of further potential research in this direction.

Beyond that, a topic that possesses an overarching importance for the whole work is the symmetry that is imposed by the crystal structure. The group theoretical treatment ties all points into a common framework that binds different aspects to restrictive properties, thereby limiting the possibilities for interaction to only a few relevant that need to be examined. Its implications on a respective entity will be discussed as necessary in the individual chapters.

Chapter 2.

Theoretical preliminaries

2.1. Band structure

The key element to successfully investigate optical phenomena in a semiconductor is a thorough understanding of its band structure. Its basic properties, such as curvature, spacing and orientation between bands determine the fundamental interaction with light. Another characteristic, that is also of specific interest for the case of Cu_2O, is the symmetry of the different bands. The most important bands are usually the lowest conduction and the highest valence bands.

While the rough characteristic of a semiconductor spectrum is generally set by the distance between bands, the intricate details are determined by curvature and symmetry. The absorption of photons generally starts taking place at the shortest energetic distance between the lowest conduction and highest valence bands, i.e. at their extrema. Due to the small wave number of the photon ($\sim 10^{-3} - 10^{-2}\,\mathrm{nm}^{-1}$) in relation to the size of a generic Brillouin zone ($\sim 1 - 10\,\mathrm{nm}^{-1}$), an excitation via photons between bands is usually assumed to be an almost vertical transition. If the extrema of both bands are in the same position in momentum space, as it is the case in, e.g. Cu_2O and gallium arsenide (GaAs) (direct band gap semiconductors), a direct transition by photons is possible[1]. If their positioning in momentum space differs as in, e.g. selenium (Se) or germanium (Ge) (indirect band gap semiconductors), the transition usually involves additional relaxation processes by phonons to energetically favourable states. The curvature of any particular band results from its interaction with the neighbouring bands. This gives us retroactively the possibility to obtain information of the coupling between those bands, if the curvature is known. Additionally, it is highly influential on the properties of excitons, which will be discussed in the upcoming section 2.3.2. Excitonic effects in Cu_2O are in the focus of this work; therefore, a thorough knowledge of the band structure establishes the foundation for all the upcoming examinations. For further reading refer to [49–53].

[1] If symmetry of the bands allows for a transition. This will be discussed in section 2.3.

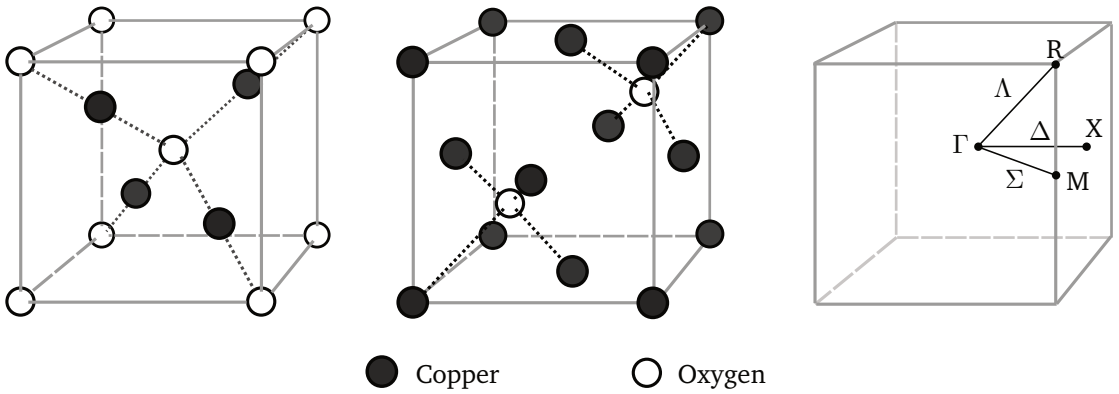

Figure 2.1.: Left and centre: unit cell for the crystal structure of Cu_2O, with the O bcc (left) and Cu fcc (centre) sublattice as the base. Right: Points of high symmetry in the Brillouin zone of a simple cubic lattice.

2.1.1. Composition and symmetry

Cu_2O is assembled in a simple cubic Bravais lattice. There are four copper ions and two oxygen ions in a unit cell. The O atom are arranged in a body-centered cubic (bcc) sublattice with the Cu atoms superimposed in a face-centered cubic (fcc) sublattice. The sublattices are shifted by a quarter of the lattice diagonal; thus, effectively orienting a tetrahedron of Cu atoms around every O atom (see Fig. 2.1). Cu_2O is part of the $Pn\bar{3}m$ (O_h^4) space group, which is a nonsymmorphic space group [54]. The multiplication table for the O_h group can be found in the appendix A.2. The site symmetry of Cu is $D_{3\mathrm{d}}$, and T_d for O [55], which results in the irreducible representation of the different electronic orbitals, as shown in Tab. 2.1. We are mainly interested in the symmetries around the zone centre Γ, because most of the investigated exciton physics take place at this point. In the O_h point group, there exist two more or less equally popular notations for the symmetry around the Γ point, the Koster (K) and the Bouckaert (BSW) notation [50]. The transcription between these two is given in Tab. A.2, in this work we will stick to the Koster notation.

The electronic configuration of our components establishes the band structure and the corresponding symmetries. Oxygen possesses the electron configuration of $(1s)^2(2s)^2(2p)^4$, while copper consists of $(1s)^2(2s)^2(2p)^6(3s)^2(3p)^6(3d)^{10}(4s)^1$. In the bulk composite of Cu_2O, we can conceive the occurrence of a charge shift of the Cu $4s$ orbitals towards the O atoms. The resulting vacancies at the Cu atoms make Cu_2O a p semiconductor [45]. For our purposes, we are mostly interested in the emerging bands in the vicinity of the band gap. Thus, for Cu we assume the $3d$, $4s$ and $4p$, and for O $2s$ and $2p$ to be the crucial electron orbitals that compose Cu_2O's band structure in this region. A contemporary result for the band structure of Cu_2O, calculated with spin density functional theory (sDFT) in the generalized gradient approximation (GGA), can be seen in Fig. 2.2 [56].

	Γ, R	M	X
Cu s	$\Gamma_1^+ \oplus \Gamma_5^+$	$M_1 \oplus M_4$	$X_1 \oplus X_3$
Cu p	$\Gamma_2^- \oplus \Gamma_3^- \oplus 2\Gamma_4^- \oplus \Gamma_5^-$	$M_1 \oplus 2M_2 \oplus M_3 \oplus 2M_4$	$X_1 \oplus 2X_2 \oplus 2X_3 \oplus X_4$
Cu d	$\Gamma_1^+ \oplus 2\Gamma_3^+ \oplus 2\Gamma_4^+ \oplus 3\Gamma_5^+$	$3M_1 \oplus 2M_2 \oplus 2M_3 \oplus 3M_4$	$3X_1 \oplus 2X_2 \oplus 3X_3 \oplus 2X_4$
O s	$\Gamma_1^+ \oplus \Gamma_2^-$	M_4	X_3
O p	$\Gamma_4^- \oplus \Gamma_5^+$	$M_1 \oplus M_2 \oplus M_4$	$X_1 \oplus X_2 \oplus X_3$

Table 2.1.: Irreducible representations of the Cu ($D_{3\mathrm{d}}$) and O (T_d) orbitals on points of high symmetry in the Brillouin zone [55].

Several band structure calculations agree, that the oxygen $2s$ and $2p$ induced valence bands are way below the copper bands [54–60]. In fact, the upmost valence bands almost exclusively result from the Cu $3d$ orbital with symmetry $\Gamma_1^+ \oplus 2\Gamma_3^+ \oplus 2\Gamma_4^+ \oplus 3\Gamma_5^+$ at the zone centre. The bands split further by the crystal field into one significantly higher Γ_5^+, with the other seven bands being tightly packed around $\sim -2\,\mathrm{eV}$ below. The upmost Γ_5^+ band splits via spin-orbit interaction (Γ_6^+) further into a nondegenerate upper Γ_7^+ band and lower, twofold degenerate Γ_8^+ bands (disregarding the twofold electron spin degeneracy) with a splitting of $\Delta_\mathrm{p} = 131\,\mathrm{meV}$ at the Γ point [61, 62]. The energetic position of the Γ_7^+ band at zone centre is assumed to be at the Fermi level; thus, other band positions are always given in relation to the highest Γ_7^+ valence band. The $2p$ orbital of O contributes a Γ_4^- band, expectedly $\sim -5\,\mathrm{eV}$ below the Γ_7^+ valence band. This will be of noticeable importance at a later point.

The lowest conduction bands stem from the Cu $4s$ and $4p$ orbitals. The Cu $4s$ orbital splits into two contributions, the lowest conduction band of symmetry Γ_1^+ and a much higher located Γ_5^+ band that is of no further concern. Since Γ_1^+ of the O_h group is equivalent to the identity, the band does not split any further under spin-orbit interaction, but yields a nondegenerate band with the resulting symmetry $\Gamma_1^+ \otimes \Gamma_6^+ = \Gamma_6^+$. The next higher conduction band is of Γ_3^- symmetry and originates from the Cu $4p$ orbital [54]. The other bands that result from $4p$ are located significantly higher, with the two Γ_4^- bands being the lowest at an energy $\sim 9.5\,\mathrm{eV}$ and $\sim 11\,\mathrm{eV}$, followed by the Γ_5^- band around $\sim 13\,\mathrm{eV}$ and a Γ_2^- band beyond that. The Γ_3^- also does not split further via spin-orbit interaction, but takes the symmetry of Γ_8^-. For our purposes, we are only interested in the two lowest conduction bands ($\Gamma_6^+ \oplus \Gamma_8^-$) and two highest valence bands ($\Gamma_7^+ \oplus \Gamma_8^+$), since they form the four known exciton series of Cu_2O: the yellow ($\Gamma_6^+ \otimes \Gamma_7^+$), green ($\Gamma_6^+ \otimes \Gamma_8^+$), blue ($\Gamma_8^- \otimes \Gamma_7^+$) and violet ($\Gamma_8^- \otimes \Gamma_8^+$).

The energetical positions of the associated bands are known fairly well from experiments [11, 61–65]. The energies of the bands beyond the exciton series' are for the most part only known by band structure calculations [54–60]. However, since these calculations, depending on their initial approach, tend to over- or underestimate band spacings[2], we are left with rough approximations for their energetic band positions. Calculations in GGA are known to

[2] E.g. periodic Hartree-Fock methods generally overestimate the band gap due to the negligence of electronic correlation [59], while DFT approaches always underestimate the band gap [56].

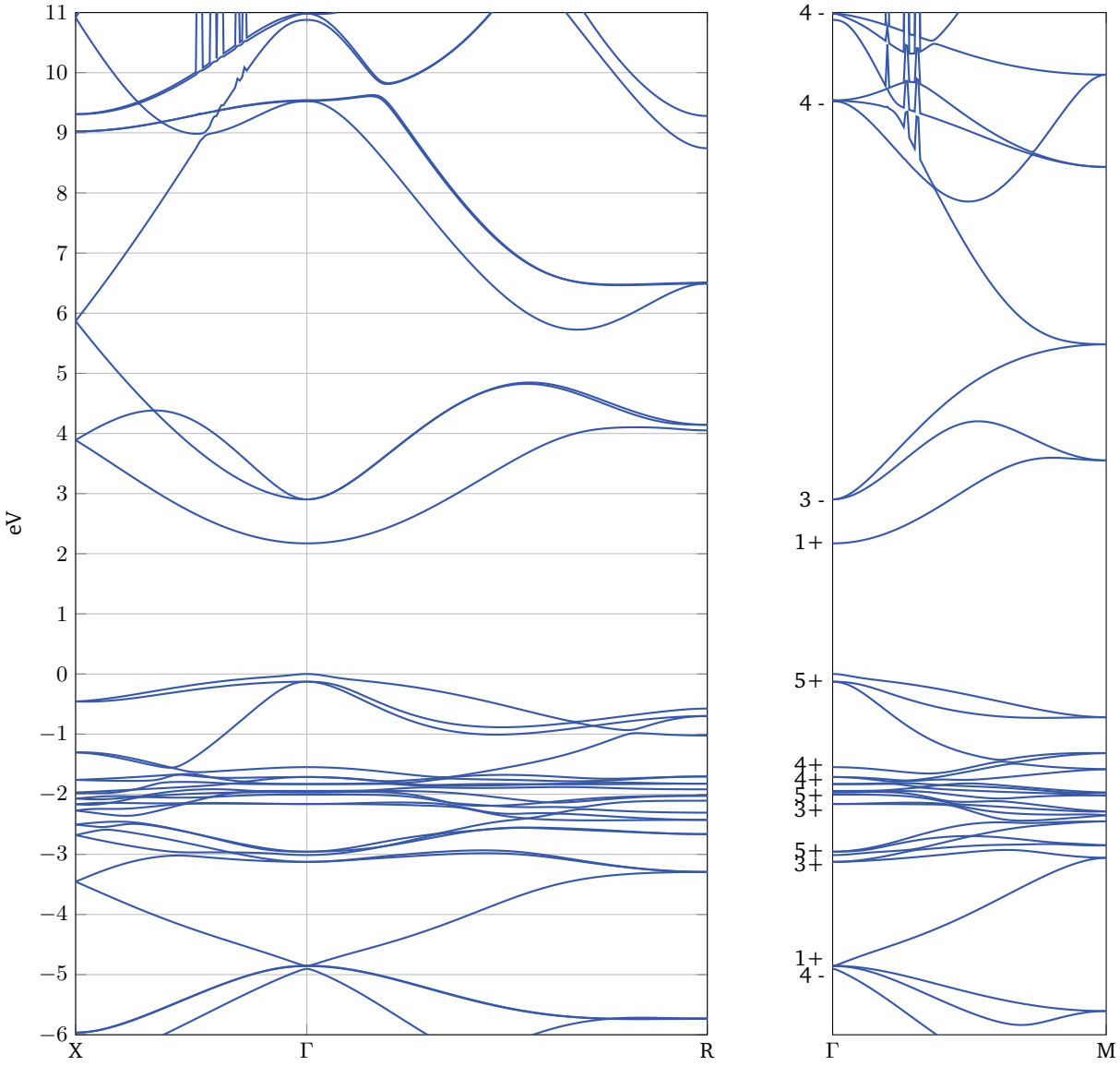

Figure 2.2.: Band structure of Cu_2O calculated with sDFT [56]. The conduction bands were shifted to match the experimentally known band gap E_y. The symmetries at zone centre are denoted at the right figure. The irregularities at energies $\gtrsim 9\,\mathrm{eV}$ stem from numerical errors.

drastically underestimate the value of the band gap. Self-consistent GW calculations converge towards the right band gap; although, they mainly shift the bands, keeping the actual band dispersion intact. Thus, the conduction bands in Fig. 2.2 were subsequently shifted to match the experimentally measured band gap $E_y = 2.172\,\mathrm{eV}$ [11]. This, however, overestimates the position of the Γ_3^- conduction bands about $250\,\mathrm{meV}$ [64]. This illustrates our predicament of not knowing the exact energy positions of higher located conduction and lower valence bands. The curvature of the dispersion matches previous calculations [54, 55, 57, 58, 60] as well as experimental results [66, 67], vindicating the use of the dispersion slopes for our calculations.

2.2. $\mathbf{k}\cdot\mathbf{p}$ theory

The idea of $\mathbf{k}\cdot\mathbf{p}$ theory stems from the concept of investigating a single isolated band by the one-electron Schrödinger Hamiltonian

$$H_{\mathrm{e}}(\mathbf{r}) = \frac{p^2}{2m_0} + V(\mathbf{r}) + \frac{\hbar}{4m_0^2c^2}(\boldsymbol{\sigma}\times\boldsymbol{\nabla}V)\cdot\mathbf{p}\,, \tag{2.1}$$

with a kinetic term, a local periodic crystal potential, and the spin-orbit interaction term. If the self-consistency of the local periodic crystal potential is assumed, the translational invariance allows for the separation of the single-electron wave function into a plane wave times the periodicity function of the lattice $u_{n,\mathbf{k}}(\mathbf{r})$. The product is known as Bloch wave function $\psi_{n,\mathbf{k}}(\mathbf{r}) = e^{\mathrm{i}\mathbf{k}\cdot\mathbf{r}}u_{n,\mathbf{k}}(\mathbf{r})$. Solving Eq. (2.1) with the Bloch wave function results in a Schrödinger equation for the periodic function. The emerging terms for the wave vectors of the Brillouin zone $\mathbf{k}$ are treated perturbatively; thus, we can calculate the band dispersion around any value $\mathbf{k}_0$. Then, in $\mathbf{k}\cdot\mathbf{p}$ theory, the periodical wave function in second-order nondegenerate perturbation theory yields

$$|u_{i,\mathbf{k}}\rangle \simeq |u_{i,\mathbf{k}_0}\rangle + \frac{\hbar}{m_0}\sum_{j\neq i}\frac{\langle u_{j,\mathbf{k}_0}|\,(\mathbf{k}-\mathbf{k}_0)\cdot\boldsymbol{\pi}|u_{i,\mathbf{k}_0}\rangle}{E_i(\mathbf{k}_0)-E_j(\mathbf{k}_0)}\,|u_{j,\mathbf{k}_0}\rangle\,, \tag{2.2}$$

with

$$\boldsymbol{\pi} = \mathbf{p} + \frac{\hbar}{4m_0c^2}(\boldsymbol{\sigma}\times\boldsymbol{\nabla}V)\,. \tag{2.3}$$

This works only for a small region around $\mathbf{k}_0$, since only low order terms of the wave vector k, k^2, etc., are considered. Similarly, the corresponding energy eigenvalue can be expressed as

$$\begin{aligned} E_i(\mathbf{k}) = E_i(\mathbf{k}_0) + \frac{\hbar^2(\mathbf{k}-\mathbf{k}_0)^2}{2m_0} + \frac{\hbar}{m_0}\langle u_{i,\mathbf{k}_0}|(\mathbf{k}-\mathbf{k}_0)\cdot\boldsymbol{\pi}|u_{i,\mathbf{k}_0}\rangle \\ + \frac{\hbar^2}{m_0^2}\sum_{j\neq i}\frac{\left|\langle u_{i,\mathbf{k}_0}|(\mathbf{k}-\mathbf{k}_0)\cdot\boldsymbol{\pi}|u_{j,\mathbf{k}_0}\rangle\right|^2}{E_i(\mathbf{k}_0)-E_j(\mathbf{k}_0)}\,. \end{aligned} \tag{2.4}$$

We are exclusively interested in the transition at the band extrema responsible for the predominant excitations. In most direct gap semiconductors, these are positioned at the high symmetry point of Γ, i.e. $\mathbf{k}_0 = 0$. In this case, the linear term of $\mathbf{k}$ in Eq. (2.4) vanishes, because we are investigating an extremum. Assuming the one-electron Hamiltonian to be invariant under time reversal, the energy dispersion possesses inversion symmetry $E_i(\mathbf{k}) = E_i(-\mathbf{k})$ [50]. The time-reversal symmetry is also responsible for the twofold spin-degeneracy of the bands as long as the crystal possesses inversion symmetry and no magnetic fields are present. This is known as Kramers' degeneracy theorem [68, 69]. The second derivative of Eq. (2.4) at $\mathbf{k}_0 = 0$

yields the effective mass tensor

$$(m_i^{-1})_{mn} = \frac{1}{\hbar^2}\frac{\partial^2}{\partial k_m\,\partial k_n}E_i(\mathbf{k}) = \frac{1}{m_0}\delta_{mn} + \frac{k_m k_n}{m_0^2}\sum_{j\neq i}\frac{\langle u_{i,0}|\pi_m|u_{j,0}\rangle\langle u_{j,0}|\pi_n|u_{i,0}\rangle + \langle u_{i,0}|\pi_n|u_{j,0}\rangle\langle u_{j,0}|\pi_m|u_{i,0}\rangle}{E_i(0) - E_j(0)} \quad (2.5)$$

which is occasionally referred to as effective mass sum rule [52]. If the tensor is diagonal and its elements are equal, the band structure is considered to be isotropic (around $\mathbf{k}_0 = 0$) and depicts the intuitive picture of an electron with an effective mass. In the lattice potential, the electron moves without energy dissipation due to the periodicity of the Bloch waves. However, any perturbances that lead to a disruption of symmetry, such as impurities in the crystal or interaction with phonons, entail a dissipation. The interaction with phonons will be tackled in the upcoming section 2.4.

A few conclusions about the band dispersion can be drawn from Eq. (2.5). The energy denominator shows that coupling to higher and lower bands increases and decreases the effective mass, respectively. Also distant bands are expected to be less important. The mass of a particular band is only affected by interaction with other bands if the coupling to those other bands is allowed by group theory, i.e. the dipole matrix element between the bands does not vanish. The highest valence bands are known to possess negative mass; therefore, the coupling dipole transition matrix element to the neighbouring conduction bands must be strong enough (usually it is around an order of magnitude bigger than the band gap [52]) to bend the valence bands down. A vacant electron spot in a valence band is usually described as a quasiparticle with the electrons negative wave vector $-\mathbf{k}$ and a negative valence band mass, denoted as hole.

The next step is the determination of the relevant dipole matrix transition elements, or to be more precise, the analysis of the band symmetry and the investigation which dipole transition matrix elements are actually nonzero. In this work, we are mainly interested in the band dispersions around the band gap, starting with the lowest conduction band.

2.2.1. Conduction band

As we have seen in the previous section, the conduction band in Cu_2O originates from the Cu $4s$ orbital and has a Γ_1^+ symmetry. For cubic semiconductors, the Γ_1^+ state transforms as the unity operator $\mathbf{1}$; thus, the conduction band can be treated in a nondegenerate fashion, and we can drop the spin-orbit interaction for this part, setting $\boldsymbol{\pi} = \mathbf{p}$. The momentum operator $\mathbf{p}$ exhibits a Γ_4^- symmetry in the point group of O_h. This immediately restricts the ammount of potentially coupling bands drastically, as the intermediate states in Eq. (2.4) (or Eq. (2.5), respectively) need to fulfill the symmetry relation $\Gamma_1^+ \otimes \Gamma_4^- = \Gamma_4^-$. Keep in mind that this symmetry restraint is only strictly valid for the symmetry Γ point. This restriction alleviates the further we are

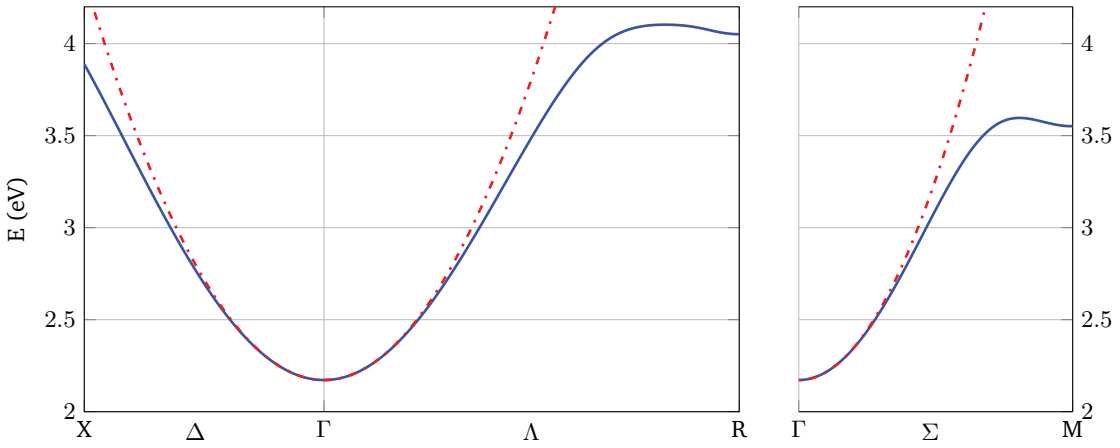

Figure 2.3.: The Γ_6^+ conduction band disperion for the three different symmetry directions. The continuous blue lines are calculated by sDFT [56], the red dotted lines depict the isotropic and parabolic approximation as given by Eq. (2.7) with an electron mass of $m_{1c} \simeq 0.945 m_0$.

away from symmetry points. The Γ_1^+ state is denoted by α^+ and the three Γ_4^- states can be expressed in the basis $\delta_1^- \sim x$, $\delta_2^- \sim y$, $\delta_3^- \sim z$. According to the Wigner-Eckart theorem, the coupling coefficients are then determined by $\langle \alpha^+ | p_x | x \rangle = \langle \alpha^+ | p_y | y \rangle = \langle \alpha^+ | p_z | z \rangle = \mathrm{i}\frac{p_{14}}{\sqrt{3}}$ [70]. The coupling strength between Γ_4^- and Γ_1^+ bands is evenly distributed, thus resulting in an isotropic deformation. Without loss of generality we can assume that the periodic functions are real, making the matrix elements purely imaginary [50]. In Fig. 2.2 we recognise three bands that possess the Γ_4^- symmetry, two higher located conduction bands around $9.5\,\mathrm{eV}$ and $11\,\mathrm{eV}$, respectively, and a valence band around $-5\,\mathrm{eV}$. Taking these three bands into account, the resulting effective mass of the conduction band is calculated via Eq. (2.5) as

$$\frac{m_0}{m_{1c}} = 1 + \frac{2\,p_{14_1}^2}{m_0(E_{1c} - E_{4c_1})} + \frac{2\,p_{14_2}^2}{m_0(E_{1c} - E_{4c_2})} + \frac{2\,p_{14_3}^2}{m_0(E_{1c} - E_{4v_3})}\,. \tag{2.6}$$

The first two terms increase the effective mass, and the last one decreases it. Similarly, we can evaluate Eq. (2.4) and receive the corresponding energy dispersion. The nondegenerate treatment results in a quadratic, isotropic energy dispersion

$$E_{1c}(k) = E_{1c}(0) + \frac{\hbar^2 k^2}{2 m_{1c}}\,. \tag{2.7}$$

If we know the coupling between the bands, we can thusly calculate the conduction bands mass and, therefore, determine its energy dispersion around the Γ point. Usually, however, we know the band masses well to a certain degree (e.g. from time-resolved cyclotron resonance) and aspire to obtain the coupling between the bands, which is not explicitly possible with Eq. (2.6). Even worse, the fact that in Cu_2O the conduction band mass is close to the free electron mass leaves us no means to evaluate the coupling even qualitatively. The most probable presumption would be, that the coupling to all of the three bands is rather weak,

partially due to their large separation from the Γ_1^+ conduction band. The inclusion of quartic terms does not solve the conundrum, as it would introduce additional coupling terms and is not improving the fit significantly [25].
The mass of the Γ_6^+ conduction band is known from experiments as $\tilde{m}_{1c} = 0.985m_0$ [67]. However, there exist two polar phonon branches in Cu_2O that increase the actual electron mass. Considering the phonon induced broadening, the band mass can be calculated as $m_{1c} \simeq 0.945m_0$. The origin of this deviation will be discussed further in the upcoming section 2.4. Extracting the electron mass of the Γ_6^+ band from the DFT band structure calculation indeed shows a good agreement with this estimated value in the region around the Γ point. A closeup of the Γ_6^+ band including the parabolic approximation around zone centre is depicted in Fig. 2.3

2.2.2. Valence band

Apart from the spin-degeneracy, the conduction band is nondegenerate and thus, can be treated easily in the approach illustrated above. Next, we discuss several ways to treat degenerate bands, as it is the case for the highest valence bands in Cu_2O. For this, the coupling between the degenerate bands needs to be taken into account explicitly, adding off-diagonal contributions to the one-particle Hamiltonian. Hence, for degenerate bands there are always band mixing effects that need to be considered when evaluating transition matrix elements. As already stated previously, the valence band stems from the Cu $3d$ orbital and has Γ_5^+ symmetry. The periodic wave functions can be expressed in the basis functions $\varepsilon_1^+ \sim yz$, $\varepsilon_2^+ \sim xz$, $\varepsilon_3^+ \sim xy$.
We start off again without considering the spin. We set $\boldsymbol{\pi} = \mathbf{p}$ in Eq. (2.1) and receive a 3×3 matrix for the three basis functions of the Γ_5^+ band. The first-order terms vanish due to the parity change that is imposed by the dipole operator $\mathbf{p}$. Therefore, we need second-order degenerate perturbation theory with the matrix elements being

$$H_{5v}(\mathbf{k}) = E_{5v}(0) + \frac{\hbar^2 k^2}{2m_0} + H^{(2)}(\mathbf{k})\,, \tag{2.8}$$

$$H_{ij}^{(2)}(\mathbf{k}) = \frac{\hbar^2}{m_0^2} \sum_{\nu} \frac{\langle \varepsilon_i^+ | \mathbf{k}\cdot\mathbf{p} | u_{\nu,0} \rangle \langle u_{\nu,0} | \mathbf{k}\cdot\mathbf{p} | \varepsilon_j^+ \rangle}{E_{5v}(0) - E_\nu(0)}\,. \tag{2.9}$$

Here, ν conglomerates the spin states and the different bases of all coupling bands. The resulting matrix of the second order perturbation term $H^{(2)}$ is known as Dresselhaus-Kip-Kittel (DKK) Hamiltonian [71]. The possibility for a nonzero coupling between band states via $\mathbf{p}$ is

limited by group theory [70]. The resulting matrix takes the form

$$H^{(2)}(\mathbf{k}) = \begin{pmatrix} Lk_x^2 + M(k_y^2 + k_z^2) & Nk_xk_y & Nk_xk_z \\ Nk_xk_y & Lk_y^2 + M(k_x^2 + k_z^2) & Nk_yk_z \\ Nk_xk_z & Nk_yk_z & Lk_z^2 + M(k_x^2 + k_y^2) \end{pmatrix} . \tag{2.10}$$

It turns out that there exist three independent parameters L, M, N. Those parameters emerge solely by considering the transformational operations the different components of the momentum operator $\mathbf{p}$ exert on the wave functions of Γ_5^+ [71]. The composition of these parameters is given in appendix B.1.1.
In the next step, we reintroduce the spin-orbit coupling term from Eq. (2.1). Applying the Bloch wave function yields two contributions for the Hamiltonian of the periodicity function

$$H_{\mathrm{so}}(\mathbf{k}) = \frac{\hbar}{4m_0^2c^2}(\boldsymbol{\sigma} \times \boldsymbol{\nabla} V) \cdot \mathbf{p} + \frac{\hbar^2}{4m_0^2c^2}(\boldsymbol{\sigma} \times \boldsymbol{\nabla} V) \cdot \mathbf{k} = H_{\mathrm{so,p}} + H_{\mathrm{so,k}} \, . \tag{2.11}$$

For the first part $H_{\mathrm{so,p}}$, the first order perturbation term does not vanish. Since spin-orbit interaction is generally considered to be much weaker than interband coupling, higher order perturbation terms of this participation are usually neglected. The second part $H_{\mathrm{so,k}}$ requires second order perturbation, due to the Γ_4^- symmetry of $\boldsymbol{\nabla} V$. It will later be known as the momentum dependent spin-orbit coupling term. The triple product of the first term can be rearranged via a circular shift to

$$H_{\mathrm{so,p}} \propto (\boldsymbol{\sigma} \times \boldsymbol{\nabla} V) \cdot \mathbf{p} = (\boldsymbol{\nabla} V \times \mathbf{p}) \cdot \boldsymbol{\sigma} = \tilde{H}_{\mathrm{so,p}_i} \sigma_i \, . \tag{2.12}$$

The pseudovector $\boldsymbol{\nabla} V \times \mathbf{p}$ is an axial vector with symmetry Γ_4^+; hence, there exists only one independent spin-orbit matrix element for $H_{\mathrm{so,p}}$, which is usually expressed as [72]

$$\Delta_{\mathrm{p}} = \frac{3\mathrm{i}\hbar}{4m_0^2c^2} \langle xy | (\boldsymbol{\nabla} V \times \mathbf{p})_x | xz \rangle \, . \tag{2.13}$$

Further examinations need to include the spin functions $s^{\pm} = \pm 1/2$ to the basis states. Multiplying the two spin states to the three band basis states results in a six dimensional basis. However, the parts of the new wave functions still act separately on the different components of the right hand side of Eq. (2.12), with the spin function $s^{\pm}$ only acting on $\boldsymbol{\sigma}$ and the band states of Γ_5^+ only on $\tilde{H}_{\mathrm{so,p}}$, respectively. With this, the evaluation of Eq. (2.12) is straightforward if we utilise the Pauli matrices

$$\sigma_x = \begin{pmatrix} 0 & 1 \\ 1 & 0 \end{pmatrix} , \quad \sigma_y = \begin{pmatrix} 0 & -\mathrm{i} \\ \mathrm{i} & 0 \end{pmatrix} , \quad \sigma_z = \begin{pmatrix} 1 & 0 \\ 0 & -1 \end{pmatrix} . \tag{2.14}$$

For the second term we perform a similar circular shift to obtain

$$H_{\mathrm{so,k}} \propto (\boldsymbol{\sigma} \times \boldsymbol{\nabla} V) \cdot \mathbf{k} = (\mathbf{k} \times \boldsymbol{\sigma}) \cdot \boldsymbol{\nabla} V \,. \tag{2.15}$$

The base wave functions separate again, and the cross product is easily calculated via the Pauli matrices and the spin function $s^{\pm}$. The matrix elements $\langle u_{5^+,\mathbf{k}} | \boldsymbol{\nabla} V | u_{5^+,\mathbf{k}} \rangle$ need to be expanded in $\mathbf{k} \cdot \mathbf{p}$ theory. The diagonal matrix elements $\langle \varepsilon_i | \boldsymbol{\nabla} V | \ell \rangle \langle \ell | \mathbf{k} \cdot \mathbf{p} | \varepsilon_i \rangle + \langle \varepsilon_i | \mathbf{k} \cdot \mathbf{p} | \ell \rangle \langle \ell | \boldsymbol{\nabla} V | \varepsilon_i \rangle$ vanish due to $\langle \varepsilon_i | \boldsymbol{\nabla} V | \ell \rangle$ being real and $\langle \varepsilon_i | \mathbf{p} | \ell \rangle$ being imaginary. Physically, this is easily comprehensible since there exists no spin-orbit coupling of a band component with itself. The remaining off-diagonal terms take the form

$$\frac{1}{2m_0 c^2} \langle \varepsilon_i | \boldsymbol{\nabla} V | \varepsilon_j \rangle = -\mathrm{i} \, \left(k_i \mathbf{e}_j - k_j \mathbf{e}_i + 0 \, \mathbf{e}_\ell \right) \, \Delta_{\mathrm{k}} \,, \tag{2.16}$$

with $i, j, \ell \sim 1, 2, 3$ for the left- and $i, j, \ell \sim x, y, z$ for the right-hand side, and

$$\Delta_{\mathrm{k}} = \frac{\mathrm{i}\,\hbar}{2m_0^2 c^2} \sum_{\ell} \frac{\langle xy | \partial_x V | \ell \rangle \langle \ell | p_z | yz \rangle + \langle xy | p_z | \ell \rangle \langle \ell | \partial_x V | yz \rangle}{E_{5v} - E_\ell} \,. \tag{2.17}$$

We recognise that, similar to Eq. (2.10), the off-diagonal terms can be summarised in one coupling constant. The constant Δ_{k} will be known as the quadratic spin-orbit coupling coefficient.

In the six-dimensional basis, the mixing between the states of the Γ_5^+ band leads to a splitting of the degeneracy. The six states transform according to $\Gamma_5^+ \otimes \Gamma_6^+ = \Gamma_7^+ \oplus \Gamma_8^+$, splitting the degeneracy of the valence band into the higher nondegenerate Γ_7^+ and twofold degenerate Γ_8^+ bands[3]. Constructing a new basis under the premise of $s^{\pm} \otimes \varepsilon_i^+$ is known as LS representation. It is the most straightforward approach, as we are able to immediately recycle the resulting Hamiltonian of Eq. (2.10). However, in some cases it is advantageous to utilise a different base representation: The Γ_5^+ bands transform similarly to the atomic p wave functions, i.e. states with angular momentum $\ell = 1$. Combined with the spin states $s^{\pm} = \pm 1/2$, we can transform our basis into the JM representation (see appendix B.1.2), which aptly represents the newly emerged bands as twofold degenerate $j = 1/2$ (Γ_7^+) and fourfold degenerate $j = 3/2$ (Γ_8^+) states. In this case, $H_{\mathrm{so,p}}$ becomes diagonal. This illustrates that the term is responsible for the splitting of the degenerate bands about a fixed value Δ_{p}, but beyond that does not contribute to any further coupling between the bands.

In the weak spin-orbit interaction regime, the $H_{\mathrm{so,k}}$ term of Eq. (2.11) is usually considered negligible. Transforming the DKK Hamiltonian $H^{(2)}$ into JM representation and adding the spin-orbit splitting $H_{\mathrm{so,p}}$ as well as the free electrons kinetic energy yields what is commonly known as Luttinger-Kohn (LK) Hamiltonian [73], although the same Hamiltonian was introduced prior by R. Elliott [74]. It can be found in appendix B.1.2. The resulting Hamiltonian cannot be diagonalised analytically; however, if we assume that the split off bands can be

[3] These bands are also still doubly spin degenerated, according to Kramers' theorem.

decoupled from each other, we receive a 2×2 and a 4×4 block, which can be evaluated separately. The determinants of the two blocks yield three distinct eigenvalues which represent the energy dispersions around $k = 0$.
For the application within this work, we will employ a more general Hamiltonian which allows for arbitrarily strong spin-orbit interaction (within the boundary that perturbation terms beyond second order are still negligible small), i.e. taking $H_{\mathrm{so,k}}$ into account too.

2.2.3. Suzuki-Hensel Hamiltonian

The Hamiltonian that was introduced by K. Suzuki and J. Hensel (SH) [75] was originally derived for Ge but is still overall valid for all bands with Γ_4, Γ_5 symmetry in semiconductors of the point group O_{h}. In its most general form, it contains the interband coupling terms of the DKK Hamiltonian, both parts of the spin-orbit interaction of Eq. (2.11) and additionally the interaction with an external magnetic field, as well as the influence of uniform strain. For our purposes, we neglect the last two contributions, since they are irrelevant in the upcoming evaluations. This leaves us effectively with a "light" version of the SH Hamiltonian for consideration.
Contrary to the preceding derivation of the valence band Hamiltonian via perturbation theory of the Bloch wave functions, SH initially construct the Hamiltonian solely on the basis of symmetry. For this approach, the wave vector $\mathbf{k}$ and its different orders in power are arranged according to the irreducible representations. The zeroth order only contains the unit matrix; thus, it correlates with the identity Γ_1^+. The first order terms obviously correspond to the irreducible representation of $\mathbf{k}$, namely Γ_4^-. For the second order terms the product of the symmetries yields $\Gamma_4^- \otimes \Gamma_4^- = \Gamma_1^+ \oplus \Gamma_3^+ \oplus \Gamma_4^+ \oplus \Gamma_5^+$. From this we can infer the different basis functions for the irreducible representations as [75]

$$\begin{aligned}
\Gamma_1^+ &: \quad 1,\, k^2\,; \\
\Gamma_4^- &: \quad k_x,\, k_y,\, k_z\,; \\
\Gamma_3^+ &: \quad k_x^2 - k_y^2,\, k_y^2 - k_z^2\,; \\
\Gamma_4^+ &: \quad [k_y, k_z],\, [k_x, k_z],\, [k_x, k_y]\,; \\
\Gamma_5^+ &: \quad \{k_y, k_z\},\, \{k_x, k_z\},\, \{k_x, k_y\}\,,
\end{aligned} \tag{2.18}$$

where $[k_i, k_j]$ is the normal commutator and $\{k_i, k_j\} = \frac{1}{2}(k_i k_j + k_j k_i)$ is the anticommutator. Similarly, the three angular momentum matrices for $I = 1$ (and the unit matrix) form a basis of nine linearly independent matrices $1,\, I_x,\, I_y,\, I_z,\, I_x^2,\, I_y^2,\, \{I_y, I_z\},\, \{I_x, I_z\}, \{I_x, I_y\}$. This phenomenological approach for the angular momentum matrices[4] I_i was first introduced by J. Luttinger [76]. He determined the irreducible representations that can be constructed from

[4] The angular momentum matrices correspond to a pseudovector; hence, they possess Γ_4^+ symmetry.

angular momentum and assigned the matrices and their products according to their symmetry representation

$$\begin{aligned}
\Gamma_1^+ &: \quad 1\,; \\
\Gamma_4^+ &: \quad I_x,\, I_y,\, I_z\,; \\
\Gamma_3^+ &: \quad I_x^2 - I_y^2,\, I_y^2 - I_z^2\,; \\
\Gamma_5^+ &: \quad \{I_y, I_z\},\, \{I_x, I_z\},\, \{I_x, I_y\}\,.
\end{aligned} \tag{2.19}$$

The quadratic contribution with Γ_1^+ symmetry yields I^2 which corresponds to the unit matrix, and for Γ_4^+ symmetry it consists of commutator terms that due to the commutator relation of the angular momentum matrices $[I_i, I_j] = iI_k$ are reduced back to the linear terms of I.
Comparing the symmetry of the wave vector components with the symmetry of the angular momentum matrices yields the possible combinations of their products. The compatible terms of I and k need to be invariant under any arbitrary symmetry transformation; hence, the symmetry product needs to include the identity Γ_1^+. As it can be seen in the multiplication table of the cubic group in appendix A.2, this only applies for products that contain identical irreducible representations, i.e. $(\Gamma_i^\pm \otimes \Gamma_j^\pm) \ni \Gamma_1^+$ is only valid for $i = j$. This enables us to establish a phenomenological angular momentum Hamiltonian that is accurate up to the order of k^2 solely in the framework of symmetry considerations and without the need of any perturbation theory. In principle, this can be done for higher orders of k without any restriction of validity and was done for, e.g. the order of k^4 by [25]; however, this drastically increases the number of unknown variables while not bearing too much of an improvement. Therefore, we are content with the order k^2.
In the abovementioned derivation of Luttinger, he only takes the similarity between Γ_5^+ bands and atomic p orbitals (hence $I = 1$) into account and does not yet intrinsically include the spin-orbit interaction within the Γ_5^+ bands. In actuality, Luttinger does insert the spin-orbit interaction separately afterwards, but only considers the spin-orbit induced band splitting of $H_{\mathrm{so,p}}$.
SH listed the 36 independent matrices that are constructed from the angular momentum I and the spin matrices σ [75]. The resulting base functions can be found in the appendix in Tab. A.4. Comparing the table with the relations (2.18), under the previously mentioned condition that symmetry subscripts need to coincide for the product of representations to contain Γ_1^+ symmetry, it yields the individual parts of the Hamiltonian. Let us begin evaluating the products by systematically inspecting the different orders of k, starting with the lowest.
The zeroth order of k is 1, thus only possesses Γ_1^+ symmetry. Correspondingly, Tab. A.4 contains two matching basis functions, 1 and $\mathbf{I}\cdot\boldsymbol{\sigma}$. The first term is simply a product of unit matrices resulting in a new unit matrix, which is recognised as the fixed energetic shift of the band at zone centre within the entire ensemble of the band structure. The product with the second basis function yields the spin-orbit splitting at $\mathbf{k} = 0$. It describes a static energy shift

between the different band states as it was already seen in the term $H_{\mathrm{so,p}}$. Indeed, comparing the product of the basis functions $\mathbf{I}\cdot\boldsymbol{\sigma}$ to Eq. (2.12) we recognise that they produce identical matrices. Utilising the nomenclature introduced in Eq. (2.13) the second zeroth order term of k results in

$$H_{\mathrm{so,p}} = -\frac{1}{3}\,\Delta_{\mathrm{p}}\,(\mathbf{I}\cdot\boldsymbol{\sigma})\,. \tag{2.20}$$

The first order terms of k (Γ_4^-) do not possess any matching parity with the matrices contructed from I and σ; thus, they automatically vanish. The second order k terms are summarised in the momentum dependent Hamiltonian

$$\begin{aligned} H_{\mathrm{k}} = \frac{\hbar^2}{2m_0}\Big(& \left[A_1 + B_1(\mathbf{I}\cdot\boldsymbol{\sigma})\right] k^2 && \big|\ \Gamma_1^+ \\ & + \left[A_2(I_x^2 - \frac{1}{3}I^2) + B_2(I_x\sigma_x - \frac{1}{3}\mathbf{I}\cdot\boldsymbol{\sigma})\right] k_x^2 \ +\ \mathrm{c.p.} && \big|\ \Gamma_3^+ \\ & + \left[A_3(I_xI_y + I_yI_x) + B_3(I_x\sigma_y + I_y\sigma_x)\right]\{k_x,k_y\} \ +\ \mathrm{c.p.}\Big)\,, && \big|\ \Gamma_5^+ \end{aligned} \tag{2.21}$$

with A_i and B_i $(i = 1,2,3)$ being yet unknown parameters and $\mathrm{c.p.}$ denoting the cyclic permutation. The quadratic parts with Γ_4^+ symmetry vanish due to the commutator relation yielding $[k_i, k_j] = 0$. This property is invalidated when an external magnetic field is applied. In fact, the magnetic field can be expressed via the commutator relation of k as $\mathbf{H} = \frac{\mathrm{i}\hbar c}{e}\mathbf{k}\times\mathbf{k}$ [75].
Similar to Eq. (2.20), it is advantageous to compare the resulting momentum dependent Hamiltonian of Eq. (2.21) to its $\mathbf{k}\cdot\mathbf{p}$ theory resolved counterpart. It can be shown, that the relation between them is just $H_{\mathrm{k}} = H^{(2)} + H_{\mathrm{so,k}}$. This allows the determination of the parameters A_i and B_i in terms of the parameters that emerge from $\mathbf{k}\cdot\mathbf{p}$ theory (cf. appendix B.1.3). While the valence band Hamiltonian $H_{5\mathrm{v}} = E_{5\mathrm{v}}(0) + H_{\mathrm{so,p}} + H_{\mathrm{k}}$, as it is deduced by SH solely on the foundation of symmetry analogies, presents the band structure Hamiltonian in a very concise and elegant way, and is generally valid up to the order of k^2, the comparison with $\mathbf{k}\cdot\mathbf{p}$ theory is necessary to assign physical meaning to the generic parameters. Some of these parameters are known from experiments, the remaining will be determined by a fit to the DFT calculations of Fig. 2.2.
Cu_2O is a p type semiconductor due to the vacancies of the Cu atoms; therefore, the Fermi level is set to the tip of the Γ_5^+ valence band $E_{5\mathrm{v}}(0) = 0\,\mathrm{eV}$. It was already mentioned that $H_{\mathrm{so,p}}$ becomes diagonal in JM representation and thus Δ_{p} denotes the spin-orbit splitting of the Γ_7^+ and Γ_8^+ bands at zone centre. That difference is well established in experiment [61, 62] and theory [56] as $\Delta_{\mathrm{p}} = 131\,\mathrm{meV}$ as it is directly tied to the yellow and green exciton series. The general 6×6 matrix spanned by Hamiltonian H_{k} as it is given in Eq. (2.21) cannot be evaluated analytically. However, for two of the three high symmetry directions, namely Δ towards the X ([100]) and Λ towards the R ([111]) point, it is possible to diagonalise the matrix, resulting in three independent (each twofold degenerate) eigenvalues. They correspond to the

quadratic momentum dependence of the band dispersion. The band dispersions of $H_{5\mathrm{v}}$ for both directions are

$$E_7^i(k) = \frac{1}{12}\left(P_1^i\,k^2 - 6\Delta_\mathrm{p} + \sqrt{P_2^i\,k^4 + P_3^i\,\Delta_\mathrm{p}\,k^2 + 36\Delta_\mathrm{p}^2}\right), \tag{2.22a}$$

$$E_{8_1}^i(k) = \frac{1}{12}\left(P_1^i\,k^2 - 6\Delta_\mathrm{p} - \sqrt{P_2^i\,k^4 + P_3^i\,\Delta_\mathrm{p}\,k^2 + 36\Delta_\mathrm{p}^2}\right), \tag{2.22b}$$

$$E_{8_2}^i(k) = \frac{\hbar^2}{2m_0}\,\frac{1}{6}\left(6A_1 + 2A_i - 5\Delta_\mathrm{k}\right)k^2 - \Delta_\mathrm{p}\,, \tag{2.22c}$$

with

$$P_1^i = \frac{\hbar^2}{2m_0}\left(12A_1 - 2A_i + 5\Delta_\mathrm{k}\right), \tag{2.23a}$$

$$P_2^i = \left(\frac{\hbar^2}{2m_0}\right)^2 3\left(12A_i^2 + 20A_i\Delta_\mathrm{k} + 331\Delta_\mathrm{k}^2\right), \tag{2.23b}$$

$$P_3^i = \frac{\hbar^2}{2m_0}\,12\left(2A_i + 31\Delta_\mathrm{k}\right). \tag{2.23c}$$

The parameters A_i correspond to $i = 2$ in the Δ direction and $i = 3$ in the Λ direction. The nonparabolic Eqs. (2.22a) and (2.22b) can be expanded around $\mathbf{k} = 0$ which yields their parabolic participation

$$\begin{aligned} E_{7,0}^i(k) &= \frac{1}{144}\left(12P_1^i + P_3^i\right)k^2 \\ &= \frac{\hbar^2}{2m_0}\left(A_1 + 3\Delta_\mathrm{k}\right)k^2\,, \end{aligned} \tag{2.24a}$$

$$\begin{aligned} E_{8_1,0}^i(k) &= \frac{1}{144}\left(12P_1^i - P_3^i\right)k^2 - \Delta_\mathrm{p} \\ &= \frac{\hbar^2}{2m_0}\,\frac{1}{6}\left(6A_1 - 2A_i - 13\Delta_\mathrm{k}\right)k^2 - \Delta_\mathrm{p}\,. \end{aligned} \tag{2.24b}$$

It is noticeable that the mass of the Γ_7^+ band at zone centre seems to be independent of spatial orientation, which is not the case for either of the Γ_8^+ bands. The hole mass of the Γ_7^+ band at zone centre is known from time-resolved cyclotron resonance to be $\tilde{m}_{7\mathrm{v}} = 0.575\,m_0$ [67]. However, similar to the conduction band this value refers to the polaron mass of the hole. After detracting the polaronic mass increase, the band hole mass is given as $m_{7\mathrm{v}} \simeq 0.55\,m_0$. From the expansion in Eq. (2.24a) we recognise that $-m_0/m_{7\mathrm{v}} = A_1 + 3\Delta_\mathrm{k}$, leaving two unknown variables to fit for each direction. As to be expected, attempting to fit Eqs. (2.22) reveals that Δ_k is small compared to the A_i. In actuality, Δ_k turns out to be too small to reliably converge to a consistent value, and with its values ranging about two orders of magnitude below the A_i we set $\Delta_\mathrm{k} = 0$. This effectively puts the result of Eqs. (2.22) on par with the LK Hamiltonian, with A_1 being directly identified by the hole mass and the other two A_i by the fits. The resulting SH

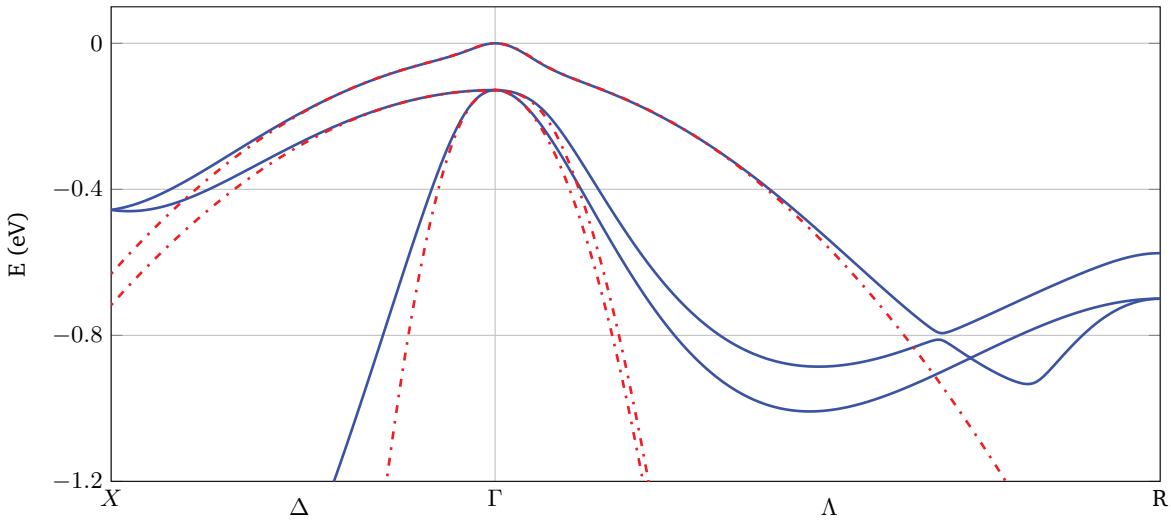

Figure 2.4.: The Γ_5^+ valence bands in the direction towards the symmetry points X ([100]) and R ([111]). The continuous blue curve is calculated by sDFT [56], the dotted red line represents the fit of the parameters A_2 and A_3 of Eqs. (2.22).

parameter for the Γ_5^+ valence band of Cu_2O are

$$A_1 = -1.818\,, \qquad A_2 = 4.601\,, \qquad A_3 = -2.269\,, \qquad \Delta_\mathrm{k} = 0\,. \tag{2.25}$$

The fit is shown in Fig. 2.4. For the Γ_7^+ valence band, the result from sDFT [56] and the fit of Eq. (2.22a) agree fairly well over a wide range around the Γ point. The fits of the Γ_8^+ bands only seem to align for a small interval around zone center due to an early departure from the quadratic behaviour of the sDFT bands. The Γ_8^+ heavy hole band in X direction is an exception as it possesses a significantly larger mass.

2.3. Excitons in Cu_2O

Up to this point, we established a solid foundation of knowledge about the composition of the bulk semiconductor Cu_2O, its symmetries and means to describe its band structure. However, the key aspect of this work are the optical properties of excitons; therefore, we now inspect some of their fundamental features and lay out their basic mathematical description. The optical excitation of an electron $\mathbf{k}_\mathrm{e}$ from a valence band into a conduction band leaves a vacant spot in the original position of the electron within the valence band. That vacancy can be described via a quasiparticle with opposite charge and momentum of the electron $\mathbf{k}_\mathrm{h} = -\mathbf{k}_\mathrm{e}$, referred to as a hole. The bound state formed via Coulomb interaction between electron and hole in turn constitutes the quasiparticle that is known as an exciton. This system resembles

the interaction within the hydrogen atom[5]; thus, excitons can be (roughly) categorised by the same set of quantum numbers n, ℓ, m that are already known from atomic physics. However, contrary to the hydrogen atom the 1S state is not the ground state but rather the lowest excited state of the system. The ground state is known as the "excitonic vacuum", i.e. the state in which no excitons are present in the semiconductor.

The concept of excitons was first introduced by Frenkel in 1931 [1,2] and was subsequently refined and expanded by Peierls and Wannier [3,4]. The two models that emerged from Frenkels and Wanniers work, albeit starting from the same initial point, effectively describe two limiting cases. Thus, there is a distinction between Frenkel and Wannier excitons. Frenkel proposed a tight binding solution for the case of the electron and hole residing in the same location. His model is still a valid basis to describe the energy transfer within molecules or the excitation at localised defects in semiconductors. Wanniers model, on the other hand, assumes a weak binding limit, in which electron and hole are separated over multiple unit cells, thus exhibiting a large exciton Bohr radius. In this case, the interaction with the remaining crystal is modelled by an effective Coulomb potential.
Historically, Cu_2O is the semiconductor material in which the formation of excitons was confirmed experimentally for the first time. A hydrogen-like series of narrow absorption peaks below the band gap was observed [7]. In recent years, the research of Cu_2O experienced a renaissance with the experimental achievement of resolving its P excitons up to a principal quantum number of $n = 25$ [11]. These highly excited states are known as Rydberg excitons, a name that originates from their counterpart of highly excited atomic states. The measurement of Rydberg excitons in Cu_2O, and their absence in other semiconductors so far, demonstrates that Cu_2O is predestined for the research on excitons. In the next sections, we will discuss the different exciton series, their symmetries and respective properties.

2.3.1. Exciton series

We already mentioned previously that the four most interesting bands in Cu_2O are the energetically lowest Γ_6^+ and second lowest Γ_8^- conduction bands, as well as the two highest valence bands $\Gamma_7^+ \oplus \Gamma_8^+$ that both emerge from the same Γ_5^+ valence band, which splits under spin-orbit interaction. Those bands construct a total of four exciton series in Cu_2O, with all of them being in the visible range: yellow ($\Gamma_7^+ \otimes \Gamma_6^+$), green ($\Gamma_8^+ \otimes \Gamma_6^+$), blue ($\Gamma_7^+ \otimes \Gamma_8^-$) and violet ($\Gamma_8^+ \otimes \Gamma_8^-$). The bands they are associated with are shown in Fig. 2.5 in a phenomenologial depiction of the band structure around the band gap.

In the effective mass approximation (see section 2.3.3) the exciton mass simply results from the sum of electron and hole mass. For the $n \geq 2$ excitons of the yellow series this approxima-

[5] Although a comparison to positronium would be more appropriate, due to the effective mass of electron and hole being in the same order of magnitude.

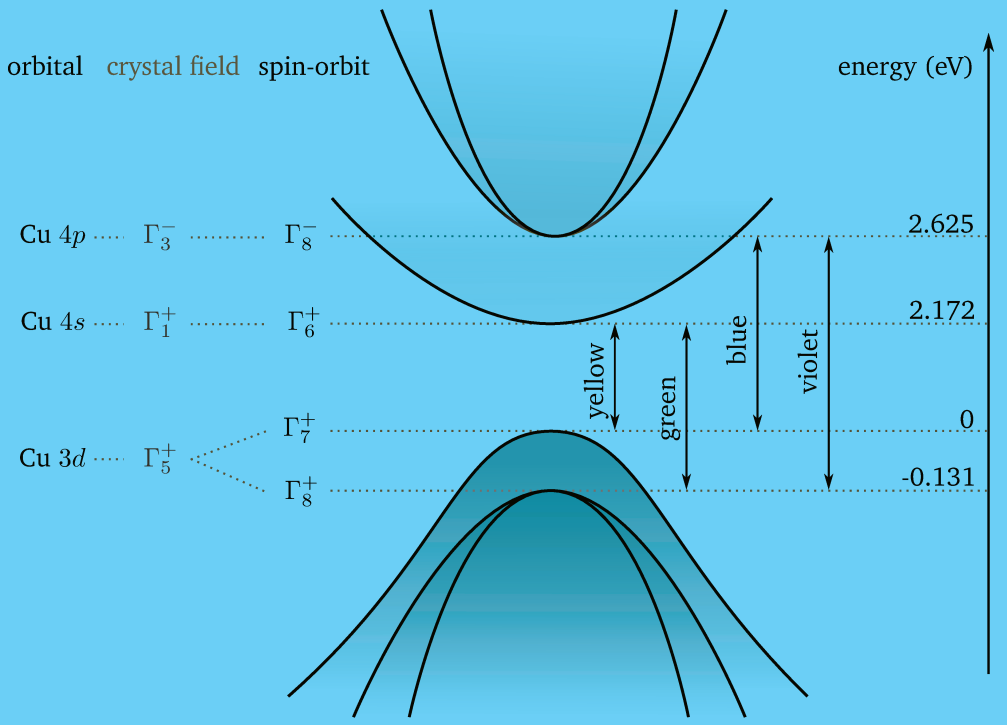

Figure 2.5.: Phenomenologial depiction of the two highest valence and two lowest conduction bands of Cu_2O, the atomic orbitals they originate from, their symmetries and energies at zone centre and the four distinct exciton series they form.

tion agrees quite well with a resulting mass of $M_\mathrm{y} \simeq 1.5\, m_0$; however, the 1S exciton falls out of line with an exciton mass of $M_{1\mathrm{Sy}} \simeq 2.6\, m_0$ [77, 78]. This value is confirmed by our calculations in chapter 4 for the 1S paraexciton. The explanation for this peculiar behaviour lies in the spatial extension of the yellow 1S exciton in momentum space: its wave function reaches far beyond the parabolic portion of the band structure, hence $m_{7\mathrm{v}} \simeq 0.55\, m_0$ is not a valid approximation for the hole mass. This consequently affects the other parameters of the yellow series. The relatively small extension in position space of low n excitons leads to them experiencing a weaker screening of the Coulomb interaction than Rydberg excitons, which subsequently imposes a difference in the excitonic Bohr radii and their Rydberg energies. The Rydberg energies of the Cu_2O exciton series are already quite large for Wannier excitons, due to a relatively weak screening, compared to other semiconductors. The 1S paraexciton demonstrates a binding energy of $E_{1\mathrm{Sy}} = 151\,\mathrm{meV}$ [25, 62] and a Bohr radius of $a_{1\mathrm{Sy}} = 0.51\,\mathrm{nm}$ (cf. section 4.3.2), while for higher n, the exciton states converge to a Rydberg energy of $\mathrm{Ry}^{(\mathrm{y})} = 86.04\,\mathrm{meV}$ and a Bohr radius of $a_\mathrm{y} = 1.1\,\mathrm{nm}$ (cf. section 3.2.2).

The anisotropies of the Γ_8^- conduction and Γ_8^+ valence bands inhibit a sensible prediction of the other series exciton masses via effective mass approximation. For the excitonic radii, we can employ the solution of the Wannier equation and with the Rydberg energies known from experiments we derive “empirical” Bohr radii to work with.

2.3.2. Symmetry

The exciton wave function is i.a. composed of the tensor product of the conduction and valence band states it is formed of. Consequently, the symmetry of an excitation at zone centre should result from the tensor product of the respective band symmetries $\Gamma_\mathrm{c} \otimes \Gamma_\mathrm{v}$. With this, we receive the electron and hole spin configuration and the corresponding symmetry of the constructed state. For the yellow series this would result in $\Gamma_{6\mathrm{c}}^+ \otimes \Gamma_{7\mathrm{v}}^+ = \Gamma_2^+ \oplus \Gamma_5^+$. In the cartesian basis of Γ_5^+ these correspond to a triplet of states, known as orthoexcitons (Γ_5^+), and the singlet known as paraexciton (Γ_2^+). For the green series we get $\Gamma_{6\mathrm{c}}^+ \otimes \Gamma_{8\mathrm{v}}^+ = \Gamma_3^+ \oplus \Gamma_4^+ \oplus \Gamma_5^+$, for blue $\Gamma_{8\mathrm{c}}^- \otimes \Gamma_{7\mathrm{v}}^+ = \Gamma_3^- \oplus \Gamma_4^- \oplus \Gamma_5^-$ and for violet $\Gamma_{8\mathrm{c}}^- \otimes \Gamma_{8\mathrm{v}}^+ = \Gamma_1^- \oplus \Gamma_2^- \oplus \Gamma_3^- \oplus 2\Gamma_4^- \oplus 2\Gamma_5^-$. These states are composed of superpositions of the band wave functions, including the electron and hole spin of the bands. The wave functions of the band states as well as the excitons can be found in the appendix B.2. The pure electron and hole spins can be oriented in a triplet state of parallel spin and a singlet state for antiparallel spin; hence, the corresponding wave functions are chosen symmetric $s_\mathrm{e}^+ s_\mathrm{h}^+$, $s_\mathrm{e}^- s_\mathrm{h}^-$, $(s_\mathrm{e}^+ s_\mathrm{h}^- + s_\mathrm{e}^- s_\mathrm{h}^+)/\sqrt{2}$ or antisymmetric $(s_\mathrm{e}^+ s_\mathrm{h}^- - s_\mathrm{e}^- s_\mathrm{h}^+)/\sqrt{2}$. It should be noted that the exchange part of the Coulomb interaction will only affect spin states with opposite spin, thus the antisymmetric spin singlet state [51, 79]. The different exciton states of each series can also be expressed in this singlet-triplet notation. Consequently, only the states of each series that incorporate singlet terms are affected by electron-hole exchange interaction. As an example, in the yellow series the paraexciton is only comprised of triplet spin states, while the orthoexcitons all possess singlet terms. This leads to an additional splitting between these two subseries by an exchange splitting, shifting the orthoexcitons energetically upwards about $\Delta_\mathrm{1S} = 12.1\,\mathrm{meV}$ for the yellow 1S exciton [62]. Hence, the yellow 1S paraexciton is actually the lowest excited state in Cu_2O.

The optical absorption into exciton states requires the transition from excitonic vacuum into the specific state via the electron-radiation Hamiltonian. In a semiclassical approach in which light is regarded propagating as a plane wave $e^{\mathrm{i}\mathbf{q}\cdot\mathbf{r}}$ and its momentum $\mathbf{q}$ is assumed to be small, the electron-radiation Hamiltonian can be expressed as a Taylor expansion of the plane wave and splits into separate contributions. The first term is the strongest and describes the electric dipole transition $\mathbf{p}$. Since $\mathbf{p}$ transforms like an axial vector, it carries the symmetry of Γ_4^- in the O_h point group (see appendix A.2) [72]. The next order term takes the form $\mathbf{p}(\mathbf{q}\cdot\mathbf{r})$ and thusly has the symmetry $\Gamma_4^- \otimes \Gamma_4^- = \Gamma_1^+ \oplus \Gamma_3^+ \oplus \Gamma_4^+ \oplus \Gamma_5^+$, with $\Gamma_3^+ \oplus \Gamma_5^+$ representing electric quadrupole and Γ_4^+ magnetic dipole transitions. Transition terms beyond that are usually negligible as the oscillator strength of the electric quadrupole and magnetic dipole transitions is on the order of 10^{-6} smaller than the oscillator strength of the electric dipole excitation [62]. For an optical transition to be allowed, the transition matrix element needs to obey the restrictions of symmetry; therefore, the symmetry product of the transition operator with the exciton states needs to contain unity. To fulfill this requirement the subscript and parity of the exciton state need to coincide with the transition operators symmetry. This restriction would imply that, if

$\otimes$ envelope $\longrightarrow$ $\downarrow$series	**S** (Γ_1^+)	**P** (Γ_4^-)
yellow ($\Gamma_6^+ \otimes \Gamma_7^+$)	$\Gamma_2^+ \oplus \Gamma_5^+$	$\Gamma_2^- \oplus \Gamma_3^- \oplus \Gamma_4^- \oplus 2\Gamma_5^-$
green ($\Gamma_6^+ \otimes \Gamma_8^+$)	$\Gamma_3^+ \oplus \Gamma_4^+ \oplus \Gamma_5^+$	$\Gamma_1^- \oplus \Gamma_2^- \oplus 2\Gamma_3^- \oplus 3\Gamma_4^- \oplus 3\Gamma_5^-$
blue ($\Gamma_8^- \otimes \Gamma_7^+$)	$\Gamma_3^- \oplus \Gamma_4^- \oplus \Gamma_5^-$	$\Gamma_1^+ \oplus \Gamma_2^+ \oplus 2\Gamma_3^+ \oplus 3\Gamma_4^+ \oplus 3\Gamma_5^+$
violet ($\Gamma_8^- \otimes \Gamma_8^+$)	$\Gamma_1^- \oplus \Gamma_2^- \oplus \Gamma_3^- \oplus 2\Gamma_4^- \oplus 2\Gamma_5^-$	$2\Gamma_1^+ \oplus 2\Gamma_2^+ \oplus 4\Gamma_3^+ \oplus 6\Gamma_4^+ \oplus 6\Gamma_5^+$

Table 2.2.: The exciton states of Cu_2O categorised by their symmetries around zone centre. The coloured boxes indicate possible transitions from the excitonic vacuum into the respective state, with green denoting electric dipole, yellow magnetic dipole and red electric quadrupole allowed transitions [70].

exciton symmetry is solely resulting from band symmetry, the yellow and green series could not be excited via a dipole transition. Since we are aware from the P exciton spectrum that this is false, another symmetry component needs to be present.

As already stated, the interaction between electron and hole of an exciton can be described, in a very simple manner, as an analogon to the hydrogen atom; hence, it is favourable to categorise excitons by a set of quantum numbers n, ℓ, m. The angular distribution of the exciton wave function is then described by spherical harmonics $Y_{\ell,m}$, as will be seen in the upcoming section. From this the angular quantum number ℓ of the envelope wave function carries an additional symmetry, thus leading to an actual exciton symmetry that is constructed as

$$\Gamma_{\mathrm{exc}} = \Gamma_{\mathrm{env}} \otimes \Gamma_{\mathrm{c}} \otimes \Gamma_{\mathrm{v}} \,. \tag{2.26}$$

For S ($\ell = 0$) type excitons (Γ_1^+) there is no change in symmetry in regard to the direct band transition. For P ($\ell = 1$) type excitons (Γ_4^-) the envelope incorporates the requisite symmetry and parity which enables the direct electric dipole excitation of P excitons of the yellow and green series. Similar we recognise that for the blue and violet series the S states are dipole allowed. For the two lowest angular quantum numbers S and P the different resulting exciton states for all four series with their symmetries are listed in Tab. 2.2. For envelopes with larger angular quantum number the categorisation of all the individual exciton states to their respective symmetry quickly gets overblown and to a certain degree unnecessary. The most notable property is the parity change that is imposed by the electric dipole operator, or the lack thereof for magnetic dipole and electric quadrupole transitions, respectively. The envelope wave functions of the atomic orbitals are known to possess positive parity for even ℓ and negative parity for odd ℓ quantum numbers. Thus the manner of excitation alternates between electric dipole and magnetic dipole/electric quadrupole with incremental ℓ and is initially dependent on the product of valence and conduction band parity, as can be seen in the swapping of colour schemes in Tab. 2.2.

Though the S states of yellow and green series are only quadrupole allowed, these exciton states are still accessible over different means and play an important role for optical absorption. The most prevalent way, which is also the dominant contribution in the absorption spectrum, is the phonon-assisted transition. For this the symmetry of the interacting phonon has to be taken into account. Some remarks concerning the phonons in Cu_2O are found in the upcoming section 2.4.1, and the phonon-assisted absorption will be further analysed in chapter 5. Additionally, it is possible to drive intraexcitonic transitions in the infrared regime [80]. Those transitions generally require a change of the angular quantum number from an odd to an even ℓ or vice versa, since the transition matrix element of initial and final exciton state via dipole operator requires the symmetry product to yield unity. Another way would be the absorption via a two photon process, which again yields the necessary symmetry $\Gamma_4^- \otimes \Gamma_4^- = \Gamma_1^+ \oplus \Gamma_3^+ \oplus \Gamma_4^+ \oplus \Gamma_5^+$ to excite orthoexcitons.
On a side note, strain on the crystal also breaks symmetry, thus softening the symmetry restrictions for excitations [75, 81]. As a consequence the yellow paraexciton, which is usually supposedly invisible in the spectrum, is able to be excited.

2.3.3. Wannier equation

The mathematical description of excitons in semiconductors is usually based on the Wannier equation [49–51]. In the limit of large excitons, or weak binding energies, respectively, the long range Coulomb interaction between electron and hole constitutes the most important of their interaction terms; thus, other interactions are neglected for now. The interaction with the rest of the crystal is incorporated in a medium specific dielectric constant that screens the Coulomb interaction. In the effective mass approximation, the Schrödinger equation of the two-particle system is then

$$\left(\frac{\mathbf{p}_\mathrm{e}^2}{2m_\mathrm{e}} + \frac{\mathbf{p}_\mathrm{h}^2}{2m_\mathrm{h}} + V_\mathrm{eff}(|\mathbf{r}_\mathrm{e} - \mathbf{r}_\mathrm{h}|) \right) \Psi(\mathbf{r}_\mathrm{e}, \mathbf{r}_\mathrm{h}) = E\, \Psi(\mathbf{r}_\mathrm{e}, \mathbf{r}_\mathrm{h}) \,, \tag{2.27}$$

with $\mathbf{p}_i$ and m_i being the momentum operator and effective mass, respectively. The effective Coulomb potential $V_\mathrm{eff}(r) = -\mathrm{e}^2/(4\pi\varepsilon_0\varepsilon_\mathrm{r} r)$ is modified by the dielectric constant, which is generally frequency- and momentum-dependent, i.e. $\varepsilon_\mathrm{r} = \varepsilon_\mathrm{r}(\omega, \mathbf{k})$. It is advantageous to rewrite the coordinates $\mathbf{r}_\mathrm{e}$ and $\mathbf{r}_\mathrm{h}$ into the centre of mass (COM) coordinate $\mathbf{R}$ and relative coordinate $\mathbf{r}$ via

$$\mathbf{R} = \frac{m_\mathrm{e}\mathbf{r}_\mathrm{e} + m_\mathrm{h}\mathbf{r}_\mathrm{h}}{M} \,, \qquad \mathbf{r} = \mathbf{r}_\mathrm{e} - \mathbf{r}_\mathrm{h} \,, \tag{2.28}$$

which consequently translates into

$$\mathbf{P} = \mathbf{p}_\mathrm{e} + \mathbf{p}_\mathrm{h} \,, \qquad \mathbf{p} = \frac{m_\mathrm{h}\mathbf{p}_\mathrm{e} - m_\mathrm{e}\mathbf{p}_\mathrm{h}}{M} \,. \tag{2.29}$$

Here, we introduced the exciton mass $M = m_\mathrm{e} + m_\mathrm{h}$. Next, we presume the wave function can be deconstructed into a product state $\Psi(\mathbf{R}, \mathbf{r}) = F(\mathbf{R})\ \phi(\mathbf{r})$. Under this assumption, the Schrödinger equation is decoupled, since the COM component is unaffected by the Coulomb interaction

$$\frac{\mathbf{P}^2}{2M}\ F(\mathbf{R}) = E_\mathbf{R}\ F(\mathbf{R})\,, \tag{2.30}$$

with its solution readily obtainable

$$F(\mathbf{R}) = \frac{1}{\sqrt{\Omega}}\, e^{i\mathbf{K}\cdot\mathbf{R}}\ , \qquad E_\mathbf{R} = \frac{\hbar^2 K^2}{2M}\,. \tag{2.31}$$

As this corresponds to a free particle equation, it describes the overall COM propagation of the exciton through the crystal. The second part of the decoupled Schrödinger equation characterises the relative motion between electron and hole and their envelope function, respectively,

$$\left(\frac{\mathbf{p}^2}{2\mu} + V_\mathrm{eff}(r)\right)\ \phi_\nu(\mathbf{r}) = E_\nu\ \phi_\nu(\mathbf{r})\,, \tag{2.32}$$

with the reduced mass $\mu^{-1} = m_\mathrm{e}^{-1} + m_\mathrm{h}^{-1}$. This equation is known as Wannier equation and is analogous to the Schrödinger equation of the hydrogen atom. This allows us to separate the envelope wave function as

$$\phi_{n,\ell,m}(\mathbf{r}) = R_{n,\ell}(r)\ Y_{\ell,m}(\mathbf{n_r})\,, \tag{2.33}$$

where $R_{n,\ell}(r)$ can be expressed via associated Laguerre polynomials, and $Y_{\ell,m}(\mathbf{n_r})$ are spherical harmonics, with $\mathbf{n_r}$ being the normal vector of $\mathbf{r}$. Following the comparison to the hydrogen problem, the resulting energy eigenvalues are

$$E_n = \Delta E_\mathrm{b} - \frac{\mathrm{Ry}^*}{n^2}\,, \tag{2.34}$$

with ΔE_b being the energy difference between the bands involved, e.g. for the yellow series $\Delta E_\mathrm{b} = E_\mathrm{y}$, and Ry^* being the excitonic Rydberg energy defined as

$$\mathrm{Ry}^* = \frac{\mu\ \mathrm{e}^4}{2^5\pi^2\,\hbar^2\varepsilon_0^2\varepsilon_\mathrm{r}^2} = \frac{\mu}{m_0}\frac{1}{\varepsilon_\mathrm{r}^2}\ \mathrm{Ry}\,. \tag{2.35}$$

As expected, the Wannier equation results in a set of discretely excitable energy states below the corresponding energy gap.

In this work, we will take the effective mass approximation beyond the parabolic approximation by utilising the valence band dispersion of the Suzuki-Hensel Hamiltonian introduced in the preceding section. In this case, the Schrödinger equation of the two-particle system does not decouple for COM and relative coordinates any longer. In chapter 3 we will assume

the exciton momentum $\mathbf{K}$ to be negligible small, ignoring COM contributions and receiving a modified Wannier equation, that is sufficient to determine the binding energies of the excitonic Rydberg P states. In chapter 4, we additionally refine the effective interaction potential by considering polar phonon resonances and solve the two-particle Schrödinger equation without decoupling to receive the exciton dispersions of the yellow S paraexcitons.

2.4. Phonons

The discussion of phonons is inevitable for this work as they represent one of the most rudimentary processes in semiconductors. The concept of phonons was first introduced by I. Tamm, supposedly around 1929 [82]. Phonons are quasiparticles that describe the different vibrational modes of the atoms within crystal lattice. The electron-phonon interaction can be visualised (in terms of a first order Taylor expansion) as the static displacement of the lattice atoms. On a mesoscopic scale this displacement can be compared to a deformation of the crystal. Such a deformation can impose changes on the electronic states in the band structure. There exist four types of long-wavelength phonons, longitudinal acoustic (LA), transverse acoustic (TA), longitudinal optical (LO) and transvere optical (TO).
Longitudinal acoustic phonons cause a change in the crystal volume. This dilation can result in a change of the position and/or slope of the energy bands, it does, however, not change the symmetry of the crystal. Therefore scattering processes via LA phonons must possess the symmetry of a unitary transformation, i.e. Γ_1^+. Transverse acoustic phonons show a Γ_4^- symmetry and only inflict a shear strain which does not impose a noteworthy effect on the energy of the bands, but is known to lower the crystal symmetry and, thus, lift band degeneracies [50]. Acoustic phonons are low energy phonons and exhibit a linear dispersion relation in momentum space around zone centre, with their energy being zero at the Γ point. Mathematically, the interaction of acoustic phonons with the crystal lattice is described by the acoustic deformation potential. They are usually responsible for intraband scattering processes, since their energy is too low for interband scattering.
In crystals with more than one atom per unit cell, optical phonons describe the atomic displacement within the unit cell. Due to the distortion being on microscopic length scales, they do not cause a macroscopic dilation of the crystal, although they can influence the properties of the band structure in a similar fashion as acoustic phonons. In nonpolar and monoatomic crystals, they induce an atomic displacement that is usually sufficient to treat via an optical phonon deformation potential. However, in polar crystals, which are usually present if the unit cell is constructed of multiple types of atoms, a relative displacement due to LO phonons causes shifts in the atomic charge distributions, inducing a macroscopic polarisation. Generally, the polarisation that is caused by atomic vibrations on the optical scale strongly couples electrons and holes to LO-phonons. The interaction of carriers with this field (phonon cloud)

can be constituted as quasiparticles known as polarons. The mathematical description of this interaction is done by the Fröhlich or Holstein Hamiltonian [50, 52, 53]. The energy dispersions of optical phonons generally do not vary too drastically within momentum space; thus, their energy is usually assumed to be more or less constant. High energy phonons contribute to interband scattering via the deformation potential. Polarons only allow for intraband scattering, due to the orthonormality of the Bloch functions[6]. Generally crystals are neither purely polar or nonpolar, but occupy a niche in between; thus, aspects of all phonon interactions can be observed in most semiconductors.

2.4.1. Phonons in Cu_2O

Cu_2O features six atoms in the primitive unit cell; hence, there is a total of 18 different phonon modes [84]. Those modes are further differentiated as three acoustic branches and 15 optical branches. By examining the permutation of the atoms in the primitive unit cell under the symmetry operations of the T_d point group, the symmetries of the 18 zone-centre mode phonons are derived to be $\Gamma_2^- \oplus \Gamma_3^- \oplus 3\Gamma_4^- \oplus \Gamma_5^- \oplus \Gamma_5^+$ [50]. One of the three triply degenerate Γ_4^- states corresponds to the acoustic phonons, while the other two represent the polar optical phonons, with their LO components being infrared-active. The Γ_5^+ phonon is Raman-active due to its positive parity. The remaining optical phonons $\Gamma_2^- \oplus \Gamma_3^- \oplus \Gamma_5^-$ are called silent modes. The energies of the different phonon modes and their vibrational behaviour are listed in Tab. 2.3, in Fig. 2.6 the atomic movement is indicated.

In the context of this work, we are interested in two prospects phonons entail. The first is the formation of the polaron quasiparticle. The polaron is interesting in this case, as it incorporates two effects upon the system, namely a change of the effective masses, as well as a change of the screening background. The second effect is the direct interaction with excitons and the process of interband scattering between the different exciton series in regards to phonon-assisted absorption.
The polarisation that is induced by a carrier to its surroundings via Coulomb interaction can be visualised as a polarisation cloud that will move according to the carriers movement. In terms of phonons, the polarisation cloud can be understood as the perpetual creation and annihilation of virtual LO phonons around the carrier. The distortion of the lattice that is caused by the polarisation leads to an increased effective mass of the polaron $\tilde{m}_i$ in comparison to the effective mass of the "undisturbed" carrier m_i. In the weak coupling limit, i.e. the large

[6] The scalar potential of the LO interaction does not modify the Bloch functions, hence can be extracted from the transition matrix elements [83].

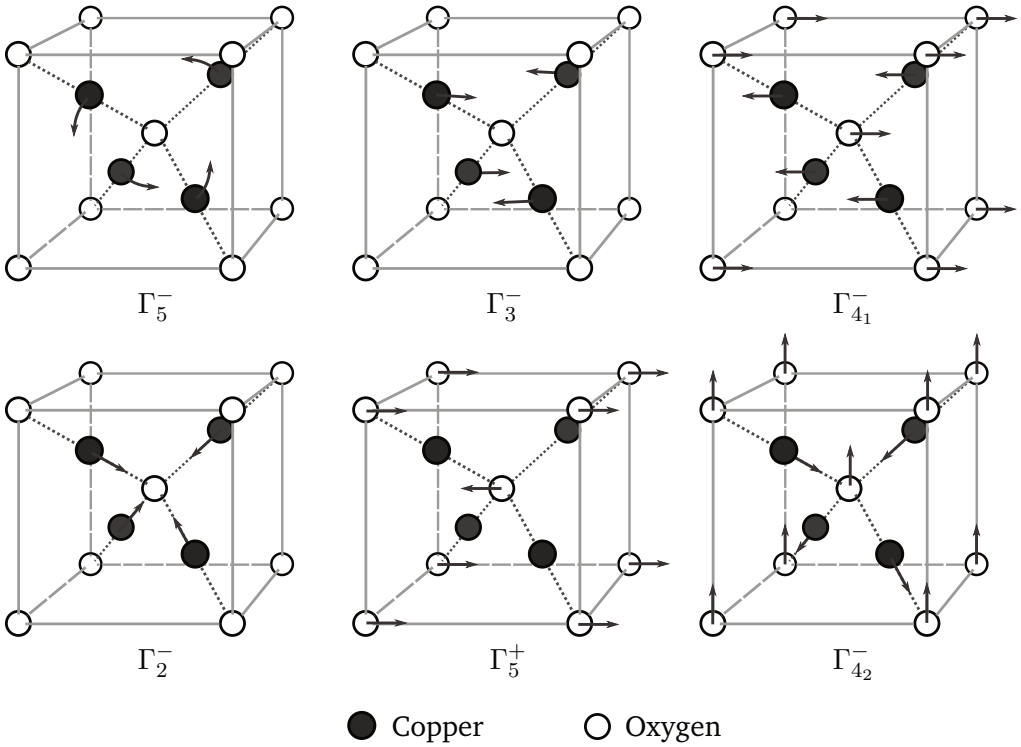

Figure 2.6.: The unit cell with the O bcc sublattice as base and the normal modes of vibration indicated by arrows. Description of the movement is found in Tab. 2.3.

polaron, the mass difference between the two is roughly approximated as [85]

$$\tilde{m}_i \simeq m_i \left(1 + \sum_\lambda \frac{\alpha_\lambda}{6}\right), \tag{2.36}$$

with

$$\alpha_\lambda = \frac{e^2}{4\pi\varepsilon_0\varepsilon_\lambda^*\hbar}\sqrt{\frac{m_0}{2\hbar\omega_{\mathrm{LO},\lambda}}}, \tag{2.37}$$

$$\frac{1}{\varepsilon_\lambda^*} = \frac{1}{\varepsilon_{\lambda+1}} - \frac{1}{\varepsilon_\lambda} \tag{2.38}$$

and $\hbar\omega_{\mathrm{LO},\lambda}$ being the energy of the corresponding phonon branch λ. The ε_λ denote the values of the permittivity, energetically below and beyond the LO phonon resonances. The charge displacement that is caused by the Γ_4^- LO phonons also leads to a local perturbation in screening strength of the charge distribution around the polaron. For small excitons that consist of "polaronic" electron and hole, the influence of the background screening is diminished and, thus, the effective Coulomb interaction between them is modified. For Rydberg excitons, however, this effect quickly becomes irrelevant. The influence of the polaron effect on the Coulomb potential will be discussed in chapter 4. The limiting values for ε_λ are known experimentally, but only for room temperature [23, 84]. The static dielectric constant is known to be more

	E (meV)	description
${}^3\Gamma_4^-$	0	acoustic modes
${}^3\Gamma_5^-$	10.7	rigid rotation of the Cu tetrahedron around O centre, bends the O-Cu-O bonds
${}^2\Gamma_3^-$	13.6	skewing of the Cu tetrahedron by parallel oscillation of the Cu atoms
${}^3\Gamma_{4_1}^-$	18.8 (TO) 19.1 (LO)	contrarious movement of the Cu and O lattices
${}^1\Gamma_2^-$	43.4	breathing mode of the Cu tetrahedron
${}^3\Gamma_5^+$	63.8	contrarious movement of the intertwined simple cubic O lattices
${}^3\Gamma_{4_2}^-$	78.5 (TO) 82.1 (LO)	Cu atoms move in the same cardinal direction along the bonds, O atoms compensate by moving in the opposite direction

Table 2.3.: The 18 phonon branches of Cu_2O sorted by their energy [81,87] at zone centre Γ with their respective symmetries and description of the vibration behaviour. A depiction of the atom movement imposed by the optical phonons is shown in Fig. 2.6.

or less constant over wide temperature ranges and approaches $\varepsilon_1 = \varepsilon(\omega = 0) \simeq 7.5$ for low temperatures [86]. The intermediate and high frequency limit values are approximated via the Lyddane-Sachs-Teller relation [50, 52]

$$\frac{\omega_{\mathrm{LO},\lambda}^2}{\omega_{\mathrm{TO},\lambda}^2} = \frac{\varepsilon_\lambda}{\varepsilon_{\lambda+1}}\,, \tag{2.39}$$

as $\varepsilon_2 \simeq 7.27$ and $\varepsilon_3 = \varepsilon(\omega \to \infty) \simeq 6.65$, using the phonon energies of Tab. 2.3. These permittivities are necessary to determine the modified effective Coulomb potential and additionally allow us to calculate the band masses that we required in section 2.2.1 and 2.2.3, via Eq. (2.36).

For interband transitions, i.e. phonon-assisted transitions between two exciton series, we need to ensure that the phonon symmetry coincides with the symmetry product of the transitory band states. Phonon driven interband transitions always incorporate only transitions between either conduction or valence bands. As an example, the transition between the Γ_3^- and Γ_1^+ conduction bands requires a phonon with symmetry $\Gamma_3^- \otimes \Gamma_1^+ = \Gamma_3^-$. It should be noted that, if we take the same product with the symmetries after including spin-orbit interaction, we receive $\Gamma_8^- \otimes \Gamma_6^+ = \Gamma_3^- \oplus \Gamma_4^- \oplus \Gamma_5^-$, hence additional possibilities for transition. However, these require the occurrence of a spin-flip of the electron, thus reducing the probability for $\Gamma_4^- \oplus \Gamma_5^-$ scattering drastically. In the case of phonon-assisted absorption, the symmetry of the final exciton state has to be contained in the product of the dipole operator Γ_4^- and the corresponding phonon symmetry. It is easy to show that a Γ_5^+ exciton can couple to all odd parity phonons,

while a Γ_4^+ state could couple to all odd parity phonons exept the Γ_2^- mode. From luminescence spectroscopy we know that the Γ_3^- optical phonon is the dominant phonon branch [81]. The contributions of all other phonons is much weaker, except the $\Gamma_{4_2}^-$ LO phonon. Note that the coupling mechanism for all phonon modes is via the optical deformation potential, since Fröhlich coupling, as one might think in case of the polar Γ_4^- LO modes, only gives rise to intraband processes. The even parity Γ_5^+ mode can in principle also contribute to the absorption by a wave vector dependent deformation potential, which has odd parity [26].

Chapter 3.

Quantum defects of the excitonic Rydberg series

Colleagues of the Technische Universität Dortmund recently found P excitons up to high principal quantum numbers $n = 25$ [11]. These highly excited states are referred to as Rydberg excitons, a term that is coined in relation to their counterpart from atomic physics: highly excited electron states in atoms that are known as Rydberg states. Before, the research of Rydberg excitons was of no interest, partially because their realisation was not deemed feasible nor sustainable. Most excitons possess very small binding energies as well as the short lifetimes. Furthermore, an e-h plasma induced band gap shift indicates, that highly excited excitons would be swallowed by the continuum and vanish before reaching a principal quantum number that would open the window to novel quantum phenomena [31].
Cu_2O counters most of the shortcomings mentioned before and is therefore a suitable candidate for the research of Rydberg excitons. Especially the reproduction of phenomena already observed in atomic physics but in a less restrictive environment and, hence, in a much more experimentalist friendly framework (e.g. effects such as Rydberg blockade are identifiable at $T = 1\,\mathrm{K}$ [11]) is a promising prospect. Additionally, it is possible to examine new properties due to the unique setting within the semiconductor itself [13–16, 24, 88–91].

In this chapter, we resort to the SH Hamiltonian we introduced in section 2.2.3 to establish an advanced Wannier equation. In this case, we merely model the influence of the nonparabolicity of the valence band. To depict the deviation from the standard Wannier equation, we reintroduce the concept of quantum defects in semiconductors. The results of this chapter are published in [91, 92].

3.1. Origin of the excitonic quantum defect

Rydberg atoms, i.e. atoms that have a valence electron excited to large a principal quantum number n, demonstrate some extraordinary properties that are not present in their ground-state counterpart. Atomic spectra are an extremely rich source of information about the interactions of electrons and the ionic core, and their study laid the foundations of the development of quantum mechanics. Historically, the Balmer series of hydrogen was the first attempt to classify the discrete emission lines of an atom [93], revealing an $1/n^2$-scaling of the observed lines as explained naturally by quantum mechanics. However, already the spectra of alkali, i.e. hydrogen-like, atoms required a modification of the spectrum. J. Rydberg introduced an empirical correction to the term scheme, which later had been incorporated into the binding energy by replacing the principal quantum number n by a non-integer number $n^* = n - \delta$ where δ is introduced as a quantum defect [12]. The quantum defect treatment allows one to systematically map complex many-body effects in atomic spectra onto a set of parameters. They serve as a measure for the deviation between energy levels of many-electron atoms from the hydrogen levels as it results from the influence of the polarisable ionic core on the valence electrons. The charges of the nucleus are partially screened by the charges of the inner electron, which leads to a subsequent modification of the Coulomb potential [12, 94]. It generally decreases with increasing orbital quantum number ℓ as the partial probability overlap of the Rydberg electron with the core gradually decreases. For increasing n it slowly increases up to a point where it almost becomes constant for $n \to \infty$. The concept of the quantum defect has proven to be extremely successful, in particular in the description of highly excited alkali and alkaline-earth atoms.

The possibility to measure Rydberg exciton states to a high precision requires a certain set of properties for the semiconductor. Cu_2O is of particular interest for experiments due to a relatively large hole mass and a favourably small screening of the electron-hole Coulomb interaction via the crystal lattice. This leads to the comparably large exciton binding energy. For comparison, the P excitons in Cu_2O yield a Rydberg energy of $\mathrm{Ry}^* = 86\,\mathrm{meV}$, while for other semiconductors the Rydberg energy resides in the range of, e.g. GaAs with $\mathrm{Ry}^* = 4.94\,\mathrm{meV}$ and CdS with $\mathrm{Ry}^* = 31.4\,\mathrm{meV}$ [95] up to ZnO with $\mathrm{Ry}^* = 59\,\mathrm{meV}$ [50]. The direct band gap allows a direct excitation with photons without requiring additional phonon transitions. It is easily excitable by light in the visible range (the gap is around a wavelength of $\lambda_G \simeq 571\,\mathrm{nm}$), a range that also conveniently possesses tunable diode laser sources with high precision. Another notable benefit that favours Cu_2O over other semiconductor materials is a relatively long exciton lifetime [96].

3.1.1. Central-cell corrections

In semiconductor physics, the exciton concept translates the bound states of an electron-hole pair onto a hydrogen-like series. By using hydrogen-like wave functions as the excitonic envelope function, as it is done throughout the entirety of this work, we identify the different exciton resonances by the same quantum numbers known from atomic physics and the position of the resonances result as the bound state solution eigenvalues of the Wannier equation. The even parity of the conduction and valence band at zone centre inhibits a direct dipole transition of S like states; however, we are mainly interested in P type excitons since the Γ_4^- symmetry of their envelopes allows for dipole excitation. Similar to alkaline systems, additional phenomena within the semiconductor lead to a modification of the Coulomb interaction between electron and hole and therefore to a shift from the hydrogen-like series that results from the standard Wannier equation. The modified excitonic Rydberg formula for the binding energy $E_{n,\ell}$ reads

$$E_{n,\ell} = -\frac{\mathrm{Ry}^*}{(n-\delta_{n,\ell})^2}\,, \tag{3.1}$$

with Ry^* being the exciton Rydberg energy. The excitonic quantum defect $\delta_{n,\ell}$ is a set of individual functions for the different orbital quantum numbers ℓ, slowly varying over n or energy, respectively. It incorporates the several semiconductor-specific properties that cause the energy shift. These different effects are conveniently conglomerated under the terminology of central-cell corrections [23, 97].
One issue that was already elaborated in chapter 2.1 is the nonparabolicity of the bands, in the case of Cu_2O the valence band especially. The interaction of electron and hole with the two LO-phonon modes leads to a frequency- and momentum-dependent dielectric function which subsequently modifies the Coulomb interaction. Additionally, the spin-dependent exchange interaction between electron and hole can lift the degeneracy of singlet- and triplet-exciton states. The latter two will not be treated in detail in this chapter; however, in the upcoming passages we will shortly discuss their expected influences on the spectral distribution of exciton resonances and explain why we are able to skip an in-depth treatment.
From the theory of the hydrogen atom the exchange interaction is known to scale as [98]

$$|\phi_{n,\ell}(0)|^2 \propto \begin{cases} n^{-3} & \text{for } \ell = 0 \\ 0 & \text{for } \ell > 0\,, \end{cases} \tag{3.2}$$

here $\phi_{n,\ell}(\mathbf{r})$ denotes the hydrogen wave function in position space. As a consequence, we assume that only S like excitons are affected by the exchange splitting. The energy shift of the exchange interaction only applies to electron-hole singlet states due to their negative spin-exchange parity. Therefore, it only affects orthoexcitons, since the paraexcitons solely consist

of triplet states. As already stated, we are mainly interested in the highly excited P excitons, so our Hamiltonian does not explicitly contain a term that includes the exchange interaction; therefore, we expect to receive only the paraexciton energies of the S states from our treatment. However, the measured values of S excitons that will be used for the quantum defect treatment are orthoexcitons, due to the paraexciton transition being completely forbidden in a nonstressed crystal. We apply a phenomenological ansatz to extract the paraexcitons from the experimental orthoexcitons. The value of the exchange splitting for the 1S state is well established as $\Delta_{1\mathrm{S}} = 12.1\,\mathrm{meV}$ [62]. Taking the relation of (3.2) we shift the other S states as

$$\Delta_{n\mathrm{S}} = \frac{\Delta_{1\mathrm{S}}}{n^3}\,, \tag{3.3}$$

to get approximate values for the paraexcitons.
The energy of the lower of the two LO-phonons is known to be $\hbar\omega_4^{(1)} = 19.1\,\mathrm{meV}$. The exciton resonances beyond $n \geq 3$ all exhibit binding energies well below $\hbar\omega_4^{(1)}$, which leaves them mostly unaffected by the LO-phonons. The $n = 1, 2$ states require special attention as the interaction with the LO-phonons causes a significant modification of the effective Coulomb interaction. These low n states are not well assessed; however, the beauty of the presented approach is the opportunity to treat most of the derivation analytically. The coupling to the LO-phonons will become of interest in chapter 4 where we are investigating the dispersion of the 1S paraexciton.
The nonparabolicity of the valence band is the major intrinsic influence on the energy shift of the Rydberg exciton states. There exist potential external factors that can lead to additional shifts. External fields can lead to a splitting and shifting of degenerate states via the Stark and Zeeman effect, for static electric and magnetic fields, respectively [91]. For higher n states we can expect additional shifts of peak positions due to influence of a Rydberg blockade effect [12, 99, 100]. The blockade stems from interaction between the large dipole moments of Rydberg excitons. It leads to an increase of the linewidth for the respective resonance and an energy shift for the neighbouring states [11]. Another notable effect is the shift in stressed crystal systems. Here, the main participant is a general red shift of the band gap, though there is also a slight diminishment of excitonic binding energies which is mainly discernible [75, 101].

3.2. The modified Wannier equation

In the previous section, we discussed the different factors that lead to potential shifts of the excitonic Rydberg series and thence, are incorporated by the excitonic quantum defect. We established, that the band nonparabolicity should be the predominant influence on the Rydberg excitons; thus, we will now introduce a band structure modified Wannier equation in

this chapter. Unlike the usual approach [19–25] the main difference in our calculation is the handling in momentum space rather than position space. The derivations done in this chapter are heavily oriented on an approach introduced by R. Szmytkowski [102] for the momentum-space Schrödinger equation of an N-dimensional Coulomb problem, however, modified for semiconductor systems and with the addition of the nonparabolic dispersion. This work is primarily concerned with the treatment of isotropic dispersions, for an attempt to solve the same problem with anisotropic bands, refer to [103].

3.2.1. Determination of the energy eigenvalues

As mentioned in chapter 2.3, in effective mass approximation the general electron-hole interaction Hamiltonian can be decoupled into a free-particle Schrödinger equation for the COM component $(\mathbf{R}, \mathbf{P})$ and the Wannier equation for the relative electron-hole motion $(\mathbf{r}, \mathbf{p})$. Introducing a nonparabolicity to the band dispersions the Schrödinger equation for COM and relative coordinates does not decouple any longer, resulting in a nonlinear partial differential equation

$$\left(T(\mathbf{P}, \mathbf{p}) + V_{\text{eff}}(\mathbf{r})\right) \Psi(\mathbf{R}, \mathbf{r}) = E\, \Psi(\mathbf{R}, \mathbf{r})\,. \tag{3.4}$$

The term $T(\mathbf{P}, \mathbf{p})$ incorporates the sum of kinetic energies of electron and hole transformed into COM and relative coordinates. Equation (3.4) generally requires a numerical or perturbative treatment. At low temperatures, exciton momentum is assumed to be primarily dependent on the incoming photon momentum, which is on the order of $10^{-2}\,\pi/a_{\text{L}}$ at a photon energy around $2\,\text{eV}$ (with $a_{\text{L}} = 0.43\,\text{nm}$ being the lattice constant of Cu_2O) and, thus, comparably small. The binding energies used in our analysis are taken at temperatures around $T \simeq 1\,\text{K}$ [11, 62, 91], reasonably close to fulfilling that criterion. Therefore, as a zeroth order approximation, exciton momentum $\mathbf{K}$ is set to zero. Consequently, we are left with the evaluation of the Wannier equation

$$\left(\frac{\mathbf{p}^2 + D(\mathbf{p})}{2\mu} + V_{\text{eff}}(\mathbf{r})\right) \phi_\nu(\mathbf{r}) = E_\nu\, \phi_\nu(\mathbf{r})\,. \tag{3.5}$$

It resembles the normal Wannier Eq. (2.32), with the additional term $D(\mathbf{p})$ describing the nonparabolicity. The eigenfunctions $\phi_\nu(\mathbf{r})$ are the hydrogen-like envelope functions in position space with ν being the corresponding set of quantum numbers (n, ℓ, m). Instead of solving Eq. (3.5) as it is, we transform it into momentum space

$$\left(\frac{\hbar^2\left(k^2 + D(k^2)\right)}{2\mu} - E_\nu\right) \varphi_\nu(\mathbf{k}) = -\frac{\Omega}{(2\pi)^3} \int \mathrm{d}^3\mathbf{k}'\; V_{\text{eff}}(\mathbf{k} - \mathbf{k}')\, \varphi_\nu(\mathbf{k})\,. \tag{3.6}$$

Here, we already inserted the assumption that the nonparabolicity $D(k^2)$ is only dependent on squared terms of k. The coefficient $\Omega/(2\pi)^3$, with Ω being the crystal volume, stems from a peculiarity of solid state physics, as the distribution of momentum states is technically not continuous but discrete. The spacing between adjacent momentum states is $\Delta k = 2\pi/L$ per dimension and with a spatial expansion L of the solid body in that dimension. In bulk semiconductors ($L \to \infty$, and $\Omega = L^3$) the sum over discrete momentum states $\mathbf{k}$ then transforms into a continuous integral

$$\sum_{\mathbf{k}} \longrightarrow \frac{\Omega}{(2\pi)^3} \int \mathrm{d}^3\mathbf{k}\,. \tag{3.7}$$

Thus, in this work, all sums in momentum space will be transformed in this fashion. The convolution of the Coulomb potential with the wave function in Eq. (3.6) turns the nonlinear partial differential equation (3.5) effectively into a linear homogeneous integral equation. The Coulomb potential in momentum space is given by its Fourier transform

$$V_{\mathrm{eff}}(\mathbf{k}) = -\frac{\mathrm{e}^2}{\Omega\,\varepsilon_0\varepsilon_\mathrm{r}\,\mathbf{k}^2}\,. \tag{3.8}$$

For the static permittivity we choose the value for small energies $\varepsilon_\mathrm{r} = \varepsilon_1$ (see section 2.4.1). The inclusion of the crystal volume Ω originates from the Fourier transform again. The same approach applies for the eigenfunctions $\varphi_\nu(\mathbf{k}) = \mathcal{F}\{\phi_\nu(\mathbf{r})\}$. Similar to the ansatz in position space, the hydrogen-like wave functions in momentum space are separated into radial and angular parts

$$\varphi_{n,\ell,m}(\mathbf{k}) = F_{n,\ell}(k)\; Y_{\ell,m}(\mathbf{n_k})\,. \tag{3.9}$$

The angular part is described by a spherical harmonic $Y_{\ell,m}(\mathbf{n_k})$ with $\mathbf{n_k}$ being the normal vector of $\mathbf{k}$. The radial part is yet to be determined. In the next step we try to reduce the dimensionality of the integral in Eq. (3.6). Inserting Eq. (3.9) enables us to separate the integral as

$$\left(k^2 + D(k^2) + q_{n,\ell,m}^2\right) F_{n,\ell}(k)\, Y_{\ell,m}(\mathbf{n_k}) = \frac{q_\mathrm{B}}{\pi^2} \int_0^\infty \mathrm{d}k'\; k'^2 F_{n,\ell}(k') \iint \mathrm{d}\Omega_{\mathbf{k}'}\; \frac{Y_{\ell,m}(\mathbf{n_{k'}})}{|\mathbf{k}-\mathbf{k}'|^2}\,, \tag{3.10}$$

with $q_{n,\ell,m} = \sqrt{-2\mu\, E_{n,\ell,m}/\hbar^2}$ ($E_{n,\ell,m} < 0$) being the renormalised binding energy, and introducing the constant $q_B = \mu\mathrm{e}^2/(4\pi\,\hbar^2\,\varepsilon_0\varepsilon_1)$. The angular integration can be rewritten as

$$\iint \mathrm{d}\Omega_{\mathbf{k}'}\; \frac{Y_{\ell,m}(\mathbf{n_{k'}})}{|\mathbf{k}-\mathbf{k}'|^2} = \frac{1}{2\,kk'} \iint \mathrm{d}\Omega_{\mathbf{k}'}\; \frac{Y_{\ell,m}(\mathbf{n_{k'}})}{\frac{k^2+k'^2}{2kk'} - \mathbf{n_k}\cdot\mathbf{n_{k'}}}\,. \tag{3.11}$$

In this representation we can apply the Funk-Hecke formula for the case of spherical harmonics [104]

$$\iint \mathrm{d}\Omega_{\mathbf{k}'}\; K(\mathbf{n}_{\mathbf{k}} \cdot \mathbf{n}_{\mathbf{k}'})\, Y_{\ell,m}(\mathbf{n}_{\mathbf{k}'}) = 2\pi\; Y_{\ell,m}(\mathbf{n}_{\mathbf{k}}) \int_{-1}^{1} \mathrm{d}\tau\; K(\tau)\, P_{\ell}(\tau) \qquad \Big(\forall\, K \in L^1(-1,1)\Big)\,, \tag{3.12}$$

and subsequently exploit the relation between Legendre polynomials $P_\ell(\tau)$ and Legendre functions of second kind $Q_\ell(z)$ [105]

$$Q_\ell(z) = \frac{1}{2} \int_{-1}^{1} \mathrm{d}\tau\, \frac{P_\ell(\tau)}{z-\tau} \qquad \big(\,\forall\, z \in \mathbb{C}\backslash(-\infty, 1]\,\big)\,. \tag{3.13}$$

This results in an analytical expression of the angular integral. It should be stated that in the case of $k = k'$ the integrand of the angular integration is diverging. Therefore, strictly speaking, this derivation does not hold in this case since $z = (k^2 + k'^2)/(2kk') = 1$ and as a consequence $K(\tau) \notin L^1(-1,1)$. However, for all $k \neq k'$ it results in $z > 1$, thus fulfilling $f(t) \in L^1(-1,1)$. The angular integration is now expressed as

$$\frac{1}{2\,kk'} \iint \mathrm{d}\Omega_{\mathbf{k}'}\; \frac{Y_{\ell,m}(\mathbf{n}_{\mathbf{k}'})}{\frac{k^2+k'^2}{2kk'} - \mathbf{n}_{\mathbf{k}} \cdot \mathbf{n}_{\mathbf{k}'}} = \frac{2\pi}{kk'}\, Y_{\ell,m}(\mathbf{n}_{\mathbf{k}})\, Q_\ell\left(\frac{k^2+k'^2}{2\,kk'}\right)\,, \tag{3.14}$$

leaving a single integration over the radial part of the wave function

$$\Big(k^2 + D(k^2) + q_{n,\ell}^2\Big)\, F_{n,\ell}(k) = \frac{2\,q_B}{\pi\,k} \int_0^{\infty} \mathrm{d}k'\; k'\, Q_\ell\left(\frac{k^2+k'^2}{2\,kk'}\right) F_{n,\ell}(k')\,. \tag{3.15}$$

For the isotropic Wannier equation the renormalised binding energy $q_{n,\ell}$ drops the dependence of the magnetic quantum number m due to the averaging of the spherical harmonic that is conducted by Eq. (3.12). For Eq. (3.15) to be solvable, the kernel of the integral equation needs to vanish for $k' \to \infty$. Under the premise that for a numerical evaluation the indefinite upper limit needs to be replaced by a discrete, sufficiently large upper boundary, we are able to formally treat the result as a homogeneous Fredholm equation of the second type by introducing an eigenvalue parameter $\lambda_{n,\ell}(q)$

$$\Big(k^2 + D(k^2) + q^2\Big)\, F_{n,\ell}(k) = \lambda_{n,\ell}(q)\, \frac{2\,q_B}{\pi\,k} \int_0^{\infty} \mathrm{d}k'\; k'\, Q_\ell\left(\frac{k^2+k'^2}{2\,kk'}\right) F_{n,\ell}(k')\,. \tag{3.16}$$

The eigenvalue $\lambda_{n,\ell}$ is a function of the renormalised energy parameter q. In the case of $\lambda_{n,\ell}(q_{n,\ell,\alpha}) = 1$ the corresponding renormalised energy $q_{n,\ell,\alpha}$ satisfies the energy eigenvalue problem of Eq. (3.15) again. The additional index α denotes the potential for a branch of $\lambda_{n,\ell}$

to fulfill the requirement for multiple renormalised energies q.
By solving the eigenvalue problem of $\lambda_{n,\ell}$ for a sufficiently wide energy range, we automatically receive the binding energies of Eq. (3.15). To evaluate the Fredholm equation further, we rely on its specific properties. First, by substituting

$$f_{n,\ell}(q,k) = \sqrt{k^2 + D(k^2) + q^2}\; k\; F_{n,\ell}(k)\,, \tag{3.17}$$

and expanding the Legendre function of second kind as [105]

$$\begin{aligned} Q_\ell\left(\frac{k^2+k'^2}{2\,kk'}\right) = 2^{2\ell+1}\,(\,\ell!\,)^2 \left(\frac{2\,qk}{q^2+k^2}\right)^{\ell+1} \left(\frac{2\,qk'}{q^2+k'^2}\right)^{\ell+1} \\ \times \sum_{\eta=0}^{\infty} \frac{\eta!}{(\eta+2\ell+1)!}\, C_\eta^{(\ell+1)}\left(\frac{q^2-k^2}{q^2+k^2}\right)\, C_\eta^{(\ell+1)}\left(\frac{q^2-k'^2}{q^2+k'^2}\right)\,, \end{aligned} \tag{3.18}$$

with $C_\eta^{(\ell+1)}(\tau)$ being the Gegenbauer polynomials, we can symmetrise the kernel. Employing Eq. (3.17) on Eq. (3.16), the integral equation transforms to

$$f_{n,\ell}(q,k) = \lambda_{n,\ell}(q) \int_0^\infty \mathrm{d}k'\; M_\ell(q,k,k')\, f_{n,\ell}(q,k')\,. \tag{3.19}$$

For the new kernel M_ℓ we utilise Eq. (3.18) to receive

$$M_\ell(q,k,k') = \frac{2q_B}{\pi} \frac{Q_\ell\left(\frac{k^2+k'^2}{2\,kk'}\right)}{\sqrt{k^2+D(k^2)+q^2}\sqrt{k'^2+D(k'^2)+q^2}} = \sum_{\eta=0}^{\infty} h_{\eta,\ell}(q,k) h_{\eta,\ell}(q,k')\,, \tag{3.20}$$

$$h_{\eta,\ell}(q,k) = \sqrt{\frac{q_B\;\eta!}{\pi(\eta+2\ell+1)!}} \frac{\ell!}{\sqrt{k^2+D(k^2)+q^2}} \left(\frac{2\,qk}{q^2+k^2}\right)^{\ell+1} C_\eta^{(\ell+1)}\left(\frac{q^2-k^2}{q^2+k^2}\right)\,. \tag{3.21}$$

Thus, Eq. (3.19) can also be written as

$$f_{n,\ell}(q,k) = \lambda_{n,\ell}(q) \sum_{\eta=0}^{\infty} h_{\eta,\ell}(q,k) \int_0^\infty \mathrm{d}k'\; h_{\eta,\ell}(q,k')\, f_{n,\ell}(q,k')\,. \tag{3.22}$$

In the next step, the eigenfunctions are expanded into the symmetric kernel functions as $f_{n,\ell}(q,k) = \sum_{\eta=0}^{\infty} c_{n,\ell,\eta}\, h_{\eta,\ell}(q,k)$, which results in

$$\sum_{\eta'=0}^{\infty} c_{n,\ell,\eta'}\, h_{\eta',\ell}(q,k) = \lambda_{n,\ell}(q) \sum_{\eta=0}^{\infty}\sum_{\eta'=0}^{\infty} c_{n,\ell,\eta'}\, h_{\eta,\ell}(q,k) \int_0^\infty \mathrm{d}k'\; h_{\eta,\ell}(q,k')\, h_{\eta',\ell}(q,k')\,. \tag{3.23}$$

In the case of $D(k^2)=0$ the symmetric kernel functions (3.21) are orthogonal and normalised as $\int_0^\infty \mathrm{d}k\; h_{\eta,\ell}(q,k) h_{\eta,\ell'}(q,k) = q_B\,\delta_{\eta,\eta'}/(q(\eta+\ell+1))$, hence reducing Eq. (3.23) to an analytical expression for the eigenvalue $\lambda_{\eta,\ell} = (\eta+\ell+1)q/q_B$. For the criterion of the energy eigenvalues

$\lambda_{\eta,\ell} = 1$ and the relation $n = \eta + \ell + 1$ [102] we return to the standard Rydberg series solution of the Wannier equation as expected, since setting $D(k^2)$ to zero removes the nonparabolicity, thus yielding the solution for parabolic band dispersions. In the case of a finite deviation $D(k^2)$, the symmetric kernel functions $h_{\eta,\ell}(q,k)$ lose their orthogonality and need to be solved numerically. It is recognisable that Eq. (3.23) is equivalent to an algebraic eigenvalue problem of the form

$$\mathbf{A}_\ell(q) \cdot \mathbf{c}_{n,\ell}(q) = \lambda_{n,\ell}^{-1}(q)\, \mathbf{c}_{n,\ell}(q)\,. \tag{3.24}$$

The eigenvectors $\mathbf{c}_{n,\ell}$ correspond to the expansion coefficients $c_{n,\ell,\eta}$ and the symmetric matrix $\mathbf{A}_\ell$ consists of

$$(A_\ell(q))_{\eta,\eta'} = \int_0^\infty \mathrm{d}k\; h_{\eta,\ell}(q,k)\, h_{\eta',\ell}(q,k)\,. \tag{3.25}$$

The resulting eigenvalue problem needs to be diagonalised numerically. First, the size of the infinite dimensional matrix of Eq. (3.25) is truncated. As already stated, the indices η of the matrix are linked to principal and angular quantum number via $n = \eta + \ell + 1$. Thence, for a set ℓ, we choose the matrix dimension as a principal quantum number $n_{\max}$, which is successively increased until the resulting eigenvalues are sufficiently converged. As we are interested in states up to $n = 25$ we found that $n_{\max} = 100$ is sufficient to ensure convergence in the range of our interest. We predict an energy interval E_q which is supposed to contain our wanted energy eigenvalues and divide it into a suitable grid G_q. For each $q_i \in G_q$, Eq. (3.24) is now solved to obtain $\lambda_{n,\ell}^{-1}$. The integrals of Eq. (3.25) are solved numerically. The discrete values on the grid G_q can be interpolated, resulting in a set of monotonous, energy dependent functions $\lambda_{n,\ell}^{-1}(q)$ over the interval E_q. The roots of $\lambda_{n,\ell}^{-1}(q) - 1$ then yield our wanted energy eigenvalues.

3.2.2. Nonparabolicity $D(k^2)$

The mathematical approach that was just depicted is generally valid for any isotropic deviation of the band structure from the parabolic approximation. In the case of Cu_2O, we use the band dispersions that result from the SH Hamiltonian [75]. It is possible to diagonalise the SH Hamiltonian in two symmetry directions, namely the Δ and Λ directions. Their respective dispersions are given in Eqs. (2.22). To receive an isotropic band dispersion we take the geometrical average of those two directions, depending on the multiplicity of their axes. Since Rydberg excitons were only observed for the yellow P series thus far, we limit our analysis to the yellow excitons, i.e. the Γ_7^+ valence band

$$E_7^{\mathrm{av}}(k) = \frac{1}{7}\left(3E_7^{\Delta}(k) + 4E_7^{\Lambda}(k)\right)\,. \tag{3.26}$$

This approach works fairly well, partly since the effective masses for $E_7^i(k=0)$ are identical, as it was shown in Eq. (2.24). The sum of kinetic energies for electron and hole then reads

$$E_6(k) + E_7^{\mathrm{av}}(k) = \left(\frac{\hbar^2}{2m_{6\mathrm{c}}} - \frac{3P_1^{\Delta} + 4P_1^{\Lambda}}{84} \right) k^2 - \frac{S^{\Delta}(k)}{28} - \frac{S^{\Lambda}(k)}{21} + \frac{\Delta_{\mathrm{p}}}{2} \tag{3.27}$$

$$= \frac{\hbar^2}{2\mu} \left(k^2 + D(k^2) \right) \tag{3.28}$$

with $S^i(k) = \sqrt{P_2^i k^4 + P_3^i \Delta_{\mathrm{p}} k^2 + 36\Delta_{\mathrm{p}}^2}$. We have a certain degree of freedom when choosing $D(k^2)$ and thus μ, respectively. The most sensible choice is

$$\frac{\partial^2}{\partial k^2} D(k^2)\big|_{k=0} = 0\,. \tag{3.29}$$

The nonparabolicity results in

$$\frac{\hbar^2}{2\mu} D(k^2) = \frac{1}{42}(3A_2 + 4A_3)k^2 - \frac{S^{\Delta}(k)}{28} - \frac{S^{\Lambda}(k)}{21} + \frac{\Delta_{\mathrm{p}}}{2}\,. \tag{3.30}$$

Incidentally, the reduced mass at zone centre is then given as

$$\mu = \left(\frac{1}{m_{6\mathrm{c}}} - A_1 \right)^{-1} = 0.352\, m_0\,, \tag{3.31}$$

with a corresponding excitonic Rydberg energy of $\mathrm{Ry}^* = 86.04\,\mathrm{meV}$.
To check whether the dispersions we used are assessing the band structure well enough, we exploit the equivalence between exciton and hydrogen atom again. The uncertainty of the radial momentum k_{r} is known to be [106]

$$(\Delta k_{\mathrm{r}})_{n,\ell} = \frac{1}{n\, a_{\mathrm{y}}} \sqrt{1 - \frac{\ell\,(\ell+1)}{n\left(\ell + \frac{1}{2}\right)}}\,, \tag{3.32}$$

with a_{y} being the excitonic Bohr radius of the yellow exciton series, calculated from the Rydberg energy as $a_{\mathrm{y}} = 1.1\,\mathrm{nm}$. This implies that our dispersions need to fit the band structure well enough up to $(\Delta k)_{n,\ell}$ to reliably describe the corresponding exciton. For $n \geq 2$ states this means $(\Delta k)_{2\mathrm{S}} \simeq 0.07\,\pi/a_{\mathrm{L}}$ in terms of Cu_2O's lattice constant $a_{\mathrm{L}} = 0.43\,\mathrm{nm}$ [107]. This condition is easily satisfied by the parabolic fit for the Γ_6^+ conduction band (cf. Fig. 2.3) and the SH dispersions for the Γ_7^+ valence band (cf. Fig. 2.4). In case of the 1S exciton state[1] we receive $(\Delta k)_{1\mathrm{S}} \simeq 0.27\,\pi/a_{\mathrm{L}}$, which is still reasonably well met by these approximations.

[1] The uncertainty for the 1S state is calculated with an exciton radius of $a_{1\mathrm{Sy}} = 0.51\,\mathrm{nm}$, which is the result of the upcoming chapter (see section 4.3.2).

3.3. Exitonic quantum defect

By now, we are able to solve the modified Wannier equation for the isotropic averaged band dispersion of the Γ_7^+ valence band and thus, determine its influence on the deviation from the ideal Rydberg series. As a first step, we calculate the energy dependent functions $\lambda_{n,\ell}^{-1}(q)$ for the respective angular quantum numbers ℓ. The binding energies of the exciton states correspond to the eigenvalues of the integral equation for which the condition $\lambda_{n,\ell}^{-1}(q) = 1$ is met; therefore, we extract the values at this point to receive the energy eigenvalues $E_{n,\ell}$ of the modified Wannier equation. The course of the functions $\lambda_{n,\ell}^{-1}(q)$ is shown exemplary for the yellow P ($\ell = 1$) excitons in Fig. 3.1. The resulting binding energies for the S, P, D and F exciton series, up to $n = 25$, are given in appendix A.4.2.
The results of the numerical calculations can be presented in form of the quantum defect

$$\delta_{n,\ell} = n - \sqrt{-\frac{\mathrm{Ry}^*}{E_{n,\ell}}}\,. \tag{3.33}$$

The quantum defect is very sensitive towards shifts in binding energies. This is especially the case for higher principal quantum numbers n. A deviation $\Delta E_{n,\ell}$ between the real binding energy and the numerical result affects the quantum defect by

$$|\Delta\delta_{n,\ell}| = \left|\frac{1}{2}\frac{(n-\delta_{n,\ell})^3}{\mathrm{Ry}^*}\Delta E_{n,\ell}\right|\,. \tag{3.34}$$

We recognise that the error increases with $\sim n^3$ for large n; hence, in order to keep the quantum defect at $|\Delta\delta_{25,\ell}| \leq 0.01$ accuracy, the energy discrepancy shall not be beyond $|\Delta E_{25,\ell}| < 1\ \mu\mathrm{eV}$. We utilise this property to estimate the band gap energy up to a high degree of precision.
Since the experimental binding energies are always in relation to the band gap, a precise value for the band gap is necessary for a qualitative comparison between experiment and theory. As a consequence, we require the band gap energy up to an accuracy on the order of $1\,\mu\mathrm{eV}$. However, the direct determination of the band gap energy from experimental data, e.g. by absorption [11, 108] or luminescence spectroscopy [81, 87, 109–111], is not precise enough. Additional effects such as an electron-hole plasma or defect induced band gap shift [31] further complicate an appropriate determination of the "unperturbed" band gap. In [11], the gap energy of Cu_2O is given as $E_\mathrm{y} = 2.17208\,\mathrm{eV}$ which implies an uncertainty on the order of $10\,\mu\mathrm{eV}$. By fitting the experimental peak values of the P excitons to the numerically calculated binding energies, we receive a yellow band gap energy of $E_\mathrm{y} = 2.1720737\,\mathrm{eV}$. This agrees to the last significant digit with the experiment and will be used throughout the rest of this work. The experimental values[2] used can be found in appendix A.4.1.

[2]It should be noted, that the listed values correspond to the orthoexcitons; thus, to compensate the shift of the exchange energy we apply Eq. (3.3) to the S excitons to receive the paraexciton energies.

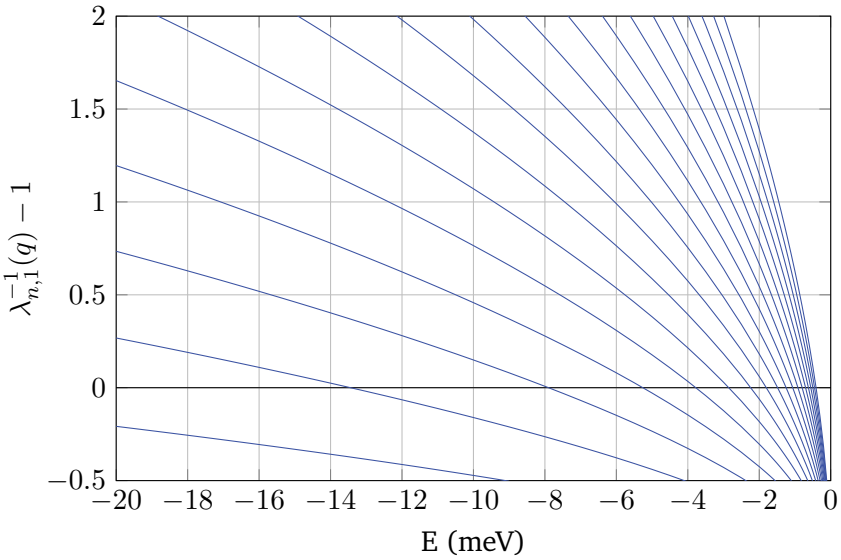

Figure 3.1.: The energy dependent functions $\lambda_{n,1}^{-1}(q) - 1$ for the yellow P excitons up to $n = 20$ are depicted. The roots of the functions give the binding energies of the exciton states.

The quantum defects for the numerical results as well as for the band gap reduced experimental data are aquired via Eq. (3.33), and are shown in Fig. 3.2. For the F excitons it should be noted that the experiments observe a splitting into a triplet, according to its different magnetic quantum numbers m [24]. This splitting cannot be explained since the magnetic quantum numbers are averaged out in this approach of isotropic band dispersions. The quantum defects for these lines correspond more to the general shift of the triplet rather than to one specific m.

Previously in this chapter the quantum defect was introduced as a concept, originally stemming from atomic physics, to describe deviations of highly excited states from the ideal Rydberg series. However, this is obviously only one way to illustrate the energetic deviation. An alternative representation for the deviation from the ideal Rydberg series is the relative binding energy deviation

$$\alpha_{n,\ell} = \left| \frac{E_{n,\ell} - E_n^*}{E_{n+1}^* - E_n^*} \right| , \tag{3.35}$$

with $E_{n,\ell}$ being the binding energy obtained from calculation (or experiment respectively), and E_n^* denoting the binding energy of the ideal Rydberg series. The relative binding energy deviation has the advantage that it shows directly the difference in relation to the corresponding ideal Rydberg energies. For large n, its behaviour coincides with the quantum defect. Another

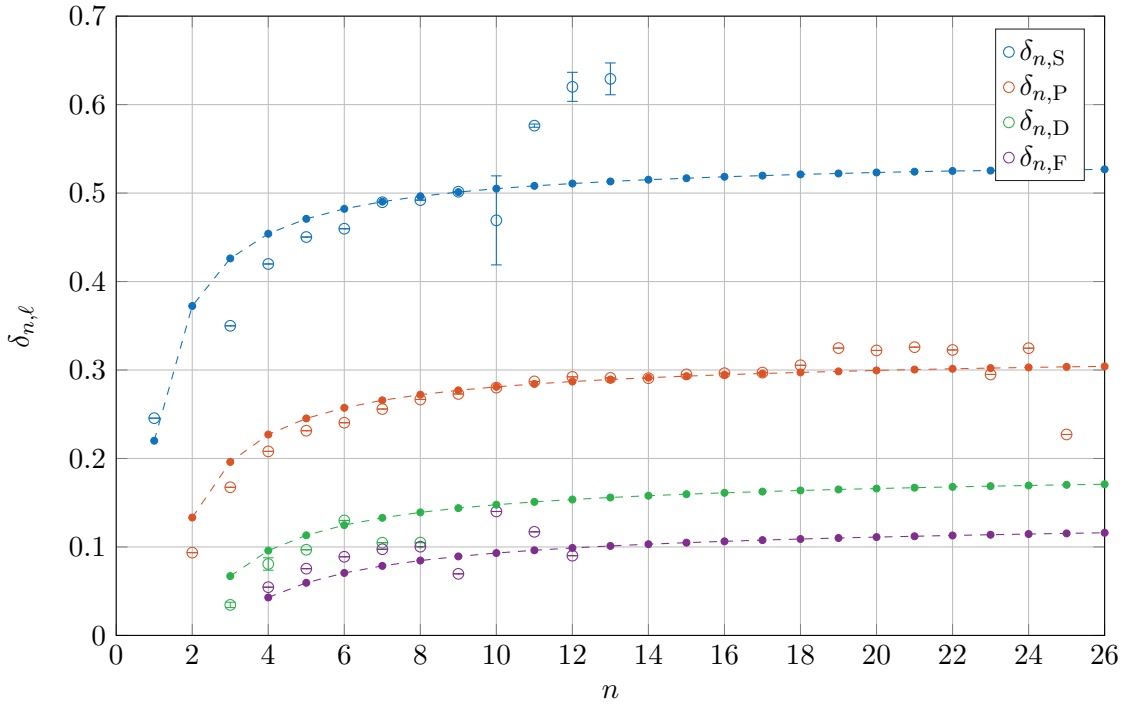

Figure 3.2.: Comparison between the quantum defects of the experimental (hollow circles) and numerical results (filled circles). The lines serve as a guide to the eye for an easier distinction between numerical and experimental values.

representation is the relative enhancement

$$\beta_{n,\ell} = \left| \frac{E^{\mathrm{th}}_{n,\ell} - E^{\mathrm{exp}}_{n,\ell}}{E^{*}_{n} - E^{\mathrm{exp}}_{n,\ell}} \right| , \tag{3.36}$$

which can be understood as the improvement of the numerical results by including the non-parabolicity $E^{\mathrm{th}}_{n,\ell}$, with respect to the experimental values $E^{\mathrm{exp}}_{n,\ell}$, in comparison to the parabolic band solution, i.e. the ideal Rydberg series E^{*}_{n}. The improvements are generally on the orders of 10 to 100 for almost all n and ℓ. Both alternative representations are shown in Fig. 3.3.

3.4. Discussion

The quantum defect of the P excitons matches exceptionally well, especially for larger principal quantum numbers n; however, that is to be expected as we utilised these lines to redefine our yellow gap energy and already noticed a good agreement with the experimental value. The model provides a relatively good fit to the D and F excitons overall, and for the S excitons at least in the range between $n = 7$ and $n = 10$.

All four series show a systematic overestimation of the binding energies for small n, except for

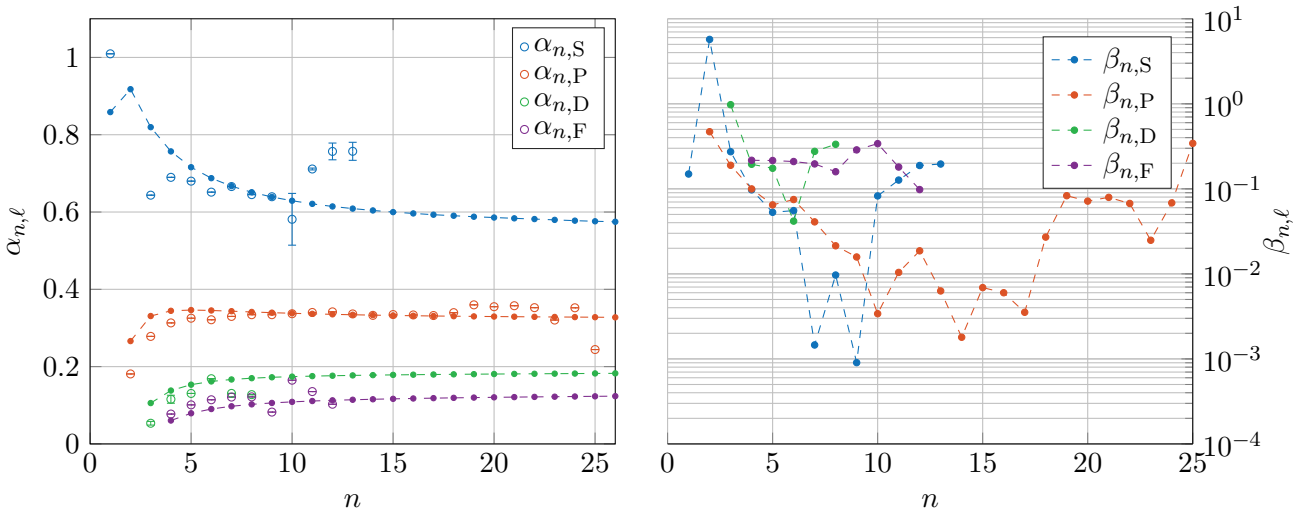

Figure 3.3.: Left: comparison of the relative binding energy deviation $\alpha_{n,\ell}$ for experimental (hollow) and numerical (filled) values. Right: the relative enhancement $\beta_{n,\ell}$ to the ideal Rydberg series by assessing the nonparabolicty. The lines are ment as a guide to the eye in both figures.

the F lines. At first glance, one would suggest that the assumption of a fixed valued dielectric constant is not valid for these excitons. In this regime the coupling to the two LO phonons needs to be considered. They lead to a modification of the background screening and thus, to an alteration of the Coulomb interaction and binding energies. Generally it is to be expected, as the permittivity decreases for higher energies (see chapter 2.4.1), that a treatment including the frequency dependent dielectric constant would lead to further increased binding energies. However, in the current evaluation there is already an overestimation of the numerically determined binding energies; hence, this would lead to an even stronger deviation from the experiment. There are several influences that could potentially explain this discrepancy. First and foremost, we need to keep in mind that we obtained the nonparabolicity from a fit to an *ab initio* sDFT calculation, and while we set the mass at zone centre to match with the experimentally known hole mass, we cannot verify the validity of the dispersion slope further into the Brillouin zone, the region that becomes significantly more important for smaller n. In the same vein, there is the possibility, that our weighted average for the isotropic valence band dispersion is resulting in a markedly inaccurate slope for finite momenta. Another point, that has not been discussed extensively so far is the mixing between the different exciton series. The unitary transformation that is required to diagonalise the SH Hamiltonian technically needs to transform the Coulomb interaction as well, leading to a coupling between the split off Γ_7^+ and the degenerate Γ_8^+ bands. This mixing becomes less important for excitons with large n, i.e. excitons with a small extension within momentum space, and, thus, is a good approximation for Rydberg excitons. For small n excitons this coupling should be taken into consideration.

Inspecting the Rydberg states of the P excitons, we recognise another slight deviation between numerical and experimental results for $n \geq 19$. This shift is probably due to the steady buildup of a Rydberg blockade by the highly excited excitons. This would match the finding of [11], as the effect of the Rydberg blockade leads to a shift of the resonances.

3.5. Conclusion

The energy eigenvalues of the modified Wannier equation fit remarkably well to the experimentally obtained exciton resonances [11, 24, 91]. This strongly supports the idea that the nonparabolicity of the valence band is responsible for the majority of the deviation and that, at least for the Γ_7^+, the anisotropy for the different directions is minor enough to justify the use of an isotropic average for the band dispersion. Especially the evaluation of the highly excited P exciton states was successful, which supports the approximation of neglecting the other central-cell corrections (see section 3.1.1). At principal quantum numbers beyond $n = 19$, the emergence of the Rydberg blockade leads to an additional energy shift, which is not considered in this approach. For small principal quantum numbers n, we see an overestimation of the numerical results in comparison to the experimental values. A few possible reasons for that observation were discussed above.
The treatment of the yellow exciton series leaves the question for an investigation of the green series. For the green exciton series, we would need to consider strong mixing effects between the degenerate Γ_8^+ bands. With the method of this chapter, however, we would be obliged to apply the pure band dispersions which would yield two distinctly separate exciton series. The existence of those two separate series (apart from the exchange interaction split subseries) is not confirmed experimentally and rejected by theory [19–22]. One particularity that is certain is that the green exciton series should exhibit negative quantum defects, since the bending direction of the nonparabolicity in regards to the parabola of the effective mass approximation predefines the sign of the correction, and, thus, the sign of the quantum defect. A negative quantum defect is a property that is not known from atomic systems and would present a unique feature of excitons in semiconductors. Calculations that predict the green exciton quantum defects, as well as an attempt to treat the anisotropy of the bands can be found in [103].
There are still some unanswered questions and possibilities for improvement; however, the approach outlined in this chapter generally represents a significant enhancement upon the generic Rydberg series of the normal Wannier equation.

Chapter 4.

Excitonic dispersion of the yellow 1S paraexciton

In the previous chapter, we introduced an approach to determine energy resonances of highly excited Rydberg excitons. The improvement in comparison to the generic approach that results in the Wannier equation, was the inclusion of the nonparabolicity of the band structure, which consequently redound to an improved Wannier equation that had to be solved. This ansatz still relies on a multitude of approximations such as a small exciton momentum, nearly isotropic band dispersions, a constant permittivity, and negligible coupling between the split off Γ_7^+ and the twofold degenerate Γ_8^+ valence bands. Nevertheless, it yields satisfiying results for large principal quantum numbers n, especially for the P excitons. However, for small n we recognised a marked deviation from the experimentally known resonances. In this chapter, we will approach some of the abovementioned approximations to improve upon the result of last chapter and to obtain the excitonic energy dispersion, in this case on the example of the yellow 1S paraexciton resonance.

The yellow 1S exciton depicts a very special case as its properties suggested Cu_2O for a long time to be the predestined semiconductor for the detection of an excitonic Bose-Einstein condensate (BEC) [36,112–114]. In particular the 1S paraexcitons are of interest as they represent the lowest excited state of the crystal and possess a very long lifetime [96]. Both traits can be retraced to their Γ_2^+ symmetry, which spares them from exchange interaction and inhibits all optical transitions and most of phonon interactions[1]. However, the yellow 1S excitons are also unique within the yellow series as their excitonic mass and Rydberg energy varies significantly from the values that are known for the rest of the series, which were, i.a. obtained in chapter 3. Therefore, a better description of the 1S exciton state will only improve the understanding of the residuary excitons of the series.

Two things are tackled in this chapter, the inclusion of the exciton momentum and the conundrum of a constant permittivity. As a first step, the Schrödinger equation will be solved with the

[1] In experimental setups the excitons are usually confined in a potential trap induced by pressure, whereby the symmetrical restrictions are “softened” by the strain [81].

nonparabolicity and a finite exciton momentum via a variational method for a static screened potential. Afterwards, we introduce a new potential that includes the polaron character of electron and hole and, thus, deals with the changes of the permittivity that are induced by the LO phonons (see section 2.4.1).

4.1. Schrödinger equation

As a starting point, we begin with the general Schrödinger equation of the two-particle system, similar to the one we introduced in Eq. (2.27), although written in a slightly different, more universal manner as

$$\left(W(\mathbf{p}_\mathrm{e}.\mathbf{p}_\mathrm{h}) + V_\mathrm{eff}(r) + \Sigma_\mathrm{ex}\right)|\Psi_{\nu,\mathbf{K}}\rangle = E_{\nu,\mathbf{K}}\,|\Psi_{\nu,\mathbf{K}}\rangle\,. \tag{4.1}$$

Here, $W(\mathbf{p}_\mathrm{e}.\mathbf{p}_\mathrm{h})$ inherits all kinetic terms, $V_\mathrm{eff}(r)$ is the interaction between electron and hole and Σ_ex describes their self-energy contributions. The parameter ν describes the state of the wave function and $\mathbf{K}$ is the exciton momentum. Similar to the rest of this work, we will use hydrogen-like wave functions as a close approximate for the actual eigenfunctions of the system. The corresponding energy eigenvalues will be determined by a variational ansatz. In this case, the energetical minimum is found by varying the excitonic Bohr radius a_y.
As we associate the kinetic energies of electron and hole with their respective band dispersions, the kinetic energy term can be split into separate parts $W(\mathbf{p}_\mathrm{e}.\mathbf{p}_\mathrm{h}) = W_\mathrm{6c}(\mathbf{p}_\mathrm{e}) + W_\mathrm{7v}(\mathbf{p}_\mathrm{h})$. The excitonic wave function for the yellow series is given by

$$|\Psi_{\nu,\mathbf{K}}\rangle = \sum_\mathbf{q} \varphi_{\nu,\mathbf{q}}\,|\psi_{\mathrm{6c},\frac{\mathbf{K}}{2}+\mathbf{q}}\rangle \otimes |\psi_{\mathrm{7v},\frac{\mathbf{K}}{2}-\mathbf{q}}\rangle\,, \tag{4.2}$$

with $\varphi_{\nu,\mathbf{q}}$ being a hydrogen-like envelope wave function, and $\psi_{i,\mathbf{q}}$ are the Bloch functions for the respective band i. Analogue to the previous chapter, we attempt to solve the Schrödinger equation in momentum space. For either part of the kinetic energy the expectation value is then given by

$$\begin{aligned}
\langle\Psi_{\nu,\mathbf{K}}|W_i|\Psi_{\nu,\mathbf{K}}\rangle &= \sum_{\mathbf{q},\mathbf{q}'} \varphi^*_{\nu,\mathbf{q}'}\varphi_{\nu,\mathbf{q}}\,\langle\psi_{i,\frac{\mathbf{K}}{2}\pm\mathbf{q}'}|W_i|\psi_{i,\frac{\mathbf{K}}{2}\pm\mathbf{q}}\rangle\,\langle\psi_{j,\frac{\mathbf{K}}{2}\mp\mathbf{q}'}|\psi_{j,\frac{\mathbf{K}}{2}\mp\mathbf{q}}\rangle \\
&= \sum_\mathbf{q} |\varphi_{\nu,\mathbf{q}}|^2\, W_i\left(\mathbf{K}/2 \pm \mathbf{q}\right) && \text{(4.3a)} \\
&= \sum_\mathbf{q} \left|\varphi_{\nu,\mathbf{q}\mp\frac{\mathbf{K}}{2}}\right|^2\, W_i(\mathbf{q})\,. && \text{(4.3b)}
\end{aligned}$$

As the kinetic Hamiltonian W_i only applies on either of the bands states, the other one utilises the orthonormality of the Bloch functions and yields a Kronecker delta that subsequently eliminates the second sum. Since the remaining sum runs to infinity, we can shift the exciton

momentum in the argument of the summands. This makes no difference for the resulting kinetic energies of the bands; however, this nomenclature will be useful in the evaluation of the valence band dispersion. Next, we assume that the electronic momentum states are packed up tightly enough to be considered quasi-continuous [cf. Eq. (3.7)]. Since the conduction band is described by an isotropic parabolic dispersion, its energetic contribution can be calculated analytically. For all nS excitons it reads

$$\begin{aligned}\langle \Psi_{n\mathrm{S},\mathbf{K}} | W_{6\mathrm{c}} | \Psi_{n\mathrm{S},\mathbf{K}} \rangle &= \frac{\Omega}{(2\pi)^3} \int \mathrm{d}^3\mathbf{q}\, |\varphi_{n\mathrm{S},\mathbf{q}}|^2 \left(\frac{\hbar^2 (\mathbf{K}/2 + \mathbf{q})^2}{2m_{6\mathrm{c}}} + E_{\mathrm{y}} \right) , \\ &= \frac{\hbar^2}{2m_{6\mathrm{c}}} \left(\frac{1}{(n\, a_{\mathrm{y}})^2} + \frac{K^2}{4} \right) + E_{\mathrm{y}} \,. \end{aligned} \tag{4.4}$$

As to be expected for an isotropic band dispersion, the angular dependence of the exciton momentum has vanished. For the calculation, we used the hydrogen wave function in momentum space. They are well established and in general take the form [115]

$$\begin{aligned}\varphi^{(i)}_{n\ell m,\mathbf{k}} = {} & 2^{2\ell+4} \pi\, \ell!\, (n\, a_i)^{3/2} \sqrt{\frac{n(n-\ell-1)!}{\Omega\, (n+\ell)!}} \frac{(n\, a_i k)^\ell}{((n\, a_i k)^2 + 1)^{\ell+2}} \\ & \times\, C^{(\ell+1)}_{n-\ell-1} \left(\frac{(n\, a_i k)^2 - 1}{(n\, a_i k)^2 + 1} \right)\, Y_{\ell,m}(\vartheta_{\mathbf{k}}, \phi_{\mathbf{k}}) \,, \end{aligned} \tag{4.5}$$

consisting of the Gegenbauer polynomials $C^{(\alpha)}_n(z)$ and spherical harmonics $Y_{\ell,m}(\vartheta, \phi)$. The a_i is the excitonic Bohr radius to the corresponding series. It should be noted that this is the semiconductor specific wave function; therefore, it varies from the literature [115] with respect to its normalisation about a factor $\frac{\Omega}{(2\pi)^3}$ that is owed to the spatial normalisation of the bulk semiconductor, as seen in Eq. (3.7).
With this done, we will now proceed to the calculation of the valence band contribution.

4.1.1. Energy eigenvalue of the Γ_7^+ valence band

The SH Hamiltonian and its results are of recurring interest throughout this whole thesis. Similar to the preceding chapter, we will make use of its resulting energy dispersions to describe the Γ_7^+ valence band; however, in contrast to the previous approach, the diagonalisation of the Hamiltonian in Eq. (2.21) will be done numerically this time. This allows us to determine the excitonic energy dispersion for any arbitrary angle.
For the treatment of the valence band dispersion we will employ Eq. (4.3b) as a starting point. While a numerical calculation of the threefold integral at hand could be executed immediately, we first want to simplify Eq. (4.3b) to some extent. The square of the envelope wave function is expanded into a series of Legendre polynomials, which then in turn is expanded into

spherical harmonics

$$\Omega \left|\varphi_{\nu,\mathbf{q}-\frac{\mathbf{K}}{2}}\right|^2 = \sum_{\ell=0}^{\infty} a_{\nu,\ell}(q,K)\; P_\ell\left(\cos\sphericalangle(q,K)\right)\,, \tag{4.6a}$$

$$= \sum_{\ell=0}^{\infty} \frac{4\pi\, a_{\nu,\ell}(q,K)}{2\ell+1} \sum_{m=-\ell}^{\ell} Y_{\ell,m}(\Omega_{\mathbf{K}})\; Y^*_{\ell,m}(\Omega_{\mathbf{q}})\,. \tag{4.6b}$$

Similarly, the band dispersion is expanded into spherical harmonics as

$$W_{7\mathrm{v}}(\mathbf{q}) = \sum_{\ell=0}^{\infty} \sum_{m=-\ell}^{\ell} b_{\ell,m}(q)\; Y_{\ell,m}(\Omega_{\mathbf{q}})\,. \tag{4.7}$$

The two expansion coefficients are given by

$$a_{\nu,\ell}(q,K) = \frac{\Omega(2\ell+1)}{2} \int_{-1}^{1} \mathrm{d}z_{qK}\; P_\ell(z_{qK})\; \left|\varphi_{\mathbf{q}-\frac{\mathbf{K}}{2}}\right|^2\,, \tag{4.8}$$

$$b_{\ell,m}(q) = \int_{\Omega_{\mathbf{q}}} \mathrm{d}\Omega_{\mathbf{q}}\; Y^*_{\ell,m}(\Omega_{\mathbf{q}})\; W_{7\mathrm{v}}(\mathbf{q}) \tag{4.9}$$

with $z_{qK} = \cos\sphericalangle(q,K)$. Inserting the product of Eq. (4.6) and Eq. (4.7) into Eq. (4.3b) we utilise the orthonormality of the spherical harmonics to eliminate the angular integration. The expectation value for the valence band dispersion is then given by

$$\langle\Psi_{\nu,\mathbf{K}}|W_{7\mathrm{v}}|\Psi_{\nu,\mathbf{K}}\rangle = \frac{1}{2\pi^2} \int_0^{\infty} \mathrm{d}q\; q^2 \sum_{\ell,m} \frac{a_{\nu,\ell}(q,K)}{2\ell+1}\, b_{\ell,m}(q)\; Y_{\ell,m}(\Omega_{\mathbf{K}})\,, \tag{4.10a}$$

$$= \frac{\Omega}{4\pi^2} \int_0^{\infty} \mathrm{d}q \int_{-1}^{1} \mathrm{d}z_{qK}\; q^2 \left|\varphi_{\nu,\mathbf{q}-\frac{\mathbf{K}}{2}}\right|^2 \sum_{\ell,m} P_\ell(z_{qK})\, b_{\ell,m}(q)\, Y_{\ell,m}(\Omega_{\mathbf{K}})\,. \tag{4.10b}$$

In this representation, the angular dependence of $\mathbf{K}$ is extracted into a single spherical harmonic. Furthermore, the angular dependence of $\mathbf{q}$ is completely gathered in $a_{\nu,\ell}(q,K)$ and at that, only relative to the exciton momentum $\mathbf{K}$. The second expansion coefficient $b_{\ell,m}(q)$ serves as a measurement for the contribution strength for angular states of the respective orbital quantum number ℓ and magnetic quantum number m to the band structure. Since the Hamiltonian is solely constructed from s- and d-like spherical harmonics (cf. appendix B.1.2), selection rules limit the possible couplings to states with even ℓ.

4.2. S exciton dispersion without polaron coupling

For the remaining terms of the Schrödinger equation, we start off by initially considering a static screened Coulomb potential $V_{\mathrm{C}}(r) = -\mathrm{e}^2/(4\pi\varepsilon_0\varepsilon_{\mathrm{r}} r)$ and neglecting the self-energies. In this case, the potential contribution is not dependent on the band states nor exciton momentum $\mathbf{K}$. The integration over the envelope functions in position space is sufficient and easily obtained analytically. The result yields

$$\begin{aligned}\langle \Psi_{n\mathrm{S},\mathbf{K}} | V_{\mathrm{C}} | \Psi_{n\mathrm{S},\mathbf{K}} \rangle &= \int \mathrm{d}^3\mathbf{r}\ |\phi_{n\mathrm{S}}(\mathbf{r})|^2\ V_{\mathrm{C}}(r)\,, \\ &= -\frac{\mathrm{e}^2}{4\pi\varepsilon_0\varepsilon_{\mathrm{r}}\, n^2\, a_{\mathrm{y}}}\,. \end{aligned} \tag{4.11}$$

The static permittivity is again chosen as $\varepsilon_{\mathrm{r}} = \varepsilon_1$, as it was done in chapter 3. With this we will ensure that the resulting minimised energy truly represents an upper boundary. There is no reason to believe that this approach will lead to a precise estimation of the binding energy, as we are already aware that the two LO phonon modes cause a significant change of the permittivity in the energy range of the low n excitons. However, it is still interesting to see to which extent this calculation differs from the result of the previous chapter, especially since we are determining the three fundamental parameters of the exciton: excitonic Bohr radius, binding energy and exciton mass.

Before starting the evaluation, there is one very drastic approximation that needs to be addressed. Even though we suggested in section 2.2.2 that in the JM representation of the SH Hamiltonian the Γ_7^+ can be associated by the $j = 1/2$ states, the off-diagonal elements of the Hamiltonian and the warping of the band structure insinuate additional mixing terms with the $j = 3/2$ states. The diagonalisation of the 6×6 valence band Hamiltonian for any angle always requires a unitary transformation that is inevitably momentum dependent. While this unitary transformation has no further influence on the diagonal shape of the conduction band Hamiltonian, the additional momentum dependence would act upon the hole momentum within the interaction potential. Thence, this creates non-diagonal terms in the interaction Hamiltonian that represents the coupling between $j = 1/2$ and $j = 3/2$ states. Under this consideration, Eq. (4.11) would seem like an oversimplification. However, there are two reasons that justify the assumption of a diagonal interaction potential. In contrast to the coupling within the $j = 3/2$ states, the coupling to the split-off band is relatively small due to the energetic separation to the Γ_8^+ valence bands [116]. Furthermore, a perturbational treatment of the off-diagonal elements would in first order only lead to a renormalisation of the interaction potential which is effectively reflected in a renormalisation of the Bohr radius. Thus, the variational method is already partially compensating for the missing coupling terms.

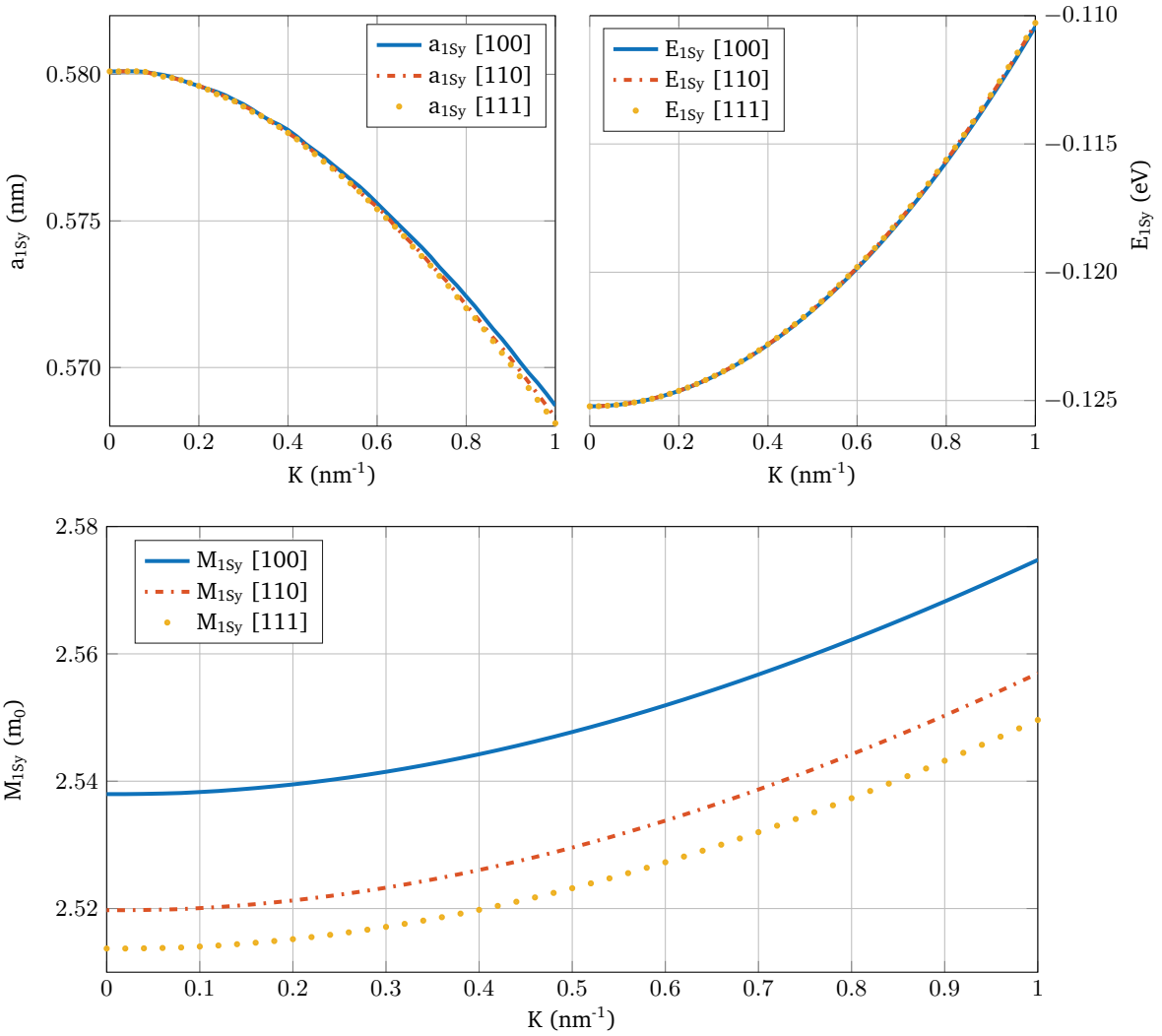

Figure 4.1.: Results of the variational approach for the 1S exciton without the consideration of polaron coupling. The upper left panel depicts the exciton radius as a function of exciton momentum K. The corresponding energy eigenvalues are shown in the upper right panel. The bottom panel displays the exciton mass. All figures present respective curves for three symmetry directions.

Due to the additional integrations in $W_{7\mathrm{v}}$, the evaluation of the variational approach has to be done numerically. The exciton radius is varied over a set interval of values $a_{\mathrm{y},i}$ until the condition

$$\frac{\partial}{\partial a_{\mathrm{y}}}\langle\Psi_{\nu,\mathbf{K}}|W_{6\mathrm{c}}+W_{7\mathrm{v}}+V_{\mathrm{C}}|\Psi_{\nu,\mathbf{K}}\rangle=0 \tag{4.12}$$

is met, i.e. the energy eigenvalue is minimal. It should be noted that the slope at the root shall be obtained as well since in some fringe cases, maxima can occur in regions of bigger radii, which the numerical procedure should not confuse with the minima. The gap energy E_{y} in Eq. (4.4) only causes a static shift and is therefore neglected. By solving Eq. (4.12) we directly

receive the exciton Bohr radius and binding energy for a fixed total exciton momentum $\mathbf{K}$. The total exciton mass is determined through the calculated exciton dispersion $E_{\mathrm{Sy}}(\mathbf{K})$ via

$$\frac{1}{M_{\mathrm{Sy}}} = \frac{1}{\hbar^2} \frac{\partial^2 E_{\mathrm{Sy}}(\mathbf{K})}{\partial K^2} \,. \tag{4.13}$$

The results for the three parameters are shown in Fig. 4.1. For the sake of clarity and to emphasise deviations, the calculations are only shown for the three high symmetry directions: Δ (100), Σ (110), and Λ (111).

4.2.1. Discussion

We recognise for all three parameters a slight deviation for the different spatial directions. Judging the energy dispersions, one could presume that they are parabolic and very close to isotropic, though the figure of the exciton mass negates that assumption strictly speaking. The momentum dependence depicted for the exciton radius can be a bit deceiving at first glance due to the chosen range of the axis. However, the radius changes over the depicted exciton momentum range about 2%, the difference at the biggest deviation between the spatial orientations is on the order of 0.1%; hence, the excitonic Bohr radius can be considered isotropic and more or less constant over a wide range of exciton momentum. A similar conclusion is found for the exciton mass and consequential for the dispersion. For the mass, the deviation between the spatial directions is less than 1%, over the range of exciton momentum it is about 1.5%. Therefore, it is save to approximate the exciton dispersion as an isotropic parabola, although one could have expected the deviations from a parabolic dispersion to be more substantial, due to the strong nonparabolicity of the valence band and the anisotropy that was measured for the orthoexciton mass [78].

As expected, the calculated binding energy at $K \simeq 0$ around $E_{1\mathrm{Sy}}^{(\mathrm{calc})}(0) = -125.2\,\mathrm{meV}$ is still significantly differing from the experimentally known value of $E_{1\mathrm{Sy}}^{(\mathrm{exp})} = -151\,\mathrm{meV}$ [10, 77]. The exciton mass $M_{1\mathrm{Sy}}^{(\mathrm{calc})} \simeq 2.53\,m_0$, however, shows a drastic improvement over the ideal Rydberg solution $M = m_{6\mathrm{c}} + m_{7\mathrm{v}}$ and is already close to the experimentally obtained mass $M_{1\mathrm{Sy}}^{(\mathrm{exp})} = 2.61\,m_0$ [77]. The excitonic Bohr radius is effectively halved in comparison to the exciton radius that was calculated for the excitonic Rydberg states in section 3.2.2. Comparing the 1S binding energy from the previous chapter $E_{1\mathrm{Sy}}^{(\mathrm{QD})} = -141.4\,\mathrm{meV}$ we again notice a significant deviation, even though for $\mathbf{K} = 0$ we receive the same initial Wannier equation for both cases. This is easily explained as both calculations yield different eigenfunctions for their results. The variational method only considers states with an s symmetry, while in the solution of last chapter the off-diagonal elements in Eq. (3.25) lead to an additional mixing with higher order n states.

4.3. Considering the polaron effect

While the previous result already shows a significant improvement, the deviation from the experimentally verified 1S paraexciton binding energy is still more than 17%. To improve upon that, we will now consider the influence of the polaron effect. The polaron is a quasiparticle constructed from the interaction of an electron (or hole, respectively) with the polar LO phonons. The concept of the polaron was already further examined in section 2.4.1. To account for the polaron effect on the electron and hole, we introduce a new interaction potential that includes the LO phonon induced frequency dependence of the permittivity and the corresponding self-energy.
A very early approach for the treatment of the polaron effect on excitons was proposed by H. Haken in 1956 [117]. In his fundamental work, he adopted the structure of the polaron Hamiltonian into the excitonic Hamiltonian. In this approach, two contributions emerge that modify the Coulomb interaction. First, the polarisation caused by the bound electrons that leads to an increase of the dielectric constant by ε_∞, and second the dislocation of the lattice ions, that causes an additional screening potential. Solving the corresponding Schrödinger equation then yields a self-consistent field problem for the additional screening potential. However, some assumptions for the functions describing the ion displacement are not necessary plausible (e.g. neglecting the dependence of the relative motion), and the perturbational treatment he applied is only valid in the limit of weak phonon coupling, as well as for weak binding energies or large exciton radii, respectively. Thus, we attempt to work with an advanced version of his theory.

4.3.1. Pollmann-Büttner potential and self-energy

J. Pollmann and H. Büttner build on Haken's theoretical foundation to derive a rigorous upper boundary expression for the binding energies, that ought to perform well over the whole region of coupling and binding parameters. For this they treated the same polaron Hamiltonian via a variational ansatz after applying some additional transformations. In this section, we will shortly summarise their approach and list the resulting potential and self-energy terms. For the exact mathematical derivation, see [118].
In their approach, the constituents of the excitons are no longer treated by two separate polarons but rather as two coupled particles in the same phonon field. Starting point is the Hamiltonian for electron and hole, interaction with each other via a screened Coulomb poten-

tial and the additional coupling to LO phonons described by Fröhlich interaction [50]

$$H_{PB} = \frac{\mathbf{P}^2}{2M} + \frac{\mathbf{p}^2}{2\mu} - \frac{\mathrm{e}^2}{4\pi\varepsilon_0\varepsilon_\infty} + \sum_\lambda \sum_{\mathbf{k}'} \hbar\omega_\lambda \, c^\dagger_{\lambda,\mathbf{k}'} c_{\lambda,\mathbf{k}'} + \sum_{\mathbf{k}''} \left(\sqrt{\hbar\omega_\lambda} \, v_{\lambda,k''} \, \rho_{\mathbf{k}''}(\mathbf{r}) \, c_{\lambda,\mathbf{k}''} \, e^{\mathrm{i}\mathbf{k}''\cdot\mathbf{R}} + \mathrm{H.c.} \right) , \tag{4.14}$$

with

$$\rho_{\mathbf{k}}(\mathbf{r}) = \exp\left(\mathrm{i} \frac{m_\mathrm{h}}{M} \mathbf{k}\cdot\mathbf{r} \right) - \exp\left(-\mathrm{i} \frac{m_\mathrm{e}}{M} \mathbf{k}\cdot\mathbf{r} \right) , \tag{4.15}$$

and the Fröhlich interaction

$$\sqrt{\hbar\omega_\lambda} \, v_{\lambda,k} = -\frac{\mathrm{i}}{k} \sqrt{\frac{\mathrm{e}^2 \hbar\omega_\lambda}{2\Omega \, \varepsilon_0 \varepsilon^*_\lambda}} \, . \tag{4.16}$$

The index λ denotes the different LO phonon modes, the $c^\dagger_{\lambda,\mathbf{k}}$ are the phonon creation operators and $\hbar\omega_\lambda$ are the corresponding phonon energies[2]. Upon this, two unitary transformations are applied. The first eliminates the center of mass coordinate, the second works under the assumption that the eigenfunctions can be reasonably good approximated by a coherent state. The unitary displacement operator then serves for the second transformation[3]. For the result, the vacuum state is assumed to be phonon ground state, and in turn they attempt to find an optimal choice for the displacement operator. By taking an independent particle ansatz they receive a set of coupled equations that interconnect all relevant quantities. To simplify the general solution significantly, we will utilise the interaction terms that are determined for the case of exciton momentum $\mathbf{K} = 0$ which in our case is rectified by the assumption that the influence of the center of mass motion on the polaron coupling is rather small in comparison to the relative motion of electron and hole. In coherence with the choice for the eigenfunction of Eq. (4.1), the system is then solved for a hydrogen-like wave function to yield an effective interaction potential and self-energy as functions of the excitonic Bohr radius. They bear the form

$$V^\nu_{\mathrm{PB}}(r) = -\frac{\mathrm{e}^2}{4\pi \, \varepsilon_0 \varepsilon_\infty \, r} + 2 \sum_\lambda \sum_{\mathbf{k}} |v_{\lambda,k}|^2 \left(f^{\nu,\mathrm{e}}_{\lambda,\mathbf{k}} + f^{\nu,\mathrm{h}}_{\lambda,\mathbf{k}} - f^{\nu,\mathrm{e}}_{\lambda,\mathbf{k}} \, f^{\nu,\mathrm{h}}_{\lambda,\mathbf{k}} \right) \cos(\mathbf{k}\cdot\mathbf{r}) \, , \tag{4.17}$$

[2] In contrast to section 2.4.1, the subscript LO will be omitted, as all energies $\hbar\omega_\lambda$ throughout the rest of this chapter refer to LO phonons.

[3] Although due to an additional dependence on the momentum operator $\mathbf{p}$, the unitary displacement operator would no longer yield a coherent state.

and

$$\sigma_{\mathrm{ex}}^{\nu} = \sigma_{\mathrm{e}}^{\nu} + \sigma_{\mathrm{h}}^{\nu}\,, \tag{4.18}$$

$$\sigma_{i}^{\nu} = -2\sum_{\lambda}\sum_{\mathbf{k}} |v_{\lambda,k}|^2 \left(f_{\lambda,\mathbf{k}}^{\nu,i} - \frac{1}{2}\left(1 + R_{\lambda,i}^2\, k^2\right)\left(f_{\lambda,\mathbf{k}}^{\nu,i}\right)^2 \right)\,, \tag{4.19}$$

with

$$f_{\lambda,\mathbf{k}}^{\nu,i} = \frac{(1-G_{\mathbf{k}}^{\nu})(1+L_{\lambda,\mathbf{k}}^{\nu}+R_{\lambda,j}^2\,k^2)}{(1+R_{\lambda,i}^2\,k^2)(1+R_{\lambda,j}^2\,k^2)-(L_{\lambda,\mathbf{k}}^{\nu})^2}\,, \tag{4.20}$$

$$G_{\mathbf{k}}^{\nu} = \langle\varphi_{\nu}|e^{\mathrm{i}\,\mathbf{k}\,\cdot\,\mathbf{r}}|\varphi_{\nu}\rangle\,, \tag{4.21}$$

$$L_{\lambda,\mathbf{k}}^{\nu} = G_{\mathbf{k}}^{\nu}\left(1 - \frac{1}{2}(R_{\lambda,\mathrm{e}}^2 - R_{\lambda,\mathrm{h}}^2)k^2\right)\,, \tag{4.22}$$

$$R_{\lambda,i} = \sqrt{\frac{\hbar}{2m_i\omega_{\lambda}}}\,. \tag{4.23}$$

The $R_{\lambda,i}$ are the polaron radii for particle i, coupled to phonon λ. The dependence of the exciton radius is confined to the auxiliary function $G_{\mathbf{k}}^{\nu}$. The interaction terms $V_{\mathrm{PB}}^{\nu}(r)$ and $\sigma_{\mathrm{ex}}^{\nu}$ will be referred to as Pollmann-Büttner (PB) potential and self-energy, respectively. In the next step, we determine the expectation values of these terms.

4.3.2. S exciton dispersion with polaron coupling

Since we are only interested in S excitons, the abovementioned terms and, thus, the expectation values can be simplified up to a certain point. The isotropic nature of the S envelope function immediately eliminates the angular dependences in Eq. (4.21), which subsequently transfers onto Eq. (4.20) and Eq. (4.22). The sum in Eq. (4.17) transforms according to Eq. (3.7) and with

$$G_k^{n\mathrm{S}} = 2\pi\int_0^{\infty}\mathrm{d}r\;|\phi_{n\mathrm{S}}(r)|^2\frac{2\,r\sin(kr)}{k}\,, \tag{4.24}$$

as well as the other auxiliary functions only depending on the absolute value of $k = |\mathbf{k}|$, the integration over the angular components of $\mathbf{k}$ is solved analytically to be

$$\int\limits_{\Omega_{\mathbf{k}}}\mathrm{d}\Omega_{\mathbf{k}}\cos(\mathbf{k}\cdot\mathbf{r}) = 4\pi\frac{\sin(kr)}{kr}\,. \tag{4.25}$$

The expectation value for the PB potential is given by

$$\langle\Psi_{n\mathrm{S},\mathbf{K}}|V_{\mathrm{PB}}^{n\mathrm{S}}|\Psi_{n\mathrm{S},\mathbf{K}}\rangle = 4\pi\int\limits_0^{\infty}\mathrm{d}r\;r^2|\phi_{n\mathrm{S}}(r)|^2\,V_{\mathrm{PB}}^{n\mathrm{S}}(r)\,. \tag{4.26}$$

Inserting Eq. (4.17) we recognise that the first part is equivalent to the result of Eq. (4.11). The integration over position space in the second part reduces to $G_k^{n\mathrm{S}}$; therefore, Eq. (4.26) takes the form

$$\langle \Psi_{n\mathrm{S},\mathbf{K}} | V_{\mathrm{PB}}^{n\mathrm{S}} | \Psi_{n\mathrm{S},\mathbf{K}} \rangle = -\frac{\mathrm{e}^2}{4\pi\varepsilon_0\varepsilon_3 n^2 a_\mathrm{y}} + \frac{2}{\pi}\int_0^\infty \mathrm{d}k\; G_k^{n\mathrm{S}} \sum_\lambda |\tilde{v}_\lambda|^2 \left(f_{\lambda,k}^{n\mathrm{S,e}} + f_{\lambda,k}^{n\mathrm{S,h}} - f_{\lambda,k}^{n\mathrm{S,e}}\, f_{\lambda,k}^{n\mathrm{S,h}} \right), \tag{4.27}$$

with $|\tilde{v}_\lambda|^2 = 2\pi/(\Omega k^2)|v_{\lambda,k}|^2 = \mathrm{e}^2/(4\pi\varepsilon_0\varepsilon_\lambda^*)$. The PB self-energies of the individual particles also do simplify under the assumption of nS excitons to

$$\sigma_i^{n\mathrm{S}} = -\frac{2}{\pi}\int_0^\infty \mathrm{d}k \sum_\lambda |\tilde{v}_\lambda|^2 \left(f_{\lambda,k}^{n\mathrm{S},i} - \frac{1}{2}\left(1 + R_{\lambda,i}^2\, k^2\right)(f_{\lambda,k}^{n\mathrm{S},i})^2 \right). \tag{4.28}$$

With this, we have obtained all necessary parts to include the polaron coupling into our variational calculation.

The procedure for determining the excitonic radius, dispersion, and mass is almost equal to the one described in section 4.2. This time, the exciton radius is varied until

$$\frac{\partial}{\partial a_\mathrm{y}} \langle \Psi_{\nu,\mathbf{K}} | W_{6\mathrm{c}} + W_{7\mathrm{v}} + V_{\mathrm{PB}} + \sigma_{ex}^\nu | \Psi_{\nu,\mathbf{K}} \rangle = 0 \tag{4.29}$$

is satisfied. This again yields exciton radius and the corresponding minimised energy that serves as an upper boundary for the binding energy for a predefined exciton momentum $\mathbf{K}$. The mass is then obtained from the dispersion by Eq. (4.13). There are two LO phonon branches λ in Cu_2O that need to be treated. One would assume that this is sufficient to evaluate the current results.

However, compared to the non-polaron case, the inclusion of the polaron interaction carries two additional peculiarities that need to be addressed. The self-energy effectively leads to a renormalisation of the gap energy that needs to be taken into consideration. In the limit case of weak coupling the self-energy of Eq. (4.19) is given by

$$\lim_{a_\nu/\mathrm{Ry}_\nu \to \infty} \sigma_i^\nu = -\sqrt{\frac{m_i}{m_0}} \sum_\lambda \alpha_\lambda\, \hbar\omega_\lambda = \sigma_i^{\mathrm{cont}}, \tag{4.30}$$

with α_λ being the phonon coupling constant given by Eq. (2.37). This corresponds to the self-energy of the Sommerfeld enhanced continuum states. Now if we introduce a gap energy E_y^* of a hypothetical crystal with no phonon interaction, the band gap of the real crystal would be given by $E_\mathrm{y} = E_\mathrm{y}^* + \sigma^{\mathrm{cont}}$ with $\sigma^{\mathrm{cont}} = \sigma_\mathrm{e}^{\mathrm{cont}} + \sigma_\mathrm{h}^{\mathrm{cont}}$. The same relation holds true with σ_ex^ν for discrete exciton states; however, in experiments the binding energy is always specified in relation to the real band gap E_y. Thus, for a proper evaluation, the gap energy in Eq. (4.4) needs to be replaced by E_y^*. Alternatively, for a treatment that is independent of the gap energy,

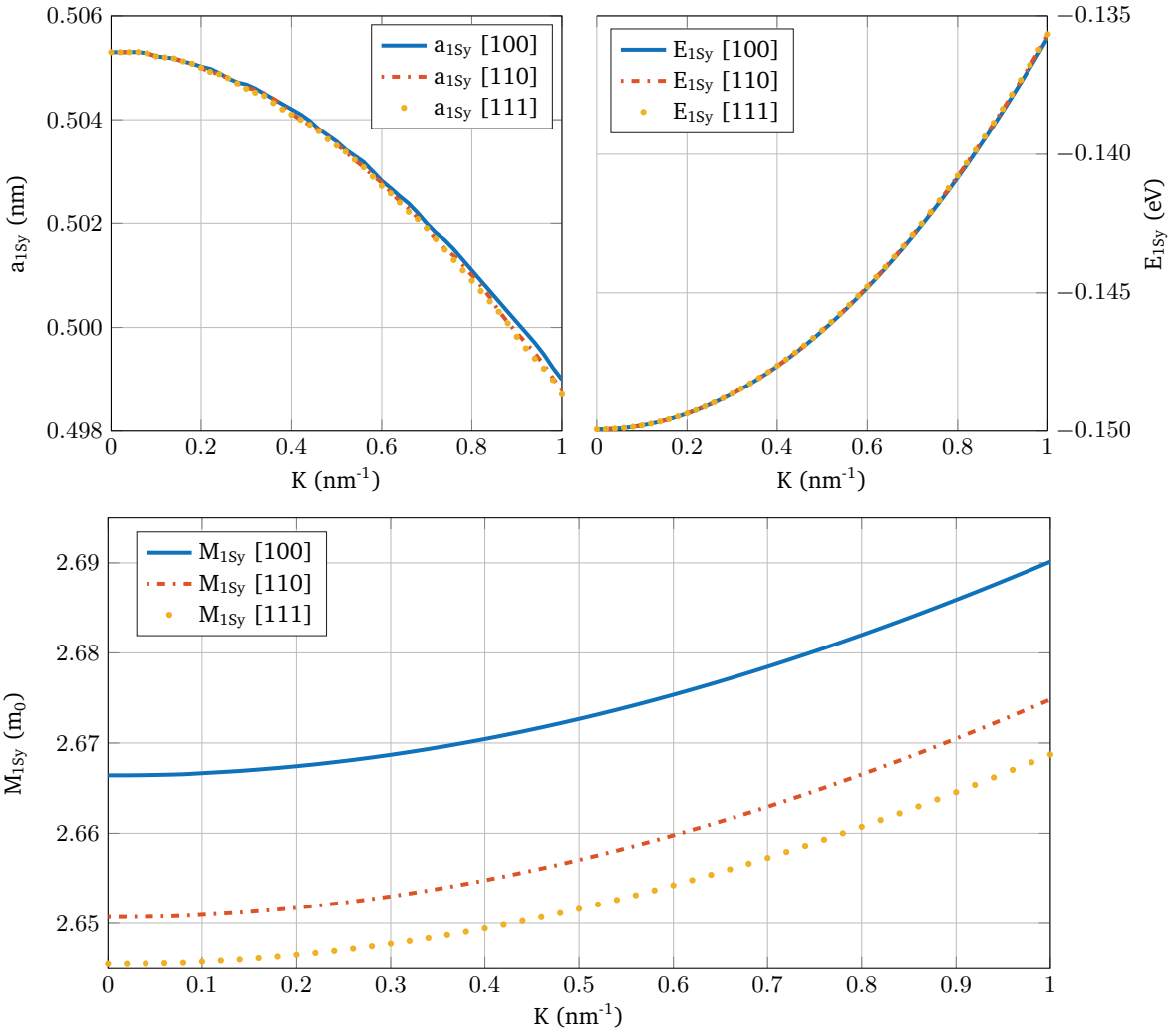

Figure 4.2.: Results of the variational approach for the 1S exciton with the PB interaction potential and self-energy. The upper left panel depicts the exciton radius, the energy eigenvalues are shown in the upper right panel. The bottom panel displays the exciton mass.

equal to the evaluation done in section 4.2, the self-energy in Eq. (4.29) has to be replaced by $\sigma_{\mathrm{ex}}^{\nu *} = \sigma_{\mathrm{ex}}^{\nu} - \sigma^{\mathrm{cont}}$.

The second particularity is found within the polaron radii. As it can be seen in Eq. (4.23), the polaron radius exhibits a dependence on the effective mass of the respective band. While this poses no issue for the conduction band where the band mass is constant over a wide momentum range, the nonparabolicity of the valence band would suggest, that the corresponding polaron radius has to be treated as a function of momentum,

$$R_{\lambda,h}(\mathbf{k}) = \sqrt{\frac{\hbar}{2\, m_{7\mathrm{v}}(\mathbf{k})\, \omega_{\lambda}}}\,. \tag{4.31}$$

As a matter of fact, if the calculation of Eq. (4.29) is done with a static polaron radius with $m_{7\mathrm{v}} \simeq 0.55 m_0$ (see section 2.2.3), the resulting binding energy at $\mathbf{K} = 0$ yields $E^{\mathrm{st}}_{1\mathrm{Sy}} = 153\,\mathrm{meV}$, which is already quite close to experiment; however, it no longer represents an upper boundary for the binding energy and is, therefore, of questionable accuracy. We have already seen in Fig. 2.4 and shown in chapter 3 that an isotropic approximation for the Γ_7^+ band works fairly well, and to retain the structure of Eqs. (4.27) and (4.28) we integrate the Γ_7^+ band dispersion over all angles to receive an averaged band dispersion $\bar{E}_{7\mathrm{v}}(k)$ of which we extract the momentum dependent mass $m_{7\mathrm{v}}(k)$.
With those two problems addressed, we are finally able to evaluate Eq. (4.29) properly. The emerging parameters are shown in Fig. (4.2).

4.3.3. Discussion

The resulting dispersion shows great agreement with the experimentally known values. The calculated binding energy $E^{(\mathrm{calc})}_{1\mathrm{Sy}}(0) = 150.0\,\mathrm{meV}$ only deviates about 0.7% from the experiment. The exciton radii and masses show the same general behaviour as in the nonpolaronic calculations, as it was to be expected, since the momentum dependence is almost exclusively contained within the band dispersions. However, they vary on absolute values and slope. Their relative change over $\mathbf{K}$ is even lesser than in the nonpolaronic treatment, substantiating the assumption that both, paraexciton radius and mass, can be treated more or less as constant. For the exciton mass it is advisable to utilise an average mass. A weighted average with respect to the three symmetry directions results in an exciton mass of $\bar{M}_{1\mathrm{Sy}} = 2.653\,m_0$, which is barely out of the range of the uncertainty of the experimental results $M^{(\mathrm{exp})}_{1\mathrm{Sy}} = 2.61 \pm 0.4\,m_0$ [77]. As to be expected, the excitonic Bohr radius decreased further in comparison to the result shown in Fig. 4.1.

4.4. Conclusion

The significant deviations of the yellow 1S paraexciton mass and binding energy in comparison to the parameters of the residual states of the yellow series were reproduced by considering the nonparabolicity of the valence band and the polaron-induced modification of the crystal permittivity. The calculation of our variational approach yields an astonishingly good agreement between experiment and calculation. There are a few interesting factors that emerge from this result.
First and foremost, it appears that the specific parameters of the yellow 1S exciton can be retraced almost exclusively to the nonparabolicity of the valence band and the frequency-dependent permittivity. In particular, for two approximations one could have expected a more significant impact. In contrast to the previous chapter, the eigenfunctions used in this approach

are pure hydrogen-like wave functions. While the solution of the ideal Wannier equation will be frequently used within this work, it is technically not sufficient at this point anymore as the emerging hydrogen solutions are not the optimal wave functions for the excitons. One reason for that is the fact that angular momentum is not a good quantum number [91]. Interestingly enough the variation with a wave function that only contains s symmetry was already sufficient to produce precise values for the 1S exciton.

According to [25], an additional participation of the Γ_8^+ valence bands of about 5.5% to the yellow 1S paraexciton should be present. The impact of state mixing was already discussed at the beginning of this chapter. As mentioned, it is not deemed too relevant for yellow excitons, as the energetical distance diminishes the coupling and the variational treatment already partially compensates the negligence of the coupling terms that would emerge for the interaction potentials.

For the chapter at hand, we neglected the exchange interaction again. If it were to be included, we would notice an additional splitting of the 1S exciton energy into the examined Γ_2^+ para- and the higher located Γ_5^+ orthoexcitons. This should not be of importance, since the result for the paraexcitons is not affected by the inclusion of exchange interaction, and the splitting between ortho- and paraexcitons is already well established experimentally [6, 61] and theoretically [56]. However, comparing the almost isotropic paraexciton mass obtained in this chapter with the measured anisotropy of the orthoexciton mass [78] would imply that the anisotropy is either caused by the exchange interaction or an additional effect that is neglected in our calculations. Since the anisotropy was not yet measured for the paraexciton [77], further conjecture is pointless.

Although the mixing of the band states appears to be of minor importance for the yellow series, the examination of the green series would certainly require a proper treatment of the coupling. Considering the bands as separate entities is no longer a viable option as there exists a strong coupling between the different $j = 3/2$ states and an evaluation with the depicted approach would yield two separate green exciton series[4], which is not confirmed as of yet. To solve this problem we would need the unitary transformation that diagonalises the SH Hamiltonian and apply it to the interaction potential. Additionally, the anisotropy of the two Γ_8^+ bands is significantly stronger than the anisotropy of the Γ_7^+ band, which would complicate the numerical calculation.

[4]This should not be confused with the splitting into the subseries of the green para- and orthoexciton.

Chapter 5.

Phonon-assisted absorption

In section 2.1, we examined the symmetry of the highest valence and lowest conduction bands at zone centre and how they originate from the different atomic orbitals. Based on this knowledge, section 2.3 introduces the excitons as bound-state solutions to the Wannier equation, utilising the similarity to the hydrogen problem to describe the relative motion by hydrogen like wave functions. This enables a rather convenient familiar describtion via quantum numbers and consequently provides us with the corresponding symmetries. As a result, it was shown that S type excitations are only feasible for the blue and violet series, while transitions into exciton states of the yellow and green series should predominantly be shaped by P type envelopes. However, as it can be seen in numerous experimental spectra, the exciton resonances of the yellow series are underlayed by a strong absorption background [51, 108, 119]. This background stems from a strong phonon-assisted absorption of the yellow 1S exciton.

This chapter is dedicated to investigate this absorption edge in more detail. For this, we will improve upon the textbook solution that utilises second order perturbation theory and was derived by R. Elliott in 1957 [120]. The results for the phonon-assisted absorption at low temperatures are published in [121].

5.1. Transition probability

The absorption coefficient will be obtained from the transition probability, which can be received by Fermi's Golden rule as

$$P_{ij} = \frac{2\pi}{\hbar} \left| M_{ij} \right|^2 \, \delta(E_i - E_j) \, . \tag{5.1}$$

The transition matrix element M_{ij} can be evaluated, starting with the one-electron Hamiltonian, including the electron-radiation and electron-phonon interactions and treating them in second order perturbation theory. The associated wave functions can be chosen as Slater determinants consisting of the electron Bloch functions. As a consequence, the transition matrix

element would describe all transitions purely between the Bloch states of the related energy dispersion. Taking into account the creation of a hole as a quasiparticle, the wave function can also be expressed as a product state of Slater determinants for electron and hole, respectively. These determinants are only superimposed for states that fulfill $\mathbf{K} = \mathbf{k_e} - \mathbf{k_h}$ due to the translational symmetry. Their diagonalisation then yields the wave function in exciton representation; hence, we assume all transition states to be excitons. The indirect transition from excitonic vacuum into an arbitrary final state μ, under the aid of phonon absorption or emission can be derived in second order perturbation theory as

$$P_{0,\mu}(\mathbf{k},\omega) = \frac{2\pi}{\hbar} \sum_{\mathbf{Q},\lambda,\sigma} \left| \sum_{\nu} \frac{\langle \Psi_{\mu,\mathbf{Q}+\mathbf{k}} | h_{\lambda,\mathbf{Q}} | \Psi_{\nu,\mathbf{k}} \rangle \langle \Psi_{\nu,\mathbf{k}} | h_{\mathrm{ph}} | \Psi_0 \rangle}{E_\nu(\mathbf{k}) - \hbar\omega} \right|^2 \delta\left[E_\mu(\mathbf{Q}+\mathbf{k}) \mp \hbar\omega_{\lambda,\mathbf{Q}} - \hbar\omega \right], \tag{5.2}$$

which describes, depending on the sign within the delta distribution, the absorption of a phonon with momentum $\mathbf{Q}$ or the emission of a phonon with mometum $-\mathbf{Q}$. The subscripts μ and ν contain a set of quantum numbers (n, ℓ, m) of the respective excitonic envelope function. The two transition elements consist of the electron-radiation interaction h_{ph} and the phonon interaction Hamiltonian $h_{\lambda,\mathbf{Q}}$, with λ denoting the associated phonon branch. The state Ψ_ν denotes an intermediate virtual state. $E_i(\mathbf{k})$ represents the energy dispersion of state i and will usually assumed to be in terms of the effective mass approximation $\frac{\hbar^2 k^2}{2M_i}$, with M_i being the excitonic mass. The energy $\hbar\omega_{\lambda,\mathbf{Q}}$ is the respective phonon dispersion. The sum over σ denotes the summation of the different spin states. At a later point, the treatment of the spin functions will be shifted into the transition matrix element M_{ij}; therefore, the sum will be dropped for the moment.

The physical interpretation of this process can be depicted as the excitation of a virtual state Ψ_ν via the incoming photon with a successive transition into the final state Ψ_μ via the emission or absorption of a phonon. Technically, this chain of processes could be inverted. This is a prominent feature in indirect semiconductors in which phonon-assisted intraband scattering processes can equally occur before the photonic transition to lead to an energetically favorable position for the intermediate or final state. However, photonic transitions in direct gap semiconductors are usually assumed to happen at the smallest energy gap between the extrema of conduction and valence band anyway[1]; thus, they do generally not benefit energetically from intraband transitions. Regarding interband transitions, the energy range of the photons required exceeds the phonon energy about an order of magnitude. Regarding Eq. (5.2), we notice the transition probability to be inversely dependent on the energy difference between the initial and intermediate state; hence, it is save to assume that the photon transition always precedes the phonon transition.

In the fundamental work of Elliott [120] the intermediate states Ψ_ν are approximated, under the assumption of weak electron-hole interaction, as Bloch states and solely the final state Ψ_μ

[1] At least at low temperatures this approximation is valid.

is considered as an exciton. This effectively represents transitions of free pairs within the electronic band structure with the effects of the excitonic nature of the final state being addressed by a Sommerfeld enhancement. Back then, Elliott used this approximation to ensure the emergence of an analytical solution and to avoid numerical inconveniences. Today, his work is well established in literature and became a textbook example. However, while it is able to describe the shape of the phonon-assisted absorption to a certain degree of accuracy, it fails to reliably model the absorption shape over a wide energy range, as we will see in this chapter. If the bands involved in the formation of the intermediate state are known to form excitons and their corresponding parameters (i.e. excitonic mass and Rydberg energy) are known, it is advantageous to use excitonic intermediate states.

In the following, we will impose a few restrictions upon Eq. (5.2). We start off by investigating the final states μ. The main contribution of the phonon-assisted absorption originates from the S ($\ell = 0$) states of the yellow and green series; therefore, we will restrict the final states to nS excitons. Their odd ℓ states can be reached via direct dipole excitation, but not with the phonon-assisted process, since the relevant phonons in Cu_2O all exhibit negative parity. Therefore, it requires a double parity change to receive a positive parity state, i.e. the even ℓ states. For this reason all even ℓ states should be under consideration. It will be shown that the participation of 2S and higher nS states is already considerably smaller, making a good case for ignoring states with $\ell > 0$. A similar logic applies to the intermediate ν states. The states that will contribute the most are 1S states. It was already discussed in section 2.3.2, that the direct transition into yellow and green S type states is dipole forbidden. Checking experimental spectra for the yellow 1S orthoexciton resonance, one realises quickly that its contribution to the spectrum, which is due to quadrupole transitions[2], is negligibly small. Extrapolating this thought to the second order perturbation theory, it becomes obvious that the photonic transition to the intermediate state needs to be a dipole allowed S exciton for the transition probability to provide a significant contribution to the absorption spectrum. In the semi-classical approach, the electron-radiation interaction in electric-dipole approximation reads as [50, 51]

$$\langle \Psi_\nu | h_{\mathrm{ph}} | \Psi_0 \rangle = \frac{\mathrm{e}}{m_0} \langle \Psi_\nu | \mathbf{A} \cdot \mathbf{p} | \Psi_0 \rangle \,, \tag{5.3}$$

with $\mathbf{A} = \mathbf{A}(\mathbf{r}, t)$ being the vector potential of the electromagnetic field. Furthermore, we assume photon momentum to be small enough to be neglected, making photonic transitions effectively take place at zone centre (which is only valid for direct band gap semiconductors). In this case, final exciton momentum only depends on the phonon momentum $\mathbf{Q}$. The transi-

[2] In contrast to the 1S paraexcitons which cannot be excited directly. We established that in section 2.3.2.

tion probability then takes the form

$$P_{0,n\mathrm{S}}(\omega) = \sum_{\lambda} \bar{P}_n^{\lambda}(\omega)\,, \tag{5.4}$$

$$\bar{P}_n^{\lambda}(\omega) = \frac{2\pi \mathrm{e}^2}{\hbar\, m_0^2} \sum_{\mathbf{Q}} \left| \sum_{\nu} \frac{\langle \Psi_{n\mathrm{S},\mathbf{Q}} | h_{\lambda,\mathbf{Q}} | \Psi_{\nu,0} \rangle \langle \Psi_{\nu,0} | \mathbf{A}\cdot\mathbf{p} | \Psi_0 \rangle}{E_\nu(0) - \hbar\omega} \right|^2 \delta\left[E_{n\mathrm{S}}(\mathbf{Q}) \mp \hbar\omega_{\lambda,\mathbf{Q}} - \hbar\omega \right], \tag{5.5}$$

which can be considered the linchpin equation of this chapter.

5.1.1. Symmetry considerations

Next, we consider the possible intermediate states and phonon interactions. The transition probability features a sum over all bands which are not the final conduction and valence band, as well as a sum over all phonon modes. However, the number of terms can be drastically reduced by considering the symmetry properties of the individual terms. Since we are only interested in S like (Γ_1^+) intermediate states, it is sufficient to evaluate the symmetry of the bands directly [cf. Eq. (2.26)].

As already mentioned, the dipole operator $\mathbf{p}$ possesses Γ_4^- symmetry; hence, it incorporates a parity change. We recognise that both Γ_1^+ conduction and Γ_5^+ valence band possess positive parity at the zone centre, which restricts our choice for intermediate states ν to bands with negative parity. If we aim to excite an electron off of the Γ_5^+ valence band into an intermediate conduction band, the choice of bands is confined to $\Gamma_4^- \otimes \Gamma_5^+ = \Gamma_2^- \oplus \Gamma_3^- \oplus \Gamma_4^- \oplus \Gamma_5^-$ symmetries. If we were to excite an electron from an intermediate band below the Γ_5^+ valence band up to the Γ_1^+ conduction band (which is analogous to imagining an initial hole being "excited" down into an intermediate valence band), the intermediate band requires a symmetry of $\Gamma_4^- \otimes \Gamma_1^+ = \Gamma_4^-$. The energy denominator in Eq. (5.5) denotes the energy difference between radiation and the virtual intermediate state; thus, the further away a band is located, the smaller the probability to participate in the transition. The closest band that possesses the right symmetry and negative parity is the Γ_3^- conduction band. As we established in section 2.3.1, the $\Gamma_{5\mathrm{v}}^+$ and $\Gamma_{3\mathrm{c}}^-$ bands are known to form the blue and violet exciton series, which provide optimal intermediate states.

Subsequently, the second transition needs to adhere to the symmetry of intermediate and final state. As $\Gamma_{3\mathrm{c}}^- \otimes \Gamma_{1\mathrm{c}}^+ = \Gamma_3^-$, this would suggest that the transition is predominantly driven by the Γ_3^- phonon. Considering the spin symmetry of both conduction bands leads to more possible transitions with $\Gamma_{8\mathrm{c}}^- \otimes \Gamma_{6\mathrm{c}}^+ = \Gamma_3^- \oplus \Gamma_4^- \oplus \Gamma_5^-$. However, the Γ_4^- and Γ_5^- symmetries emerge under the condition, that the spin configuration in the transition between both bands is modified by the interaction. Since phonons are not capable of altering the spin configuration, those two additional symmetries do not warrant further attention [51]. Measurements of the luminescence spectrum detected the Γ_3^- optical phonon to be the strongest phonon branch in Cu_2O [110].

Thus, the transition over the blue (violet) excitons and the consecutive relaxation into the yellow (green) series via a Γ_3^- phonon is expected to be predominant in the absorption spectrum. Simultaneously, our exciton states themselves are limited in their ability of phonon coupling. In the yellow series we distinguish between para-(Γ_2^+) and orthoexcitons (Γ_5^+). While orthoexcitons are allowed to couple to phonons of symmetry $\Gamma_5^+ \otimes \Gamma_4^- = \Gamma_2^- \oplus \Gamma_3^- \oplus \Gamma_4^- \oplus \Gamma_5^-$, the paraexcitons are restricted to $\Gamma_2^+ \otimes \Gamma_4^- = \Gamma_5^-$ phonons. Hence, there is no Γ_3^- phonon-assisted absorption into yellow paraexciton states.

Besides this major transition channel, there is another visible transition around the phonon energy of one of the Γ_4^- LO phonons (namely $\hbar\omega_{\mathrm{LO},2} = 82.1\,\mathrm{meV}$) [108]. The coupling of an intermediate state with a Γ_4^- phonon to the $\Gamma_{1\mathrm{c}}^+$ band necessitates a symmetry of $\Gamma_4^- \otimes \Gamma_1^+ = \Gamma_4^-$. A dipole allowed photon absorption can also only be accomplished into bands with $\Gamma_4^- \otimes \Gamma_1^+ = \Gamma_4^-$ symmetry. Hence, a transition via Γ_4^- phonons would always require a Γ_4^- symmetry conduction or valence band. Revisiting section 2.1, we notice that there are two $\Gamma_{4\mathrm{c}}^-$ conduction and one $\Gamma_{4\mathrm{v}}^-$ valence bands. Unfortunately, this multitude of potentially coupling bands does inhibit a decisive determination of transition matrices. Additionally, these bands are energetically quite far away from the band gap, leaving us with no precise data, but estimated values from band structure calculations about their dispersions. Even though their contribution is minor, they should be mentioned and will be included in the final representation of the absorption spectrum for the sake of completeness.
While we will treat the dominant part of the absorption spectrum with the Γ_3^- phonon, the Γ_4^- phonon transitions are miniscule enough to treat them with the square root solution that emerges, if pure Bloch functions are used as intermediate states.

5.1.2. Phonon transition element

There are three different types of phonon interactions. The macroscopic dilation of the crystal by acoustic phonons, localised dilations on the scale of the primitive unit cell caused by optical phonons and the dislocation of electric charges that stem from LO phonons. The first two can be described in a similar approach using the nomenclature of the deformation potential, the third effect is usually depicted as the polaron quasiparticle [50–53]. Since we are interested in two optical phonons, both will be characterised by optical-phonon deformation potentials. The polaron effect of the Γ_4^- LO phonon is only relevant for intraband scattering processes [83]; thus, its consideration is not necessary. The electron optical-phonon interaction between two band states is given by [38]

$$\langle \psi_i | h_{\lambda,\mathbf{Q}} | \psi_j \rangle = D_{\lambda;ij}(\mathbf{Q}) \sqrt{\frac{\hbar}{2\Omega\,\rho\,\omega_{\lambda,\mathbf{Q}}}} \sqrt{\begin{Bmatrix} n_\lambda \\ n_\lambda + 1 \end{Bmatrix}}, \tag{5.6}$$

with $D_{\lambda;ij}(\mathbf{Q})$ being the optical-phonon deformation potential, Ω the crystal volume, and ρ the material specific density of Cu_2O. The second square root term contains the phonon distribution for absorption and emission, respectively, with n_λ being the phonon occupation number. In equilibrium, it can be expressed by the Bose-Einstein distribution function

$$n_\lambda(\omega_{\lambda,\mathbf{Q}}) = \left(\mathrm{e}^{\hbar\omega_{\lambda,\mathbf{Q}}/k_B\,T} - 1\right)^{-1} . \tag{5.7}$$

The Γ_3^- phonon matrix element shall be treated with exciton states; therefore, Eq. (5.6) is not sufficient as it defines the deformation potential in relation to the band states. Taking the phonon transition element from Eq. (5.5) and employing excitonic wave functions, it can be rewritten terms of excitonic envelope and Bloch functions $\psi_{n,\mathbf{q}}$ as

$$\begin{aligned}\langle\Psi^{(\mathrm{y})}_{n\mathrm{S},\mathbf{Q}}|h_{3,\mathbf{Q}}|\Psi^{(\mathrm{b})}_{n'\mathrm{S},0}\rangle &= \sum_{\mathbf{q},\mathbf{q}'} \varphi^{(\mathrm{y})}_{n\mathrm{S},\mathbf{q}}\,\varphi^{(\mathrm{b})}_{n'\mathrm{S},\mathbf{q}'}\,\langle\psi_{6\mathrm{c},\frac{\mathbf{Q}}{2}+\mathbf{q}}|h_{3,\mathbf{Q}}|\psi_{8\mathrm{c},\mathbf{q}'}\rangle\,\langle\psi_{7\mathrm{v},\frac{\mathbf{Q}}{2}-\mathbf{q}}|\psi_{7\mathrm{v},-\mathbf{q}'}\rangle \\ &= \sum_{\mathbf{q}} \varphi^{(\mathrm{y})}_{n\mathrm{S},\mathbf{q}}\,\varphi^{(\mathrm{b})}_{n'\mathrm{S},\mathbf{q}-\frac{\mathbf{Q}}{2}}\,\langle\psi_{6\mathrm{c},\frac{\mathbf{Q}}{2}+\mathbf{q}}|h_{3,\mathbf{Q}}|\psi_{8\mathrm{c},\mathbf{q}-\frac{\mathbf{Q}}{2}}\rangle\,. \end{aligned} \tag{5.8}$$

The $\varphi^{(i)}_{n\mathrm{S},\mathbf{q}}$ are the excitonic envelope functions with the superscript i denoting the corresponding exciton series, in this case the transition from the blue (b) to the yellow (y) series. The transition from the violet (v) to the green (g) series is equivalent and is received by substituting $\mathrm{y}\to\mathrm{g}$ and $\mathrm{b}\to\mathrm{v}$. We shall keep that in mind for later, for now we stick with the nomenclature of the blue/yellow transition for the sake of clarity.

The second matrix element yields a Kronecker delta which conserves hole momentum and consequently annihilates one of the momentum sums. We are assuming, that the remaining matrix element in Eq. (5.8) is approximately independent over the whole range of $\mathbf{q}$ and can be expressed via the optical phonon deformation potential of Eq. (5.6). Consequently, the remainder of the sum reads as $\sum_{\mathbf{q}} \varphi^{(\mathrm{y})}_{n\mathrm{S},\mathbf{q}}\,\varphi^{(\mathrm{b})}_{n'\mathrm{S},\mathbf{q}-\frac{\mathbf{Q}}{2}}$. Again, we will consider the envelope functions to be hydrogen-like wave functions.

The sum can now be evaluated in two different approaches. The sum in Eq. (5.8) is rewritten as an integral

$$\langle\Psi^{(\mathrm{y})}_{n\mathrm{S},\mathbf{Q}}|h_{3,\mathbf{Q}}|\Psi^{(\mathrm{b})}_{n'\mathrm{S},0}\rangle = \frac{1}{(2\pi)^3}\sqrt{\frac{\Omega\,\hbar}{2\rho\,\omega_{3,\mathbf{Q}}}}\,\sqrt{\left\{\begin{array}{c} n_{3,\mathbf{Q}} \\ n_{3,\mathbf{Q}}+1 \end{array}\right\}}\,D_{3;68}(\mathbf{Q})\int \mathrm{d}^3\mathbf{q}\;\varphi^{(\mathrm{y})}_{n\mathrm{S},\mathbf{q}}\,\varphi^{(\mathrm{b})}_{n'\mathrm{S},\mathbf{q}-\frac{\mathbf{Q}}{2}}\,. \tag{5.9}$$

Inserting the momentum wave functions as they were given in Eq. (4.5) into Eq. (5.9), the triple integral can be evaluated either numerically or analytically for smaller quantum numbers. Considering S states, the integration simplifies to

$$\mathcal{S}^{(\mathrm{y,b})}_{n,n'}(Q) = \frac{\Omega}{(2\pi)^2}\int_{-\pi}^{\pi}\int_{0}^{\infty}\mathrm{d}\cos\vartheta\;\mathrm{d}q\;\varphi^{(\mathrm{y})}_{n\mathrm{S},q}\,\varphi^{(\mathrm{b})}_{n'\mathrm{S},\sqrt{q^2+Q^2/4-qQ\cos\vartheta}}\,\sin\vartheta\,. \tag{5.10}$$

Alternatively, it is possible to treat the expression as a threedimensional convolution with offset $\mathbf{Q}/2$ and integrate in position space. In this case of S type envelopes the spherical harmonics only contribute a factor $1/(4\pi)$, leaving us with a single integral

$$\mathcal{S}^{(\mathrm{y,b})}_{n,n'}(Q) = \sum_{\mathbf{q}} \varphi^{(\mathrm{y})}_{n\mathrm{S},\mathbf{q}}\, \varphi^{(\mathrm{b})}_{n'\mathrm{S},\mathbf{q}-\frac{\mathbf{Q}}{2}} = \frac{2}{Q}\int\limits_0^\infty \mathrm{d}r\; r\, R^{(\mathrm{y})}_{n\mathrm{S}}(r)\, R^{(\mathrm{b})}_{n'\mathrm{S}}(r)\, \sin\frac{Q\,r}{2}\,, \tag{5.11}$$

with $R^{(i)}_{n\ell}(r)$ being the radial hydrogen wave functions. It should be noted, that in both cases this reduction of integrals only works for S type envelopes due to their isotropy, for higher ℓ states the angular dependence of $\mathbf{Q}$ does not vanish. As mentioned, those integrals can be, up to a certain degree, solved analytically. As we will see later, the most important term is

$$\mathcal{S}^{(\mathrm{y,b})}_{1,1}(Q) = \frac{2^7\sqrt{\beta^3}(1+\beta)}{\left(4(1+\beta)^2 + a_\mathrm{b}^2 Q^2\right)^2}\,, \tag{5.12}$$

where $\beta = a_\mathrm{b}/a_\mathrm{y}$.

5.2. Absorption coefficient

The analysis of the phonon matrix element has lead to its description via a deformation potential and the convolution of exciton envelope wave functions. The electron-radiation interaction in Eq. (5.5) coincides with the direct transition matrix element from excitonic vaccum into a blue exciton state and, therefore, corresponds to the textbook solution [50–53, 119, 122]

$$\langle \Psi^{(\mathrm{b})}_{n'\mathrm{S},0} | \mathbf{A}\cdot\mathbf{p} | \Psi_0 \rangle = \; A_0\, \phi^{(\mathrm{b})}_{n'\mathrm{S}}(\mathbf{r}{=}0)\; p_{78}\,, \tag{5.13}$$

with the dipole transition matrix element between two band states being $p_{78} = \langle u_{8\mathrm{c},0} | \mathbf{e}\cdot\mathbf{p} | u_{7\mathrm{v},0}\rangle$. The excitonic envelope function $\phi^{(\mathrm{b})}_{n'\mathrm{S}}(\mathbf{r})$ is given in position space. For S like states at position $\mathbf{r}=0$, it abides to $\phi^{(\mathrm{b})}_{n'\mathrm{S}}(0) = \left(\pi\,(a_\mathrm{b}\,n')^3\right)^{-1/2}$. Taking this into account, we get for the transition probability

$$\begin{aligned}\bar{P}^{(3)}_{n,\mathrm{y}}(\omega) =& \frac{\mathrm{e}^2 A_0^2}{\Omega m_0 \rho\, \omega_3 a_\mathrm{b}^3}\frac{|p_{78}|^2}{m_0}\sum_{\mathbf{Q}} |D_{3;68}(\mathbf{Q})|^2 \left|\sum_{n'}\frac{\mathcal{S}^{(\mathrm{y,b})}_{n,n'}(Q)}{n'^{3/2}\left(E_{n'\mathrm{Sb}} - \hbar\omega\right)}\right|^2 \\ &\times \begin{Bmatrix} n_{3,\mathbf{Q}} \\ n_{3,\mathbf{Q}}+1 \end{Bmatrix} \delta\left[E_{n\mathrm{Sy}}(\mathbf{Q}) \mp \hbar\omega_{3,\mathbf{Q}} - \hbar\omega\right].\end{aligned} \tag{5.14}$$

We possess no specific knowledge about the angular dependence of the deformation potential $D_{3;68}$, thus assuming it to be isotropic. The dispersions of optical phonons are often considered to be only varying marginally and are frequently approximated as constants ω_λ. Indeed, this

holds true for our phonons of interest, as it can be seen in [26,29,123]. Contrary to our results for the 1S paraexciton in chapter 4, it was experimentally shown that the 1S orthoexciton mass is quite anisotropic [78]. For the upcoming calculations we assume an average mass of $M_{1\mathrm{Sy}}^{(\mathrm{o})} = 2.7\, m_0$ [109]. Approximating the final state dispersion to be independent of the phonon angle, the delta distribution only depends on the absolute value of the momentum. Under these circumstances, the sum in Eq. (5.14) can be evaluated and the transition probability takes the final form

$$\begin{aligned}\bar{P}_{n,\mathrm{y}}^{(3)}(\omega) =& \frac{\mathrm{e}^2 A_0^2}{2\pi^2\hbar^2\rho\, a_{\mathrm{b}}^3}\frac{M_{\mathrm{y}}}{m_0}\frac{q_n^{(3)}}{\omega_3}\frac{|p_{78}|^2}{m_0}|D_{3;68}(q_n^{(3)})|^2 \\ &\times\left|\sum_{n'}\frac{\mathcal{S}_{n,n'}^{(\mathrm{y,b})}(q_n^{(3)})}{n'^{3/2}(E_{n'\mathrm{Sb}}-\hbar\omega)}\right|^2 \Theta\left(q_n^{(3)}\right)\begin{Bmatrix} n_3 \\ n_3+1\end{Bmatrix}. \end{aligned} \tag{5.15}$$

This expression describes the transition probability over all intermediate blue n'S exciton states into the yellow nS exciton state via the absorption or emission of a Γ_3^- optical phonon. The function $q_n^{(\lambda)}$ represents the final momentum and is defined as

$$q_n^{(\lambda)}(\omega) = \sqrt{\frac{2M_{\mathrm{y}}}{\hbar^2}}\sqrt{\hbar\omega \pm \hbar\omega_\lambda - E_{n\mathrm{Sy}}}\,. \tag{5.16}$$

Eventually, we receive the absorption coefficient from the transition probability. It is defined as [51]

$$\alpha_{\mathrm{y}}(\omega) = \sum_{n,\lambda}\alpha_{n,\mathrm{y}}^{\lambda}\,, \tag{5.17}$$

$$\alpha_{n,\mathrm{y}}^{\lambda}(\omega) = \frac{2\hbar}{\varepsilon_0 n_{\mathrm{R}} c\omega A_0^2}\bar{P}_{n,\mathrm{y}}^{\lambda}(\omega)\,, \tag{5.18}$$

with n_{R} being the material specific refractive index of Cu_2O around the excitation energy $\hbar\omega$. Inserting Eq. (5.15) yields

$$\begin{aligned}\alpha_{n,\mathrm{y}}^{(3)}(\omega) =& \frac{\mathrm{e}^2}{\pi^2\hbar\,\rho\,\varepsilon_0 n_{\mathrm{R}} c\, a_{\mathrm{b}}^3}\frac{M_{\mathrm{y}}}{m_0}\frac{q_n^{(3)}}{\omega\,\omega_3}\frac{|p_{78}|^2}{m_0}\left|D_{3;68}(q_n^{(3)})\right|^2 \\ &\times\left|\sum_{n'}\frac{\mathcal{S}_{n,n'}^{(\mathrm{y,b})}(q_n^{(3)})}{n'^{3/2}\,(E_{n'\mathrm{Sb}}-\hbar\omega)}\right|^2 \Theta(q_n^{\lambda})\begin{Bmatrix} n_3 \\ n_3+1\end{Bmatrix}. \end{aligned} \tag{5.19}$$

Although Eq. (5.19) provides us with an analytical result for the absorption background, it still bears two uncertainties: The strength and precise momentum dependence of the optical phonon deformation potential $D_{3;68}$. Fortunately, the absorption edge of the Γ_3^- phonon into the $1\mathrm{S}$ yellow state has a very wide and undisturbed shape and is well suited for fitting. Usually, the deformation potential is assumed to vary only slightly with phonon momentum and is often

assumed to be constant. We expand the deformation potential with respect to the square of phonon momentum Q to

$$\begin{aligned} D_{\lambda,68}(Q) &= D^{(0)}_{\lambda,68} \;+\; D^{(2)}_{\lambda,68}\, Q^2 \;+\ldots \\ &\simeq D^{(0)}_{\lambda,68} \left(1 \;+\; \bar{D}^{(2)}_{\lambda,68}\, Q^2\right) . \end{aligned} \tag{5.20}$$

We consider the zeroth and first order of this expansion. It will be seen, that the first order approach is sufficient to satisfactorily describe the absorption edge. Higher order terms only increase the number of variables to fit and do not improve the result noticeably.

Before concerning ourselves with the application of the theory, we shall shortly assess the formalism for absorption via the Γ_4^- LO phonon. Starting again from Eq. (5.5), we assume the intermediate states to be pure band states. The absorption is obtained in a similar, yet much easier way than the preceding deduction of the absorption via exciton states and results in

$$\alpha^{(4)}_{n,\mathrm{y}} = \frac{2\,\mathrm{e}^2\;|\varphi^{(\mathrm{y})}_{n\mathrm{S}}(0)|^2}{\pi\hbar\rho\varepsilon_0 n_\mathrm{R} c}\,\frac{M_\mathrm{y}}{m_0}\,\frac{q^{(4)}_n}{\omega\,\omega_4}\sum_\nu \frac{|p_\nu|^2}{m_0}\,\frac{|D_{4;\nu}(q^{(4)}_n)|^2}{\left(E_\nu-\hbar\omega\right)^2}\;\Theta(q^{(4)}_n)\;\left\{\begin{array}{c} n_4 \\ n_4+1 \end{array}\right\} . \tag{5.21}$$

Here, the exciton wave function of the final state corresponds to a Sommerfeld enhancement factor and yields $\varphi^{(\mathrm{y})}_{n\mathrm{S}}(0) = \left(\pi\,(a_\mathrm{y}\,n)^3\right)^{-1/2}$. It is important to note that the sum over ν does not indicate a single band but always a pair of associated bands, namely the initial and intermediate band. In this case, these are two $\Gamma^+_{7\mathrm{v}} \otimes \Gamma^-_{4\mathrm{c}}$ transitions and one $\Gamma^+_{1\mathrm{c}} \otimes \Gamma^-_{4\mathrm{v}}$ transition. As a consequence, the energy E_ν corresponds the absolute energy difference between those bands, e.g. $E_{1\mathrm{c},4\mathrm{v}} = E_{1\mathrm{c}} - E_{4\mathrm{v}}$. The definition for $q^{(4)}_n$ corresponds to Eq. (5.16).

5.3. Absorption into nS excitons at low temperatures

The absorption spectrum close to $T = 0\,\mathrm{K}$ yields the most detailed depiction of different absorption effects in Cu_2O. As we discussed in chapter 3, it is possible to excite P excitons up to very high principal quantum numbers, where novel physical properties are revealed, which were prior unseen in semiconductors. Similarly, a multitude of underlying phonon-assisted excitations can be determined. Their origin and proper theoretical description are required to improve the general comprehension of the absorption spectrum of Cu_2O around the band gap as a whole.

5.3.1. Considerations concerning different absorption strengths

At low temperatures, there exist no phonons in equilibrium, which can also be seen in the vanishing of the Bose-Einstein distribution in Eq. (5.7). Consequently, this reduces Eq. (5.19) to only one possible process, the transition into the yellow S state via a preceding emission of a phonon.
Another point of interest is the percentage of the different transitional channels. It was already mentioned previously that the impact of the 1S blue to nS yellow state transition is dominating in the absorption spectrum. This can easily be seen by investigating the ratio between the convolution coefficients of Eq. (5.11) with different intermediate principal quantum numbers n'. Considering that the energy difference between the blue energy states and the incoming light is larger than the blue series' Rydberg energy, the energy fraction can be assumed to be approximately one. The ratio of contribution strength is then approximately given by

$$\chi_{n;n',n''} = \frac{\mathcal{S}^{(\mathrm{y,b})}_{n,n'}}{\mathcal{S}^{(\mathrm{y,b})}_{n,n''}} \frac{n''^{3/2}}{n'^{3/2}} \,. \tag{5.22}$$

The ratios, although still dependent on the momentum $q_n^{(\lambda)}$, converge to maximal contributions. As an example, the ratio $\chi_{1;2,1}$ yields a maximal percentage of 12.3%, for $\chi_{1;3,1}$ it is 3.7%, and so forth. We notice that these values are close to the inverse of the third power of the principal quantum number n'. It turns out, the ratio for the contribution of intermediate S states can be approximated via an upper boundary $\chi_{n;n',n''} \lesssim (n''/n')^3$. This provides us with an easy estimation tool to assess which terms of the sum over the intermediate states n' are actually relevant. As the sum occurs within the quadrature, all squared terms except for the lowest, namely $n' = 1$, are already negligibly small; however, the mixed terms with $n' = 1$ are still of significant strength.
In a similar fashion one can analyse the ratios between the final yellow nS states. For a simplified analytical evaluation, we assume that exciton mass is constant for all final states and that binding energies are degenerate. The ratio of absorption strength between final states, thus, is approximated by

$$\frac{\alpha^{(3)}_{n_1,\mathrm{y}}}{\alpha^{(3)}_{n_2,\mathrm{y}}} \simeq \left| \frac{\sum_{n'} \mathcal{S}^{(\mathrm{y,b})}_{n_1,n'}}{\sum_{n''} \mathcal{S}^{(\mathrm{y,b})}_{n_2,n''}} \right|^2 \,. \tag{5.23}$$

Similar to Eq. (5.22), this ratio behaves asymptotically, with $(n_1/n_2)^3$ being an upper boundary. Therefore, the absorption strength of the 2S exciton state is expected to be maximal 12.5% of the 1S state. It is known from experiment [77, 78] and from our investigations in chapter 4, that the yellow 1S exciton mass differs considerably from the masses of the remaining series. As it will be seen in the upcoming sections, that difference of exciton mass will further inhibit the absorption strength of higher nS states.

5.3.2. Absorption into the yellow 1S exciton state

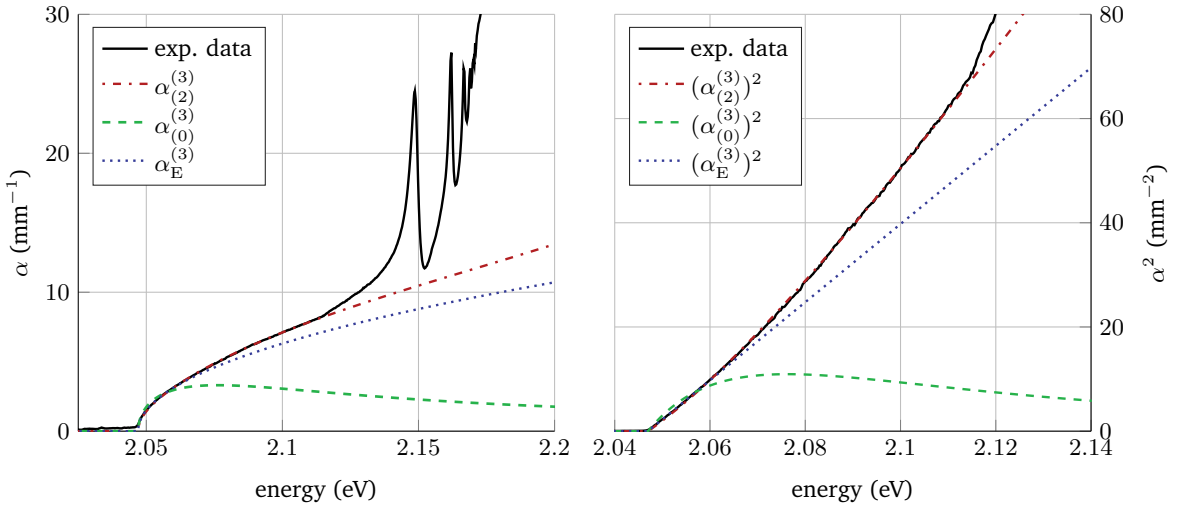

Figure 5.1.: Fit of the absorption coefficient to the experimental spectrum. The left figure scales linear with the absorption coefficient, the right one quadratically. The subscripts on the α's denote the fitted curve, with (2) indicating the use of Eq. (5.19) with a momentum dependent deformation potential, (0) uses a constant deformation potential and (E) uses the Elliott formula, as seen in Eq. (5.21) with a constant deformation potential. The data comes from a bulk Cu_2O sample ($\simeq 160\,\mu\mathrm{m}$ thickness) at $T = 2\,\mathrm{K}$ and are property of [108].

As mentioned before, the absorption edge of the Γ_3^- phonon into the 1S yellow exciton features a distinctive spectral shape. We will utilise this advantage to do a one time fit of Eq. (5.19) unto the experimental data, that consequently can be used to describe all Γ_3^- transitions. In Figs. 5.1 we show the resulting fit of the absorption edge under different circumstances. The absorption coefficient $\alpha^{(3)}_{(0)}$ uses Eq. (5.19) under the assumption of a constant deformation potential. It is immediately obvious, that the fit fails horrendously. The textbook solution derived from Elliott $\alpha^{(3)}_{(\mathrm{E})}$ [120] adapts well for a small region around the absorption edge, but it starts to deviate significantly for higher energies. Using Eq. (5.19) with a mometum dependent deformation potential as defined in Eq. (5.20), $\alpha^{(3)}_{(2)}$ provides a very good matching of the fit with the experimentally obtained spectral data. This is especially apparent in the right plot which scales the absorption coefficient quadratically. If the square root behaviour of the textbook solution would suffice, the absorption would display a linearly rising slope, which is definitely not the case. Additionally the squared plot amplifies the recognisability of the LO phonon absorption edge around $2.117\,\mathrm{eV}$.

From the fitted curve of $\alpha^{(3)}_{(2)}$ we are able to extract the deformation potential and its momentum dependence. The most necessary parameters can be found in appendix A.1. The Bohr radius of the blue excitons is not explicitly known; thus, for a systematic treatment they were calculated from the binding energies via $a_\mathrm{b} = \mathrm{Ry}\ a_\mathrm{B}/(\mathrm{Ry}^{(\mathrm{b})}\varepsilon_1) = 1.72\,\mathrm{nm}$, with Ry and a_B being the hydrogen Rydberg energy and Bohr radius, and the blue Rydberg energy being given by $\mathrm{Ry}^{(\mathrm{b})} = E_\mathrm{b} - E_{1\mathrm{Sb}} = 57\,\mathrm{meV}$. The dipole transition element of the blue exciton is related

to the oscillator strength by

$$\frac{f_{\mathrm{b}}}{\Omega_{\mathrm{uc}}} = \frac{2}{\hbar\omega}\frac{|p_{78}|^2}{m_0}\left|\varphi_{1\mathrm{S}}^{(\mathrm{b})}(0)\right|^2 = \frac{2}{\pi a_{\mathrm{b}}^3\,\hbar\omega}\frac{|p_{78}|^2}{m_0}\,, \tag{5.24}$$

with $\Omega_{\mathrm{uc}} = a_{\mathrm{L}}^3$ being the volume of the unit cell, and a_{L} the lattice constant. The oscillator strength was measured to be $f_{\mathrm{b}} = 1.2 \times 10^{-2}$ [124]. This yields for the dipole transition element

$$\frac{|p_{78}|^2}{m_0} = 2.726\,\mathrm{eV}\,. \tag{5.25}$$

However, this approach is cubically dependent on the blue excitons Bohr radius a_{b}, which is only roughly approximated. Therefore, we employ a second derivation to double check the result. The dipole transition element for the blue exciton series is related to the transition matrix element of the $\Gamma_{5\mathrm{v}}^{+}$ and $\Gamma_{3\mathrm{c}}^{-}$ band basis states by [70]

$$p_{78} = -\sqrt{\frac{2}{3}}\,\langle\varepsilon_3^+|\,\mathbf{p}\,|\gamma_2^-\rangle\,. \tag{5.26}$$

The transition matrix element between those bands also occurs in $\mathbf{k}\cdot\mathbf{p}$ theory, as can be seen in appendix B.1.1 [cf. Eqs. (B.3)]. The required parameter G describes the coupling of all Γ_3^- bands to the respective $\Gamma_{5\mathrm{v}}^{+}$ band. In appendix B.1.3 the parameter G was determined under the assumption that no Γ_2^- band is present close to the $\Gamma_{5\mathrm{v}}^{+}$ band. As there is also only one Γ_3^- band in the vicinity of the $\Gamma_{5\mathrm{v}}^{+}$ band, the coupling coefficient G can be associated with the matrix element in Eq. (5.26), hence

$$\frac{|p_{78}|^2}{m_0} = 2.662\,\mathrm{eV}\,. \tag{5.27}$$

Both results are in fairly good agreement. For the estimation of the static deformation potential, we use Eq. (5.27). The resulting fit parameters for the deformation potential of the Γ_3^- phonon-assisted absorption are

$$D_{3;68}^{(0)} = 25.45\,\frac{\mathrm{eV}}{\mathrm{nm}}\,, \tag{5.28}$$

$$\bar{D}_{3;68}^{(2)} = 0.168\,\mathrm{nm}^2\,. \tag{5.29}$$

The value for the static deformation potential $D_{3;68}^{(0)}$ is in well accordance to previous estimations [38, 125].

With the fit of Γ_3^- phonon-assisted absorption into the yellow $1\mathrm{S}$ state, we are able to assess the absorption edge up to the yellow $2\mathrm{P}$ exciton resonance, now the next goal will be to reproduce the absorption spectrum beyond that.

5.3.3. Absorption beyond the yellow 1S exciton

The obtained deformation potential is independent of principal quantum number; hence, it can be immediately used to obtain the absorption edge of the yellow $n \geq 2\mathrm{S}$ states. However, we already discussed in section 5.3.1 that, although their contribution seems not negligible, their impact on the actual absorption spectrum is minor. The major advantage of fitting the Γ_3^- phonon-assisted transition to the yellow exciton is the fact, that it inherently contains the transition to the green series. Since both stem from the Γ_{5v}^+ band which only subsequently splits via spin-orbit interaction into $\Gamma_{7\mathrm{v}}^+$ and $\Gamma_{8\mathrm{v}}^+$, the transitions of both series' are connected. Analysing the symmetry of the individual valence band states via group theory [70] yields for the oscillator strengths the relation

$$f_{\mathrm{y,b}}^{(3)} : f_{\mathrm{g,v}}^{(3)} \;=\; 1 : 2\,. \tag{5.30}$$

The exact derivation can be found in appendix B.3. Thus, we receive the Γ_3^- phonon-assisted absorption edge of the green Γ_5^+ orthoexciton.
We will now attempt to depict the absorption spectrum beyond the yellow band gap E_{y}. To achieve this, we additionally require the absorption participations of the Γ_4^- phonon-assisted transition, as well as the yellow P absorption. The treatment of both is done in appendix B.4. The total absorption coefficient only requires the absorption channels that significantly participate and is therefore composed of

$$\alpha_{\mathrm{tot}} = \alpha_{1,\mathrm{y}}^{\Gamma_3^-} + \alpha_{2,\mathrm{y}}^{\Gamma_3^-} + \alpha_{1,\mathrm{g}}^{\Gamma_3^-} + \alpha_{1,\mathrm{y}}^{\Gamma_4^-} + \alpha_{1,\mathrm{g}}^{\Gamma_4^-} + \alpha_{\mathrm{P}}\,. \tag{5.31}$$

α_{P} conglomerates all absorption contributions of the yellow P absorption. The remaining parameters needed to evaluate α_{tot} are listed in appendix A.1. The green and violet Bohr radii are obtained in the same fashion, as it was done for the blue exciton. The yellow 2S exciton mass stems from the sum of effective electron and hole mass. Due to the almost equal binding energy of the yellow 1S paraexciton and the green 1S orthoexciton, and since they experience the same screening, it is expected that both masses are about equal. The different contributions as well as the sum α_{tot} in comparision to the experimental data can be seen in Fig. 5.2.

5.3.4. Discussion

We recognise that, as expected, the absorption spectrum is mainly constructed out of the Γ_3^- phonon-assisted transition of the yellow and green 1S exciton state, as well as the excitonic resonances and the absorption into the continuum at the band edge. The theoretical result is in unison with the data up to the yellow band gap E_{y}; however, a few remarks need to be made for the upper energy range. At an energy range around $2.2\,\mathrm{eV}$ the summed up absorption coefficient α_{tot} appears to slightly overestimate the absorption, beyond $2.22\,\mathrm{eV}$ the experimentally

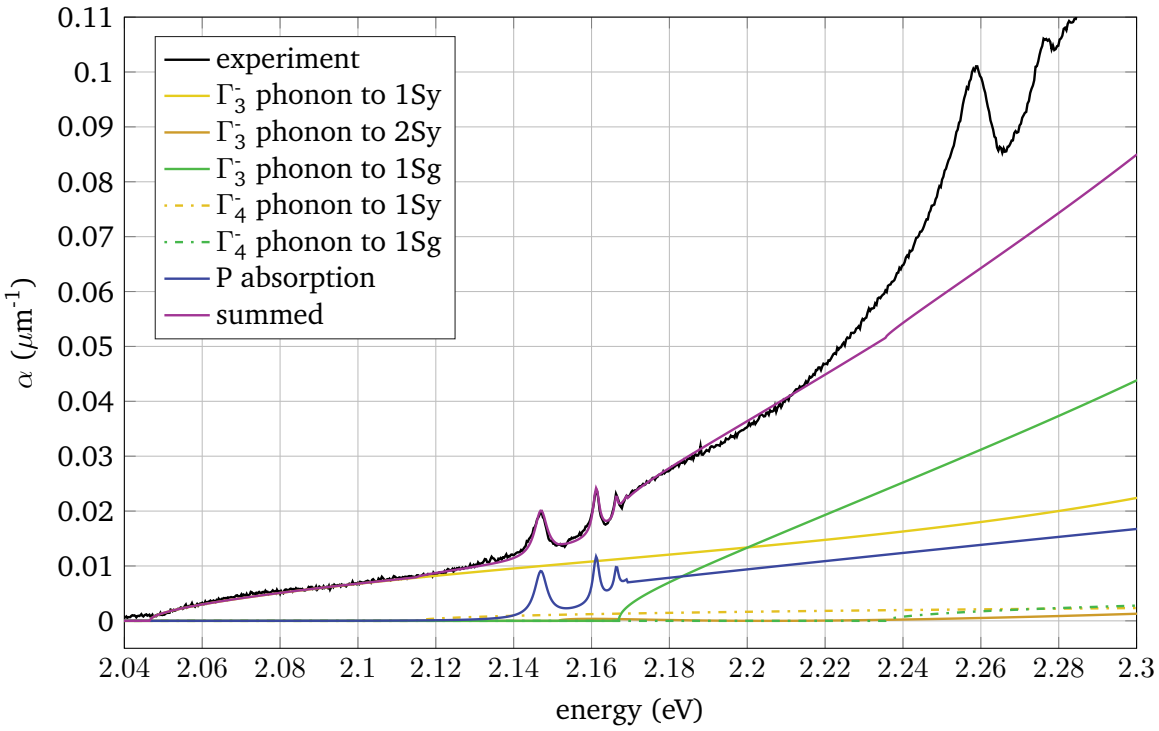

Figure 5.2.: Depiction of the experimental data, all individually participating absorption channels and the sum of them. The experiments were made in a Cu_2O sample of around $10\,\mu\mathrm{m}$ thickness at $T = 2\,\mathrm{K}$ and are property of [108].

measured spectrum shows a steady increase in the absorption slope that is not reproducable in this theory.

The overshot of the theoretical result around $2.2\,\mathrm{eV}$ is most likely linked to an overestimation of the phonon-assisted absorption into the green 1S state. The issue in extrapolating the result of the yellow 1S exciton to the green 1S exciton is the fact that two of the essential exciton parameters are not explicitly known. The excitonic Bohr radii used throughout this work, except for the yellow 1S exciton, are all extracted from their respective binding energies. They play an important role in the overlap integrals in Eq. (5.11). The other parameters that influence the strength of the absorption significantly are the exciton translational masses. While the mass of the yellow 1S state was determined experimentally [109], it is not known for the 2S yellow and the green exciton states. Excitons with large principal quantum numbers are composed of valence and conduction band states near the zone centre; thus, the approximation $M_\mathrm{X} = m_\mathrm{c} + m_\mathrm{v}$ is considered valid to estimate the mass of the yellow 2S state. The wave function of the green 1S state extends due to its large binding energy far into the Brillouin zone. The influence of the nonparabolicity of the Γ_8^+ valence bands on effective mass and Bohr radius are therefore expected to be similar to that for the yellow 1S exciton. Arguing with a heuristical relation between binding energy and translational mass to the yellow paraexci-

ton, we approximated the mass to be of similar size. All these quantities are just first order approximations, and will require extensive future work to improve.

Next, we shall discuss the steady increase of absorption in the region around $2.22\,\mathrm{eV}$. This cannot be explained by the choice of parameters or the wave function used. It could be explained by introducing additional absorption channels, e.g. additional phonon interactions or exciton resonances. However, several points argue against this suggestion. The Γ_5^+ phonon resonance would be the only phonon with a suitable energy to compensate the missing absorption (cf. Tab. 2.3). This possibility can be ruled out, since the phonon process must also occur in comparable strength for the yellow 1S state, which could not be identified in the analysis. Additionally, it possesses the wrong parity. The existence of a potential light hole green exciton series was considered, but no such additional exciton series should exist since the Γ_8^+ valence bands are heavily coupled [19]. Both concepts also seem improbable, as the increase of the slope appears to be continuous, while an additional phonon-assisted absorption edge should rise up abruptly in the spectrum.
The most logical explanation is a dependence of excitonic parameters on exciton momentum. As we have seen in chapter 4, both, exciton mass and Bohr radius of the 1S paraexciton potentially possess an, albeit small, momentum dependence. If the orthoexciton mass is expected to steadily increase with exciton momentum, a smooth increase in phonon-assisted absorption with photon energy should be observed [cf. Eq. (5.16)], as it can be seen in the experiment. A similar effect is expected, if the green exciton Bohr radius increases, as the overlap functions would increase [cf. Eq. (5.11)].

Finally, the topic of mixing between yellow and green exciton states needs to be addressed. In a recent study of the even exciton series in Cu_2O [25] the lowest orthoexciton resonance is a mixture of yellow and green states with 7.2% green contribution. If we take this into account in our analysis, this would require the redetermination of the deformation potential $D_{3;68}$ in the low energy part of the spectrum, but the correction is expected to be only on the order of some percent due to the low green admixture. The influence of mixing on the absorption of the yellow 2S and the green 1S state should be much more noticeable. The first has supposedly more than 10% of green contributions, which would enhance its absorption strength considerably and potentially overestimate its absorption contribution. The green 1S state, on the other hand, would only show a green percentage of about 40%, which should result in about half the absorption strength. Both effects are not consistent with the experimental data. A systematic analysis, however, would require the full wavefunctions of these exciton states.

5.4. Absorption of the yellow 1S exciton at high temperatures

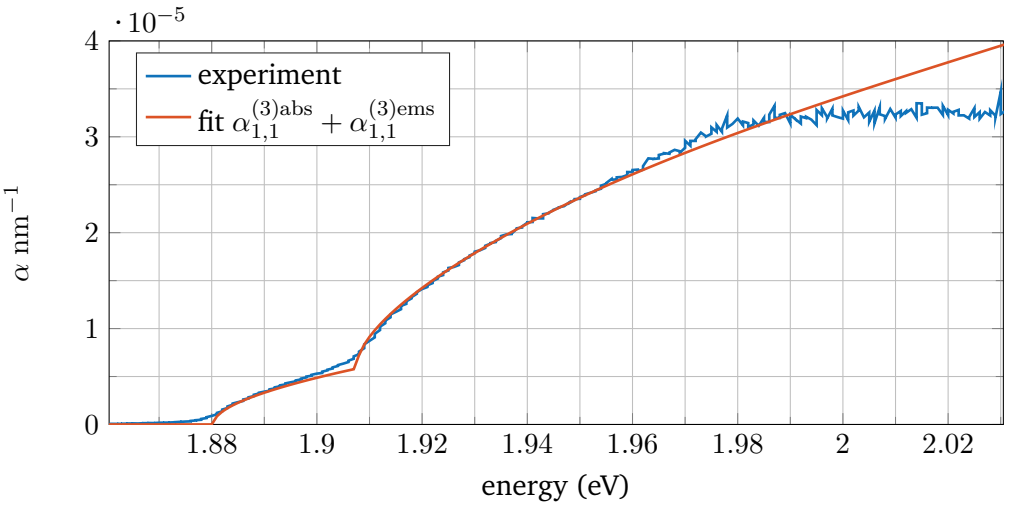

Figure 5.3.: Absorption edge of a Cu_2O sample of thickness $220\,\mu\mathrm{m}$ at room temperature [126]. The two Γ_3^- absorption steps are clearly visible until the saturation of the spectrum.

In this section, we shortly take another look at the same problem for higher temperatures. At room temperature, the absorption spectrum is usually not of much interest, since it is generally not favorable to validate (or invalidate for that matter) novel theories or concepts. We are only able to see the Γ_3^- phonon-assisted absorption edge. At these temperatures there is an additional absorption step from the phonon-absorption process which is nonexistent at lower temperatures. In Fig. 5.3 the absorption edge at room temperature and the fit of the Γ_3^- absorption into the yellow $1\mathrm{S}$ state is shown. The resulting parameters for Eq. (5.19) are

$$D_{3;68}^{(0)} = 32.21\,\frac{\mathrm{eV}}{\mathrm{nm}}\,, \tag{5.32}$$

$$\bar{D}_{3;68}^{(2)} = 0.179\,\mathrm{nm}^2\,. \tag{5.33}$$

While the momentum dependence of the deformation potential barely changes and the difference to Eq. (5.29) is almost within the uncertainty of the fitting procedure, the static deformation potential shows a significant increase of about 26% to its low temperature counterpart in Eq. (5.28). On one hand, this could imply that the deformation potential possesses an intrinsic temperature dependence that might be based on the dilation of the crystal. On the other hand, the transition dipole matrix element we consulted is technically only valid in the low temperature regime and a change of the polarisability of Cu_2O could lead to an increase of said dipole matrix element. In the latter case, the static deformation potential might as well be close to temperature independent, and the result of Eq. (5.32) should be taken with a grain of salt. A red shift of the band gap about $\Delta E_{\mathrm{rs}} \simeq 140\,\mathrm{meV}$ is observed as well. This is to be expected due to the dilation of the crystal and the associated change of crystal constants.

5.5. Conclusion

The presented theory for describing the phonon-assisted absorption works pretty well for the yellow exciton series and the experimental absorption edge up to the yellow $2\mathrm{P}$ resonance can be properly reproduced. Comparision to the textbook solution suggests that the assumption of excitonic intermediate states instead of Bloch states provides the superior description of the absorption background. However, this only holds true as long as the momentum dependence of the deformation potential is not neglected. Still, the derived result improves the description of the phonon-assisted absorption while keeping the elegance of an analytical solution. In regard to the intermediate state we came to the conclusion that the $1\mathrm{S}$ state contributes the dominant part of the spectrum. The fitted value for the static deformation potential is in good agreement with earlier estimations [38, 125].
Beyond the Γ_3^- phonon transition, the fit of the other absorption terms is treated on a basic level; however, this is nonproblematic since the main goal of this chapter was to improve upon the description of the phonon-assisted absorption as it was derived by Elliot [120], which can be achieved by treating the Γ_3^- process by itself. Furthermore, it was shown that the Γ_3^- phonon processes dominate the absorption background; hence, a rough depiction of the other absorption channels is sufficient.
The reproduction of the absorption spectrum works well up to the yellow band gap. In higher energy regions the imprecise knowledge of excitonic translational masses and Bohr radii, as well as a potential momentum dependence of these parameters leads to significant deviations. Theoretically, the radii and masses can be obtained from the solution of the momentum-dependent effective mass equations. Experimentally, the masses can be obtained from resonance Raman studies involving the green P and the green 1S states, similar to that reported in [26, 27] for the yellow exciton states. Here, especially Raman processes involving acoustical phonons are of interest, since their Raman shift depends on their momentum, thus giving directly the dispersion of the green 1S states.
The estimated fits of the deformation potential will be further utilised in the next chapter to determine the phonon-assisted Auger decay.

Chapter 6.

Auger decay of excitons

Around a hundred years ago, S. Bose and A. Einstein postulated one of the most fundamental quantum phenomena, the macroscopic occupation of the same momentum state by multiple particles with integer spin [127, 128]. Beyond critical values for particle density and temperature, the macroscopic occupation of the ground state occurs, which is fittingly named Bose-Einstein Condensation (BEC). Ever since their groundbreaking theoretical work there has been a thriving effort to create and research this specific particle state experimentally. Even though the first successful observation of a BEC was realized in atomic gases [129,130], for a long time excitons in semiconductors were deemed to be a more suitable system [32, 33]. Bose-Einstein statistics predict, that the critical temperature is inversely proportional to particle mass. Since the hole effectively substitutes for the atomic core, exciton masses are considerably smaller than atomic mass. Therefore, excitons provide experimentalists allegedly with an ideal setting for measuring a BEC, predicting the critical temperature required to be several orders of magnitude higher than for atomic systems. The sufficient temperature for condensation was initially assumed to be around a few Kelvin [131]. Despite that assumption no explicit proof for the existence of excitonic BECs has been experimentally found in bulk semiconductors up to this point.

One particular effect that is accused to inhibit the formation of an excitonic BEC is the non-radiative Auger decay [38, 40]. The collision between two excitons leads to a recombination of one exciton and the ionisation into a high-energy electron-hole pair. This increases the systems mean temperature as well as decreasing exciton density, hence doubly counteracting the necessary experimental requirements to achieve condensation. The attempt to find a suitable theoretical explanation for this excitonic Auger decay will be the focus of this chapter. The result for the phonon-assisted Auger decay is published as a part of [132].

6.1. Theoretical preliminaries

We consider a system that primarily consists of yellow 1S excitons. The paraexcitons possess an extraordinarily long lifetime[1] in the range of hundreds of nanoseconds (in a strain induced potential trap [36, 133, 134]) up to a few microseconds [96] and, thus, represent an ideal excitonic ground state for supposed condensation. Auger decay can occur in two distinct channels that will be addressed separately.

The first is the direct Auger decay mechanism, which is the most rudimentary transition. It can be visualised as the collision of two excitons, leading to the recombination of one exciton and transfering the generated excess energy to the second participant which, in consequence, gets ionised. In consideration of a system of exclusively yellow 1S excitons, the occurence of this event is improbable. As known from section 2.3, orthoexciton recombination is only quadrupole allowed, while paraexcitons in bulk Cu_2O are not able to recombine without additional interactions.

The second decay channel is the phonon-assisted Auger decay. In this case, upon collision one exciton enters a virtual intermediate state via emission of a phonon, which then recombinates and subsequently ionises the other exciton. Preceding theoretical works [38, 125, 135] already illustrated that the share of directly recombining S excitons in Cu_2O via Auger scattering has to be several orders of magnitude smaller than the phonon-assisted process. However, their results for the phonon-assisted Auger process still deviate several orders of magnitude from experimentally estimated values. This originates from two approximations which can not neccessarily be rectified:

1. Previous calculations drop the exciton wave function of the intermediate states, including the associated wave vectors, for the sake of simplicity.

2. The deformation potential $D_{\lambda,ij}$ of the phonon interaction is most of the time assumed to vary sufficiently slow to be considered constant. As it was shown in the previous chapter, it can be dependent on the phonon wave vector $\mathbf{Q}$ to a non-negligible degree.

The considerations in this chapter lean on the derivations of the beforementioned theoretical calculations, but additionally will take these two points into consideration. The starting point is Fermi's golden rule

$$P_{i,f} = \frac{2\pi}{\hbar} |M_{i,f}|^2 \, \delta\left(E_i - E_f\right) \, . \tag{6.1}$$

Most generally, for the direct recombination process the matrix element simply reads as

$$M_{i,f}^{(\mathrm{d})} = \langle \Psi_f | V_{\mathrm{eff}} | \Psi_i \rangle \, . \tag{6.2}$$

[1] One could say paraexcitons in Cu_2O "Live long and prosper." - L. Nimoy *Star Trek*, S2E1 (1968).

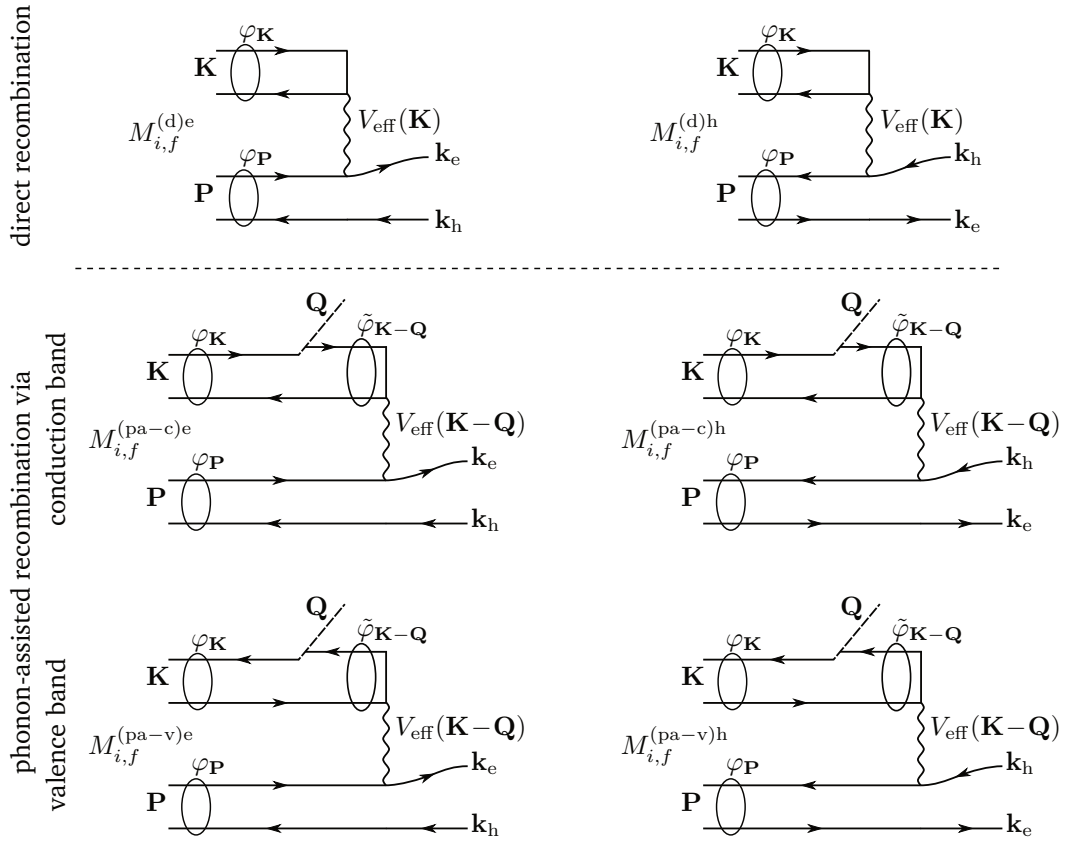

Figure 6.1.: Feynman diagrams of the different possibilites for Auger decay via direct and phonon-assisted recombination. Lines going forward correspond to electrons, backwards lines to holes. Circles suggest the formation of an exciton with the associated envelope function $\varphi_{\mathbf{k}}$.

The expression for the phonon-assisted Auger decay results from second order perturbation theory as

$$M_{i,f}^{(\mathrm{pa})} = \sum_{\lambda,\nu} \frac{\langle \Psi_f | V_{\mathrm{eff}} | \Psi_\lambda \rangle \langle \Psi_\lambda | h_{\nu,\mathbf{Q}} | \Psi_i \rangle}{E_i - E_\lambda} = \sum_{\lambda,\nu} \frac{M_{\lambda,f}^{(\mathrm{d})} \langle \Psi_\lambda | h_{\nu,\mathbf{Q}} | \Psi_i \rangle}{E_i - E_\lambda} \,. \tag{6.3}$$

In our system, the initial state Ψ_i consists of two yellow 1S excitons with momentum $\mathbf{K}$ and $\mathbf{P}$ whereby the $\mathbf{K}$ exciton needs to be an orthoexciton. The energy transfer of the recombinated exciton is treated via the effective Coulomb potential V_{eff}. The final state Ψ_f consists of the ionised components of the yellow $\mathbf{P}$ exciton, i.e. an electron in the conduction band Γ_6^+ and a hole in valence band Γ_7^+. The Hamiltonian $h_{\nu,\mathbf{Q}}$ represents the phonon interaction, with ν denoting the phonon branch and $\mathbf{Q}$ being the phonon momentum. In the intermediate state Ψ_λ the yellow $\mathbf{K}$ exciton is transformed into a virtual λ state exciton with momentum $\mathbf{K} - \mathbf{Q}$. In Fig. 6.1 the direct and the phonon-assisted processes are visualised by means of Feynman diagrams. Since electron and hole of exciton $\mathbf{P}$ scatter independently, the energy is always only transfered to one of them. Therefore, we need to distinguish between two

cases. The phonon-assisted process has two additional processes for either the conduction or valence band interacting with the phonon ν. However, as we will see in the upcoming section, the only relevant intermediate state belongs to the blue exciton series which corresponds to a transition between conduction bands, so the valence band processes are only listed for the sake of completion.

6.1.1. Symmetry considerations

The symmetry considerations for the phonon-assisted recombination are analogue to the symmetry treatment done in section 5.1.1, and will only be summarised shortly.
The possibilites for phonon transition of orthoexcitons are set by $\Gamma_2^- \oplus \Gamma_3^- \oplus \Gamma_4^- \oplus \Gamma_5^-$, while paraexcitons are limited to Γ_5^-. Approximated coupling rates between possible phonons and our respective exciton states are known experimentally from luminesence spectroscopy [81]. They reveal that the Γ_3^- phonon provides the dominant coupling term to the orthoexciton and that the Γ_3^- phonon coupling is around 500 times stronger than the coupling of the paraexciton to the Γ_5^- phonon. For this reason, we will only include the Γ_3^- phonon scattering of orthoexcitons. This subsequently restricts the amount of intermediate terms. In chapter 5, we have seen that the blue excitons provide a significant contribution to the phonon-assisted absorption. They are comprised of the transition between the $\Gamma_{3\mathrm{c}}^-$ and $\Gamma_{5\mathrm{v}}^+$ bands, and, thus, possess dipole allowed transition states. Also, as seen in section 2.1, the $\Gamma_{3\mathrm{c}}^-$ band is decisively the band closest to the band gap E_y, and since the transition strength is inversely proportional to $E_i - E_\lambda$ [cf. Eq. (6.3)], they represent ideal intermediate states.
For the direct scattering process, we will Taylor expand the Bloch functions in the upcoming section. The emerging intermediate Bloch functions are required to obey the symmetry products of dipole operator with initial and final state. Both only share the common symmetry of Γ_4^-; hence, we only need to consider the coupling to bands with Γ_4^- symmetry.
In the next section, we start out with a short description of the direct scattering process to depict the general ansatz for treatment and then discuss the phonon-assisted scattering in more detail.

6.2. Direct Auger scattering matrices

In the following, we will give a short résumé of the derivation of the direct scattering matrix element $M_\mathrm{y}^{(\mathrm{d})}$, an in-depth derivation of the different transition matrix elements is given by [38]. The initial transition matrix elements as seen in Fig. 6.1 read as

$$M_\mathrm{y}^{(\mathrm{d})\mathrm{e}} = \sum_{\mathbf{q}} V_\mathrm{eff}(\mathbf{K})\, \varphi_{\mathbf{q}}^{(\mathrm{y})}\, \varphi_{\mathbf{k}_\mathrm{h}-\mathbf{P}/2}^{(\mathrm{y})} \langle u_{7\mathrm{v},\mathbf{q}-\mathbf{K}/2} | u_{6\mathrm{c},\mathbf{q}+\mathbf{K}/2} \rangle \langle u_{6\mathrm{c},\mathbf{k}_\mathrm{e}} | u_{6\mathrm{c},\mathbf{k}_\mathrm{e}+\mathbf{K}} \rangle\, \delta_{\mathbf{k}_e+\mathbf{k}_h,\mathbf{K}+\mathbf{P}}\,, \qquad (6.4)$$

for the transfer of the energy to the electron and

$$M_{\mathrm{y}}^{(\mathrm{d})\mathrm{h}} = -\sum_{\mathbf{q}} V_{\mathrm{eff}}(\mathbf{K})\, \varphi_{\mathbf{q}}^{(\mathrm{y})}\, \varphi_{\mathbf{k}_\mathrm{e}-\mathbf{P}/2}^{(\mathrm{y})} \langle u_{7\mathrm{v},\mathbf{q}-\mathbf{K}/2} | u_{6\mathrm{c},\mathbf{q}+\mathbf{K}/2} \rangle \langle u_{7\mathrm{v},\mathbf{k}_\mathrm{h}} | u_{7\mathrm{v},\mathbf{k}_\mathrm{h}+\mathbf{P}} \rangle\, \delta_{\mathbf{k}_e+\mathbf{k}_h,\mathbf{K}+\mathbf{P}}\,, \quad (6.5)$$

for the transfer to the hole. The sign changes due to the interaction of the Coulomb potential with the electron or hole, respectively. The $u_{6\mathrm{c},\mathbf{k}_i}$, $u_{7\mathrm{v},\mathbf{k}_j}$ are the periodic functions of the $\Gamma_{6\mathrm{c}}^{+}$ and $\Gamma_{7\mathrm{v}}^{+}$ bands, respectively. We can restrict the calculations to one conduction and one valence band due to the orthogonality of the Bloch states for different bands. In both equations, the first ovelap integral of the periodic functions illustrates the recombination process of the exciton with momentum $\mathbf{K}$. The second overlap integral is the transfer of momentum to the electron (or hole, respectively) of the second exciton $\mathbf{P}$. The $\varphi_{\mathbf{k}}^{(i)}$ are the 1S envelope wave functions in momentum space[2].

In order to effectively utilise these matrix elements, we need to employ a few approximations. The magnitude of the exciton momenta $\mathbf{K}$ and $\mathbf{P}$ is determined by the thermal energy of the system, while the momenta of the isonised particles is in the range of the energy gap due to the absorption of the excess energy of the recombination. We consider a low temperature system, i.e. the exciton momenta are negligible compared to the ionised particles momenta $|\mathbf{k}_\mathrm{e}|, |\mathbf{k}_\mathrm{h}| \gg |\mathbf{K}|, |\mathbf{P}|$. This allows us to expand the Bloch wave functions according to $\mathbf{k}\cdot\mathbf{p}$ theory. It should be noted that Eqs. (6.4) and (6.5) only account for processes within the first Brillouin-zone. Processes that reach beyond that are called Umklapp-processes and need to be treated separately. However, the assumption of small exciton momentum at low temperatures also allows us to consider them to be negligibly small [38]. For the evaluation of the overlap integrals we perform a Taylor expansion similar to Eq. (2.2) and receive

$$|u_{i,\mathbf{q}+\mathbf{K}/2}\rangle \simeq |u_{i,\mathbf{q}}\rangle + \frac{\hbar}{2m_0} \sum_{j\neq i} \frac{\langle u_{j,\mathbf{q}} | \mathbf{K}\cdot\mathbf{p} | u_{i,\mathbf{q}} \rangle}{E_i(\mathbf{q}) - E_j(\mathbf{q})} |u_{j,\mathbf{q}}\rangle + \dots\,. \quad (6.6)$$

Applying this to Eqs. (6.4) and (6.5) they simplify accordingly. For the first overlap element, the expansion results in

$$\langle u_{7\mathrm{v},\mathbf{q}-\mathbf{K}/2} | u_{6\mathrm{c},\mathbf{q}+\mathbf{K}/2} \rangle = \frac{\hbar^2}{4m_0^2} \sum_{i\neq 6\mathrm{c},7\mathrm{v}} \frac{\langle u_{7\mathrm{v},q} | \mathbf{K}\cdot\mathbf{p} | u_{i,q} \rangle \langle u_{i,q} | \mathbf{K}\cdot\mathbf{p} | u_{6\mathrm{c},q} \rangle}{(E_{7\mathrm{v}}(\mathbf{q}) - E_i(\mathbf{q}))\,(E_{6\mathrm{c}}((\mathbf{q}) - E_i(\mathbf{q}))}\,, \quad (6.7)$$

as the lowest order term that does not vanish due to orthogonality and conservation of parity. The second overlap element is considered to be approximately one. This is justified by the ionised particle momentum being at least one order of magnitude larger than the exciton momentum. Additionally, higher order terms partly vanish due to orthogonality of the periodic functions. Since the matrix elements of Eqs. (6.4) and (6.5) are additive we can combine both

[2] Since we only treat 1S excitons in this chapter, the 1S subscript is dropped to enhance readability.

processes into a single one

$$\begin{aligned} M_{\mathrm{y}}^{(\mathrm{d})} =& M_{\mathrm{y}}^{(\mathrm{d})\mathrm{e}} + M_{\mathrm{y}}^{(\mathrm{d})\mathrm{h}} \\ =& \frac{\hbar^2}{4m_0^2}\, V_{\mathrm{eff}}(\mathbf{K}) \sum_{\mathbf{q}} \varphi_{\mathbf{q}}^{(\mathrm{y})} \sum_{i\neq 6\mathrm{c},7\mathrm{v}} \frac{\langle u_{7\mathrm{v},q}|\mathbf{K}\cdot\mathbf{p}|u_{i,q}\rangle \langle u_{i,q}|\mathbf{K}\cdot\mathbf{p}|u_{6\mathrm{c},q}\rangle}{(E_{7\mathrm{v}}(\mathbf{q}) - E_i(\mathbf{q}))\,(E_{6\mathrm{c}}((\mathbf{q}) - E_i(\mathbf{q}))} \\ & \times \underbrace{\left[\varphi^{(\mathrm{y})}_{\mathbf{k}_\mathrm{e}-\mathbf{P}/2-\mathbf{K}} - \varphi^{(\mathrm{y})}_{\mathbf{k}_\mathrm{e}-\mathbf{P}/2}\right]}_{\simeq(\mathbf{K})\cdot\frac{\partial\varphi^{(\mathrm{y})}_{\mathbf{k}}}{\partial\mathbf{k}}\big|_{\mathbf{k}_\mathrm{e}-\mathbf{P}/2\simeq\mathbf{k}_\mathrm{e}}} \delta_{\mathbf{k}_\mathrm{e}+\mathbf{k}_\mathrm{h};\mathbf{K}+\mathbf{P}}\,. \end{aligned} \tag{6.8}$$

In this case the delta distribution was utilised to redistribute the momentum dependence of one of the yellow envelope functions. In accordance to the rest of this work, we assume that the modified hydrogen wave functions suffice the exciton envelope wave functions. The hydrogen-like exciton wave function in momentum space was introduced in Eq. (4.5). In the case of the 1S exciton it is known as

$$\varphi_{\mathbf{k}}^{(i)} = \sqrt{\frac{a_i^3\,\pi}{\Omega}}\,\frac{8}{(1+a_i^2\,k^2)^2}\,, \tag{6.9}$$

while its derivative is given as

$$\frac{\partial\varphi_{\mathbf{k}}^{(i)}}{\partial\mathbf{k}} = -\sqrt{\frac{a_i^3\,\pi}{\Omega}}\,\frac{32\,a_i^2\mathbf{k}}{(1+a_i^2\,k^2)^3}\,. \tag{6.10}$$

The effective Coulomb potential in momentum space is

$$V_{\mathrm{eff}}(\mathbf{K}) = -\frac{\mathrm{e}^2}{\Omega\,\varepsilon_0\varepsilon_\mathrm{r}\mathbf{K}^2}\,. \tag{6.11}$$

In this case, the permittivity corresponds again to the low frequency limit $\varepsilon_\mathrm{r} = \varepsilon_1$.
To be able to evaluate Eq. (6.8) any further, we assume the dipole transition elements to be (almost) constant over the whole range of $\mathbf{q}$. Furthermore, the energy difference between the bands far exceeds the energy difference imposed by the curvature of the bands themselves; hence, we drop the $\mathbf{q}$ dependence of the energy denominator. The sum can be written in integral form [cf. Eq. (3.7)], which simplifies to

$$\begin{aligned} &\sum_{\mathbf{q}} \varphi_{\mathbf{q}}^{(\mathrm{y})} \sum_{i\neq 6\mathrm{c},7\mathrm{v}} \frac{\langle u_{7\mathrm{v},\mathbf{q}}|\mathbf{K}\cdot\mathbf{p}|u_{i,\mathbf{q}}\rangle \langle u_{i,\mathbf{q}}|\mathbf{K}\cdot\mathbf{p}|u_{6\mathrm{c},\mathbf{q}}\rangle}{(E_{7\mathrm{v}}(\mathbf{q}) - E_i(\mathbf{q}))\,(E_{6\mathrm{c}}((\mathbf{q}) - E_i(\mathbf{q}))} \\ &\qquad \simeq \sum_{i\neq 6\mathrm{c},7\mathrm{v}} \frac{(\mathbf{K}\cdot\mathbf{p}_{7\mathrm{v},i})\,(\mathbf{K}\cdot\mathbf{p}_{i,6\mathrm{c}})}{\Delta E_{7\mathrm{v}i}\,\Delta E_{i6\mathrm{c}}} \sum_{\mathbf{q}} \varphi_{\mathbf{q}}^{(\mathrm{y})} = \sqrt{\frac{\Omega}{\pi a_\mathrm{y}^3}} \sum_{i\neq 6\mathrm{c},7\mathrm{v}} \frac{(\mathbf{K}\cdot\mathbf{p}_{7\mathrm{v},i})\,(\mathbf{K}\cdot\mathbf{p}_{i,6\mathrm{c}})}{\Delta E_{7\mathrm{v}i}\,\Delta E_{i6\mathrm{c}}}\,, \end{aligned} \tag{6.12}$$

with $\mathbf{p}_{i,j} = \langle u_{i,0}|\mathbf{p}|u_{j,0}\rangle$ and ΔE_{ij} being the energy difference between bands at $\mathbf{q} = 0$. Then Eq. (6.8) takes its final form as

$$M_{\mathrm{y}}^{(\mathrm{d})} = \frac{2^3 a_{\mathrm{y}}^2 \mathrm{e}^2 \hbar^2}{m_0^2 \Omega \varepsilon_0 \varepsilon_{\mathrm{r}}} \frac{\mathbf{K}\cdot\mathbf{k}_{\mathrm{e}}}{(1+a_{\mathrm{y}}^2 k_{\mathrm{e}}^2)^3} \sum_{i\neq 6\mathrm{c},7\mathrm{v}} \frac{(\mathbf{K}\cdot\mathbf{p}_{7\mathrm{v},i})\,(\mathbf{K}\cdot\mathbf{p}_{i,6\mathrm{c}})}{K^2\;\Delta E_{7\mathrm{v}i}\;\Delta E_{i6\mathrm{c}}}\;\delta_{\mathbf{k}_{\mathrm{e}}+\mathbf{k}_{\mathrm{h}};\mathbf{K}+\mathbf{P}}\,. \tag{6.13}$$

The summation includes all band states that couple to both, conduction and valence band, via the momentum operator $\mathbf{p}$. As mentioned in the previous section, the symmetry of initial and final state limit the coupling states i to bands with Γ_4^- symmetry[3].
Before we proceed with the determination of the decay rate, we shall investigate the transition matrix element of the phonon-assisted process.

6.3. Phonon-assisted Auger scattering matrices

As it can be seen in Eq. (6.3), the recombination part of the phonon-assisted matrix element can be expressed in terms of a direct recombination matrix. Hence, one could initially assume we already treated one half of the phonon-assisted process with the derivation of the previous section. However, the alteration of one exciton state by the phonon interaction modifies the system sufficiently enough to prevent us from simply adopting the result of the previous section. We shortly revise the derivation of the direct recombination part before analysing the phonon interaction.

6.3.1. Direct recombination process

As it can be seen in Fig. 6.1, the emission of a phonon transfers one of the excitons into an intermediate exciton state. In section 6.1.1 we discussed the candidates for these intermediate states and concluded that the blue exciton is preferential. Therefore, we now examine the direct Auger scattering process between a blue and a yellow exciton. The initial matrix elements of this direct recombination process vary slightly from the ones shown in Eq. (6.4) and (6.5). We consider

$$\begin{aligned} M_{\mathrm{b}}^{(\mathrm{d})\mathrm{e}} = &\sum_{\mathbf{q}} \varphi^{(\mathrm{y})}_{-\mathbf{k}_{\mathrm{h}}+\mathbf{P}/2}\; V_{\mathrm{eff}}(\mathbf{K}-\mathbf{Q})\; \varphi^{(\mathrm{b})}_{\mathbf{q}-(\mathbf{K}-\mathbf{Q})/2} \\ &\times \langle u_{7\mathrm{v},\mathbf{q}-(\mathbf{K}-\mathbf{Q})/2}|u_{8\mathrm{c},\mathbf{q}+(\mathbf{K}-\mathbf{Q})/2}\rangle \langle u_{6\mathrm{c},\mathbf{k}_{\mathrm{e}}}|u_{6\mathrm{c},\mathbf{k}_{\mathrm{e}}-(\mathbf{K}-\mathbf{Q})}\rangle\; \delta_{\mathbf{k}_{\mathrm{e}}+\mathbf{k}_{\mathrm{h}},\mathbf{K}-\mathbf{Q}+\mathbf{P}}\,, \end{aligned} \tag{6.14}$$

[3] In contrast to [38, 135], who claim that the Γ_3^- conduction band plays an important role for the direct Auger process.

and

$$M_{\mathrm{b}}^{(\mathrm{d})\mathrm{h}} = \sum_{\mathbf{q}} \varphi^{(\mathrm{y})}_{\mathbf{k}_\mathrm{e}-\mathbf{P}/2}\, V_{\mathrm{eff}}(\mathbf{K}-\mathbf{Q})\, \varphi^{(\mathrm{b})}_{\mathbf{q}-(\mathbf{K}-\mathbf{Q})/2} \times \langle u_{7\mathrm{v},\mathbf{q}-(\mathbf{K}-\mathbf{Q})/2} | u_{8\mathrm{c},\mathbf{q}+(\mathbf{K}-\mathbf{Q})/2} \rangle \langle u_{7\mathrm{v},\mathbf{k}_\mathrm{h}} | u_{7\mathrm{v},\mathbf{k}_\mathrm{h}-(\mathbf{K}-\mathbf{Q})} \rangle\, \delta_{\mathbf{k}_\mathrm{e}+\mathbf{k}_\mathrm{h},\mathbf{K}-\mathbf{Q}+\mathbf{P}}\,, \tag{6.15}$$

with $\mathbf{Q}$ being the momentum of the emitted phonon. Similar to the previous section, the first overlap integral depicts the recombination process, in this case of the blue exciton, while the second overlap integral describes the absorption of the surplus recombination energy. Again, we assume exciton momenta to be negligibly small compared to the resulting ionised particles. The periodic functions are expanded according to Eq. (6.6). The recombination overlap integral between the valence and conduction band of the blue exciton series vanishes in zeroth order, the first order term yields

$$\langle u_{7\mathrm{v},\mathbf{q}-(\mathbf{K}-\mathbf{Q})/2} | u_{8\mathrm{c},\mathbf{q}+(\mathbf{K}-\mathbf{Q})/2} \rangle = \frac{\hbar}{m_0} \frac{\langle u_{7\mathrm{v},\mathbf{q}} | (\mathbf{K}-\mathbf{Q})\cdot\mathbf{p} | u_{8\mathrm{c},\mathbf{q}} \rangle}{E_{8\mathrm{c}}(\mathbf{q}) - E_{7\mathrm{v}}(\mathbf{q})}\,. \tag{6.16}$$

The quadratic term is neglected again due to the parity change imposed by the dipole operator. The second overlap integral is approximately one again. The matrix elements of Eqs. (6.14) and (6.15) can be combined into

$$\begin{aligned} M_{\mathrm{b}}^{(\mathrm{d})} =& M_{\mathrm{b}}^{(\mathrm{d})\mathrm{e}} + M_{\mathrm{b}}^{(\mathrm{d})\mathrm{h}} \\ =& \frac{\hbar}{m_0} V_{\mathrm{eff}}(\mathbf{K}-\mathbf{Q}) \sum_{\mathbf{q}} \varphi^{(\mathrm{b})}_{\mathbf{q}-(\mathbf{K}-\mathbf{Q})/2} \frac{\langle u_{7\mathrm{v},\mathbf{q}} | (\mathbf{K}-\mathbf{Q})\cdot\mathbf{p} | u_{8\mathrm{c},\mathbf{q}} \rangle}{E_{8\mathrm{c}}(\mathbf{q}) - E_{7\mathrm{v}}(\mathbf{q})} \\ & \times \underbrace{\left[\varphi^{(\mathrm{y})}_{\mathbf{k}_\mathrm{e}-\mathbf{P}/2-\mathbf{K}+\mathbf{Q}} - \varphi^{(\mathrm{y})}_{\mathbf{k}_\mathrm{e}-\mathbf{P}/2}\right]}_{\simeq (\mathbf{K}-\mathbf{Q})\cdot \frac{\partial \varphi^{(\mathrm{y})}_{\mathbf{k}}}{\partial \mathbf{k}}\big|_{\mathbf{k}_\mathrm{e}-\mathbf{P}/2 \simeq \mathbf{k}_\mathrm{e}}} \delta_{\mathbf{k}_\mathrm{e}+\mathbf{k}_\mathrm{h};\mathbf{K}-\mathbf{Q}+\mathbf{P}}\,. \end{aligned} \tag{6.17}$$

The envelope wave function, its derivative and the effective Coulomb potential are given by Eqs. (6.9)–(6.11). Next, we evaluate the sum over $\mathbf{q}$

$$\sum_{\mathbf{q}} \varphi^{(\mathrm{b})}_{\mathbf{q}-(\mathbf{K}-\mathbf{Q})/2} \frac{\langle u_{7\mathrm{v},\mathbf{q}} |\, \mathbf{K}\cdot\mathbf{p}\, | u_{8\mathrm{c},\mathbf{q}} \rangle}{E_{8\mathrm{c}}(\mathbf{q}) - E_{7\mathrm{v}}(\mathbf{q})} \simeq (\mathbf{K}\cdot\mathbf{p}_{78}) \sum_{\mathbf{q}} \frac{\varphi^{(\mathrm{b})}_{\mathbf{q}-(\mathbf{K}-\mathbf{Q})/2}}{\frac{\hbar^2 q^2}{2\tilde{\mu}_{87}} + \Delta E_{87}}\,, \tag{6.18}$$

with the dipole transition element $\langle u_{7\mathrm{v},0} |\, \mathbf{p}\, | u_{8\mathrm{c},0} \rangle = \mathbf{p}_{78}$ being assumed to be almost independent of $\mathbf{q}$. Contrary to the previous section, we only consider one particular intermediate band. The energy band dispersions in the denominator are assumed to be parabolic with a reduced mass $\tilde{\mu}_{87}^{-1} = m_{8\mathrm{c}}^{-1} - m_{7\mathrm{v}}^{-1}$ and ΔE_{87} being the energy difference between bands at $\mathbf{q} = 0$. The

sum in Eqs. (6.18) can then be evaluated analytically

$$\sum_{\mathbf{q}} \frac{\varphi^{(\mathrm{b})}_{\mathbf{q}-(\mathbf{K}-\mathbf{Q})/2}}{\frac{\hbar^2 q^2}{2\tilde{\mu}_{87}} + \Delta E_{87}}$$

$$= 4\sqrt{\frac{a_b \Omega}{\pi}} \left[2\frac{\hbar^2}{\tilde{\mu}_{87}} + 8\sqrt{\frac{\hbar^2}{2\tilde{\mu}_{87}} \Delta E_{87}}\, a_{\mathrm{b}} + \left(4\Delta E_{87} + \frac{\hbar^2 |\mathbf{K}-\mathbf{Q}|^2}{2\tilde{\mu}_{87}} \right) a_{\mathrm{b}}^2 \right]^{-1}, \tag{6.19}$$

$$\simeq \sqrt{\frac{a_{\mathrm{b}}\,\Omega}{\pi}} \left[\sqrt{\frac{\hbar^2}{2\tilde{\mu}_{87}}} + \sqrt{\Delta E_{87}}\, a_{\mathrm{b}} \right]^{-2} \quad = \quad \sqrt{\frac{a_{\mathrm{b}}\,\Omega}{\pi}} \tilde{B}_{87}\,, \tag{6.20}$$

in which Eq. (6.20) only holds true under the assumption that the kinetic energy of exciton and phonon is considerably smaller than the blue gap energy ΔE_{87}, which is consistent with previous approximations. Note that a_{b} is the effective Bohr radius of the blue 1S exciton. Compiling the individual results, the matrix element for the direct recombination is given by

$$M_{\mathrm{b}}^{(\mathrm{d})} = \frac{\hbar}{m_0} \frac{\mathrm{e}^2}{\Omega\, \varepsilon_0\, \varepsilon_{\mathrm{r}} (\mathbf{K}-\mathbf{Q})^2} \left(-\sqrt{\frac{a_{\mathrm{y}}^3\, \pi}{\Omega}}\, \frac{32\, a_{\mathrm{y}}^2}{(1 + a_{\mathrm{y}}^2\, k_{\mathrm{e}}^2)^3} \right)$$
$$\times \left((\mathbf{K}-\mathbf{Q}) \cdot \mathbf{k}_{\mathrm{e}} \right) \left((\mathbf{K}-\mathbf{Q}) \cdot \mathbf{p}_{78} \right) \sqrt{\frac{a_{\mathrm{b}}\,\Omega}{\pi}} \tilde{B}_{87}\, \delta_{\mathbf{k}_{\mathrm{e}}+\mathbf{k}_{\mathrm{h}}, \mathbf{K}-\mathbf{Q}+\mathbf{P}}\,. \tag{6.21}$$

Due to the minimal bending of the Γ_3^- phonon dispersion, their particle density is primarily localised on the edge of the Brillouin zone, in regions of finite momentum beyond the particle density of the excitons. Therefore, we assume momentum of the excitons to be negligibly small compared to phonon momentum $|\mathbf{K}| \ll |\mathbf{Q}|$, leaving us with

$$M_{\mathrm{b}}^{(\mathrm{d})} = -\frac{32\, a_{\mathrm{y}}^4\, \beta^{1/2}\, \mathrm{e}^2 \hbar}{\Omega\, \varepsilon_0\, \varepsilon_{\mathrm{r}}\, m_0}\, \tilde{B}_{87}\, \frac{(\mathbf{Q}\cdot\mathbf{k}_{\mathrm{e}})(\mathbf{Q}\cdot\mathbf{p}_{78})}{Q^2 (1 + a_{\mathrm{y}}^2\, k_{\mathrm{e}}^2)^3}\, \delta_{\mathbf{k}_{\mathrm{e}}+\mathbf{k}_{\mathrm{h}}, \mathbf{K}-\mathbf{Q}+\mathbf{P}}\,, \tag{6.22}$$

with $a_{\mathrm{b}} = \beta\, a_{\mathrm{y}}$. The following part is concerned with the initial phonon scattering from the yellow into the blue state.

6.3.2. Phonon scattering

As already discussed in section 6.1.1 the strongest phonon interaction channel is the optical Γ_3^- phonon; thus, we restrict our analysis to this single phonon interaction. The starting point is the matrix element

$$\langle \Psi_{1\mathrm{Sb}}(\mathbf{K}-\mathbf{Q}) | h_{3,\mathbf{Q}} | \Psi_{1\mathrm{Sy}}(\mathbf{K}) \rangle$$
$$= \sum_{\mathbf{q},\mathbf{q}'} \varphi^{(\mathrm{b})}_{\mathbf{q}}\, \varphi^{(\mathrm{y})}_{\mathbf{q}'} \left[\langle \psi_{8\mathrm{c},\mathbf{q}'+\frac{\mathbf{K}-\mathbf{Q}}{2}} | \otimes \langle \psi_{7\mathrm{v},-\mathbf{q}'+\frac{\mathbf{K}-\mathbf{Q}}{2}} | \right] h_{3,\mathbf{Q}} \left[|\psi_{6\mathrm{c},\mathbf{q}+\frac{\mathbf{K}}{2}}\rangle \otimes |\psi_{7\mathrm{v},-\mathbf{q}+\frac{\mathbf{K}}{2}}\rangle \right]. \tag{6.23}$$

The overlap integral of the valence band reduces to a delta distribution $\delta_{-\mathbf{q}'+\frac{\mathbf{K}-\mathbf{Q}}{2};-\mathbf{q}+\frac{\mathbf{K}}{2}}$, eliminating one of the sums. In chapter 2.4 we discussed the different possible descriptions for phonon interaction, and concluded that the Γ_3^- phonon is best expressed via the optical deformation potential. Assuming that the exciton momentum is comparably small to the phonon momentum $|\mathbf{K}| \ll |\mathbf{Q}|$ and that the phonon matrix element is invariant under a shift in $\mathbf{q}$, we can utilise the electron optical-phonon interaction of Eq. (5.6)[4]. The remaining sum over $\mathbf{q}$ runs solely over the wave functions. Inserting the envelope function from Eq. (6.9), we obtain

$$\sum_{\mathbf{q}} \varphi_{\mathbf{q}}^{(\mathrm{b})}\, \varphi_{\mathbf{q}-\frac{\mathbf{Q}}{2}}^{(\mathrm{y})} = \frac{2^7\sqrt{\beta^3}(1+\beta)}{\left(4(1+\beta)^2 + a_\mathrm{b}^2\, Q^2\right)^2} = \mathcal{S}_{1,1}^{(\mathrm{b,y})}(Q)\,. \tag{6.24}$$

Hence, for $\mathbf{K} = 0$, this is identical to the sum of Eq. (5.12). Not surprisingly, the final result for the phonon transition then matches the result from chapter 5.1.2 and reads as

$$\langle \Psi_{1\mathrm{Sb}}(\mathbf{K}-\mathbf{Q})|h_{3,\mathbf{Q}}|\Psi_{1\mathrm{Sy}}(\mathbf{K})\rangle \simeq\ \mathcal{S}_{1,1}^{(\mathrm{b,y})}(Q)\, D_{3;68}(Q)\sqrt{\frac{\hbar}{2\rho\,\Omega\,\omega_3}}\,. \tag{6.25}$$

Again, the connection to the previous chapter becomes more apparent, in the phenomenological treatment, as well as the theoretical description of the Auger decay. Equipped with the knowledge of the matrix elements we now turn back to Eq. (6.1) to calculate the decay rates.

6.4. Direct Auger decay rate

Utilising the previously accumulated results, we are now able to establish a definite form for the Auger decay rate via Fermi's golden rule. For the direct scattering rate we initially start with

$$\begin{aligned}\Gamma_{\mathrm{Auger}}^{(\mathrm{d})} =& \frac{2\pi}{\hbar} \sum_{\mathbf{K},\mathbf{P},\mathbf{k}_\mathrm{e},\mathbf{k}_\mathrm{h}} \left| M_\mathrm{y}^{(\mathrm{d})}(\mathbf{K},\mathbf{P},\mathbf{k}_\mathrm{e},\mathbf{k}_\mathrm{h}) \right|^2 \\ & \times \delta\Big[E_{1\mathrm{Sy}}(\mathbf{K}) + E_{1\mathrm{Sy}}(\mathbf{P}) - E_{6c}(\mathbf{k}_\mathrm{e}) - E_{7v}(\mathbf{k}_\mathrm{h}) \Big]\,.\end{aligned} \tag{6.26}$$

Extracting the delta distribution $\delta_{\mathbf{k}_\mathrm{e}+\mathbf{k}_\mathrm{h};\mathbf{K}+\mathbf{P}}$ from the matrix element $M_\mathrm{y}^{(\mathrm{d})}$ the sum over $\mathbf{k}_\mathrm{h}$ can be eliminated. We further assume that $\mathbf{K}, \mathbf{P} \to 0$. This simplifies the delta distribution to a great extent and additionally drops the sums over $\mathbf{K}$ and $\mathbf{P}$. The dependence of $\mathbf{K}$ within the matrix element cannot be neglected due to the angular relations imposed by the scalar

[4] For low temperatures the phonon distribution n_3 converges to zero, meaning that effectively only phonon emission is possible; thus, the second square root in Eq. (5.6) can be set to one.

products. The new decay rate reads as

$$\Gamma^{(\mathrm{d})}_{\mathrm{Auger},\mathbf{K}} = \frac{2\pi}{\hbar}\,\frac{\Omega}{8\pi^3}\int \mathrm{d}^3\mathbf{k}_\mathrm{e}\,\left|M^{(\mathrm{d})}(\mathbf{K},\mathbf{k}_\mathrm{e})\right|^2 \delta\Big[2E_{1\mathrm{Sy}}(0) - \big(E_{6c}(\mathbf{k}_\mathrm{e}) + E_{7v}(-\mathbf{k}_\mathrm{e})\big)\Big]\,, \tag{6.27}$$

where $\Gamma^{(\mathrm{d})}_{\mathbf{K}}$ is now a function of exciton momentum $\mathbf{K}$.
To evaluate the matrix element we only take the xy component of the valence bands into account. In this way, we commit to one spatial orientation. Under the assumption of S envelope states and isotropic bands the spatial dependence is averaged out by the angular integration and regains it general validity. The matrix element is determined by coupling coefficients [70] and results, without spin consideration, in

$$\langle\Gamma^+_{5v}|\mathbf{K}\cdot\mathbf{p}|\Gamma^-_{4_i}\rangle\langle\Gamma^-_{4_i}|\mathbf{K}\cdot\mathbf{p}|\Gamma^+_{1c}\rangle \to \langle xy|\mathbf{K}\cdot\mathbf{p}|\Gamma^-_{4_i}\rangle\langle\Gamma^-_{4_i}|\mathbf{K}\cdot\mathbf{p}|\Gamma^+_{1c}\rangle = \frac{2}{\sqrt{6}}K_xK_y\;p_{14_i}\,p_{4_i5}\,, \tag{6.28}$$

with $|\mathbf{p}_{m,n}| = p_{m,n}$. The index i represents the three different Γ^-_4 bands that were shown in section 2.1. These processes occur independently of one another and the square of the matrix element applies on each term separately. Thus, we define

$$\sum_{i=1}^{3}\left|\frac{\langle\Gamma^+_{5v}|\mathbf{K}\cdot\mathbf{p}|\Gamma^-_{4_i}\rangle\langle\Gamma^-_{4_i}|\mathbf{K}\cdot\mathbf{p}|\Gamma^+_{1c}\rangle}{\Delta E_{54_i}\;\Delta E_{14i}}\right|^2 = \frac{2}{3}\,K_x^2K_y^2\;P^{(\mathrm{d})}\,. \tag{6.29}$$

Next, we evaluate the integral over $\mathbf{k}_\mathrm{e}$. The angular integration results in a factor $4\pi/3$. To eliminate the integration over the the absolute value, the delta distribution in Eq. (6.27) is rewritten in terms of momentum as

$$\delta\Big[2E_{1\mathrm{Sy}}(0) - \big(E_{6\mathrm{c}}(\mathbf{k}_\mathrm{e}) + E_{7\mathrm{v}}(-\mathbf{k}_\mathrm{e})\big)\Big] = \frac{\mu_{67}}{\hbar^2k_0}\,\delta\big[k-k_0\big]\,, \tag{6.30}$$

with the renormalised Fermi vector $k_0^2 = \frac{2\mu_{67}}{\hbar^2}(2E_{1\mathrm{Sy}}(0) - E_\mathrm{y})$ and the effective mass $1/\mu_{67} = 1/m_{6\mathrm{c}} + 1/m_{7\mathrm{v}}$. For this the dispersions for conduction and valence band need to be assumed as nearly parabolic. While the effective mass of the conduction band is chosen as $m_{6\mathrm{c}} = \tilde{m}_{1\mathrm{c}} = 0.985\,m_0$, the valence band mass with an approximate momentum of $k_\mathrm{h} \approx 7\,\mathrm{nm}^{-1}$ needs to be addressed by the heavy hole mass region of the dispersion (cf. Fig. 2.4) and is estimated to be around $m_{7\mathrm{v}}^{\mathrm{hh}} \approx -2\,m_0$. The decay rate Eq. (6.27) takes the form

$$\Gamma^{(\mathrm{d})}_{\mathrm{Auger},\mathbf{K}} = \frac{2^7a_\mathrm{y}^4e^4\hbar}{9\Omega\varepsilon_0^2\varepsilon_\mathrm{r}^2m_0}\,\frac{\mu_{67}}{m_0}\,\frac{K_x^2K_y^2}{K^2}\,\frac{P^{(\mathrm{d})}}{m_0^2}\,\frac{k_0^3}{(1+a_\mathrm{y}^2k_0^2)^6}\,. \tag{6.31}$$

The resulting decay rate is admittedly tricky to evaluate because of two reasons: First is the remaining $\mathbf{K}$ dependence, second the unknown values of the dipole matrix elements within $P^{(\mathrm{d})}$.

We try to average over the angular dependencies and insert a rough estimate for the absolute value of $\mathbf{K}$. Since Eq. (6.31) is still specific to the xy orientation of the exciton, to obtain an angular independent expression for the direct decay rate we integrate over the unit sphere of $\mathbf{K}$. This results in

$$\Gamma_K^{(\mathrm{d})} = \frac{2^7 a_\mathrm{y}^4 e^4 \hbar}{135\pi\Omega\varepsilon_0^2\varepsilon_\mathrm{r}^2 m_0}\frac{\mu_{67}}{m_0}\frac{P^{(\mathrm{d})}}{m_0^2}\frac{k_0^3\ K^2}{(1+a_\mathrm{y}^2 k_0^2)^6}\,. \tag{6.32}$$

To estimate the absolute value K we treat the excitons as an ideal gas, thus yielding a thermal energy of $E_K = \frac{3}{2}k_\mathrm{B}T$. It should be noted that this approximation might give a good quantitative estimation for the thermal energy of excitons at low densities; however, at high densities this assumption loses its validity. Nevertheless, for an approximate evaluation it shall be considered sufficient. At low temperatures it is reasonable to assume that the kinetic energy is comparable to the thermal energy. Since the scattering rate Eq. (6.32) is quadratically dependent of K we choose $T = 1\,\mathrm{K}$ as a temperature beyond experimental setups [36] to provide an upper threshold for the exciton momentum K_th and, therefore, for the scattering rate. The resulting momentum is $K_\mathrm{th} \simeq 0.096\,\mathrm{nm}^{-1}$.
Since the required dipole matrix elements are unknown, we are restricted to approximations. For II-VI semiconductors the coupling between Γ_1^+ and Γ_4^- bands is known to be around $|p_{14}|^2/m_0 \simeq 10\,\mathrm{eV}$ [50]. The coupling between Γ_5^+ and Γ_4^- bands is far more intricate, but for the sake of the approximation we assume $|p_{14}| \simeq |p_{45}|$. Taking the energetic positions of the different bands from chapter 2.1 we derive a rough estimate for the factor $P^{(\mathrm{d})}/m_0^2 \simeq 0.56\,\mathrm{eV}^{-2}$. While this is most certainly far fetched from a qualitative utilisable result, for a simple estimation of the scale of the direct Auger decay it is considered satisfactory. In other works, the Auger decay is generally expressed in terms of a position- and density-independent Auger coefficient A [38, 40, 136]. The relation between the Auger coefficient and the scattering rates is defined as $A = \Omega\Gamma$. Inserting the values we deduced into Eq. (6.32), the Auger coefficient yields

$$A^{(\mathrm{d})} \simeq \Omega\,\Gamma_{K_\mathrm{th}}^{(\mathrm{d})} \ = \ 1.6\times10^{-26}\,\mathrm{cm}^3\mathrm{ns}^{-1}\,. \tag{6.33}$$

In the context of our approximations for the dipole matrix elements and exciton momentum, this can be considered as an upper boundary for the direct Auger coefficient. This is already sufficient to rule out the direct scattering as a possible origin for the measured Auger decay rates, as we will conclude at the end of this chapter.

6.5. Phonon-assisted Auger decay rate

After treating the direct Auger decay rate and concluding that it is not the origin of the Auger decay in Cu_2O, we will now proceed to the treatment of the phonon-assisted Auger decay. Again, we start with Fermi's golden rule that takes the form of

$$\begin{aligned}\Gamma_{\mathrm{Auger}}^{(\mathrm{pa})} =& \frac{2\pi}{\hbar} \sum_{\mathbf{K},\mathbf{P},\mathbf{Q},\mathbf{k}_\mathrm{e},\mathbf{k}_\mathrm{h}} \left| M^{(\mathrm{pa})}(\mathbf{K},\mathbf{P},\mathbf{Q},\mathbf{k}_\mathrm{e},\mathbf{k}_\mathrm{h}) \right|^2 \\ & \times \delta\Big[E_{1\mathrm{Sy}}(\mathbf{K}) + E_{1\mathrm{Sy}}(\mathbf{P}) - E_{6\mathrm{c}}(\mathbf{k}_\mathrm{e}) - E_{7\mathrm{v}}(\mathbf{k}_\mathrm{h}) - \hbar\omega_3 \Big] . \end{aligned} \tag{6.34}$$

Similar to the previous section, we initially extract the delta distribution $\delta_{\mathbf{k}_\mathrm{e}+\mathbf{k}_\mathrm{h};\mathbf{K}-\mathbf{Q}+\mathbf{P}}$ from the matrix element $M^{(\mathrm{pa})}$ to eliminate the sum over $\mathbf{k}_\mathrm{h}$. We assume $\mathbf{K},\mathbf{P} \simeq 0$ again, thus dropping the sums over the exciton momenta and get

$$\begin{aligned}\Gamma_{\mathrm{Auger}}^{(\mathrm{pa})} =& \frac{2\pi}{\hbar} \left(\frac{\Omega}{8\pi^3}\right)^2 \iint \mathrm{d}^3\mathbf{k}_\mathrm{e}\, \mathrm{d}^3\mathbf{Q}\ \left| M^{(\mathrm{pa})}(\mathbf{Q},\mathbf{k}_\mathrm{e}) \right|^2 \\ & \times \delta\Big[2E_{1\mathrm{Sy}}(0) - \left(E_{6\mathrm{c}}(\mathbf{k}_\mathrm{e}) + E_{7\mathrm{v}}(-\mathbf{k}_\mathrm{e}-\mathbf{Q})\right) - \hbar\omega_3 \Big] . \end{aligned} \tag{6.35}$$

To simplify Eq. (6.35), we first attempt to execute the delta distribution, which itself needs to be simplified beforehand. We transform it via its scaling property into a shape where it can be immediately applied to the angle between $\mathbf{k}_\mathrm{e}$ and $\mathbf{Q}$. The delta distribution in Eq. (6.35) can then be rewritten as

$$\delta\Big[2E_{1\mathrm{Sy}}(0) - \left(E_{6\mathrm{c}}(\mathbf{k}_\mathrm{e}) + E_{7\mathrm{v}}(-\mathbf{k}_\mathrm{e}-\mathbf{Q})\right) - \hbar\omega_3 \Big] \;=\; \frac{|m_{7\mathrm{v}}|}{\hbar^2 k_\mathrm{e} Q}\, \delta\big[z_{\mathrm{e},Q} + f(k_\mathrm{e},Q) \big] , \tag{6.36}$$

where $z_{\mathrm{e},Q} = \cos\,\theta_{\mathrm{e},Q}$ and $\theta_{\mathrm{e},Q} \measuredangle (\mathbf{k}_\mathrm{e},\mathbf{Q})$. The newly defined function contains

$$f(k_\mathrm{e},Q) = \frac{m_{7\mathrm{v}}\tilde{E}}{\hbar^2 k_\mathrm{e} Q} + \frac{Q}{2k_\mathrm{e}} - \frac{m_{7\mathrm{v}} k_\mathrm{e}}{2\mu_{67} Q} = \frac{\sigma(Q)}{k_\mathrm{e}} - \nu(Q)\, k_\mathrm{e} , \quad \tilde{E} = 2E_{1\mathrm{Sy}} - E_\mathrm{y} - \hbar\omega_3 . \tag{6.37}$$

Next, we take a closer look at the angular orientations of $\mathbf{k}_\mathrm{e}$ and $\mathbf{Q}$ within the matrix element. The final expression for the phonon scattering in Eq. (6.25) does not contain any further spatial dependencies, so the integration over the angles of both momenta in Eq. (6.35) can be restricted to the direct recombination matrix element of Eq. (6.22)

$$\begin{aligned}& \iint\limits_{\Omega_e,\Omega_Q} \mathrm{d}\Omega_e\, \mathrm{d}\Omega_Q \left| M^{(\mathrm{d})}(\mathbf{k}_\mathrm{e},\mathbf{Q}) \right|^2 \\ & \qquad = \frac{2^{10}\, a_\mathrm{y}^8\, \beta\, \mathrm{e}^4 \hbar^2}{\Omega^2\, \varepsilon_0^2\, \varepsilon_\mathrm{r}^2\, m_0^2} \frac{\tilde{B}_{87}^2}{(1+a_\mathrm{y}^2 k_\mathrm{e}^2)^6} \iint\limits_{\Omega_e,\Omega_Q} \mathrm{d}\Omega_e\, \mathrm{d}\Omega_Q\, (\mathbf{e_Q}\cdot\mathbf{k}_\mathrm{e})^2 (\mathbf{e_Q}\cdot\mathbf{p}_{78})^2 . \end{aligned} \tag{6.38}$$

The first scalar product corresponds to the just defined $\mathbf{e_Q} \cdot \mathbf{k}_\mathrm{e} = k_\mathrm{e}\, z_{\mathrm{e},Q}$ angle. The second term requires another approximation: Again, we only take the valence bands xy component into account, under the premisse that the spatial dependence is later averaged out by an angular integration. The coupling constants of the matrix elements can be obtained as Clebsch Gordan coefficients [70] and results, without spin consideration, in

$$\langle \Gamma_{3\mathrm{c}}^- | \mathbf{Q} \cdot \mathbf{p} | \Gamma_{5\mathrm{v}}^+ \rangle \to \langle \Gamma_{3\mathrm{c}}^- | \mathbf{Q} \cdot \mathbf{p} | xy \rangle = -\sqrt{\frac{2}{3}}\, \langle \gamma_2^- | Q_z\, p_z | xy \rangle = -\sqrt{\frac{2}{3}} Q_z\, p_{78}\,. \tag{6.39}$$

The direction of Q_z is now inalterably set to the direction of the crystallographic z-axis. To proceed, we use the spherical cosine rule

$$\cos\theta_Q = \cos\theta_{\mathrm{e},Q}\, \cos\theta_\mathrm{e} + \sin\theta_{\mathrm{e},Q}\, \sin\theta_\mathrm{e}\, \cos\varphi\,, \tag{6.40}$$

to get rid of the spatial dependence between $\mathbf{Q}$ and Q_z. We start with the integration over $\mathbf{Q}$, therefore placing $\mathbf{k}_\mathrm{e}$ into the z axis. Thereby, the angle φ coincides to the azimuth angle of the unit sphere Ω_Q. Inserting Eq. (6.40) into the direct recombination matrix element of Eq. (6.38), the angular integration yields

$$\begin{aligned} &\int_0^{2\pi}\int_{-1}^{1} \mathrm{d}\varphi\, \mathrm{d}z_{\mathrm{e},Q}\, (z_{\mathrm{e},Q}\, \cos\theta_Q)^2\, \delta\big[z_{\mathrm{e},Q} + f(k_\mathrm{e}, Q)\big] \\ &\qquad = \pi f^2 \left(2\, f^2 \cos^2\theta_\mathrm{e} + (1 - f^2)\sin^2\theta_\mathrm{e}\right)\, \Theta\big[1 - f\big]\, \Theta\big[1 + f\big]\,. \end{aligned} \tag{6.41}$$

The Heaviside functions stem from the application of the delta distribution on the restricted integration intervals of the polar coordinate. Subsequently, the angular integration for $\mathbf{k}_\mathrm{e}$ can be executed and yields a rather simple solution

$$\pi f^2 \int_0^{2\pi}\int_{-1}^{1} \mathrm{d}\varphi_\mathrm{e}\, \mathrm{d}(\cos\theta_\mathrm{e}) \left(2\, f^2 \cos^2\theta_\mathrm{e} + (1 - f^2)\sin^2\theta_\mathrm{e}\right) = \frac{8}{3}\pi^2\, f^2\,. \tag{6.42}$$

with $f \equiv f(k_\mathrm{e}, Q)$. We are left with the two integrals over $|\mathbf{Q}|$ and $|\mathbf{k}_\mathrm{e}|$. The integration over electron momentum is analytically solvable and given by

$$\int_0^\infty \mathrm{d}k_\mathrm{e} \frac{k_\mathrm{e}^3\, \big(f(k_\mathrm{e}, Q)\big)^2}{\left(1 + a_\mathrm{y}^2 k_\mathrm{e}^2\right)^6}\, \Theta\big[1 - f(k_\mathrm{e}, Q)\big]\Theta\big[1 + f(k_\mathrm{e}, Q)\big]\,. \tag{6.43}$$

The Heaviside functions restrict the limits of our integration to the range of physically possible electron momenta k_e, depending on phonon momentum Q. The limits for the k_e integration

are

$$k_{\min} = \frac{\mu_{67}}{|m_{7\mathrm{v}}|} \left| Q - \sqrt{\frac{m_{7\mathrm{v}}}{m_{6\mathrm{c}}} Q^2 - \frac{m_{7\mathrm{v}}}{\mu_{67}} \tilde{k}^2} \right| , \quad k_{\max} = \frac{\mu_{67}}{|m_{7\mathrm{v}}|} \left[Q + \sqrt{\frac{m_{7\mathrm{v}}}{m_{6\mathrm{c}}} Q^2 - \frac{m_{7\mathrm{v}}}{\mu_{67}} \tilde{k}^2} \right] , \tag{6.44}$$

with $\tilde{k}^2 = -\frac{2\, m_{7\mathrm{v}}}{\hbar^2} \tilde{E}$ and $\tilde{E}$ being defined in Eq. (6.37). Note that $m_{7\mathrm{v}} < 0$ since it is the effective mass of the highest valence band dispersion, which is commonly bent downwards.
Technically, the Heaviside functions produce four boundaries, but the other two coincide with the ones given in Eqs. (6.44), mirrored to negative momentum. The two resulting lower bounds are switching places depending on Q, i.e. on the point where $k_{\min} = 0$. Thus, in the most general case the following integration over Q must be split into two separate integrals, each featuring the k_{e} integration with the corresponding positive $k_{\min}$. However, the integrand only depends on k_{e} quadratically, so the absolute value of $k_{\min}$ is sufficient and the Q integration does not need to be split.
Applying the new limits to the integration yields

$$\begin{aligned} &\int_{k_{\min}}^{k_{\max}} \mathrm{d}k_{\mathrm{e}} \frac{\sigma^2 k_{\mathrm{e}} - 2\,\sigma\nu k_{\mathrm{e}}^3 + \nu^2 k_{\mathrm{e}}^5}{\left(1 + a_{\mathrm{y}}^2 k_{\mathrm{e}}^2\right)^6} \\ &\quad = \left. \frac{-\nu^2 + (3\sigma - 5\nu k_{\mathrm{e}}^2)\nu a_{\mathrm{y}}^2 + (15\nu\sigma k_{\mathrm{e}}^2 - 10\nu^2 k_{\mathrm{e}}^4 - 6\sigma^2) a_{\mathrm{y}}^4}{60 a_{\mathrm{y}}^6 (1 + a_{\mathrm{y}}^2 k_{\mathrm{e}}^2)^5} \right|_{k_{\min}(Q)}^{k_{\max}(Q)} \\ &\quad = I_{\mathrm{e}}(Q) \,, \end{aligned} \tag{6.45}$$

with $\sigma = \sigma(Q) = -\frac{\tilde{k}^2}{2Q} + \frac{Q}{2}$ and $\nu = \nu(Q) = \frac{m_{7\mathrm{v}}}{2\mu_{67} Q}$. In the same way the integration limits of k_{e} are coupled to phonon momentum, the phonon momentum itself is inherently restricted by the excess energy of the recombination. Physically, it can be visualised as the phonon momentum not being able to exceed the energy necessary for recombination. The integration limits of Q are inherently confined to

$$Q_{\min} = 0 \,, \qquad Q_{\max} = \sqrt{\frac{m_{6\mathrm{c}}}{\mu_{67}}} \tilde{k} \,, \tag{6.46}$$

finally resulting in the definite expression for the phonon-assisted Auger decay

$$\Gamma_{\mathrm{Auger}}^{(\mathrm{pa})} = \frac{2^8\, a_{\mathrm{y}}^8 \beta \mathrm{e}^4}{9\pi^3\, \rho\Omega\varepsilon_0^2\varepsilon_{\mathrm{r}}^2\omega_3} \frac{|m_{7\mathrm{v}}|}{m_0} \tilde{B}_{87}^2 \frac{|p_{78}|^2}{m_0} \int_0^{Q_{\max}} \mathrm{d}Q \, \frac{Q \left(\mathcal{S}_{1,1}^{(\mathrm{b,y})}(Q)\, D_{3;68}(Q) \right)^2}{\left| E_{1\mathrm{Sy}}(0) - E_{1\mathrm{Sb}}(Q) \right|^2} I_{\mathrm{e}}(Q) \,. \tag{6.47}$$

All necessary parameters are found in appendix A.1. The dipole transition element was calculated in section 5.3.2. For the Q-dependent deformation potential $D_{3;68}$ we recycle the results from the previous chapter in Eqs. (5.28) and (5.29). The integration over Q is evaluated

numerically. Finally we arrive at a distinct value for the Auger coefficient

$$A^{(\mathrm{pa})} \;=\; \Omega\,\Gamma^{(\mathrm{pa})}_{\mathrm{Auger}} \;=\; 8.62\times10^{-20}\,\mathrm{cm^3ns^{-1}}\,. \tag{6.48}$$

6.6. Discussion

There are already several experimental and theoretical works that attempted to determine the Auger coefficient. However, throughout the literature there exists great controversy about this particular coefficient. There is a huge discrepancy between measured values, the earliest work stating a value of $A = 1\times10^{-20}\,\mathrm{cm^3ns^{-1}}$ [41], and following measurements range from $A = 2\times10^{-18}\,\mathrm{cm^3ns^{-1}}$ [36] over $A = 7\times10^{-17}\,\mathrm{cm^3ns^{-1}}$ [39,42] up to $A = 4\times10^{-16}\,\mathrm{cm^3ns^{-1}}$ [43]. Similarly, theoretical works that tried to calculate the coefficient end up several orders of magnitude off of the experimental values with $A = 2\times10^{-21}\,\mathrm{cm^3ns^{-1}}$ [40] and $A = 3\times10^{-22}\,\mathrm{cm^3ns^{-1}}$ [38, 125], respectively. Our calculated Auger coefficient (for the phonon-assisted scattering), while converging closer to the experimental results than the previous theoretical attempts, is still several orders of magnitude below most of the measured coefficients. A general explanation for these grave deviations is not yet found, but there is a number of potential reasons for this discrepancy. One could be an insufficient theoretical treatment. Certain approximations, like the complete negligence of exciton momentum or the rigorous cutting of the expansion of the Bloch functions are not necessarily justified. Additionally, there are effects that could potentially enhance the efficiency of the Auger decay, e.g. influence of strain or defects in the crystal [43]. The possible influence of these effects is not considered in our calculations. Besides that, there could also be additional effects in the experimental setup that lead to the diminution of exciton density which obscure the Auger contribution part. For example one reason might be the scattering on impurities due to poor sample quality, or the formation of biexcitons [40, 137].

Besides the big uncertainty about the precise value of the Auger coefficient, the temperature dependence remains unclear. The theoretical calculations predict a linear temperature dependence, while experiments found no or an inverse temperature dependence [42, 43, 81]. The linear temperature dependence of preceding theoretical works simply stems from the series expansion of the Bose-Einstein distribution of the excitons for small kinetic energies. Since we disregarded exciton momentum and thus, consequently their distribution, we would expect no temperature dependence. Of course this is only valid for low temperatures close to $T \gtrsim 0\,\mathrm{K}$. At higher temperatures the exciton distribution as well as the phonon distribution need to be considered, but since we are interested in the regime close to the potential excitonic BEC, these temperature ranges are not of interest for this work.

6.7. Conclusion

The Auger decay is usually expressed as $\mathrm{d}n/\mathrm{d}t = An^2$ where the Auger coefficient A is assumed to be independent of position and particle density. In this chapter we derived the scattering rates and thereby the Auger coefficients for the direct and phonon-assisted Auger decay process in Cu_2O.

As already predicted at the beginning of the chapter, the supposed contribution of the direct Auger scattering is with $A^{(\mathrm{d})} = 1.6 \times 10^{-26}\,\mathrm{cm}^3\mathrm{ns}^{-1}$ almost seven orders of magnitude smaller than the phonon-assisted Auger coefficient $A^{(\mathrm{pa})} = 8.62 \times 10^{-20}\,\mathrm{cm}^3\mathrm{ns}^{-1}$. Contrary to previous theoretical works [38] we argued that the expansion of the overlap integrals for direct Auger scattering can not couple to the Γ_3^- conduction band due to symmetry restrictions. This diminishes the potential contribution of the direct scattering even further than expected. The calculation of the direct Auger coefficient required the use of a number of approximations, since the required parameters are partially unavailable. However, the knowledge of precise parameters is not necessary in this case, since the calculated value represents an upper boundary, that is already sufficient to dismiss the contribution of the direct Auger decay.

For the phonon-assisted Auger scattering we were able to improve the theoretical description by introducing the momentum-dependent optical deformation potential and treating the intermediate states after the phonon emission as exciton states rather than pure band states. Furthermore, we receive the parameter of greatest uncertainty, the deformation potential, directly from the result of the previous chapter. Nevertheless, our calculated Auger coefficient still deviates about several orders of magnitude from most of the experimentally determined values. On one hand, this could suggest that some of the applied approximations are not justified. On the other hand, we see a significant variation between different experiments, which impedes a precise pinpointing of the origin of the deviation. If we assume our calculated Auger coefficient to be relatively close to the actual Auger decay rate of a high quality Cu_2O sample, according to [132, 136] the formation of a BEC could be achieved for pump powers of $P_{\mathrm{Laser}} \geq 50\,\mu\mathrm{W}$ in a system of temperature $T_{\mathrm{bath}} = 0.037\,\mathrm{K}$. This result would coincide with the BEC signatures found in [36, 133].

In retrospect, we can claim to have gained a significant improvement upon existing theoretical treatments; however, there are still issues that a need further investigation due to the complexity of semiconductor structures.

Chapter 7.

Conclusion & outlook

In this work, we evaluated several fundamental properties of excitons in Cu_2O. The first subtle but nonetheless very important result, was the evaluation of the Suzuki-Hensel Hamiltonian and the fit of its coupling parameters to spin-DFT calculations of the highest Γ_5^+ valence band. An outdated set of those parameters were published in [91] and are currently used in most of the contemporary works on Cu_2O excitons that utilise the Luttinger or Suzuki-Hensel Hamiltonian. Although the changes are miniscule it is advised to refer to the parameters introduced in this work.

The nonparabolicity of the valence band was inserted into the Wannier equation to calculate the deviation from the ideal Rydberg series. Unlike the usual approaches, the system was solved in momentum space; however, that carries the disadvantage that the presented ansatz only works for isotropic band dispersions. The resulting energy resonances have shown an overall improvement, although a very good matching was only achieved for P excitons with principal quantum number $7 \geq n \geq 18$. For lower n the mixing to the green exciton series and LO-phonon coupling yield a significant impact, for P excitons with $n > 18$ the Rydberg blockade leads to an additional shift of the binding energies.

The evaluation of the yellow 1S paraexciton necessitated, apart from the nonparabolicity, the application of a modified Coulomb interaction (in this case, the Pollmann-Büttner interaction) that incorporates the polaron nature of the excitons constituents, including the corresponding self-energy. To accomodate for the mixing of states, the two particle Schrödinger equation is solved with a variational method. The calculated binding energies and exciton masses showed very good correlation to the experimentally known values.

The phonon-assisted transition of yellow S excitons required the revision of the textbook solution derived by Elliott. His second-order perturbation approach was improved by assuming the transitory states to be excitonic and the generalisation that the phonon deformation potential exhibits a momentum dependence. The fit to the dominant Γ_3^- phonon absorption edge shows a significant improvement to the old theoretical approach and moreover the solution bears advantage that it is still derived completely analytically. A decisive statement about the higher located phonon-assisted absorption bands and the resulting implication of state mixing shall

not be made since the fitting range is highly restricted and the results are too speculative.
However, the fits of the Γ_3^- phonon absorption edge were immediately useful to revisit and generalise the derivations for the phonon-assisted Auger decay. The resulting Auger coefficient is closer to the experimental findings than earlier calculations, but still one to two orders of magnitude too small. Since the experimental results themselves show strong deviations, it is perceivable that the quality of the individual sample has a marked influence on the Auger decay, in which a theoretical treatment of an ideal crystal could only serve as an lower boundary anyway. It was also shown, that direct Auger recombination is of marginal importance.

One of the most pressing concerns, that was mostly disregarded in this work, is the coupling between the different exciton series. As we have seen up to a certain point in this work, this coupling still inherits importance for the individual exciton states of the yellow and green series, as well as for the phonon-assisted absorption. The respective participants are drastically shaping absorption strength and potentially positioning. The mixing could also by trend affect the Auger decay rate as it opens up the possiblity for the phonon-assisted decay of yellow excitons via their respective green portion.
Inevitably, the coupling between the series tangentially implies that a proper treatment of the green exciton series is necessary. The major issue of evaluating the green series with the methods presented in chapter 3 and 4, is the fact that a direct inclusion of the coupling is disregarded. While this apparently works for the yellow series, the coupling within the degenerate Γ_8^+ valence bands is nonnegligible and leads to only one distinct green exciton series (if exchange interactions are disregarded). However, the approaches used rely solely on the band dispersions and henceforth would yield two separate green exciton series. Additionally, the bands depict a strong anisotropy which complicates their general treatment and the Suzuki-Hensel Hamiltonian does not reflect the Γ_8^+ band dispersions properly over the same range as it does for the Γ_7^+ band.
The evaluation of the Auger coefficient also should realistically be done for a stressed crystal system which downgrades the symmetry and thus opens up new potential decay channels.

Despite those apparent shortcomings in the presented theoretical procedures, the emerging results still have their respective merits. The approach of chapter 3 to solve the Wannier equation in momentum space is a fresh perspective on an otherwise stale and expatiated theoretical routine, that was not taken into consideration much as of yet. The general computation of the exciton dispersion is also a topic that has not garnered much attention although it is closely related to the fundamental properties of the exciton. The derivations of chapter 5 and 6 are essentially improved theoretical models of existing theories, whereas especially the result of chapter 5 shows a significant improvement and a striking agreement with the experiments while still being analytically solvable, that it could potentially end up as a textbook solution.

Appendix A.

Tables

A.1. Parameters used throughout this work

Parameter	description	appearance	Ref.
$E_\mathrm{y} = E_\mathrm{1c}(0) = 2.1720737\,\mathrm{eV}$	band gap (y)/energy of Γ_1c^+ band	Sec. 2.1.1	[11], calc.
$E_\mathrm{b} = E_\mathrm{3c}(0) = 2.625\,\mathrm{eV}$	band gap (b)/energy of Γ_3c^- band	Sec. 2.3	[64]
$\tilde{m}_\mathrm{1c} = m_\mathrm{6c} = 0.985\,m_0$	Γ_1c^+ band mass (polaron)	Eq. (2.6)	[67]
$\tilde{m}_\mathrm{7v} = 0.575\,m_0$	Γ_7v^+ band mass (polaron)	Sec. 2.2.3	[67]
$\Delta_\mathrm{p} = 131\,\mathrm{meV}$	spin-orbit splitting	Eq. (2.13)	[61]
$\Delta_\mathrm{k} \simeq 0$	quadratic spin-orbit coupling	Eq. (2.17)	est.
$A_1 = -1.818$	SH parameters	Eq. (2.21)	fit
$A_2 = 4.601$			
$A_3 = -2.269$			
$\varepsilon(0) = \varepsilon_1 = 7.5$	permittivity in the limit cases	Eq. (2.39)	[23, 84]
$\varepsilon_\mathrm{int} = \varepsilon_2 = 7.27$			calc.
$\varepsilon(\infty) = \varepsilon_3 = 6.65$			calc.
$\mathrm{Ry}^\mathrm{(y)} = 86.04\,\mathrm{meV}$	Rydberg energy of the yellow series	Sec. 3.2.2	calc.
$a_\mathrm{L} = 0.43\,\mathrm{nm}$	lattice constant of Cu_2O	Sec. 3.2.2	[107]
$\rho = 6.14 \times 10^3\,\mathrm{kg/m^3}$	density of Cu_2O	Sec. 5.3.2	[107]
$n_\mathrm{R} = 2.94$	refractive index	Sec. 5.3.2	[77]
$E_\mathrm{1Sy}^\mathrm{(p)} = 2.020598\,\mathrm{eV}$	1S paraexc. energy (y)	Sec. 4.2.1	[77]
$E_\mathrm{1Sy}^\mathrm{(o)} = 2.03278\,\mathrm{eV}$	1S orthoexc. energy (y)	Sec. 5.3.2	[78]
$E_\mathrm{2Sy} = 2.138\,\mathrm{eV}$	2S orthoexc. energy (y)	Sec. 5.3.3	[62]

$E_{1\mathrm{Sg}} = 2.154\,\mathrm{eV}$	1S orthoexc. energy (g)	Sec. 5.3.3	[62]
$E_{1\mathrm{Sb}} = 2.569\,\mathrm{eV}$	1S orthoexc. energy (b)	Sec. 5.3.2	[64]
$E_{1\mathrm{Sv}} = 2.715\,\mathrm{eV}$	1S orthoexc. energy (v)	Sec. 5.3.3	[64]
$a_{1\mathrm{Sy}}^{(\mathrm{p})} = 0.51\,\mathrm{nm}$	Bohr radius 1S paraexc. (y)	Sec. 4.3.2	calc.
$a_{1\mathrm{Sy}}^{(\mathrm{o})} = 0.81\,\mathrm{nm}$	Bohr radius 1S orthoexc. (y)	Sec. 5.3.2	[25]
$a_{\mathrm{y}} = 1.1\,\mathrm{nm}$	Bohr radius $n \geq 2$ exc. (y)	Sec. 3.2.2	calc.
$a_{\mathrm{g}} = 0.74\,\mathrm{nm}$	Bohr radius (g)	Sec. 5.3.3	calc.
$a_{\mathrm{b}} = 1.72\,\mathrm{nm}$	Bohr radius (b)	Sec. 5.3.2	calc.
$a_{\mathrm{v}} = 1.36\,\mathrm{nm}$	Bohr radius (v)	Sec. 5.3.3	calc.
$M_{1\mathrm{Sy}}^{(\mathrm{p})} = 2.61\,m_0$	1S paraexciton mass (y)	Sec. 4.2.1	[77]
$M_{1\mathrm{Sy}}^{(\mathrm{o})} = 2.7\,m_0$	1S orthoexciton mass (y)	Sec. 5.3	[109]
$M_{\mathrm{y}} = 1.56\,m_0$	$n \geq 2$ exciton mass (y)	Sec. 5.3.3	calc.
$M_{1\mathrm{Sg}} = 2.61\,m_0$	1S exciton mass (g)	Sec. 5.3.3	est.
$\lvert p_{78}\rvert^2/m_0 = 2.66\,\mathrm{eV}$	dme betw. $\Gamma_{7\mathrm{v}}$ and $\Gamma_{8\mathrm{c}}$ bands	Sec. 5.3.2	calc.

Table A.1.: Table of all the Cu_2O specific parameters needed and their first relevant appearance in this work. They are either calculated, fitted, roughly estimated, or taken from external sources.

A.2. Tables for the O_h point group

Symmetry is a potent tool in the shed of every semiconductor physicist. It allows for restrictions and explanations of various interacting elements, narrowing down the amount of unknown variables to an almost comprehensible size. From the composition of Cu_2O, we can conclude that all symmetry transformations concerning the unit cell belong to th O_h point group [70]. In the O_h point group, there exist two, more or less equally popular, notations for the symmetry around the Γ point, the Koster (K) and the Bouckaert (BSW) notation. In this work, we stick to the Koster notation. The transcription between these two, as well as the respective basis functions are given in Tab. A.2. In Tab. A.3, we give the multiplication table for the point groups O and T_d, which is also valid for O_h, since it is the direct product of $O_\mathrm{h} = O \otimes C_1 = T_\mathrm{d} \otimes C_\mathrm{i}$ and therefore contains all the operations of the O, T_d and T_h point groups, i.e. those who send a cube into itself.

K	BSW	States	Basis functions
Γ_1^+	Γ_1	α^+	1
Γ_2^+	Γ_2	β^+	$(y^2-z^2)(x^2-z^2)(x^2-y^2)$
Γ_3^+	Γ_{12}	γ_1^+, γ_2^+	$(2z^2-x^2-y^2)\,,\,(x^2-y^2)$
Γ_4^+	$\Gamma_{15'}$	$\delta_1^+, \delta_2^+, \delta_3^+$	$yz(y^2-z^2)\,,\,xz(x^2-z^2)\,,\,xy(x^2-y^2)$
Γ_5^+	$\Gamma_{25'}$	$\varepsilon_1^+, \varepsilon_2^+, \varepsilon_3^+$	$yz\,,\,xz\,,\,xy$
Γ_1^-	$\Gamma_{1'}$	α^-	$\Gamma_2^+ \otimes \Gamma_2^-$
Γ_2^-	$\Gamma_{2'}$	β^-	xyz
Γ_3^-	$\Gamma_{12'}$	γ_1^-, γ_2^-	$\Gamma_3^+ \otimes \Gamma_2^-$
Γ_4^-	Γ_{15}	$\delta_1^-, \delta_2^-, \delta_3^-$	$x\,,\,y\,,\,z$
Γ_5^-	Γ_{25}	$\varepsilon_1^-, \varepsilon_2^-, \varepsilon_3^-$	$x(y^2-z^2)\,,\,y(x^2-z^2)\,,\,z^2(x^2-y^2)$
Γ_6^+	-	-	$\phi(\frac{1}{2},-\frac{1}{2})\,,\,\phi(\frac{1}{2},\frac{1}{2})$
Γ_7^+	-	-	$\Gamma_2^+ \otimes \Gamma_6^+$
Γ_8^+	-	-	$\phi(\frac{3}{2},-\frac{3}{2})\,,\,\phi(\frac{3}{2},-\frac{1}{2})\,,\,\phi(\frac{3}{2},\frac{1}{2})\,,\,\phi(\frac{3}{2},\frac{3}{2})$
Γ_6^-	-	-	$\Gamma_1^- \otimes \Gamma_6^+$
Γ_7^-	-	-	$\Gamma_2^- \otimes \Gamma_6^+$
Γ_8^-	-	-	$\Gamma_1^- \otimes \Gamma_8^+$

Table A.2.: States and basis functions for the different symmetries at zone centre. Additionally, it contains the transcription between the Koster (K) and the Bouckaert (BSW) notation.

Γ_1	Γ_2	Γ_3	Γ_4	Γ_5	Γ_6	Γ_7	Γ_8	$\otimes$
Γ_1	Γ_2	Γ_3	Γ_4	Γ_5	Γ_6	Γ_7	Γ_8	Γ_1
	Γ_1	Γ_3	Γ_5	Γ_4	Γ_7	Γ_6	Γ_8	Γ_2
		$\Gamma_1+\Gamma_2+\Gamma_3$	$\Gamma_4+\Gamma_5$	$\Gamma_4+\Gamma_5$	Γ_8	Γ_8	$\Gamma_6+\Gamma_7+\Gamma_8$	Γ_3
			$\Gamma_1+\Gamma_3+\Gamma_4+\Gamma_5$	$\Gamma_2+\Gamma_3+\Gamma_4+\Gamma_5$	$\Gamma_6+\Gamma_8$	$\Gamma_7+\Gamma_8$	$\Gamma_6+\Gamma_7+2\Gamma_8$	Γ_4
				$\Gamma_1+\Gamma_3+\Gamma_4+\Gamma_5$	$\Gamma_7+\Gamma_8$	$\Gamma_6+\Gamma_8$	$\Gamma_6+\Gamma_7+2\Gamma_8$	Γ_5
					$\Gamma_1+\Gamma_4$	$\Gamma_2+\Gamma_5$	$\Gamma_3+\Gamma_4+\Gamma_5$	Γ_6
						$\Gamma_1+\Gamma_4$	$\Gamma_1+\Gamma_2+\Gamma_3$	Γ_7
							$\Gamma_1+\Gamma_2+\Gamma_3+2\Gamma_4+2\Gamma_5$	Γ_8

Table A.3.: Multiplication table for the groups O and T_d.

Representation O_h	Basis operators	Projection on $J=3/2$	Projection on $J=1/2$	Cross-space $(J=3/2)\otimes(J=1/2)$
Γ_1^+	1	1	1	0
	$\mathbf{I}\cdot\sigma$	1	-2	0
Γ_2^+	$\{I_yI_z\}\sigma_x + \text{c.p.}$	$J_xJ_yJ_z + J_zJ_yJ_x$	0	0
Γ_3^+	$I_x^2 - I_y^2$	$\frac{1}{3}(J_x^2 + J_y^2)$	0	$I_x^2 - I_y^2$
	$I_x\sigma_x - I_y\sigma_y$	$\frac{2}{3}(J_x^2 + J_y^2)$	0	$-(I_x^2 - I_y^2)$
	$\{I_x(I_y\sigma_z - I_z\sigma_y)\} - \{I_y(I_z\sigma_x - uI_x\sigma_z)\}$	0	0	$-\frac{3}{2}\mathrm{i}(I_x^2 - I_y^2)$
Γ_4^+	I_x	$\frac{2}{3}J_x$	$\frac{4}{3}J_x$	I_x
	σ_x	$\frac{2}{3}J_x$	$-\frac{2}{3}J_x$	$-2I_x$
	$I_y\sigma_z - I_z\sigma_y$	0	0	$3\mathrm{i}I_X$
	$(I_x^2 - \frac{1}{3}I^2)\sigma_x + \{I_xI_y\}\sigma_y + \{I_zI_x\}\sigma_z$	$\frac{2}{9}J_x$	$-\frac{20}{9}J_x$	$\frac{5}{6}I_x$
	$(I_x^2 - \frac{1}{3}I^2)\sigma_x + \frac{2}{3}(\{I_xI_y\}\sigma_y + \{I_zI_x\}\sigma_z)$	$\frac{10}{9}J_x^3 - \frac{41}{18}J_x$	0	0
Γ_5^+	$\{I_yI_z\}$	$\frac{1}{3}\{J_yJ_z\}$	0	$\{I_yI_z\}$
	$I_y\sigma_z + I_z\sigma_y$	$\frac{4}{3}\{J_yJ_z\}$	0	$-2\{I_yI_z\}$
	$(I_y^2 - I_z^2)\sigma_x - (\{I_xI_y\}\sigma_y - \{I_zI_x\}\sigma_z)$	0	0	$3\mathrm{i}\{I_yI_z\}$
	$(I_y^2 - I_z^2)\sigma_x + 2(\{I_xI_y\}\sigma_y - \{I_zI_x\}\sigma_z)$	$2\{(J_y^2 - J_z^2)J_x\}$	0	0

Table A.4.: Tabulation of the 36 independent matrices constructed from $\mathbf{I}$ and σ, their assignment to the O_h representation of the cubic group, and their projection on the JM subspaces [75]. The remaining basis operators for symmetries Γ_3^+, Γ_4^+ and Γ_5^+ are obtained by cyclic permutation.

A.4. Exciton binding energies

A.4.1. Experiments

	S		P	D	F	
n	[91]	[62]	[11]	[91]	[24]	[24]
1		2.0330				
2		2.1544	2.1484			
3	$2.160270 \pm 2.0 \cdot 10^{-5}$	2.1603	2.16135	$2.16229 \pm 2.0 \cdot 10^{-5}$		
4	2.165555		2.16609	$2.166472 \pm 2.0 \cdot 10^{-5}$		2.1665182 2.1665448 2.1665773
5	2.168024		2.16829	2.16849480	2.16852583	2.16850568 2.16852396 2.16854615
6	2.169323		2.16948	2.16957671	2.16961126	2.16959665 2.16960891 2.16962508
7	2.170078		2.170182	2.17026399	2.17026787	2.17025707 2.17026569 2.17027629
8	2.170570		2.170635	2.17069335	2.17069497	
9	2.170899		2.170944		2.17099485	
10	$2.171139 \pm 1.0 \cdot 10^{-5}$		2.171163		2.17118868	
11	$2.17129093 \pm 2.8 \cdot 10^{-7}$		2.171324		2.17134724	
12	$2.171416 \pm 2.0 \cdot 10^{-6}$		2.171446		2.17146712	
13	$2.1715170 \pm 1.7 \cdot 10^{-6}$		2.171541			
14			2.1716159			
15			2.1716758			
16			2.1717248			
17			2.1717653			
18			2.1717989			
19			2.171827			
20			2.1718515			
21			2.1718724			
22			2.1718906			
23			2.1719068			
24			2.1719202			
25			2.1719335			

Table A.5.: Experimentally observed exciton energies. The binding energies used in chapter 3 are obtained by subtracting the yellow band gap energy E_{y} (cf. Tab. A.1). For the F excitons, the values in the right column contain the peak energies of the three absorption lines, while the left column contains an average. All values are in eV.

A.4.2. Calculated in chapter 3

n	S	P	D	F
1	−141.4425093			
2	−32.4773464	−24.6897310		
3	−12.9875971	−10.9439239	−10.0022113	
4	−6.8426871	−6.0442042	−5.6448512	−5.4947525
5	−4.1944727	−3.8058511	−3.6028649	−3.5249822
6	−2.8259740	−2.6089442	−2.4925247	−2.4472639
7	−2.0303750	−1.8972494	−1.8245452	−1.7960219
8	−1.5281196	−1.4407165	−1.3923642	−1.3732688
9	−1.1911799	−1.1307650	−1.0970176	−1.0836230
10	−0.9543465	−0.9108694	−0.8863994	−0.8766488
11	−0.7816151	−0.7492969	−0.7309972	−0.7236823
12	−0.6518059	−0.6271348	−0.6130960	−0.6074697
13	−0.5518067	−0.5325497	−0.5215466	−0.5171273
14	−0.4731504	−0.4578334	−0.4490509	−0.4455170
15	−0.4101738	−0.3977916	−0.3906707	−0.3878009
16	−0.3589731	−0.3488218	−0.3429687	−0.3406066
17	−0.3167871	−0.3083617	−0.3034927	−0.3015254
18	−0.2816184	−0.2745494	−0.2704558	−0.2688000
19	−0.2519935	−0.2460050	−0.2425308	−0.2411241
20	−0.2268058	−0.2216890	−0.2187155	−0.2175104
21	−0.2052117	−0.2008061	−0.1982417	−0.1972015
22	−0.1865588	−0.1827393	−0.1805125	−0.1796084
23	−0.1703362	−0.1670042	−0.1650586	−0.1642680
24	−0.1561393	−0.1532164	−0.1515069	−0.1508114
25	−0.1436443	−0.1410674	−0.1395575	−0.1389426
26	−0.1325897	−0.1303074	−0.1289676	−0.1284213

Table A.6.: Numerical binding energies of the yellow excitons as calculated in chapter 3. All values in meV.

Appendix B.

Additional content

B.1. Degenerate $\mathbf{k}\cdot\mathbf{p}$ theory

B.1.1. Dresselhaus-Kip-Kittel parameters

Due to the cubic symmetry of the crystal, the different basis functions are invariant under symmetry transformations and can always be retransformed back into each other. Therefore, it is sufficient to evaluate one basis function of Γ_5^+, for example $\varepsilon_1^+ \sim yz$. The three parameters of Eq. (2.10) can be identified as

$$L = \frac{\hbar^2}{m_0^2} \sum_\nu \frac{|\langle yz|p_x|\nu\rangle|^2}{E_{5\mathrm{v}} - E_\nu}\,, \tag{B.1a}$$

$$M = \frac{\hbar^2}{m_0^2} \sum_\nu \frac{|\langle yz|p_y|\nu\rangle|^2}{E_{5\mathrm{v}} - E_\nu}\,, \tag{B.1b}$$

$$N = \frac{\hbar^2}{m_0^2} \sum_\nu \frac{\langle yz|p_x|\nu\rangle\langle\nu|p_z|xy\rangle + \langle yz|p_z|\nu\rangle\langle\nu|p_x|xy\rangle}{E_{5\mathrm{v}} - E_\nu}\,. \tag{B.1c}$$

The Hamiltonian (2.10) generally describes the interband coupling interaction of the k^2 order without considering intermediate states. From group theoretical analysis, we can infer that the intermediate band symmetries need to fulfill $\nu = \Gamma_5^+ \otimes \Gamma_4^- = \Gamma_2^- \oplus \Gamma_3^- \oplus \Gamma_4^- \oplus \Gamma_5^-$ for the matrix elements to contain the unity representation Γ_1^+. Under consideration of the coupling coefficients of the O_h group [70], the interaction with the different bands can be expressed via those parameters as

$$L = \frac{\hbar^2}{2m_0}\,(F + 2G)\,, \tag{B.2a}$$

$$M = \frac{\hbar^2}{2m_0}\,(H_1 + H_2)\,, \tag{B.2b}$$

$$N = \frac{\hbar^2}{2m_0}\,(F - G + H_1 - H_2) \tag{B.2c}$$

with

$$F = \frac{2}{m_0} \sum_{\ell=\Gamma_2^-} \frac{|\langle xy|p_z|\beta^-,\ell\rangle|^2}{E_{5\mathrm{v}} - E_\ell}\,, \tag{B.3a}$$

$$G = \frac{2}{m_0} \sum_{\ell=\Gamma_3^-} \frac{|\langle xy|p_z|\gamma_2^-,\ell\rangle|^2}{E_{5\mathrm{v}} - E_\ell}\,, \tag{B.3b}$$

$$H_1 = \frac{2}{m_0} \sum_{\ell=\Gamma_4^-} \frac{|\langle xy|p_y|\delta_1^-,\ell\rangle|^2}{E_{5\mathrm{v}} - E_\ell}\,, \tag{B.3c}$$

$$H_2 = \frac{2}{m_0} \sum_{\ell=\Gamma_5^-} \frac{|\langle xy|p_y|\varepsilon_1^-,\ell\rangle|^2}{E_{5\mathrm{v}} - E_\ell}\,. \tag{B.3d}$$

The corresponding basis functions of the states used in Eqs. (B.3) are given in in Tab. A.2.

B.1.2. Luttinger-Kohn Hamiltonian in JM representation

The JM base states are given in Eqs. (B.11) and (B.12). From these we receive a matrix that represents the transformation $|JM\rangle = S|LS\rangle$ and is given by [138]

$$S = \begin{array}{c} \\ |\varepsilon_1, s^+\rangle \\ |\varepsilon_2, s^+\rangle \\ |\varepsilon_3, s^+\rangle \\ |\varepsilon_1, s^-\rangle \\ |\varepsilon_2, s^-\rangle \\ |\varepsilon_3, s^-\rangle \end{array} \begin{array}{c} \begin{array}{cccccc} |\frac{3}{2},\frac{3}{2}\rangle & |\frac{3}{2},\frac{1}{2}\rangle & |\frac{3}{2},-\frac{1}{2}\rangle & |\frac{3}{2},-\frac{3}{2}\rangle & |\frac{1}{2},\frac{1}{2}\rangle & |\frac{1}{2},-\frac{1}{2}\rangle \end{array} \\ \begin{pmatrix} \frac{1}{\sqrt{2}} & 0 & -\frac{1}{\sqrt{6}} & 0 & 0 & -\frac{1}{\sqrt{3}} \\ \frac{\mathrm{i}}{\sqrt{2}} & 0 & \frac{\mathrm{i}}{\sqrt{6}} & 0 & 0 & \frac{\mathrm{i}}{\sqrt{3}} \\ 0 & -\sqrt{\frac{2}{3}} & 0 & 0 & \frac{1}{\sqrt{3}} & 0 \\ 0 & \frac{1}{\sqrt{6}} & 0 & \frac{1}{\sqrt{2}} & \frac{1}{\sqrt{3}} & 0 \\ 0 & \frac{\mathrm{i}}{\sqrt{6}} & 0 & -\frac{\mathrm{i}}{\sqrt{2}} & \frac{\mathrm{i}}{\sqrt{3}} & 0 \\ 0 & 0 & -\sqrt{\frac{2}{3}} & 0 & 0 & \frac{1}{\sqrt{3}} \end{pmatrix} \end{array} \tag{B.4}$$

with the spin functions $s^\pm = \pm 1/2$. The LK Hamiltonian in JM base is given by

$$H_{\mathrm{LK}} = \begin{pmatrix} P+Q & -S & R & 0 & -S/\sqrt{2} & \sqrt{2}R \\ -S^\dagger & P-Q & 0 & R & -\sqrt{2}Q & \sqrt{3/2}S \\ R^\dagger & 0 & P-Q & S & \sqrt{3/2}S^\dagger & \sqrt{2}Q \\ 0 & R^\dagger & S^\dagger & P+Q & -\sqrt{2}R^\dagger & -S^\dagger/\sqrt{2} \\ -S^\dagger/\sqrt{2} & -\sqrt{2}Q & \sqrt{3/2}S & -\sqrt{2}R & P+\Delta_{\mathrm{p}} & 0 \\ \sqrt{2}R^\dagger & \sqrt{3/2}S^\dagger & \sqrt{2}Q & -S/\sqrt{2} & 0 & P+\Delta_{\mathrm{p}} \end{pmatrix} \begin{matrix} |3/2,3/2\rangle \\ |3/2,1/2\rangle \\ |3/2,-1/2\rangle \\ |3/2,-3/2\rangle \\ |1/2,1/2\rangle \\ |1/2,-1/2\rangle \end{matrix} \tag{B.5}$$

with

$$P = \frac{\hbar^2}{2m_0}\left(\frac{1}{m_{\mathrm{e}}} + \gamma_1\right)k^2 - \frac{\mathrm{e}^2}{\varepsilon\, r} \tag{B.6a}$$

$$\begin{aligned} Q &= \frac{\hbar^2}{2m_0}\gamma_2(k_x^2 + k_y^2 - 2k_z^2) \\ &= -4k^2\sqrt{\frac{\pi}{5}}\,\tilde{\gamma}_2\, Y_{2,0} = \tilde{Q}\, Y_{2,0}\, k^2 \end{aligned} \tag{B.6b}$$

$$\begin{aligned} R &= \frac{\hbar^2}{2m_0}\sqrt{3}\left[\gamma_2(k_y^2 - k_x^2) + 2i\gamma_3\, k_x k_y\right] \\ &= 2k^2\sqrt{\frac{2\pi}{5}}\left[\tilde{\gamma}_3(Y_{2,2} - Y_{2,-2}) - \tilde{\gamma}_2(Y_{2,2} + Y_{2,-2})\right] \end{aligned} \tag{B.6c}$$

$$= (\tilde{R}_1 Y_{2,2} + \tilde{R}_2 Y_{2,-2})k^2 \tag{B.6d}$$

$$\begin{aligned} S &= \frac{\hbar^2}{2m_0}2\sqrt{3}\,\gamma_3(k_x - ik_y)k_z \\ &= 4k^2\sqrt{\frac{2\pi}{5}}\tilde{\gamma}_3\, Y_{2,-1} = \tilde{S} Y_{2,-1}\, k^2 \end{aligned} \tag{B.6e}$$

and $\tilde{\gamma}_i = \hbar^2/(2m_0)\gamma_i$ as well as $Y_{\ell,m} = Y_{\ell,m}(\Omega_k)$. The γ_i are known as Luttinger parameters and connect to the SH parameters in the following way

$$\gamma_1 = -A_1 \tag{B.7a}$$

$$\gamma_2 = \frac{A_2}{6} \tag{B.7b}$$

$$\gamma_3 = \frac{A_3}{6} \tag{B.7c}$$

B.1.3. Suzuki-Hensel parameters

The A_i parameters correspond to the interband coupling as they are found in $H^{(2)}$, or in Eqs. (B.1), respectively. They can be expressed as [75]

$$A_1 = 1 + \frac{1}{3}\left(F + 2G + 2H_1 + 2H_2\right) , \tag{B.8a}$$

$$A_2 = -F - 2G + H_1 + H_2 , \tag{B.8b}$$

$$A_3 = -F + G - H_1 + H_2 , \tag{B.8c}$$

with the coupling parameters used as they are defined in Eqs. (B.3). The B_i parameters are all connected to the momentum dependent spin-orbit coupling; hence, they are connected to $H_{\mathrm{so,k}}$. They are related to each other by

$$B_2 = B_3 = -\frac{3}{2}B_1 = \Delta_{\mathrm{k}} , \tag{B.9}$$

with Δ_{k} being defined in Eq. (2.17).

The fitted SH parameters from Eq. (2.25) can be used to approximate the band coupling constants given in Eqs. (B.8). From the several band structure calculations [54–59] and in agreement with Fig. 2.2, we recognise that there exist no bands with symmetry Γ_2^- close to the Γ_5^+ valence band, thus according to Eq. (B.3a), we assume $F \simeq 0$. Then the system of equations (B.8) is solvable and we receive the band coupling constants as

$$G = -2.943 , \qquad H_1 = -0.979 , \qquad H_2 = -0.305 . \tag{B.10}$$

The coupling constant G dominates, as anticipated with the Γ_3^- conduction band being closest to the Γ_5^+ valence band. It is peculiar that all three coupling constants are negative, implying that the Γ_5^+ valence band is predominantly interacting with the conduction bands. Taking a look at Fig. 2.2, this is not surprising for G and H_2; however, for H_1 we would have expected the highest Γ_4^- valence band to yield a stronger influence on the Γ_5^+ valence band structure due to its energetically close positioning. The negative value of H_1 though indicates that the coupling strength of the Γ_4^- valence band is overcompensated significantly by the two higher located Γ_4^- conduction bands.
With the band coupling constants it is possible to calculate the dipole transition matrix elements given in Eqs. (B.3). This is of further interest in section 5.3.

B.2. Composition of S exciton wave functions

The yellow and green series of excitons in Cu_2O both stem from the coupling of the Γ_6^+ conduction band to the Γ_7^+ and Γ_8^+ valence band, respectively. However, both valence bands originate from the same Γ_5^+ valence band that subsequently splits due to spin-orbit interaction. Thus, the Bloch functions occurring in the transition matrix elements are still constructed from the Γ_5^+ valence band basis functions $\varepsilon_1^+ \sim yz$, $\varepsilon_2^+ \sim xz$, $\varepsilon_3^+ \sim xy$. The same holds true for the blue and violet exciton series'. With the aid of the coupling coefficients of the O_h point group [70], we can construct the bands of interest, starting with the Γ_7^+ valence band

$$\begin{aligned}
|7\mathrm{v}, -\tfrac{1}{2}\rangle &= -\frac{1}{\sqrt{3}}\big(\,\mathrm{i}|yz\rangle \otimes |s_\mathrm{h}^+\rangle + |xz\rangle \otimes |s_\mathrm{h}^+\rangle - \mathrm{i}|xy\rangle \otimes |s_\mathrm{h}^-\rangle\,\big)\,, \\
|7\mathrm{v}, +\tfrac{1}{2}\rangle &= -\frac{1}{\sqrt{3}}\big(\,\mathrm{i}|yz\rangle \otimes |s_\mathrm{h}^-\rangle - |xz\rangle \otimes |s_\mathrm{h}^-\rangle + \mathrm{i}|xy\rangle \otimes |s_\mathrm{h}^+\rangle\,\big)\,,
\end{aligned} \tag{B.11}$$

and the Γ_8^+ valence band

$$\begin{aligned}
|8\mathrm{v}, -\tfrac{3}{2}\rangle &= \frac{1}{\sqrt{6}}\big(\,-\mathrm{i}|yz\rangle \otimes |s_\mathrm{h}^-\rangle + |xz\rangle \otimes |s_\mathrm{h}^-\rangle + 2\mathrm{i}|xy\rangle \otimes |s_\mathrm{h}^+\rangle\,\big)\,, \\
|8\mathrm{v}, -\tfrac{1}{2}\rangle &= \frac{1}{\sqrt{2}}\big(\,\mathrm{i}|yz\rangle \otimes |s_\mathrm{h}^+\rangle - |xz\rangle \otimes |s_\mathrm{h}^+\rangle\,\big)\,, \\
|8\mathrm{v}, +\tfrac{1}{2}\rangle &= -\frac{1}{\sqrt{2}}\big(\,\mathrm{i}|yz\rangle \otimes |s_\mathrm{h}^-\rangle + |xz\rangle \otimes |s_\mathrm{h}^-\rangle\,\big)\,, \\
|8\mathrm{v}, +\tfrac{3}{2}\rangle &= \frac{1}{\sqrt{6}}\big(\,\mathrm{i}|yz\rangle \otimes |s_\mathrm{h}^+\rangle + |xz\rangle \otimes |s_\mathrm{h}^+\rangle + 2\mathrm{i}|xy\rangle \otimes |s_\mathrm{h}^-\rangle\,\big)\,.
\end{aligned} \tag{B.12}$$

In a similar fashion we can express the Γ_6^+ conduction band

$$\begin{aligned}
|6\mathrm{c}, -\tfrac{1}{2}\rangle &= |\alpha^+\rangle \otimes |s_\mathrm{e}^-\rangle\,, \\
|6\mathrm{c}, +\tfrac{1}{2}\rangle &= |\alpha^+\rangle \otimes |s_\mathrm{e}^+\rangle\,,
\end{aligned} \tag{B.13}$$

and the Γ_8^- conduction band

$$\begin{aligned}
|8\mathrm{c}, -\tfrac{3}{2}\rangle &= |\gamma_2^-\rangle \otimes |s_\mathrm{e}^+\rangle \\
|8\mathrm{c}, -\tfrac{1}{2}\rangle &= |\gamma_1^-\rangle \otimes |s_\mathrm{e}^-\rangle \\
|8\mathrm{c}, +\tfrac{1}{2}\rangle &= -|\gamma_1^-\rangle \otimes |s_\mathrm{e}^+\rangle \\
|8\mathrm{c}, +\tfrac{3}{2}\rangle &= -|\gamma_2^-\rangle \otimes |s_\mathrm{e}^-\rangle\,,
\end{aligned} \tag{B.14}$$

with α^+ and γ_i^- denoting the basis functions of Γ_1^+ and Γ_3^- symmetry, respectively. The indices on $s^\pm$ denote electron (e) and hole (h) spin functions. To simplify the calculations we transform

the hole spin functions into the "missing electron scheme" according to

$$|s_{\mathrm{h}}^{+}\rangle = |s_{\mathrm{e}}^{-}\rangle\,, \tag{B.15a}$$

$$|s_{\mathrm{h}}^{-}\rangle = -|s_{\mathrm{e}}^{+}\rangle\,. \tag{B.15b}$$

Those band states compose the four exciton series. The different states of each series are given as superpositions of these band states. Again, they are determined by the coupling coefficients of the O_{h} group [70]. For the yellow series we receive $\Gamma_{6\mathrm{c}}^{+} \otimes \Gamma_{7\mathrm{v}}^{+} = \Gamma_2^{+} \oplus \Gamma_5^{+}$

$$\begin{aligned}
|2\rangle_{\mathrm{y}} &= \frac{1}{\sqrt{2}}\big(\,|6\mathrm{c},+\tfrac{1}{2}\rangle|7\mathrm{v},-\tfrac{1}{2}\rangle - |6\mathrm{c},-\tfrac{1}{2}\rangle|7\mathrm{v},+\tfrac{1}{2}\rangle\,\big)\,,\\
|YZ\rangle_{\mathrm{y}} &= \frac{\mathrm{i}}{\sqrt{2}}\big(\,|6\mathrm{c},+\tfrac{1}{2}\rangle|7\mathrm{v},+\tfrac{1}{2}\rangle - |6\mathrm{c},-\tfrac{1}{2}\rangle|7\mathrm{v},-\tfrac{1}{2}\rangle\,\big)\,,\\
|XZ\rangle_{\mathrm{y}} &= \frac{1}{\sqrt{2}}\big(\,|6\mathrm{c},-\tfrac{1}{2}\rangle|7\mathrm{v},-\tfrac{1}{2}\rangle + |6\mathrm{c},+\tfrac{1}{2}\rangle|7\mathrm{v},+\tfrac{1}{2}\rangle\,\big)\,,\\
|XY\rangle_{\mathrm{y}} &= -\frac{\mathrm{i}}{\sqrt{2}}\big(\,|6\mathrm{c},+\tfrac{1}{2}\rangle|7\mathrm{v},-\tfrac{1}{2}\rangle + |6\mathrm{c},-\tfrac{1}{2}\rangle|7\mathrm{v},+\tfrac{1}{2}\rangle\,\big)\,,
\end{aligned} \tag{B.16}$$

for the green series $\Gamma_{6\mathrm{c}}^{+} \otimes \Gamma_{8\mathrm{v}}^{+} = \Gamma_3^{+} \oplus \Gamma_4^{+} \oplus \Gamma_5^{+}$

$$\begin{aligned}
|3_1\rangle_{\mathrm{g}} &= -\frac{1}{2}\big(\,|6\mathrm{c},-\tfrac{1}{2}\rangle|8\mathrm{v},+\tfrac{1}{2}\rangle + |6\mathrm{c},+\tfrac{1}{2}\rangle|8\mathrm{v},-\tfrac{1}{2}\rangle\,\big)\,,\\
|3_2\rangle_{\mathrm{g}} &= -\frac{1}{2}\big(\,|6\mathrm{c},-\tfrac{1}{2}\rangle|8\mathrm{v},-\tfrac{3}{2}\rangle + |6\mathrm{c},+\tfrac{1}{2}\rangle|8\mathrm{v},+\tfrac{3}{2}\rangle\,\big)\,,\\
|X\rangle_{\mathrm{g}} &= \frac{\mathrm{i}}{\sqrt{8}}\big(\sqrt{3}|6\mathrm{c},-\tfrac{1}{2}\rangle|8\mathrm{v},+\tfrac{3}{2}\rangle + \sqrt{3}|6\mathrm{c},+\tfrac{1}{2}\rangle|8\mathrm{v},-\tfrac{3}{2}\rangle - |6\mathrm{c},-\tfrac{1}{2}\rangle|8\mathrm{v},-\tfrac{1}{2}\rangle - |6\mathrm{c},+\tfrac{1}{2}\rangle|8\mathrm{v},+\tfrac{1}{2}\rangle\,\big)\,,\\
|Y\rangle_{\mathrm{g}} &= \frac{1}{\sqrt{8}}\big(|6\mathrm{c},-\tfrac{1}{2}\rangle|8\mathrm{v},-\tfrac{1}{2}\rangle + \sqrt{3}|6\mathrm{c},-\tfrac{1}{2}\rangle|8\mathrm{v},+\tfrac{3}{2}\rangle - \sqrt{3}|6\mathrm{c},+\tfrac{1}{2}\rangle|8\mathrm{v},-\tfrac{3}{2}\rangle - |6\mathrm{c},+\tfrac{1}{2}\rangle|8\mathrm{v},+\tfrac{1}{2}\rangle\,\big)\,,\\
|Z\rangle_{\mathrm{g}} &= \frac{\mathrm{i}}{\sqrt{2}}\big(\,|6\mathrm{c},+\tfrac{1}{2}\rangle|8\mathrm{v},-\tfrac{1}{2}\rangle - |6\mathrm{c},-\tfrac{1}{2}\rangle|8\mathrm{v},\tfrac{1}{2}\rangle\,\big)\,,\\
|YZ\rangle_{\mathrm{g}} &= -\frac{\mathrm{i}}{\sqrt{3}}\big(\sqrt{3}|6\mathrm{c},-\tfrac{1}{2}\rangle|8\mathrm{v},-\tfrac{1}{2}\rangle + |6\mathrm{c},-\tfrac{1}{2}\rangle|8\mathrm{v},+\tfrac{3}{2}\rangle + |6\mathrm{c},+\tfrac{1}{2}\rangle|8\mathrm{v},-\tfrac{3}{2}\rangle + \sqrt{3}|6\mathrm{c},+\tfrac{1}{2}\rangle|8\mathrm{v},+\tfrac{1}{2}\rangle\big)\,,\\
|XZ\rangle_{\mathrm{g}} &= -\frac{1}{\sqrt{3}}\big(\sqrt{3}|6\mathrm{c},-\tfrac{1}{2}\rangle|8\mathrm{v},-\tfrac{1}{2}\rangle - |6\mathrm{c},-\tfrac{1}{2}\rangle|8\mathrm{v},+\tfrac{3}{2}\rangle + |6\mathrm{c},+\tfrac{1}{2}\rangle|8\mathrm{v},-\tfrac{3}{2}\rangle - \sqrt{3}|6\mathrm{c},+\tfrac{1}{2}\rangle|8\mathrm{v},+\tfrac{1}{2}\rangle\big)\,,\\
|XY\rangle_{\mathrm{g}} &= \frac{\mathrm{i}}{2}\big(\,|6\mathrm{c},+\tfrac{1}{2}\rangle|8\mathrm{v},+\tfrac{3}{2}\rangle - |6\mathrm{c},-\tfrac{1}{2}\rangle|8\mathrm{v},-\tfrac{3}{2}\rangle\big)\,,
\end{aligned} \tag{B.17}$$

and in the same fashion, we receive the individual states for the blue $\Gamma_{8\mathrm{c}}^{-} \otimes \Gamma_{7\mathrm{v}}^{+} = \Gamma_3^{-} \oplus \Gamma_4^{-} \oplus \Gamma_5^{-}$ and the violet series $\Gamma_{8\mathrm{c}}^{-} \otimes \Gamma_{8\mathrm{v}}^{+} = \Gamma_1^{-} \oplus \Gamma_2^{-} \oplus \Gamma_3^{-} \oplus 2\Gamma_4^{-} \oplus 2\Gamma_5^{-}$. For our purposes it is sufficient to concern ourselves only with their Γ_4^{-} states, as they are the only ones that are accessible via the dipole operator $\mathbf{p}$. Also is satisfactory to investigate only one state since the result for all spatial orientations should be equivalent due to the cubic symmetry. For the blue excitons, the

Γ_4^- state of interest is

$$|Z\rangle_{\mathrm{b}} = \frac{\mathrm{i}}{\sqrt{2}}\big(\,|8\mathrm{c},+\tfrac{3}{2}\rangle|7\mathrm{v},+\tfrac{1}{2}\rangle - |8\mathrm{c},-\tfrac{3}{2}\rangle|7\mathrm{v},-\tfrac{1}{2}\rangle\,\big)\,, \tag{B.18}$$

the violet series possesses two Γ_4^- states

$$\begin{aligned}
|Z\rangle_{\mathrm{v},1} &= \frac{\mathrm{i}}{\sqrt{20}}\big(|8\mathrm{c},-\tfrac{1}{2}\rangle|8\mathrm{v},+\tfrac{1}{2}\rangle + |8\mathrm{c},+\tfrac{1}{2}\rangle|8\mathrm{v},-\tfrac{1}{2}\rangle - 3|8\mathrm{c},+\tfrac{3}{2}\rangle|8\mathrm{v},-\tfrac{3}{2}\rangle - 3|8\mathrm{c},-\tfrac{3}{2}\rangle|8\mathrm{v},+\tfrac{3}{2}\rangle\big)\,,\\
|Z\rangle_{\mathrm{v},2} &= \frac{-\mathrm{i}}{\sqrt{20}}\big(3|8\mathrm{c},-\tfrac{1}{2}\rangle|8\mathrm{v},+\tfrac{1}{2}\rangle + 3|8\mathrm{c},+\tfrac{1}{2}\rangle|8\mathrm{v},-\tfrac{1}{2}\rangle + |8\mathrm{c},+\tfrac{3}{2}\rangle|8\mathrm{v},-\tfrac{3}{2}\rangle + |8\mathrm{c},-\tfrac{3}{2}\rangle|8\mathrm{v},+\tfrac{3}{2}\rangle\big)\,.
\end{aligned} \tag{B.19}$$

All these states are only applicable to S-like excitons, since the symmetry of the envelope function was not taken into consideration.

B.3. Transition strength of the Cu_2O exciton series

The dipole operator $\mathbf{p}$ has symmetry Γ_4^- while the operator $(\mathbf{e}\cdot\mathbf{p})(\mathbf{k}\cdot\mathbf{r})$, resulting from the expansion of the plane wave $\mathrm{e}^{\mathrm{i}\mathbf{k}\cdot\mathbf{r}}$, yields the symmetry $\Gamma_4^- \otimes \Gamma_4^- = \Gamma_1^+ \oplus \Gamma_3^+ \oplus \Gamma_4^+ \oplus \Gamma_5^+$, which corresponds to the electric quadrupole ($\Gamma_3^+ \oplus \Gamma_5^+$) and the magnetic dipole transitions (Γ_4^+). We are denoting the band to band quadrupole transition matrix element between the $\Gamma_{5\mathrm{v}}^+$ and the $\Gamma_{1\mathrm{c}}^+$ band as

$$\langle\varepsilon_3^+|\,\boldsymbol{\mathcal{Q}}\,|\alpha^+\rangle = \frac{1}{\sqrt{3}}\mathcal{Q}_{15}\,, \tag{B.20}$$

and the band to band dipole transition matrix element between $\Gamma_{5\mathrm{v}}^+$ and $\Gamma_{3\mathrm{c}}^-$ bands as

$$\langle\varepsilon_3^+|\,\mathbf{p}\,|\gamma_2^-\rangle = \mathcal{P}_{35}\,. \tag{B.21}$$

The dipole transition element is known from the fit of the SH Hamiltonian, as it appears in Eq. (B.3b). We are now able to calculate the relative strength of the quadrupole transition for the yellow and green, as well as the dipole transition strength of the blue and violet transition, respectively. For the yellow and green exciton series only the orthoexcitons are quadrupole excitable; thus, we are only interested in excitons with Γ_5^+ symmetry. Due to the cubic symmetry of the semiconductor the oscillator strength of all states should be the same; hence, it is sufficient to investigate only one state. By inserting Eqs. (B.11), (B.12) and (B.13) into Eqs. (B.16)

and (B.17) we receive for the quadrupole matrix elements

$$\langle 0|\,\boldsymbol{\mathcal{Q}}\,|XY\rangle_{\mathrm{y}} = -\frac{\sqrt{2}}{3}\,\mathcal{Q}_{15}\,, \tag{B.22}$$

$$\langle 0|\,\boldsymbol{\mathcal{Q}}\,|XY\rangle_{\mathrm{g}} = \frac{2}{3}\,\mathcal{Q}_{15}\,. \tag{B.23}$$

This implies that the oscillator strength for the direct quadrupole transition is twice as strong for the green series as for the yellow series orthoexcitons

$$f_{\mathrm{y}} : f_{\mathrm{g}} \;=\; 1:2\,. \tag{B.24}$$

The relative transition strength of the blue and violet exciton states can be calculated in a similar fashion. We are only interested in the Γ_4^- states since they are accessible via the dipole operator $\mathbf{p}$. The resulting dipole transition matrix elements then read as

$$\langle 0|\,\mathbf{p}\,|Z\rangle_{\mathrm{b}} = -\sqrt{\frac{2}{3}}\,\mathcal{P}_{35}\,, \tag{B.25}$$

$$\langle 0|\,\mathbf{p}\,|Z\rangle_{\mathrm{v},1} = -\sqrt{\frac{6}{5}}\,\mathcal{P}_{35}\,, \tag{B.26}$$

$$\langle 0|\,\mathbf{p}\,|Z\rangle_{\mathrm{v},2} = -\sqrt{\frac{2}{15}}\,\mathcal{P}_{35}\,, \tag{B.27}$$

which consequently yields the ratio between oscillator strengths for a direct dipole transition to be

$$f_{\mathrm{b}} : f_{\mathrm{v},1} : f_{\mathrm{v},2} \;=\; 1 : \frac{9}{5} : \frac{1}{5}\,. \tag{B.28}$$

For the phonon assisted transition that was investigated in chapter 5, we additionally need to consider the transition strength of the phonon process. The transition probability has the form

$$P_{0,\mu} \propto \sum_{\lambda} \left| \sum_{\nu} \langle \Psi_\mu | h_\lambda | \Psi_\nu \rangle \langle \Psi_\nu | \mathbf{p} | \Psi_0 \rangle \right|^2 . \tag{B.29}$$

As we are primarily interested in the transition that is facilitated by the Γ_3^- phonon, we restrict the sum over λ to the constituents of this respective phonon branch. The intermediate blue and violet states possess Γ_4^- symmetry and thus, the Γ_3^- phonon can theoretically scatter into $\Gamma_4^- \otimes \Gamma_3^- = \Gamma_4^+ \oplus \Gamma_5^+$ states. For the yellow series only the Γ_5^+ iton states contribute, the green series exhibits Γ_5^+ ortho- as well as Γ_4^+ paraexciton states. However, since the Γ_3^- phonon transition cannot inflict a change to the spin-configuration of the intermediate state, the scattering into Γ_4^+ states is not occurring, i.e. the blue and violet Γ_4^- states are orthoexcitons; therefore, the phonon can only scatter into other orthoexcitons. This can also readily be seen when the coupling strengths of the transitions are evaluated, where the Γ_4^+ participating states cancel

each other out. The Γ_3^- phonon transition operator[1] h_3 has two constituents, η_{3_1} and η_{3_2}. Their coupling between the Γ_8^- and Γ_6^+ conduction band can be expressed via

$$\eta_{3_1}\begin{pmatrix}|8\mathrm{c},-\frac{3}{2}\rangle\\|8\mathrm{c},-\frac{1}{2}\rangle\\|8\mathrm{c},+\frac{1}{2}\rangle\\|8\mathrm{c},+\frac{3}{2}\rangle\end{pmatrix}=\frac{\tilde{D}_{3;68}}{\sqrt{2}}\begin{pmatrix}0\\|6\mathrm{c},-\frac{1}{2}\rangle\\-|6\mathrm{c},+\frac{1}{2}\rangle\\0\end{pmatrix}, \tag{B.30}$$

$$\eta_{3_2}\begin{pmatrix}|8\mathrm{c},-\frac{3}{2}\rangle\\|8\mathrm{c},-\frac{1}{2}\rangle\\|8\mathrm{c},+\frac{1}{2}\rangle\\|8\mathrm{c},+\frac{3}{2}\rangle\end{pmatrix}=\frac{\tilde{D}_{3;68}}{\sqrt{2}}\begin{pmatrix}-|6\mathrm{c},+\frac{1}{2}\rangle\\0\\0\\|6\mathrm{c},-\frac{1}{2}\rangle\end{pmatrix}, \tag{B.31}$$

with $\tilde{D}_{\lambda,ij}=\langle\psi_i|h_\lambda|\psi_j\rangle=\hbar D_{\lambda,ij}/\sqrt{2\Omega\rho\,E_\lambda}$. The transformed intermediate Γ_4^- states receive the structure of their Γ_5^+ counterparts, and utilising the orthonormality of the exciton states then eliminates coupling to most of the states. The phonon transition elements then read as follows

$$_{\mathrm{y}}\langle XY|\,\eta_{3_1}\,|Z\rangle_{\mathrm{b}}\;=0\,, \tag{B.32}$$

$$_{\mathrm{y}}\langle XY|\,\eta_{3_2}\,|Z\rangle_{\mathrm{b}}\;=-\frac{\tilde{D}_{3;68}}{\sqrt{2}}\,, \tag{B.33}$$

$$_{\mathrm{g}}\langle XY|\,\eta_{3_1}\,|Z\rangle_{\mathrm{v}_1}=0\,, \tag{B.34}$$

$$_{\mathrm{g}}\langle XY|\,\eta_{3_2}\,|Z\rangle_{\mathrm{v}_1}=-\frac{3}{2}\frac{\tilde{D}_{3;68}}{\sqrt{5}}\,, \tag{B.35}$$

$$_{\mathrm{g}}\langle XY|\,\eta_{3_1}\,|Z\rangle_{\mathrm{v}_2}=0\,, \tag{B.36}$$

$$_{\mathrm{g}}\langle XY|\,\eta_{3_2}\,|Z\rangle_{\mathrm{v}_2}=-\frac{1}{2}\frac{\tilde{D}_{3;68}}{\sqrt{2}}\,, \tag{B.37}$$

In this case, the choice of our intermediate states spares us from a separate evaluation of the η_{3_1} component. The transition probability for the phonon assisted transition into the yellow series is then given by

$$P_{0,\mathrm{y}}\propto|\,_{\mathrm{y}}\langle XY|\,\eta_{3_2}\,|Z\rangle_{\mathrm{b}}\;{}_{\mathrm{b}}\langle Z|\,\mathbf{p}\,|0\rangle\,|^2=\frac{1}{3}\tilde{D}_{3;68}^2\,\mathcal{P}_{35}^2\,, \tag{B.38}$$

[1]The momentum subscript $\mathbf{Q}$ as introduced in chapter 5 is dropped here, since it carries no relevance in these considerations and strictly speaking the symmetry restriction only apply for $\mathbf{Q}=0$.

the transition probability into the green series results in

$$P_{0,\mathrm{g}} \propto \left| \sum_{i=1}^{2} {}_{\mathrm{g}}\langle XY|\, \eta_{3_2}\, |Z\rangle_{\mathrm{v}_i}\, {}_{\mathrm{v}_i}\langle Z|\, \mathbf{p}\, |0\rangle \right|^2 = \frac{2}{3} \tilde{D}_{3;68}^2\, \mathcal{P}_{35}^2 \,. \tag{B.39}$$

From this, we concur that the ratio of oscillator strength between yellow and green phonon-assisted absorption has to be

$$f_{\mathrm{y,b}}^{(3)} : f_{\mathrm{g,v}}^{(3)} \;=\; 1 : 2 \,. \tag{B.40}$$

B.4. Minor absorption contributions of section 5.3.3

While the Γ_3^- phonon process inherits a great portion of the absorption background, there are still other processes that need to be addressed to reproduce the absorption shape faithfully. The absorption of the Γ_4^- LO phonon has already been discussed at the end of section 5.2. Its absorption edge is visible in Fig. 5.1 and will be fitted via Eq. (5.21). It results in

$$\left(\frac{|p_{74_1}|^2}{m_0} \frac{|D_{4;4_16}|^2}{(E_{4c_1} - E_{1c})^2} + \frac{|p_{74_2}|^2}{m_0} \frac{|D_{4;4_26}|^2}{(E_{4c_2} - E_{1c})^2} + \frac{|p_{64_3}|^2}{m_0} \frac{|D_{4;4_37}|^2}{(E_{4v_3})^2} \right) = 391.9 \, \frac{\mathrm{eV}}{\mathrm{nm}^2} \,. \tag{B.41}$$

This fit is imprecise and should only be considered as an indication of its magnitude for several reasons. There are potentially three bands that contribute to this process, which we cannot effectively distinguish. Additionally, their precise positions in the band structure are not known. The momentum dependence of the deformation potentials is neglected. The absorbtion edge is very close to the $2\mathrm{P}$ resonance, which only leaves a small energy range for fitting. The photon energy in the denominator is set to the gap energy since those three bands are supposedly far away from the band gap. Also, we only consider the absorption into the $1\mathrm{S}$ state since its general contribution is miniscule.

To achieve a well-rounded depiction of the absorption spectrum, the absorption into yellow P exciton states needs to be considered. In this case, there will be no further derivation nor explanation of the equations used, as this only represents an empirical fit upon the phonon-assisted absorption into the S states. For detailed information, see the respective citations.
The P absorption can be divided into three separate parts: The exciton resonances below the band gap, the direct absorption into the continuum, and the phenomenological Urbach tail

$$\alpha_{\mathrm{P}} = \sum_{n=2} \alpha_{n\mathrm{P}} + \alpha_{\mathrm{Pcont}} + \alpha_{\mathrm{Urbach}} \,. \tag{B.42}$$

Since the fit of the resonances requires the substraction of the Urbach tail, which subsequently depends on the absorption strength into the continuum, we start off by fitting the continuum

n	2P	3P	4P
$\hbar\omega_n$ [11] (eV)	2.1472	2.1612	2.16604
$C_{n\mathrm{P}}$ (10^{-5}eV/μm)	1.587	0.793	0.2645
$\Gamma_{n\mathrm{P}}$ (meV)	3.86	1.93	1.29
$\xi_{n\mathrm{P}}$ (10^{-3})	-4.32	-4.32	-4.32

Table B.1.: Fit parameters for the P exciton resonances in the $10\,\mu$m sample [108].

first. It corresponds to the direct transition between the $\Gamma_{1\mathrm{c}}$ and $\Gamma_{5\mathrm{v}}$ bands, enhanced by a Sommerfeld factor and is given by [51, 119]

$$\alpha_{\mathrm{Pcont}}(\omega) = C_{\mathrm{yP}} \frac{(\hbar\omega - \tilde{E}_{\mathrm{y}})^{3/2}}{\hbar\omega} \frac{\gamma\, e^{\gamma}}{\sinh\gamma} \left(1 + \frac{\gamma^2}{\pi^2}\right), \tag{B.43}$$

with

$$\gamma = \sqrt{\frac{\pi^2\,\mathrm{Ry}^{(\mathrm{y})}}{\hbar\omega - \tilde{E}_{\mathrm{y}}}}, \tag{B.44}$$

and C_{yP} incorporating the direct transition matrix element. Recently, it was shown that the continuum absorption is shifted by an energy Δ_{c} into the P states due to plasma screening of charged residual impurities [31]. The renormalised band gap $\tilde{E}_{\mathrm{y}} = E_{\mathrm{y}} + \Delta_{\mathrm{c}}$ reflects the band gap shift due to plasma screening. It depends on the sample properties and thus is different for the thick and thin sample. Here, we are only interested in the thin ($10\,\mu$m) sample. Roughly, Δ_{c} can be estimated from the energy of the highest visible P exciton line ($n_{\mathrm{max}} = 4$) via $-87\,\mathrm{meV}/n_{\mathrm{max}}^2$. The fit of the direct transition strength yields

$$C_{\mathrm{yP}} = 9.82 \times 10^{-02}\,(\sqrt{\mathrm{eV}}\,\mu\mathrm{m})^{-1}\,. \tag{B.45}$$

The Urbach tail is given by [139, 140]

$$\alpha_{\mathrm{Urbach}}(\omega) = C_{\mathrm{U}} \exp\left(\frac{\hbar\omega - \tilde{E}_{\mathrm{y}}}{E_{\mathrm{U}}}\right) \theta(\tilde{E}_{\mathrm{y}} - \hbar\omega)\,, \tag{B.46}$$

with E_U being the Urbach parameter. The fit results in $C_{\mathrm{U}} = 7.34 \times 10^{-03}\,\mu\mathrm{m}^{-1}$ and $E_{\mathrm{U}} = 9.8\,\mathrm{meV}$. The oscillator strength of the P resonances varies with principal quantum number as $(n^2-1)/n^5$. The lineshape of the excitons can be described via asymmetric Lorentzians as derived by Toyozawa [13, 141]

$$\alpha_{n\mathrm{P}}(\omega) = C_{n\mathrm{P}} \frac{\Gamma_{n\mathrm{P}}/2 + 2\xi_{n\mathrm{P}}\,\hbar(\omega - \omega_n)}{(\Gamma_{n\mathrm{P}}/2)^2 + \hbar^2(\omega - \omega_n)^2}\,, \tag{B.47}$$

where $C_{n\mathrm{P}}$ is proportional to the oscillator strength, $\Gamma_{n\mathrm{P}}$ the natural linewidth, ω_n the resonance frequency and $\xi_{n\mathrm{P}}$ the asymmetry parameter. The resulting values of these parameters are listed in Tab. B.1.

Appendix C.

List of publications

C.1. Published papers

(I) F. Schöne, S. O. Krüger, P. Grünwald, H. Stolz, S. Scheel, M. Aßmann, J. Heckötter, J. Thewes, D. Fröhlich, and M. Bayer
"Deviations of the exciton level spectrum in Cu_2O from the hydrogen series"
Phys. Rev. B **93**, 075203 (2016).

(II) F. Schöne, S. O. Krüger, P. Grünwald, M. Aßmann, J. Heckötter, J. Thewes, H. Stolz, D. Fröhlich, M. Bayer, and S. Scheel
"Coupled valence band dispersions and the quantum defect of excitons in Cu_2O"
J. Phys. B: At. Mol. Opt. Phys **49**, 134003 (2016).

(III) F. Schöne, H. Stolz, and N. Naka
"Phonon-assisted absorption of excitons in Cu_2O"
Phys. Rev. B **96**, 115207 (2017).

(IV) D. Semkat, S. Sobkowiak, F. Schöne, H. Stolz, Th. Koch, and H. Fehske
"Multicomponent exciton gas in cuprous oxide: cooling behaviour and the role of Auger decay"
J. Phys. B: At. Mol. Opt. Phys **50**, 204001 (2017).

C.2. Submitted papers

(I) J. Heckötter, M. Freitag, D. Fröhlich, M. Aßmann, M. Bayer, P. Grünwald, F. Schöne, D. Semkat, H. Stolz, and S. Scheel
"Rydberg excitons in the presence of an ultralow-density electron-hole plasma"
submitted on the 14/08/2017 to *Phys. Rev. Lett.*

(II) H. Stolz, F. Schöne, and D. Semkat
"Interaction of Rydberg Excitons in Cuprous Oxide with Phonons and Photons: Optical Linewidth and Polariton Effect"
submitted on the 01/09/2017 to *New J. Phys.*

C.3. Conference contributions

(I) DPG Spring Meeting 2015 (Condensed Matter Section)
Berlin, Germany, 15/03-20/03/2015
F. Schöne, H. Stolz, and S. Scheel
Talk: "Quantum defects of the Rydberg series for cuprous oxide"

(II) Fundamental optical processes in semiconductors (FOPS) 2015
Breckenridge, Colorado, USA, 02/08-07/08/2015
F. Schöne, H. Stolz, and S. Scheel
Poster: "Quantum defect of the Rydberg series of cuprous oxide"

(III) Correlation Effects in Radiation Fields (CERF) 2015
Rostock, Germany, 13/09-18/09/2015
F. Schöne, H. Stolz, and S. Scheel
Poster: "Quantum defect of the Rydberg series of cuprous oxide"

(IV) 33rd International Conference on the Physics of Semiconductors
Beijing, China, 31/07-05/08/2016
F. Schöne, and H. Stolz
Poster: "Auger decay of excitons in Cu_2O revisited"

(V) DPG Spring Meeting 2017 (Condensed Matter Section)
Dresden, Germany, 19/03-24/03/2017
F. Schöne, and H. Stolz
Poster: "Phonon assisted absorption in Cu_2O"

(VI) Fundamental optical processes in semiconductors (FOPS) 2017
Stevenson, Washington, USA, 27/08-01/09/2017
F. Schöne, H. Stolz, and N. Naka
Poster: "Phonon assisted absorption in Cu_2O"

Bibliography

[1] FRENKEL, J.: On the Transformation of light into Heat in Solids. I. In: *Phys. Rev.* 37 (1931), Jan, 17–44. http://dx.doi.org/10.1103/PhysRev.37.17. – DOI 10.1103/PhysRev.37.17

[2] FRENKEL, J.: On the Transformation of Light into Heat in Solids. II. In: *Phys. Rev.* 37 (1931), May, 1276–1294. http://dx.doi.org/10.1103/PhysRev.37.1276. – DOI 10.1103/PhysRev.37.1276

[3] PEIERLS, R.: Zur Theorie der Absorptionsspektren fester Körper. In: *Annalen der Physik* 405 (1932), Nr. 8, 905–952. http://dx.doi.org/10.1002/andp.19324050803. – DOI 10.1002/andp.19324050803. – ISSN 1521–3889

[4] WANNIER, Gregory H.: The Structure of Electronic Excitation Levels in Insulating Crystals. In: *Phys. Rev.* 52 (1937), Aug, 191–197. http://dx.doi.org/10.1103/PhysRev.52.191. – DOI 10.1103/PhysRev.52.191

[5] GROSS, E. F. ; KARRYEV, N. A.: Pogloshchenie sveta kristallom zakisi medi v infrakrasnoi i vidimoi chasti spektra. In: *Doklady Akademii Nauk SSSR* 84 (1952), Nr. 2, S. 261–264

[6] GROSS, E. F.: Optical spectrum of excitons in the crystal lattice. In: *Il Nuovo Cimento (1955-1965)* 3 (1956), Nr. 4, S. 672–701

[7] GROSS, E. F.: Excitons and their motion in crystal lattices. In: *Soviet Physics Uspekhi* 5 (1962), Nr. 2, 195. http://stacks.iop.org/0038-5670/5/i=2/a=A03

[8] HAYASHI, Masakazu ; KATSUKI, Kiichiro: Hydrogen-Like Absorption Spectrum of Cuprous Oxide. In: *Journal of the Physical Society of Japan* 7 (1952), Nr. 6, S. 599–603. http://dx.doi.org/10.1143/JPSJ.7.599. – DOI 10.1143/JPSJ.7.599

[9] MATSUMOTO, H. ; SAITO, K. ; HASUO, M. ; KONO, S. ; NAGASAWA, N.: Revived interest on yellow-exciton series in Cu_2O: An experimental aspect. In: *Solid State Communications* 97 (1996), Nr. 2, 125 - 129. http://dx.doi.org/https://doi.org/10.1016/0038-1098(95)00601-X. – DOI https://doi.org/10.1016/0038–1098(95)00601–X. – ISSN 0038–1098

[10] MOSKALENKO, S.A. ; SNOKE, D.W.: *Bose-Einstein Condensation of Excitons and Biexcitons:*

And Coherent Nonlinear Optics with Excitons. Cambridge University Press, 2000. – ISBN 9780521580991

[11] KAZIMIERCZUK, T. ; FRÖHLICH, D. ; SCHEEL, S. ; STOLZ, H. ; BAYER, M.: Giant Rydberg excitons in the copper oxide Cu_2O. In: *Nature* 514 (2014), Nr. 7522, S. 343–347. http://dx.doi.org/http://dx.doi.org/10.1038/nature13832. – DOI http://dx.doi.org/10.1038/nature13832

[12] GALLAGHER, Thomas F.: *Rydberg Atoms*. Cambridge University Press, 2005 (Cambridge Monographs on Atomic). https://www.cambridge.org/core/books/rydberg-atoms/B610BDE54694936F496F59F326C1A81B. – ISBN 9780521021661

[13] GRÜNWALD, P. ; ASSMANN, M. ; HECKÖTTER, J. ; FRÖHLICH, D. ; BAYER, M. ; STOLZ, H. ; SCHEEL, S.: Signatures of Quantum Coherences in Rydberg Excitons. In: *Phys. Rev. Lett.* 117 (2016), Sep, 133003. http://dx.doi.org/10.1103/PhysRevLett.117.133003. – DOI 10.1103/PhysRevLett.117.133003

[14] SCHWEINER, Frank ; MAIN, Jörg ; WUNNER, Günter: Magnetoexcitons Break Antiunitary Symmetries. In: *Phys. Rev. Lett.* 118 (2017), Jan, 046401. http://dx.doi.org/10.1103/PhysRevLett.118.046401. – DOI 10.1103/PhysRevLett.118.046401

[15] SCHWEINER, Frank ; ROMMEL, Patric ; MAIN, Jörg ; WUNNER, Günter: Exciton-phonon interaction breaking all antiunitary symmetries in external magnetic fields. In: *Phys. Rev. B* 96 (2017), Jul, 035207. http://dx.doi.org/10.1103/PhysRevB.96.035207. – DOI 10.1103/PhysRevB.96.035207

[16] ASSMANN, Marc ; THEWES, Johannes ; FRÖHLICH, Dietmar ; BAYER, Manfred: Quantum chaos and breaking of all anti-unitary symmetries in Rydberg excitons. In: *Nature materials* 15 (2016), Nr. 7, S. 741–745

[17] SCHWEINER, Frank ; MAIN, Jörg ; WUNNER, Günter ; FREITAG, Marcel ; HECKÖTTER, Julian ; UIHLEIN, Christoph ; ASSMANN, Marc ; FRÖHLICH, Dietmar ; BAYER, Manfred: Magnetoexcitons in cuprous oxide. In: *Phys. Rev. B* 95 (2017), Jan, 035202. http://dx.doi.org/10.1103/PhysRevB.95.035202. – DOI 10.1103/PhysRevB.95.035202

[18] KURZ, Markus ; GRÜNWALD, Peter ; SCHEEL, Stefan: Excitonic giant-dipole potentials in cuprous oxide. In: *Phys. Rev. B* 95 (2017), Jun, 245205. http://dx.doi.org/10.1103/PhysRevB.95.245205. – DOI 10.1103/PhysRevB.95.245205

[19] BALDERESCHI, A. ; LIPARI, Nunzio C.: Energy Levels of Direct Excitons in Semiconductors with Degenerate Bands. In: *Phys. Rev. B* 3 (1971), Jan, 439–451. http://dx.doi.org/10.1103/PhysRevB.3.439. – DOI 10.1103/PhysRevB.3.439

[20] BALDERESCHI, A. ; LIPARI, Nunzio O.: Spherical Model of Shallow Acceptor States in

Semiconductors. In: *Phys. Rev. B* 8 (1973), Sep, 2697–2709. http://dx.doi.org/10.1103/PhysRevB.8.2697. – DOI 10.1103/PhysRevB.8.2697

[21] BALDERESCHI, A. ; LIPARI, Nunzio O.: Cubic contributions to the spherical model of shallow acceptor states. In: *Phys. Rev. B* 9 (1974), Feb, 1525–1539. http://dx.doi.org/10.1103/PhysRevB.9.1525. – DOI 10.1103/PhysRevB.9.1525

[22] ALTARELLI, M. ; LIPARI, N. O.: Exciton dispersion in semiconductors with degenerate bands. In: *Phys. Rev. B* 15 (1977), May, 4898–4906. http://dx.doi.org/10.1103/PhysRevB.15.4898. – DOI 10.1103/PhysRevB.15.4898

[23] KAVOULAKIS, G. M. ; CHANG, Yia-Chung ; BAYM, Gordon: Fine structure of excitons in Cu_2O. In: *Phys. Rev. B* 55 (1997), Mar, 7593–7599. http://dx.doi.org/10.1103/PhysRevB.55.7593. – DOI 10.1103/PhysRevB.55.7593

[24] THEWES, J. ; HECKÖTTER, J. ; KAZIMIERCZUK, T. ; ASSMANN, M. ; FRÖHLICH, D. ; BAYER, M. ; SEMINA, M. A. ; GLAZOV, M. M.: Observation of High Angular Momentum Excitons in Cuprous Oxide. In: *Phys. Rev. Lett.* 115 (2015), Jul, 027402. http://dx.doi.org/10.1103/PhysRevLett.115.027402. – DOI 10.1103/PhysRevLett.115.027402

[25] SCHWEINER, Frank ; MAIN, Jörg ; WUNNER, Günter ; UIHLEIN, Christoph: Even exciton series in Cu_2O. In: *Phys. Rev. B* 95 (2017), May, 195201. http://dx.doi.org/10.1103/PhysRevB.95.195201. – DOI 10.1103/PhysRevB.95.195201

[26] YU, Peter Y. ; SHEN, Y. R.: Resonance Raman studies in Cu_2O. I. The phonon-assisted $1s$ yellow excitonic absorption edge. In: *Phys. Rev. B* 12 (1975), Aug, 1377–1394. http://dx.doi.org/10.1103/PhysRevB.12.1377. – DOI 10.1103/PhysRevB.12.1377

[27] YU, Peter Y. ; SHEN, Y. R.: Resonance Raman studies in Cu_2O. II. The yellow and green excitonic series. In: *Phys. Rev. B* 17 (1978), May, 4017–4030. http://dx.doi.org/10.1103/PhysRevB.17.4017. – DOI 10.1103/PhysRevB.17.4017

[28] ALLEN, P. B. ; CARDONA, M.: Theory of the temperature dependence of the direct gap of germanium. In: *Phys. Rev. B* 23 (1981), Feb, 1495–1505. http://dx.doi.org/10.1103/PhysRevB.23.1495. – DOI 10.1103/PhysRevB.23.1495

[29] BEG, M. M. ; SHAPIRO, S. M.: Study of phonon dispersion relations in cuprous oxide by inelastic neutron scattering. In: *Phys. Rev. B* 13 (1976), Feb, 1728–1734. http://dx.doi.org/10.1103/PhysRevB.13.1728. – DOI 10.1103/PhysRevB.13.1728

[30] SANDFORT, Christian ; BRANDT, Jan ; FRÖHLICH, Dietmar ; BAYER, Manfred ; STOLZ, Heinrich: Resonant phonon scattering of paraexcitons in Cu_2O. In: *Phys. Rev. B* 78 (2008), Jul, 045201. http://dx.doi.org/10.1103/PhysRevB.78.045201. – DOI 10.1103/PhysRevB.78.045201

[31] HECKÖTTER, J ; FREITAG, M ; FRÖHLICH, D ; ASSMANN, M ; BAYER, M ; GRÜNWALD, P ; SCHÖNE, F ; SEMKAT, D ; STOLZ, H ; SCHEEL, S: Rydberg excitons in the presence of an ultralow-density electron-hole plasma. In: *arXiv preprint arXiv:1709.00891* (2017)

[32] MOSKALENKO, S.A.: Fiz. tverdogo Tela 4 (1962) 276. translation. In: *Soviet Physics-Solid State* 4 (1962), S. 199

[33] BLATT, John M. ; BÖER, K. W. ; BRANDT, Werner: Bose-Einstein Condensation of Excitons. In: *Phys. Rev.* 126 (1962), Jun, 1691–1692. http://dx.doi.org/10.1103/PhysRev.126.1691. – DOI 10.1103/PhysRev.126.1691

[34] KURODA, Hiroto ; SHIONOYA, Shigeo ; SAITO, Hiroshi ; HANAMURA, Eiichi: Bose Condensation of Excitonic Moleules in CdSe. In: *Journal of the Physical Society of Japan* 35 (1973), Nr. 2, S. 534–542. http://dx.doi.org/10.1143/JPSJ.35.534. – DOI 10.1143/JPSJ.35.534

[35] GOTO, Takenari ; ANZAI, Takuchi ; UETA, Masayasu: The Possibility of the Bose Condensation of Excitons in CuCl. In: *Journal of the Physical Society of Japan* 35 (1973), Nr. 3, S. 940–940. http://dx.doi.org/10.1143/JPSJ.35.940. – DOI 10.1143/JPSJ.35.940

[36] STOLZ, Heinrich ; SCHWARTZ, Rico ; KIESELING, Frank ; SOM, Sunipa ; KAUPSCH, Maria ; SOBKOWIAK, Siegfried ; SEMKAT, Dirk ; NAKA, Nobuko ; KOCH, Thomas ; FEHSKE, Holger: Condensation of excitons in Cu_2O at ultracold temperatures: experiment and theory. In: *New Journal of Physics* 14 (2012), Nr. 10, 105007. http://stacks.iop.org/1367-2630/14/i=10/a=105007

[37] SNOKE, D. W.: When should we say we have observed Bose condensation of excitons? In: *physica status solidi (b)* 238 (2003), Nr. 3, 389–396. http://dx.doi.org/10.1002/pssb.200303151. – DOI 10.1002/pssb.200303151. – ISSN 1521–3951

[38] KAVOULAKIS, G. M. ; BAYM, G.: Auger decay of degenerate and Bose-condensed excitons in Cu_2O. In: *Phys. Rev. B* 54 (1996), Dec, 16625–16636. http://dx.doi.org/10.1103/PhysRevB.54.16625. – DOI 10.1103/PhysRevB.54.16625

[39] O'HARA, K. E. ; GULLINGSRUD, J. R. ; WOLFE, J. P.: Auger decay of excitons in Cu_2O. In: *Phys. Rev. B* 60 (1999), Oct, 10872–10885. http://dx.doi.org/10.1103/PhysRevB.60.10872. – DOI 10.1103/PhysRevB.60.10872

[40] JANG, J. I. ; WOLFE, J. P.: Auger recombination and biexcitons in Cu_2O: A case for dark excitonic matter. In: *Phys. Rev. B* 74 (2006), Jul, 045211. http://dx.doi.org/10.1103/PhysRevB.74.045211. – DOI 10.1103/PhysRevB.74.045211

[41] HULIN, D. ; MYSYROWICZ, A. ; GUILLAUME, C. B.: Evidence for Bose-Einstein Statistics in an Exciton Gas. In: *Phys. Rev. Lett.* 45 (1980), Dec, 1970–1973. http://dx.doi.

org/10.1103/PhysRevLett.45.1970. – DOI 10.1103/PhysRevLett.45.1970

[42] WARREN, J. T. ; O'HARA, K. E. ; WOLFE, J. P.: Two-body decay of thermalized excitons in Cu_2O. In: *Phys. Rev. B* 61 (2000), Mar, 8215–8223. http://dx.doi.org/10.1103/PhysRevB.61.8215. – DOI 10.1103/PhysRevB.61.8215

[43] YOSHIOKA, Kosuke ; IDEGUCHI, Takuro ; MYSYROWICZ, André ; KUWATA-GONOKAMI, Makoto: Quantum inelastic collisions between paraexcitons in Cu_2O. In: *Phys. Rev. B* 82 (2010), Jul, 041201. http://dx.doi.org/10.1103/PhysRevB.82.041201. – DOI 10.1103/PhysRevB.82.041201

[44] DENG, Hui ; HAUG, Hartmut ; YAMAMOTO, Yoshihisa: Exciton-polariton Bose-Einstein condensation. In: *Rev. Mod. Phys.* 82 (2010), May, 1489–1537. http://dx.doi.org/10.1103/RevModPhys.82.1489. – DOI 10.1103/RevModPhys.82.1489

[45] RAKHSHANI, A.E.: Preparation, characteristics and photovoltaic properties of cuprous oxide—a review. In: *Solid-State Electronics* 29 (1986), Nr. 1, 7 - 17. http://dx.doi.org/https://doi.org/10.1016/0038-1101(86)90191-7. – DOI https://doi.org/10.1016/0038–1101(86)90191–7. – ISSN 0038–1101

[46] MALERBA, C. ; BICCARI, F. ; RICARDO, C. L. ; D'INCAU, M. ; SCARDI, P. ; MITTIGA, A.: Absorption coefficient of bulk and thin film Cu_2O. In: *Solar Energy Materials and Solar Cells* 95 (2011), Nr. 10, 2848 - 2854. http://dx.doi.org/http://doi.org/10.1016/j.solmat.2011.05.047. – DOI http://doi.org/10.1016/j.solmat.2011.05.047. – ISSN 0927–0248

[47] MINAMI, Tadatsugu ; NISHI, Yuki ; MIYATA, Toshihiro: Cu_2O-based solar cells using oxide semiconductors. In: *Journal of Semiconductors* 37 (2016), Nr. 1, 014002. http://stacks.iop.org/1674-4926/37/i=1/a=014002

[48] SVENSSON, B.G. ; PEARTON, S. ; JAGADISH, C.: *Oxide Semiconductors*. Elsevier Science, 2013 (Semiconductors and Semimetals). – ISBN 9780123965455

[49] KNOX, R. S.: *Theory of excitons*. Academic Press, 1963 (Solid state physics: Supplement)

[50] YU, Peter Y. ; CARDONA, Manuel: *Fundamentals of Semiconductors: Physics and Materials Properties*. Springer Berlin Heidelberg, 2013 http://www.springer.com/de/book/9783642007095. – ISBN 9783662038482

[51] MADELUNG, Otfried: *Introduction to Solid-State Theory*. Springer, 1996 (Springer Series in Solid-State Sciences). http://www.springer.com/de/book/9783540604433. – ISBN 9783540604433

[52] SCHÄFER, W. ; WEGENER, M.: *Semiconductor Optics and Transport Phenomena*. Springer Berlin Heidelberg, 2013 (Advanced Texts in Physics). http://www.springer.com/de/

book/9783540616146. – ISBN 9783662046630

[53] RIDLEY, B.K.: *Quantum Processes in Semiconductors*. OUP Oxford, 2013. – ISBN 9780199677214

[54] ROBERTSON, John: Electronic structure and x-ray near-edge core spectra of Cu_2O. In: *Phys. Rev. B* 28 (1983), Sep, 3378–3385. http://dx.doi.org/10.1103/PhysRevB.28.3378. – DOI 10.1103/PhysRevB.28.3378

[55] DAHL, J.P. ; SWITENDICK, A.C.: Energy bands in cuprous oxide. In: *Journal of Physics and Chemistry of Solids* 27 (1966), Nr. 6, 931 - 942. http://dx.doi.org/https://doi.org/10.1016/0022-3697(66)90064-3. – DOI https://doi.org/10.1016/0022–3697(66)90064–3. – ISSN 0022–3697

[56] FRENCH, M. ; SCHWARTZ, R. ; STOLZ, H. ; REDMER, R.: Electronic band structure of Cu_2O by spin density functional theory. In: *Journal of Physics: Condensed Matter* 21 (2008), Nr. 1

[57] KLEINMAN, Leonard ; MEDNICK, Kenneth: Self-consistent energy bands of Cu_2O. In: *Phys. Rev. B* 21 (1980), Feb, 1549–1553. http://dx.doi.org/10.1103/PhysRevB.21.1549. – DOI 10.1103/PhysRevB.21.1549

[58] MARKSTEINER, P. ; BLAHA, P. ; SCHWARZ, K.: Electronic structure and binding mechanism of Cu_2O. In: *Zeitschrift für Physik B Condensed Matter* 64 (1986), Jun, Nr. 2, 119–127. http://dx.doi.org/10.1007/BF01303692. – DOI 10.1007/BF01303692. – ISSN 1431–584X

[59] RUIZ, Eliseo ; ALVAREZ, Santiago ; ALEMANY, Pere ; EVARESTOV, Robert A.: Electronic structure and properties of Cu_2O. In: *Phys. Rev. B* 56 (1997), Sep, 7189–7196. http://dx.doi.org/10.1103/PhysRevB.56.7189. – DOI 10.1103/PhysRevB.56.7189

[60] BRUNEVAL, Fabien ; VAST, Nathalie ; REINING, Lucia ; IZQUIERDO, M. ; SIROTTI, F. ; BARRETT, N.: Exchange and Correlation Effects in Electronic Excitations of Cu_2O. In: *Phys. Rev. Lett.* 97 (2006), Dec, 267601. http://dx.doi.org/10.1103/PhysRevLett.97.267601. – DOI 10.1103/PhysRevLett.97.267601

[61] GRUN, J. B. ; NIKITINE, S.: Étude de la forme des raies des séries jaune et verte de la cuprite. In: *Journal de Physique* 24 (1963), Nr. 6, 355–358. http://dx.doi.org/10.1051/jphys:01963002406035500. – DOI 10.1051/jphys:01963002406035500

[62] UIHLEIN, Ch. ; FRÖHLICH, D. ; KENKLIES, R.: Investigation of exciton fine structure in Cu_2O. In: *Phys. Rev. B* 23 (1981), Mar, 2731–2740. http://dx.doi.org/10.1103/PhysRevB.23.2731. – DOI 10.1103/PhysRevB.23.2731

[63] NIKITINE, S. ; GRUN, J.B. ; SIESKIND, M.: Étude spectrophotometrique de la serie jaune

de Cu_2O aux basses temperatures. In: *Journal of Physics and Chemistry of Solids* 17

[64] DAUNOIS, A. ; DEISS, J. L. ; MEYER, B.: Étude spectrophotométrique de l'absorption bleue et violette de Cu_2O. In: *J. Phys. France* 27 (1966), Nr. 3. http://dx.doi.org/10.1051/jphys:01966002703-4014200. – DOI 10.1051/jphys:01966002703–4014200

[65] BRAHMS, S. ; NIKITINE, S. ; DAHL, J.P.: On the band structure and the absorption spectrum of Cu_2O. In: *Physics Letters* 22 (1966), Nr. 1, 31 - 33. http://dx.doi.org/https://doi.org/10.1016/0031-9163(66)90044-8. – DOI https://doi.org/10.1016/0031–9163(66)90044–8. – ISSN 0031–9163

[66] HODBY, J. W. ; JENKINS, T. E. ; SCHWAB, C. ; TAMURA, H. ; TRIVICH, D.: Cyclotron resonance of electrons and of holes in cuprous oxide, Cu_2O. In: *Journal of Physics C: Solid State Physics* 9 (1976), Nr. 8, 1429. http://stacks.iop.org/0022-3719/9/i=8/a=014

[67] NAKA, N. ; AKIMOTO, I. ; SHIRAI, M. ; KAN'NO, K.: Time-resolved cyclotron resonance in cuprous oxide. In: *Phys. Rev. B* 85 (2012), Jan, 035209. http://dx.doi.org/10.1103/PhysRevB.85.035209. – DOI 10.1103/PhysRevB.85.035209

[68] KRAMERS, H. A.: General theory of paramagnetic rotation in crystals. In: *Proc. Acad. Sci. Amsterdam* Bd. 33, 1930, S. 959

[69] LAMB, Jeroen S. ; ROBERTS, John A.: Time-reversal symmetry in dynamical systems: A survey. In: *Physica D: Nonlinear Phenomena* 112 (1998), Nr. 1, 1 - 39. http://dx.doi.org/https://doi.org/10.1016/S0167-2789(97)00199-1. – DOI https://doi.org/10.1016/S0167–2789(97)00199–1. – ISSN 0167–2789. – Proceedings of the Workshop on Time-Reversal Symmetry in Dynamical Systems

[70] KOSTER, G. F.: *Properties of the thirty-two point groups*. Bd. 24. The MIT Press, 1963

[71] DRESSELHAUS, G. ; KIP, A. F. ; KITTEL, C.: Cyclotron Resonance of Electrons and Holes in Silicon and Germanium Crystals. In: *Phys. Rev.* 98 (1955), Apr, 368–384. http://dx.doi.org/10.1103/PhysRev.98.368. – DOI 10.1103/PhysRev.98.368

[72] VOON, L.C.L.Y. ; WILLATZEN, M.: *The k p Method: Electronic Properties of Semiconductors*. Springer Berlin Heidelberg, 2009 http://www.springer.com/de/book/9783540928713. – ISBN 9783540928720

[73] LUTTINGER, J. M. ; KOHN, W.: Motion of Electrons and Holes in Perturbed Periodic Fields. In: *Phys. Rev.* 97 (1955), Feb, 869–883. http://dx.doi.org/10.1103/PhysRev.97.869. – DOI 10.1103/PhysRev.97.869

[74] ELLIOTT, R. J.: Theory of the Effect of Spin-Orbit Coupling on Magnetic Resonance in Some Semiconductors. In: *Phys. Rev.* 96 (1954), Oct, 266–279. http://dx.doi.org/

10.1103/PhysRev.96.266. – DOI 10.1103/PhysRev.96.266

[75] SUZUKI, K. ; HENSEL, J. C.: Quantum resonances in the valence bands of germanium. I. Theoretical considerations. In: *Phys. Rev. B* 9 (1974), May, 4184–4218. http://dx.doi.org/10.1103/PhysRevB.9.4184. – DOI 10.1103/PhysRevB.9.4184

[76] LUTTINGER, J. M.: Quantum Theory of Cyclotron Resonance in Semiconductors: General Theory. In: *Phys. Rev.* 102 (1956), May, 1030–1041. http://dx.doi.org/10.1103/PhysRev.102.1030. – DOI 10.1103/PhysRev.102.1030

[77] BRANDT, Jan ; FRÖHLICH, Dietmar ; SANDFORT, Christian ; BAYER, Manfred ; STOLZ, Heinrich ; NAKA, Nobuko: Ultranarrow Optical Absorption and Two-Phonon Excitation Spectroscopy of Cu_2O Paraexcitons in a High Magnetic Field. In: *Phys. Rev. Lett.* 99 (2007), Nov, 217403. http://dx.doi.org/10.1103/PhysRevLett.99.217403. – DOI 10.1103/PhysRevLett.99.217403

[78] FRÖHLICH, Dietmar ; BRANDT, Jan ; SANDFORT, Christian ; BAYER, Manfred ; STOLZ, Heinrich: Anisotropic effective mass of orthoexcitons in Cu_2O. In: *Phys. Rev. B* 84 (2011), Nov, 193205. http://dx.doi.org/10.1103/PhysRevB.84.193205. – DOI 10.1103/PhysRevB.84.193205

[79] DASBACH, G. ; FRÖHLICH, D. ; KLIEBER, R. ; SUTER, D. ; BAYER, M. ; STOLZ, H.: Wave-vector-dependent exchange interaction and its relevance for the effective exciton mass in Cu_2O. In: *Phys. Rev. B* 70 (2004), Jul, 045206. http://dx.doi.org/10.1103/PhysRevB.70.045206. – DOI 10.1103/PhysRevB.70.045206

[80] KUWATA-GONOKAMI, Makoto ; KUBOUCHI, Motoyoshi ; SHIMANO, Ryo ; MYSYROWICZ, Andre: Time-resolved excitonic Lyman spectroscopy of Cu_2O. In: *Journal of the Physical Society of Japan* 73 (2004), Nr. 4, S. 1065–1069

[81] O'HARA, Keith E.: *Relaxation kinetics of excitons in cuprous oxide*, University of Illinois, Thesis, february 1999

[82] KOJEVNIKOV, Alexei B.: *Paul Dirac and Igor Tamm Correspondence, Part 1: 1928 — 1933*. published by Max—Planck-Institut fur Physik, Werner—Heisenberg-Institut, 1928 — 1933

[83] BIR, G. L. ; PIKUS, G. E.: *Symmetry and Strain-induced Effects in Semiconductors*. Wiley, 1974 (A Halsted Press book). – ISBN 9780470073216

[84] DAWSON, P. ; HARGREAVE, M.M. ; WILKINSON, G.R.: The dielectric and lattice vibrational spectrum of cuprous oxide. In: *Journal of Physics and Chemistry of Solids* 34 (1973), Nr. 12, 2201 - 2208. http://dx.doi.org/http://dx.doi.org/10.1016/S0022-3697(73)80067-8. – DOI http://dx.doi.org/10.1016/S0022–3697(73)80067–

8. – ISSN 0022–3697

[85] RÖSELER, J.: A new variational ansatz in the polaron theory. In: *physica status solidi (b)* 25 (1968), Nr. 1, 311–316. http://dx.doi.org/10.1002/pssb.19680250129. – DOI 10.1002/pssb.19680250129. – ISSN 1521–3951

[86] WEICHMAN, FL: Some Rationale for the Unusual Behavior of the Dielectric Constant of Cu_2O. In: *Canadian Journal of Physics* 51 (1973), Nr. 6, S. 680–685

[87] REIMANN, K. ; SYASSEN, K.: Raman scattering and photoluminescence in Cu_2O under hydrostatic pressure. In: *Phys. Rev. B* 39 (1989), May, 11113–11119. http://dx.doi.org/10.1103/PhysRevB.39.11113. – DOI 10.1103/PhysRevB.39.11113

[88] HECKÖTTER, J. ; FREITAG, M. ; FRÖHLICH, D. ; ASSMANN, M. ; BAYER, M. ; SEMINA, M. A. ; GLAZOV, M. M.: High-resolution study of the yellow excitons in Cu_2O subject to an electric field. In: *Phys. Rev. B* 95 (2017), Jan, 035210. http://dx.doi.org/10.1103/PhysRevB.95.035210. – DOI 10.1103/PhysRevB.95.035210

[89] SCHWEINER, F. ; MAIN, J. ; WUNNER, G.: Linewidths in excitonic absorption spectra of cuprous oxide. In: *Phys. Rev. B* 93 (2016), Feb, 085203. http://dx.doi.org/10.1103/PhysRevB.93.085203. – DOI 10.1103/PhysRevB.93.085203

[90] ZIELIŃSKA-RACZYŃSKA, S. ; ZIEMKIEWICZ, D. ; CZAJKOWSKI, G.: Electro-optical properties of Rydberg excitons. In: *Phys. Rev. B* 94 (2016), Jul, 045205. http://dx.doi.org/10.1103/PhysRevB.94.045205. – DOI 10.1103/PhysRevB.94.045205

[91] SCHÖNE, F. ; KRÜGER, S.-O. ; GRÜNWALD, P. ; STOLZ, H. ; SCHEEL, S. ; ASSMANN, M. ; HECKÖTTER, J. ; THEWES, J. ; FRÖHLICH, D. ; BAYER, M.: Deviations of the exciton level spectrum in Cu_2O from the hydrogen series. In: *Phys. Rev. B* 93 (2016), Feb, 075203. http://dx.doi.org/10.1103/PhysRevB.93.075203. – DOI 10.1103/PhysRevB.93.075203

[92] SCHÖNE, Florian ; KRÜGER, Sjard-Ole ; GRÜNWALD, Peter ; ASSMANN, Marc ; HECKÖTTER, Julian ; THEWES, Johannes ; STOLZ, Heinrich ; FRÖHLICH, Dietmar ; BAYER, Manfred ; SCHEEL, Stefan: Coupled valence band dispersions and the quantum defect of excitons in Cu 2 O. In: *Journal of Physics B: Atomic, Molecular and Optical Physics* 49 (2016), Nr. 13, 134003. http://stacks.iop.org/0953-4075/49/i=13/a=134003

[93] BALMER, J. J.: Notiz über die Spectrallinien des Wasserstoffs. In: *Annalen der Physik* 261 (1885), Nr. 5, 80–87. http://dx.doi.org/10.1002/andp.18852610506. – DOI 10.1002/andp.18852610506. – ISSN 1521–3889

[94] SEATON, M. J.: Quantum defect theory. In: *Reports on Progress in Physics* 46 (1983), Nr. 2, 167. http://stacks.iop.org/0034-4885/46/i=2/a=002

[95] ZIMMERMANN, R.: *Many-particle theory of highly excited semiconductors*. BSB B.G. Teubner, 1988 (Teubner-Texte zur Physik)

[96] MYSYROWICZ, A. ; HULIN, D. ; ANTONETTI, A.: Long Exciton Lifetime in Cu_2O. In: *Phys. Rev. Lett.* 43 (1979), Oct, 1123–1126. http://dx.doi.org/10.1103/PhysRevLett.43.1123. – DOI 10.1103/PhysRevLett.43.1123

[97] FRÖHLICH, D. ; KENKLIES, R. ; UIHLEIN, Ch. ; SCHWAB, C.: Assignment of the Even-Parity Excitons in Cu_2O. In: *Phys. Rev. Lett.* 43 (1979), Oct, 1260–1263. http://dx.doi.org/10.1103/PhysRevLett.43.1260. – DOI 10.1103/PhysRevLett.43.1260

[98] HERTEL, I.V. ; SCHULZ, C.P.: *Atome, Moleküle und optische Physik 1: Atomphysik und Grundlagen der Spektroskopie*. Springer Berlin Heidelberg, 2015 (Springer-Lehrbuch). http://www.springer.com/de/book/9783662531037. – ISBN 9783662468081

[99] LUKIN, M. D. ; FLEISCHHAUER, M. ; COTE, R. ; DUAN, L. M. ; JAKSCH, D. ; CIRAC, J. I. ; ZOLLER, P.: Dipole Blockade and Quantum Information Processing in Mesoscopic Atomic Ensembles. In: *Phys. Rev. Lett.* 87 (2001), Jun, 037901. http://dx.doi.org/10.1103/PhysRevLett.87.037901. – DOI 10.1103/PhysRevLett.87.037901

[100] TONG, D. ; FAROOQI, S. M. ; STANOJEVIC, J. ; KRISHNAN, S. ; ZHANG, Y. P. ; CÔTÉ, R. ; EYLER, E. E. ; GOULD, P. L.: Local Blockade of Rydberg Excitation in an Ultracold Gas. In: *Phys. Rev. Lett.* 93 (2004), Aug, 063001. http://dx.doi.org/10.1103/PhysRevLett.93.063001. – DOI 10.1103/PhysRevLett.93.063001

[101] KRÜGER, Sjard O. ; SCHEEL, Stefan: *Trapping of Rydberg excitons in Cu_2O by strain traps derived from cylindrical stressors*. – submitted to Phys. Rev. B.

[102] SZMYTKOWSKI, R.: Alternative approach to the solution of the momentum-space Schrödinger equation for bound states of the N-dimensional Coulomb problem. In: *Annalen der Physik* 524 (2012), Nr. 6-7, 345–352. http://dx.doi.org/10.1002/andp.201100330. – DOI 10.1002/andp.201100330. – ISSN 1521–3889

[103] KRÜGER, Sjard O.: *Quantum Defects of Rydberg Excitons in Cuprous Oxide*, Universität Rostock, Master Thesis, April 2016

[104] ATKINSON, K. ; HAN, W.: *Spherical Harmonics and Approximations on the Unit Sphere: An Introduction*. Springer Berlin Heidelberg, 2012 (Lecture Notes in Mathematics). http://link.springer.com/book/10.1007%2F978-3-642-25983-8. – ISBN 9783642259838

[105] JEFFREY, A. ; ZWILLINGER, D.: *Table of Integrals, Series, and Products*. Elsevier Science, 2007 (Table of Integrals, Series, and Products Series). – ISBN 9780080471112

[106] KUO, Cheng-Deng: The uncertainties in radial position and radial momentum of an

electron in the non-relativistic hydrogen-like atom. In: *Annals of Physics* 316 (2005), Nr. 2, 431 - 439. http://dx.doi.org/https://doi.org/10.1016/j.aop.2004.09.005. – DOI https://doi.org/10.1016/j.aop.2004.09.005. – ISSN 0003–4916

[107] KORZHAVYI, P. A. ; JOHANSSON, B.: *Literature review on the properties of cuprous oxide Cu_2O and the process of copper oxidation*. Swedish Nuclear Fuel and Waste Management Company, 2011

[108] NAKA, N. ; HASHIMOTO, S. ; ISHIHARA, T.: Thin Films of Single-Crystal Cuprous Oxide Grown from the Melt. In: *Japanese Journal of Applied Physics* 44 (2005), Nr. 7R, 5096. http://stacks.iop.org/1347-4065/44/i=7R/a=5096

[109] CASWELL, N. ; WEINER, J.S. ; YU, P.Y.: A study of non-thermalized luminescence spectra: the case of Cu_2O. In: *Solid State Communications* 40 (1981), Nr. 9, 843 - 846. http://dx.doi.org/https://doi.org/10.1016/0038-1098(81)90168-X. – DOI https://doi.org/10.1016/0038–1098(81)90168–X. – ISSN 0038–1098

[110] O'HARA, K. E. ; WOLFE, J. P.: Relaxation kinetics of excitons in cuprous oxide. In: *Phys. Rev. B* 62 (2000), Nov, 12909–12922. http://dx.doi.org/10.1103/PhysRevB.62.12909. – DOI 10.1103/PhysRevB.62.12909

[111] KITAMURA, Tatsuya ; TAKAHATA, Mitsuyoshi ; NAKA, Nobuko: Quantum number dependence of the photoluminescence broadening of excitonic Rydberg states in cuprous oxide. In: *Journal of Luminescence* (2017). http://dx.doi.org/https://doi.org/10.1016/j.jlumin.2017.07.060. – DOI https://doi.org/10.1016/j.jlumin.2017.07.060. – ISSN 0022–2313

[112] SNOKE, D. W. ; WOLFE, J. P. ; MYSYROWICZ, A.: Evidence for Bose-Einstein condensation of a two-component exciton gas. In: *Phys. Rev. Lett.* 64 (1990), May, 2543–2546. http://dx.doi.org/10.1103/PhysRevLett.64.2543. – DOI 10.1103/PhysRevLett.64.2543

[113] LIN, Jia L. ; WOLFE, J. P.: Bose-Einstein condensation of paraexcitons in stressed Cu_2O. In: *Phys. Rev. Lett.* 71 (1993), Aug, 1222–1225. http://dx.doi.org/10.1103/PhysRevLett.71.1222. – DOI 10.1103/PhysRevLett.71.1222

[114] YOSHIOKA, Kosuke ; CHAE, Eunmi ; KUWATA-GONOKAMI, Makoto: Transition to a Bose–Einstein condensate and relaxation explosion of excitons at sub-Kelvin temperatures. In: *Nature communications* 2 (2011), S. 328

[115] AVERY, J.S.: *Hyperspherical Harmonics and Generalized Sturmians*. Springer Netherlands, 2002 (Progress in Theoretical Chemistry and Physics). https://link.springer.com/book/10.1007/0-306-46944-8. – ISBN 9781402004094

[116] CHAO, Calvin Yi-Ping ; CHUANG, Shun L.: Spin-orbit-coupling effects on the valence-

band structure of strained semiconductor quantum wells. In: *Phys. Rev. B* 46 (1992), Aug, 4110–4122. http://dx.doi.org/10.1103/PhysRevB.46.4110. – DOI 10.1103/PhysRevB.46.4110

[117] HAKEN, Hermann: Zur Quantentheorie des Mehrelektronensystems im schwingenden Gitter. I. In: *Zeitschrift für Physik A Hadrons and Nuclei* 146 (1956), Nr. 5, S. 527–554

[118] POLLMANN, J. ; BÜTTNER, H.: Effective Hamiltonians and bindings energies of Wannier excitons in polar semiconductors. In: *Phys. Rev. B* 16 (1977), Nov, 4480–4490. http://dx.doi.org/10.1103/PhysRevB.16.4480. – DOI 10.1103/PhysRevB.16.4480

[119] KUPER, C. G.: Polarons and excitons. In: *Physics Today* 16 (1963), S. 106

[120] ELLIOTT, R. J.: Intensity of Optical Absorption by Excitons. In: *Phys. Rev.* 108 (1957), Dec, 1384–1389. http://dx.doi.org/10.1103/PhysRev.108.1384. – DOI 10.1103/PhysRev.108.1384

[121] SCHÖNE, Florian ; STOLZ, Heinrich ; NAKA, Nobuko: Phonon-assisted absorption of excitons in Cu_2O. In: *Phys. Rev. B* 96 (2017), Sep, 115207. http://dx.doi.org/10.1103/PhysRevB.96.115207. – DOI 10.1103/PhysRevB.96.115207

[122] KLINGSHIRN, Claus F.: *Semiconductor Optics*. Springer Berlin Heidelberg, 2012 (Graduate Texts in Physics). http://www.springer.com/de/book/9783642283611. – ISBN 9783642283628

[123] BOHNEN, Klaus-Peter ; HEID, Rolf ; PINTSCHOVIUS, Lothar ; SOON, Aloysius ; STAMPFL, Catherine: Ab initio lattice dynamics and thermal expansion of Cu_2O. In: *Phys. Rev. B* 80 (2009), Oct, 134304. http://dx.doi.org/10.1103/PhysRevB.80.134304. – DOI 10.1103/PhysRevB.80.134304

[124] SCHMUTZLER, Johannes ; FRÖHLICH, Dietmar ; BAYER, Manfred: Signatures of coherent propagation of blue polaritons in Cu_2O. In: *Phys. Rev. B* 87 (2013), Jun, 245202. http://dx.doi.org/10.1103/PhysRevB.87.245202. – DOI 10.1103/PhysRevB.87.245202

[125] KAVOULAKIS, G. M. ; BAYM, Gordon ; WOLFE, J. P.: Quantum saturation and condensation of excitons in Cu_2O: A theoretical study. In: *Phys. Rev. B* 53 (1996), Mar, 7227–7243. http://dx.doi.org/10.1103/PhysRevB.53.7227. – DOI 10.1103/PhysRevB.53.7227

[126] SCHWARTZ, R.: *Absorption spectrum of a Cu_2O sample of thickness $220\,\mu m$ at room temperature*. – private communication

[127] BOSE, S.N.: Planck's law and light quantum hypothesis. In: *Z. Phys* 26 (1924), Nr. 1, S. 178

[128] EINSTEIN, Albert: *Quantentheorie des einatomigen idealen Gases*. Akademie der Wissenshaften, in Kommission bei W. de Gruyter, 1924

[129] ANDERSON, M. H. ; ENSHER, J. R. ; MATTHEWS, M. R. ; WIEMAN, C. E. ; CORNELL, E. A.: Observation of Bose-Einstein Condensation in a Dilute Atomic Vapor. In: *Science* 269 (1995), Nr. 5221, 198-201. http://www.jstor.org/stable/2888436. – ISSN 00368075, 10959203

[130] DAVIS, K. B. ; MEWES, M. O. ; ANDREWS, M. R. ; DRUTEN, N. J. ; DURFEE, D. S. ; KURN, D. M. ; KETTERLE, W.: Bose-Einstein Condensation in a Gas of Sodium Atoms. In: *Phys. Rev. Lett.* 75 (1995), Nov, 3969–3973. http://dx.doi.org/10.1103/PhysRevLett.75.3969. – DOI 10.1103/PhysRevLett.75.3969

[131] CASELLA, R. C.: Excitons in InP at High Excitation Levels. In: *Journal of Applied Physics* 36 (1965), Nr. 8, 2485-2487. http://dx.doi.org/10.1063/1.1714516. – DOI 10.1063/1.1714516

[132] SEMKAT, Dirk ; SOBKOWIAK, Siegfried ; SCHÖNE, Florian ; STOLZ, Heinrich ; KOCH, Thomas ; FEHSKE, Holger: Multicomponent exciton gas in cuprous oxide: cooling behaviour and the role of Auger decay. In: *Journal of Physics B: Atomic, Molecular and Optical Physics* 50 (2017), Nr. 20, 204001. http://stacks.iop.org/0953-4075/50/i=20/a=204001

[133] SCHWARTZ, Rico ; NAKA, Nobuko ; KIESELING, Frank ; STOLZ, Heinrich: Dynamics of excitons in a potential trap at ultra-low temperatures: paraexcitons in Cu 2 O. In: *New Journal of Physics* 14 (2012), Nr. 2, 023054. http://stacks.iop.org/1367-2630/14/i=2/a=023054

[134] YOSHIOKA, Kosuke ; KUWATA-GONOKAMI, Makoto: Absorption imaging of trapped $1s$ paraexcitons in bulk Cu_2O. In: *Phys. Rev. B* 91 (2015), May, 195207. http://dx.doi.org/10.1103/PhysRevB.91.195207. – DOI 10.1103/PhysRevB.91.195207

[135] JANG, J.I. ; WOLFE, J.P.: Exciton decay in Cu_2O at high density and low temperature: Auger recombination, spin–flip scattering, and molecule formation. In: *Solid State Communications* 137 (2006), Nr. 1, 91 - 96. http://dx.doi.org/https://doi.org/10.1016/j.ssc.2005.10.001. – DOI https://doi.org/10.1016/j.ssc.2005.10.001. – ISSN 0038–1098

[136] SOBKOWIAK, Siegfried: *Theoretische Beschreibung von Exzitonen in druckinduzierten Potentialfallen bei ultratiefen Temperaturen in Kupferoxydul*, Universität Rostock, Thesis, Dezember 2014

[137] WOLFE, James P. ; JANG, Joon I.: New perspectives on kinetics of excitons in Cu_2O. In: *Solid State Communications* 134 (2005), Nr. 1, 143 -

149. http://dx.doi.org/https://doi.org/10.1016/j.ssc.2004.06.046. – DOI https://doi.org/10.1016/j.ssc.2004.06.046. – ISSN 0038–1098

[138] BASTARD, G.: *Wave mechanics applied to semiconductor heterostructures*. Les Éditions de Physique, 1988 (Monographies de physique). – ISBN 9780470217085

[139] URBACH, Franz: The Long-Wavelength Edge of Photographic Sensitivity and of the Electronic Absorption of Solids. In: *Phys. Rev.* 92 (1953), Dec, 1324–1324. http://dx.doi.org/10.1103/PhysRev.92.1324. – DOI 10.1103/PhysRev.92.1324

[140] JOHN, Sajeev ; SOUKOULIS, Costas ; COHEN, Morrel H. ; ECONOMOU, E. N.: Theory of Electron Band Tails and the Urbach Optical-Absorption Edge. In: *Phys. Rev. Lett.* 57 (1986), Oct, 1777–1780. http://dx.doi.org/10.1103/PhysRevLett.57.1777. – DOI 10.1103/PhysRevLett.57.1777

[141] TOYOZAWA, Y.: Theory of Line-Shapes of the Exciton Absorption Bands. In: *Progress of Theoretical Physics* 20 (1958), Nr. 1, 53. http://dx.doi.org/10.1143/PTP.20.53. – DOI 10.1143/PTP.20.53

Acknowledgements

This work would not have been possible without the help of many people, whom I want to thank for their support. First and foremost, I am grateful to Prof. Dr. Heinrich Stolz for his guidance, his help (whether mathematical or semiconductor related), and especially for giving me the opportunity to work as a theorist in an experimental research group. Secondly, I am grateful to Prof. Dr. Stefan Scheel, who acquiesced to house our theory branch of the semiconductor optics, for his help during our collaboration, and for allowing me to finish my thesis unhurriedly with the finish line in sight.
A lot of thanks goes to the colleagues of my office, especially Dr. Dirk Semkat for his help with all kinds of various physics problems over the years, but also Sjard Ole Krüger for the productive discussions about group theory and excitons. I also have to thank those two, as well as Dr. Markus Kurz and Melanie Schünemann for proofreading the whole work in its different stages. Furthermore I want to thank Prof. Dr. Nobuko Naka for readily sharing her data with me, as well as the nice and insightful correspondence about absorption and luminescence spectroscopy. I also need to thank Dr. Martin French for bearing a lot of my stupid questions concerning DFT and band structures.
Last but not least, I want to thank my friends and family, who helped me clear my mind when necessary, especially my parents, who enabled me to get as far as I got.

Selbstständigkeitserklärung

Hiermit versichere ich an Eides statt, dass ich die vorliegende Arbeit selbstständig angefertigt und ohne fremde Hilfe verfasst, keine außer den von mir angegebenen Hilfsmitteln und Quellen dazu verwendet und die den benutzten Werken inhaltlich und wörtlich entnommenen Stellen als solche kenntlich gemacht habe.

Florian Schöne
Rostock, den 06.11.2017